

**FABRICATION, CHARACTERIZATION AND APPLICATION OF NANO
CARBON COMPOSITE MATERIALS**

by

JOHN LANDERS

A dissertation submitted to the
Graduate School – New Brunswick
Rutgers, The State University of New Jersey
in partial fulfillment of the requirements

for the degree of

Doctor of Philosophy

Graduate Program in Chemical and Biochemical Engineering

written under the direction of

Professor Alexander V. Neimark

And approved by

New Brunswick, New Jersey

October 2012

ABSTRACT OF THE DISSERTATION

Fabrication, Characterization and Application of Porous Nano Carbon Composites

By JOHN LANDERS

Dissertation Director:

Professor Alexander V. Neimark

Nanotechnology is an emerging field with the promise for new materials and applications in a variety of fields including medicine, drug delivery, catalysis and sustainable energy. At the forefront of these endeavors are nanocarbon materials such as carbon nanotubes and graphene. Their inclusion into a host of composite materials have endowed materials with significant properties such as enhance mechanical strength, electrical and thermal conductivity and improved functions such as drug delivery and catalysis. In many cases there is a further desire to make composites of these materials porous with a high internal surface area. Doing so will allow opportunities to optimize the pore size distribution tailored towards specific applications. It is aim of this work to demonstrate the versatility of these nanocarbon materials highlighting their usage in porous materials. The fabrication of these porous nano carbon materials is detailed through several techniques including wet spinning, sol-gel chemistry and forced impregnation. The characterization aspect is discussed at length focusing primarily on the porosimetetry results obtained from gas adsorption isotherms. Finally, the application of these composites are demonstrated in their use to enhance stem cell differentiation, as fiber composites for neural tissue engineering, catalysis and in the area of ultracapacitors.

Acknowledgements

I would like to thank my advisor Prof. Alexander V. Neimark for his helpful guidance and support throughout my time as his student. His encouragement and assistance has been vital and I am extremely grateful for the freedom that he has given me to develop as a bona fide scientist by allowing me to reach out and seek outside collaborations. I believe that if not for this I would not have developed into the mature investigator I am today who possesses a deep passion for science, an attribute that unfortunately does affect some of my peers who have gone through the same process. In addition to my advisor I would like to thank and acknowledge members of my committee: Arthur Chester who has assisted me from the beginning with a great deal of support, Gerardo Callegari for his expertise and mentorship, Prabas Moghe for his invaluable critiques and advice and Joachim Kohn for shrewd discussions. I would also like to acknowledge the members of Prof. Neimark's group for sharing their knowledge, expertise, assistance, critiques, and time during my stay in the group: Chris Rasmussen, Ming-Tsung Lee, Richard Cimino, Gennady Gor and Aleksey Vishnyakov, all of whom have offered invaluable assessments of my work. I would like to thank a number of fellow graduate students who, be it through friendship, helpful discourse, or imparting experience have greatly impacted my experience here at Rutgers: Omar Haq, Mike Tomasini, Erhan Bilal, Mike Drahl, Haohan Wu and Johnny Bass to name a few. Above all I would also like to acknowledge the many undergraduates who I had the honor to mentor. The opportunity to mentor them has been a great privilege and I believe I have learned more from them than they have accumulated from me. Finally I would like to acknowledge the following people for supplementary support over the years: Jenna Budge, Glenn Fogarty, and Ryan Loughran.

Dedication

I dedicate this thesis to my parents Donna and David for their love and support while I endeavored to earn my degree. In addition I would like to thank my siblings: twin brother David, brother Jay and sister Vicki, as well as my nephews Kyle and Jayson.

Table of Contents

ABSTRACT	II
ACKNOWLEDGEMENTS	III
DEDICATION	IV
TABLE OF CONTENTS	V
LIST OF TABLES	VIII
LIST OF FIGURES	IX
CHAPTER 1 INTRODUCTION TO NANO CARBON AND POROUS MATERIALS	1
CHAPTER 2 APPLICATION OF DENSITY FUNCTIONAL THEORY METHOD FOR CHARACTERIZATION OF POROUS MATERIALS	4
2.1 Introduction.....	4
2.2 Description of the DFT Method	6
2.2.1 Non-Local Density Functional Theory	7
2.2.2 Drawbacks of NLDFT and Paths to Improvement.....	16
2.2.3 Quenched Solid Density Functional Theory	18
2.3 Recovering the pore size distribution (PSD) using DFT methods; DFT Kernels	22
2.3.1 Recovering the PSD using DFT methods	22
2.3.2 DFT Kernels for Characterization of Various Systems.....	25
2.3.3 Role of the adsorptive for characterization	27
2.4 Applications of DFT Kernels for carbonaceous and organic materials.....	28
2.4.1 Microporous carbons: NLDFT model of slit-shaped pores.....	28
2.4.2 Improvement of pore structure characterization with QSDFT model	38
2.4.3 Designer mesoporous carbons: hybrid QSDFT kernels	40
2.5 Applications of DFT Kernels for silica and other inorganic materials.....	45
2.5.1 Accounting for microporosity.	47
2.5.2 SBA-15 as the case study system.....	48
2.5.3 Oxides other than silica.	57
2.5.4 QSDFT model for silica materials.	59
2.5.5 Materials with cage-like structure: spherical pore model.....	60
2.5.6 Cavitation as a negative factor in pore size analysis	68
2.6 DFT models for interpretation of in-situ XDR data	73
2.7 Concluding Remarks	76
CHAPTER 3 FABRICATION OF NANOCARBON COMPOSITES.....	79
3.1 Properties of Carbon Nanotubes	79
3.2 Apparatus Construction.....	80

3.3	Fiber Fabrication.....	81
3.4	Fiber Fabrication with Agarose.....	89
3.5	Graphene Fibers	92
3.6	Conclusion	93
CHAPTER 4	NANO CARBON FIBER COMPOSITES FOR BIOLOGICAL APPLICATIONS	95
4.1	Introduction.....	95
4.2	Applications in Neural Tissue Engineering	96
4.2.1	Fiber fabrication.....	100
4.2.2	Agarose fiber functionalization.....	101
4.2.3	Mechanical Properties.....	106
4.2.4	Electrical properties	109
4.2.5	Cytotoxicity and cell attachment.....	111
4.2.6	In vivo evaluation	114
4.2.7	Results of in vivo characterization.....	116
4.2.8	Conclusions.....	120
4.3	Applications in Stem Cell Differentiation.....	121
4.3.1	Electrowetting of Scaffolds.....	122
4.3.2	Physics of Electrowetting.....	124
4.3.3	Electrowetting Setup	126
4.4	Forced Impregnation	128
4.5	Cell Differentiation Results	131
4.6	Electrical Stimulation.....	132
4.6.1	Tilted Scaffolds	134
4.7	Conclusion and Future Work	136
CHAPTER 5	ALUMINA CATALYST SUPPORTS	138
5.1	Experimental	140
5.1.1	Materials	140
5.1.2	Granulation and Extrusion	140
5.1.3	Characterization	142
5.2	Results and Discussion.....	143
5.2.1	Extrudate Characterization.....	143
5.2.2	Paste Characterization.....	147
5.2.3	Comparative investigation of extrudates of different mixers	149
5.3	Conclusion	152
CHAPTER 6	NANOCARBON AND ALUMINA COMPOSITES FOR ENERGY APPLICATIONS	153

6.1	Part I: Characterization and Application to Catalysis	153
6.1.1	Synthesis of Graphene Oxide.....	155
6.1.2	Characterization and Validation of Graphene Oxide	155
6.1.3	Graphene Oxide Alumina Support Synthesis.....	158
6.1.4	Impregnation and Catalysis.....	164
6.1.5	Conclusions.....	165
6.2	Part II: Applications in UltraCapacitors.....	166
6.2.1	Functionalization of GO with pseudocapacitance nanoparticles.....	169
6.2.2	Electrical measurements	170
6.3	Conclusion and Future Work	174
CHAPTER 7	CONCLUSIONS AND FUTURE PERSPECTIVES	176
REFERENCES	178

LIST OF TABLES

Table 1. Molecular interactions LJ parameters of nitrogen and argon used in NLDFT method.	10
Table 2. Parameters of the solid density distribution.	21
Table 3. Parameters of nitrogen.....	22
Table 1: CNF listed found in the literature.....	86
Table 2: Review of the literature of graphene fibers.	93
Table 3: Mechanical properties of fibers	107
Table 4: Conductivity measurements of dry and wet fibers.	111
Table 5: Electrical stimulation parameters found in the literature.....	122
Table 6: Surface area and pore volume for pastes prepared under different instrumental conditions.	150
Table 7: Graphene and metal nanoparticles for catalysis.	155
Table 8: Porosity summary of calcined alumina and calcined GO/alumina.	162
Table 9: Specific capacitance for GO/Al impregnated with KMnO_4	174

LIST OF FIGURES

Figure 1-1: Timeline of nanocarbon materials.	1
Figure 2-1. Experimental nitrogen (at 77.4 K) adsorption isotherm on MCM-41.....	11
Figure 2-2. Experimental isotherms of Ar (at 87 K) on a series of mesoporous molecular sieves.....	12
Figure 2-3. Adsorption and desorption for N ₂ (at 77 K) in MCM-41 and SBA-15	13
Figure 2-4. NLDFT N ₂ adsorption-desorption isotherm FDU-1 silica sample (points).	15
Figure 2-5. Density profiles of solid (squares) and fluid at different pressures along the adsorption branch.. (b) Prediction of krypton adsorption on SBA-15 silica at 119 K.	21
Figure 2-6. Kernels of selected equilibrium adsorption isotherms in slit-shaped pores.	24
Figure 2-7: Nitrogen adsorption isotherms at 77 K obtained for activated carbons derived from vine shoot designated as V739 and V840. Pore size distribution obtained by NLDFT	30
Figure 2-8: Differential and cumulative pore volume distributions of carbon fiber	33
Figure 2-9: Nitrogen and argon isotherms and pore size distributions	35
Figure 2-10: Pore size distribution calculated using the NLDFT slit pore model for etched and unetched CNT samples;	37
Figure 2-11: Comparison of the QSDFT and NLDFT methods for nitrogen adsorption for activated carbons.	40
Figure 2-12: Isotherm and corresponding pore size distribution CMK-3.....	42
Figure 2-13: Isotherm and corresponding pore size distribution for 3DOM materials of varying pore sizes.	44
Figure 2-14: Hard templating from silica spheres to produce mesoporous carbons.....	45
Figure 2-15: Isotherms for MCM-41 at N ₂ (77 K) and Ar at both 77 K and 87 K	47
Figure 2-16: Nitrogen isotherms for SBA-15 material.....	49
Figure 2-17: Nitrogen adsorption at 77.4 K on SBA-15 materials	51
Figure 2-18. Test of the NLDFT model for zeolite-containing materials.....	55
Figure 2-19. Pore size distributions and cumulative pore volumes for calcined nanocrystalline <i>n</i> -ZSM-5 materials prepared under high-temperature precrystallization	56
Figure 2-20 Experimental Argon (87.3 K) isotherm on socMOF	57
Figure 2-21: N ₂ isotherm at 77 K for nanoporous glass monoliths and PALS pore size distributions	58
Figure 2-22: N ₂ Desorption isotherms 77 K on extruded and calcined alumina pastes	59
Figure 2-23: High-resolution nitrogen (77.4 K) adsorption/desorption isotherm on SE3030 silica	62
Figure 2-24: Nitrogen sorption isotherms and pore size distribution of calcined mesoporous silica FDU-12	64
Figure 2-25: Nitrogen isotherms of KIT-5 treated with acid for various durations.	66
Figure 2-26: Nitrogen isotherms (at 77.4 K) in KIT-6 samples aged at different temperatures	68
Figure 2-27: Schematic illustration of cavitation and pore blocking.....	69
Figure 2-28. Distinguishing between cavitation effects in materials.....	71
Figure 2-29: N ₂ adsorption/desorption isotherms at 77.4 K for different soils.....	72
Figure 2-30: Nitrogen 77 K isotherm of a typical PHTS material.....	73
Figure 2-31. Evolution of the mass and electron density profiles of adsorbed fluid in the process of adsorption.	75
Figure 2-32. QSDFT prediction of the XRD intensities.	76
Figure 3-1: Apparatus construction of the wet spinning device.	81
Figure 3-2: Coiling mechanism of the PVA/CNT/BSA/Ascorbic Acid fibers upon drying.....	88
Figure 3-3: SEM of folded PVA/CNT/BSA/Ascorbic Acid fibers.	89
Figure 3-4. TEM images of molded fibers	91
Figure 3-5. SEM of CNT agarose fibers.	91
Figure 3-6: Schematic of dispersion mechanism for aggregates of carbon nanotube	92
Figure 3-7: Molded fibers of graphene oxide and agarose.	93
Figure 3-8: (a) Wet spinning process. (b& c) Two examples of variation in size, shape and morphology of NCAC wire-like fibers as shown by SEM. Both fibers are 200 μm wide at their largest point. (d& e) Bioactivation using fluorescent bovine serum albumin (green) and laminin (red) [227, 228]. (f) CNT based MAE[229]. (g) Microbore with 50 μm tapered opening used to produce ultrathin fibers. (h) Ultrathin NCAC electrode produced by wet spinning being approximately 26 μm in width. (i) Body image of a	

graphene/agarose produced electrode and (j) cross section of the same displaying the platelets of the graphene stacks.	94
Figure 4-1. BSAC- conjugate fibers and Laminin functionalized fibers	105
Figure 4-2. Cell viability studies	108
Figure 4-3. Immunohistochemical images of fibers inserted into rat cortex	117
Figure 4-4. Projection confocal images of fibers extracted from brains.....	119
Figure 4-5: Electrowetting set up.	127
Figure 4-6: Earlier prototype of multi pin electrode.....	128
Figure 4-7: Side view of droplets prior to electrowetting and after electrowetting.	128
Figure 4-8: Effects of electrowetting.....	128
Figure 4-9: Pressure induced wetting set up.....	129
Figure 4-10: Impregnated polymeric scaffold with an aqueous solution of CNT.	130
Figure 4-11: SEM of pressure induced wetted scaffolds.....	130
Figure 4-12: hESC Derived NSC differentiated in 2D, PLGA Scaffolds, or PLGA/CNT Scaffolds.	131
Figure 4-13: hiPSC Derived NSC differentiated in 2D, PLGA Scaffolds, or PLGA/CNT Scaffolds.	132
Figure 4-14: Schematic of the etched ITO glass with an etched non-conductive gap.....	133
Figure 4-15: Electrical stimulation board with 8 slots for application of constant current or voltage.....	133
Figure 4-16: Differentiated hESC on the PGLA scaffold and on the PGLA scaffold impregnated with carbon nanotubes.....	134
Figure 4-17: Tilted scaffolds impregnated at 5.5 °, 11 ° and 15 °.	135
Figure 4-18: Raman spectroscopy of tilted scaffold.....	136
Figure 5-1: Ideal properties of a catalyst support	138
Figure 5-2: A laboratory Fukae and an Eirich mixer used in pilot plant operations.....	142
Figure 5-3: View of the Fukae granulation as a function of time.	142
Figure 5-4: SEM of granulated particles.	143
Figure 5-5: BET surface areas results for the extruded samples as a function of mixing time.....	144
Figure 5-6: Total pore volume results for the extruded samples as a function of mixing time.	145
Figure 5-7: Pore size distribution as a function of mixing time for 0% acid	146
Figure 5-8: Pore size distribution as a function of mixing time for 1% acid.....	146
Figure 5-9: Crush strength as a function of mixing time.	147
Figure 5-10: D ₅₀ particle size values for the granulated samples as a function of mixing time.....	148
Figure 5-11: XRD patterns of uncalcined alumina pastes processed in a Fukae mixer and Eirich	148
Figure 5-12: Particle size distribution as a function of time for 1% acid.	149
Figure 5-13: Pore size distribution for pastes mixed and extruded by two different methods. The first term in parentheses signifies the type of mixer used, while the second term signifies the type of extruder used.	150
Figure 5-14: Particle size distribution as a function of time for pastes prepared via Eirich mixer.....	151
Figure 6-1: Raman spectra of graphite and graphene.	156
Figure 6-2: Raman spectroscopy of graphene oxide and graphite and X-ray photospectroscopy of graphene oxide and graphene oxide reduced via Fe nanoparticles.	157
Figure 6-3: TEM of single to a few layers of graphene oxide chemically exfoliated.....	158
Figure 6-4: Sol-gel of alumina and after mixing with graphene oxide.....	159
Figure 6-5. SEM images of granular dried sol-gels.....	159
Figure 6-6. TEM images of calcined alumina.	160
Figure 6-7. TEM images of on Pd nanoparticles on calcined GO/alumina.	161
Figure 6-8: N ₂ isotherms and corresponding pore size distribution for Alumina.	162
Figure 6-9: N ₂ isotherms and corresponding pore size distribution for GO/Alumina.	162
Figure 6-10: X-ray diffraction patterns of graphene.....	163
Figure 6-11: Powder XRD patterns of uncalcined alumina and uncalcined GO/alumina.	164
Figure 6-12: Powder XRD patterns of calcined alumina and calcined GO/alumina	164
Figure 6-13: Hydrogenation reaction of the conversion of styrene t with impregnated GO/Al and Al.....	165
Figure 6-14: Schematic of a traditional capacitor and ultracapacitor.....	167
Figure 6-15: Comparison between ultracapacitors and batteries.	168
Figure 6-16: Schematic of cyclic voltammetry for a MnO ₂ electrode cell	171
Figure 6-17: Cyclic-voltammetry measurements of GO/Al composite.	171

Figure 6-18: Cyclic-voltammetry measurements of GO/Al composite impregnated with KMnO_4 for 2 hours.	172
Figure 6-19: Cyclic-voltammetry measurements of GO/Al composite impregnated with KMnO_4 for 2 days.	172
Figure 6-20: SEM of impregnated GO/Al with KMnO_4 for 2 hours.	173
Figure 6-21: SEM of impregnated GO/Al with KMnO_4 for 24 hours.	173

Chapter 1 Introduction to nano carbon and porous materials

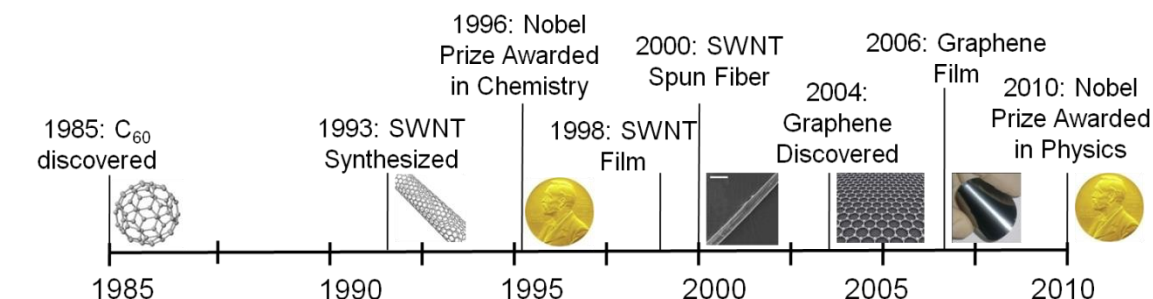


Figure 1-1: Timeline of nanocarbon materials.

Nano carbon materials have enjoyed intense research over the past three decades spurred by the discovery of fullerenes in 1985. This new allotrope of carbon was the first in a series of nano carbon materials that has attracted a lot of attention and garnered its discoverers the Nobel prize in chemistry in 1996. Shortly thereafter, in 1993, the discovery of single walled carbon nanotubes (CNT) was announced[1]. But unlike its predecessor which possessed poor electrical conducting properties (10^{-10} S/cm) and a small surface area (80-90 m²/g), CNT possessed characteristics of superior conductivity, tremendous stiffness, a high aspect ratio (1000:1) and large surface area (~1300 m²/g) that puts it on par with many activated carbons. As such, they have been extensively employed in novel materials [2-4] stemming from their ability to absorb strain and induce conductivity. In addition, it has been shown that CNT are biocompatible [5-8], making their inclusion into materials destined for medical applications very promising. However, implementation of both carbon nanotubes and fullerenes into commercial products has thus far been limited by their cost. This would change with the revelation of a new nano carbon material in 2004. Discovered by two Russian physicists from the University of Manchester, graphene came about through a simple mechanical cleavage experiment resulting in an atomically

thin layer being removed[9]. Since then alternative synthesis routes have been adopted by the scientific community including chemical vapor deposition and chemical exfoliation. With the discovery of graphene came the second Nobel Prize awarded for nano carbons this time in the field of Physics in 2010. Its discoverers were credited for showing that electrons move along the basal plane of the graphene sheet in a relativistic manner and do so at speeds close to the Fermi velocity, or 10^6 m/s[10]. This ballistic motion of the electrons is what endows graphene with its tremendous electronic properties, and with the combination of its other outstanding characteristics, has led the way for it to infiltrate nearly every field of science to date. In particular, numerous researchers are leading the effort to utilize the large surface area of graphene (~ 2630 m²/g) in fabricating porous materials. The ability to incorporate either CNT or graphene into highly porous materials will thus lead to the advancement in several fields. This last sentiment is the focal point of this work and is structured in the following manner: Characterization techniques of porous materials with an emphasis on porous carbon materials will be discussed in Chapter 2. Chapter 3 will concern the fabrication of nano carbon fiber composites. This will include fibers produced by a wet spinning procedure with either carbon nanotubes or graphene in addition to electrospun polymeric scaffolds that have been impregnated with a carbon nanotube dispersion. Chapter 4 will feature how these nano carbon fiber composites have been used for biological applications, both for neural tissue engineering as well as stem cell differentiation. Chapter 5 will describe alumina catalyst supports followed by Chapter 6 describing how these nano carbon materials have been incorporated into alumina composites for energy applications including catalysis and

ultracapacitors. Finally Chapter 7 will conclude and express any future work that may be done in order to improve on the findings found in this thesis.

Chapter 2 Application of Density Functional Theory Method for Characterization of Porous Materials

2.1 Introduction

The breakthrough discovery in the early 1990's of highly ordered mesoporous materials [1, 2] stimulated rapid development of improved methods of pore structure characterization by gas adsorption. Indeed, the conventional methods, like BET [3] and BJH [4] models, failed to distinguish between different pore structure morphologies, to account for the effects of microporosity, and to predict the pore sizes, which could be independently determined from X-ray diffraction (XRD) and transmission electron microscopy (TEM) with the precision unavailable earlier. The new nanomaterials and new high resolution experimental capabilities required new adequate theoretical methods for data analysis. This period coincided with the development of the density functional theory (DFT) for inhomogeneous and confined fluids [5-7], and, in particular with its application to the description of adsorption and capillary condensation in pores. In 1989, Seaton et al.[8] were the first to propose a DFT model for calculating the pore size distribution from adsorption isotherms, and it has been soon acknowledged that DFT provides a more reasoned and versatile approach to calculating the pore structure parameters compared to the conventional methods based on the Kelvin equation [9]. Initially developed for simple slit geometries for activated carbons, so-called non-local density functional theory (NLDFT) [10-12] has soon evolved into a library of computational methods, which incorporates various pore structures representing

characteristic pore morphologies and typical adsorbates. NLDFT methods take into consideration the complexity associated with the hysteretic nature of adsorption isotherms that cloaks a number of physical phenomena relating to the geometrical specifics of given pore structure. These phenomena include the inherent metastability of confined fluid, pore blocking and networking effects, as well as instability of adsorption films and cavitation in condensed fluid. But with the arrival of newer and more distinct DFT methods, as opposed to just one conventional BJH method, also came a problem of choice. Which DFT model should be employed for this or that particular system? Which branch of the hysteretic isotherm should be used for analysis? The latter question is extremely important, since the choice of the isotherm branch may lead to considerably different pore size distribution results. DFT approach solves, at least partially, this problem by offering different methods for treating adsorption and desorption isotherms, which produce consistent results.

The purpose of this review is to present the current state and capabilities of the DFT methods for pores structure characterization and to provide a practical guidance on the choice of the most suitable method from the currently available library of DFT kernels for particular applications. The rest of the paper is structured as follows. In section 2, a description is given of the essence of the NLDFT methodology and its evolution into a versatile tool applicable for various pore structures. This section also includes a description of the more advanced quenched solid density functional theory (QSDFT) method, which takes into account roughness and heterogeneity of the pore wall surfaces. Section 2 can be skipped by a reader interested only in practical applications of the DFT method for characterization. Section 3 shows how these methods are used to

interpret the experimental isotherms and to produce the pore size distributions. Section 4 and section 5 presents numerous examples of DFT method applications for different materials of distinct pore structures for organic materials and inorganic materials, respectively. The DFT models are then correlated and interpreted with in situ x-ray diffraction data in section 6. Finally, section 7 contains concluding remarks and future outlook.

2.2 Description of the DFT Method

In their seminal work, Seaton et al. [8] were the first to apply the density functional method for the determination of pore size distribution from adsorption isotherms. They suggested a method for treating nitrogen adsorption measurements on porous carbons based on the local mean field approximation [5-7]. A further significant improvement was made by Lastoskie et al [10], who used a NLDF model within Tarazona's smooth density approximation [13] for modeling nitrogen adsorption on carbons. Both works treated the pores as infinite slits, which is a conventional model representation of pores between graphene fragments in carbons. Near the same time, Mobil scientists developed MCM-41 mesoporous silicas with ordered hexagonal structure of cylindrical channels, which for the first time provided the opportunity for verification of the theoretical methods of pore structure analysis against reliable experimental data [1, 2]. The NLDF model for adsorption on MCM-41 suggested and verified by Neimark and Ravikovitch [12, 14, 15] became the starting point for further development of customized DFT methods applicable for mesoporous and hybrid materials of various morphologies. With this assembly of contributions, the NLDF

method soon became widely accepted to the extent that it has been recommended as the standard method by the International Standard Organization (ISO) [16].

2.2.1 Non-Local Density Functional Theory

The adsorption experiment, which is performed by equilibrating the solid-fluid (adsorbent-adsorbate) system at given temperature at a set of adsorbate gas pressures, corresponds to the conditions of the grand canonical ensemble for the system of fixed chemical potential, volume, and temperature. Therefore, the equilibrium distribution of the adsorbate in the pores corresponds to a minimum of the grand potential of the adsorption system presented as a functional of the density of adsorbed fluid. Within the conventional treatment of adsorption, the solid adsorbent is considered as inert and non-deformable, and the adsorption interactions are modeled with an effective solid-fluid spatially distributed potential $U_{ext}(\mathbf{r})$. With this assumption, the equilibrium adsorption state at a given chemical potential of the fluid μ_f is determined in NLDFT [10, 12] from the minimization of the grand potential Ω_f of the fluid confined in the pore and subjected to the external potential U_{ext} ,

$$\Omega_f[\rho_f(\mathbf{r})] = F_f[\rho_f(\mathbf{r})] - \int d\mathbf{r} \rho_f(\mathbf{r}) [\mu_f - U_{ext}(\mathbf{r})]. \quad (1)$$

Here \mathbf{r} is a position vector inside the pore, $\rho_f(\mathbf{r})$ is the fluid density, and F_f is the Helmholtz free energy of the fluid. The latter is expressed as a sum of ideal term $F_{id}[\rho_f(\mathbf{r})]$, excess hard sphere (HS) repulsion term $F_{ex}[\rho_f(\mathbf{r})]$ and attractive term calculated in a mean-field fashion given by the equation:

$$F_f[\rho_f(\mathbf{r})] = F_{id}[\rho_f(\mathbf{r})] + F_{ex}[\rho_f(\mathbf{r})] + \frac{1}{2} \iint d\mathbf{r} d\mathbf{r}' \rho_f(\mathbf{r}) \rho_f(\mathbf{r}') u_{ff}(|\mathbf{r} - \mathbf{r}'|), \quad (2)$$

where $u_{ff}(r)$ is the attractive part of the pairwise fluid-fluid potential. The fluid density profile $\rho_f(\mathbf{r})$ is thus obtained from the minimization of the grand potential (1). Once the equilibrium distribution of the fluid density is determined at each value of chemical potential μ_f , and its averaged values calculated, the adsorption isotherm can be obtained. Different models were suggested in the literature for the excess HS free energy $F_{ex}[\rho_f(\mathbf{r})]$ (see e.g. review [17]). The most popular are the smooth density approximation (SDA) of Tarazona [13], the fundamental measure theory (FMT) of Rosenfeld [18, 19], and their modifications based on either Percus-Yevick (PY) or Carnahan-Starling (CS) equations of state. Explicit expressions can be found elsewhere [12, 20]. It is worth noting, that although different versions of DFT are not in conflict, the quantitative results obtained with different functional may deviate beyond the accuracy required for the pore size distribution calculations.

The pore structure characterization is based on the physical adsorption of non-specific gases, like nitrogen and argon, which is governed mainly by dispersion interactions, that justifies the use of Lennard-Jones (LJ) intermolecular potentials for both fluid-fluid and solid-fluid interactions. The attractive part of the fluid-fluid potential $u_{ff}(r)$ for LJ model adsorbates is commonly treated with the Weeks–Chandler–Andersen (WCA) scheme [21],

$$u_{ff}^{\text{attr}}(r) = \begin{cases} -\varepsilon_{ff} & r \leq 2^{1/6} \sigma_{ff} \\ 4\varepsilon_{ff} \left[\left(\sigma_{ff}/r \right)^{12} - \left(\sigma_{ff}/r \right)^6 \right] & r > 2^{1/6} \sigma_{ff} \end{cases} \quad (3)$$

where ε_{ff} and σ_{ff} are the energy and size parameters of the LJ potential. In order to provide

a correct equation of state for the adsorbate, the fluid-fluid parameters ε_{ff} and σ_{ff} should be fitted by correlating the experimental data on liquid-vapor equilibrium, gas densities, saturation pressure and surface tension with the predictions obtained with the particular functional for the bulk fluid for liquid as described by Ravikovitch et al [15].

The solid-fluid interactions in the DFT models used for pore structure characterization are commonly based on effective potentials obtained by integrating pairwise solid-fluid LJ potential $u_{sf}(r)$ for a given pore geometry. The Steele equation[22], which assumes a graphite pore wall of infinite thickness, is conventionally employed for the slit shape carbon pores. The curvature effects in cylindrical and spherical pores are accounted for by integrating the solid-fluid LJ potential over the cylindrical and, respectively, spherical outer layer of solid atoms (carbons in case of carbonaceous materials and oxygen in case of oxides, like silica). The respective equations are given in [12] and [23]. Within this framework, the adsorption interactions are characterized by the solid-fluid LJ parameters ε_{sf} and σ_{sf} which should be fitted by correlating the experimental data on adsorption on a reference non-porous solid with the predictions obtained with the DFT model for the flat surface [15]. These parameters depend on the adsorbate-solid pair and are customized for the materials of different origin and the adsorbate employed for surface and pore size characterization. The fluid-fluid and solid-fluid parameters employed in the DFT models for carbons and silicas [24, 25] are presented in Table 1.

NLDFT interaction parameters					
NLDFT		fluid-fluid parameters		solid-fluid parameters	
adsorbent	adsorbate	ε_{ff}/k_B (K)	σ_{ff}, d_{hs} (Å)	ε_{sf}/k_B (K)	σ_{sf} (Å)
silica/zeolite	N ₂ at 77.4 K	94.45	3.575	22.53	3.17
	Ar at 87.3 K	118.05	3.305, 3.38	26.20	3.00
	Kr at 153 K	162.6	3.627	109.6	3.45
	Xe at 180 K	227.6	3.901	128.2	3.586
carbon	N ₂ at 77.4 K	95.77	3.549	150	2.69
	Ar at 87.3 K	111.95	3.358	162.18	2.595

Table 1. Molecular interactions LJ parameters of nitrogen and argon[24], krypton and xenon [25] adsorption on silica and carbon surface used in NLDFT method.

Theoretical adsorption isotherms calculated using the NLDFT model have been validated against the experimental adsorption and desorption isotherms on mesoporous crystals of MCM 41 and SBA-15 types with well characterized cylindrical pores[14, 26]. A typical example of nitrogen adsorption on an MCM-41 sample with 4.8 nm pores is shown in Fig.1. Within the NLDFT models, the position of capillary condensation in cylindrical pores is associated with so-called mechanism of delayed, or spinodal condensation occurring at the limit of stability of adsorption films, or at the vapor-liquid spinodal. The position of desorption is associated with the equilibrium capillary-condensation-evaporation transition. Also, the NLDFT model predicts the metastable states on the desorption isotherm at the pressures smaller than the equilibrium pressure down to the liquid-vapor spinodal, or the limit of stability of overstretched fluid. However, these metastable states can be observed experimentally only in the ink-bottled

and corrugated pores [27, 28]. It was shown that the NLDFT model can precisely predict the capillary condensation and desorption pressures in cylindrical pores wider than ~ 5 nm, when desorption is associated with an apparent hysteresis: as the vapor pressure decreases, the desorption occurs at a pressure lower than the pressure of condensation. In smaller pores, the experimental hysteresis progressively diminishes and the adsorption isotherm merges with the desorption isotherm, which corresponds to the equilibrium capillary condensation-evaporation transition, for pores smaller than ~ 4 nm. In pores smaller than 5 nm, the NLDFT adsorption isotherms progressively deviate from the experimental since the NLDFT model does not account for the nucleation phenomenon. This feature of the NLDFT isotherms is illustrated in Fig. 2 with examples of Ar adsorption on a series of MCM-41 samples [29]. The authors [29] suggested to distinguish three regimes of adsorption behavior: regime of developed hysteresis (pores of ~ 5 nm and wider), regime of reversible condensation (pores smaller than so-called hysteresis critical pore size, which is ~ 4 nm); and regime of developing hysteresis in intermediate pores, where the capillary condensation occurs at experimental conditions somewhat in between theoretical spinodal and equilibrium.

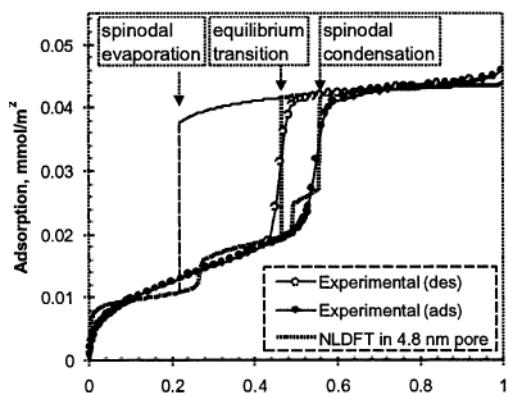


Figure 2-1. Experimental nitrogen (at 77.4 K) adsorption isotherm on MCM-41 silica and theoretical NLDFT isotherm in 4.8 nm cylindrical pore. (Adapted from [24].)

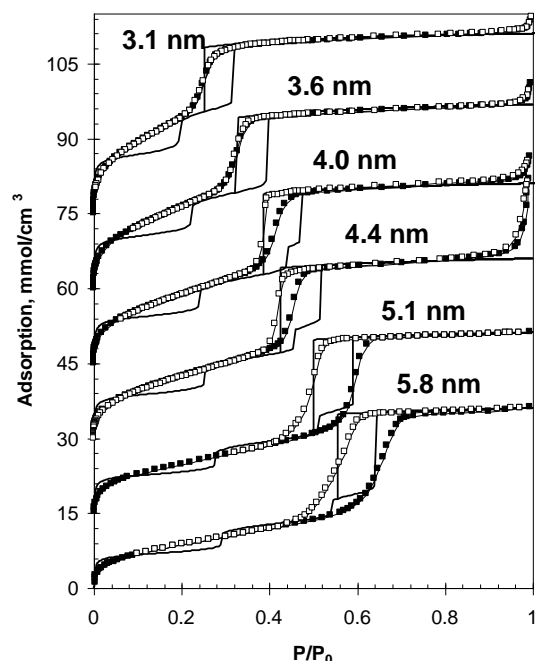


Figure 2-2. Experimental adsorption and desorption isotherms of Ar (at 87 K) on a series of mesoporous molecular sieves with cylindrical pores of characteristic diameter 3.1, 3.6, 4.0, and 4.4 nm [14], and 5.1 and 5.8 nm [30] (points) and theoretical isotherms calculated using NLDFT (solid lines). (Adapted from ref. [29])

As such, the NLDFT equilibrium isotherms in cylindrical pores can be used for calculations of the pore size distributions from the desorption branches of hysteretic adsorption isotherms, as well as from the reversible isotherms. In the range of pores wider than ~5nm, the NLDFT adsorption isotherms can be used for calculations of the pore size distributions from the adsorption branches of H1 hysteresis loops. This conclusion is confirmed in Fig. 3 by the compendium of independent experimental data of the pore sizes of MCM-41 and SBA-15 samples compared with the NLDFT predictions of the positions of capillary condensation and desorption. The agreement with experiments is excellent, in contrast to the predictions of the conventional Kelvin-Cohan equation [9] (the basis of the BJH method), which progressively underestimate the pore sizes at the nanoscale below 20 nm. This is one of the main advantages of the NLDFT method.

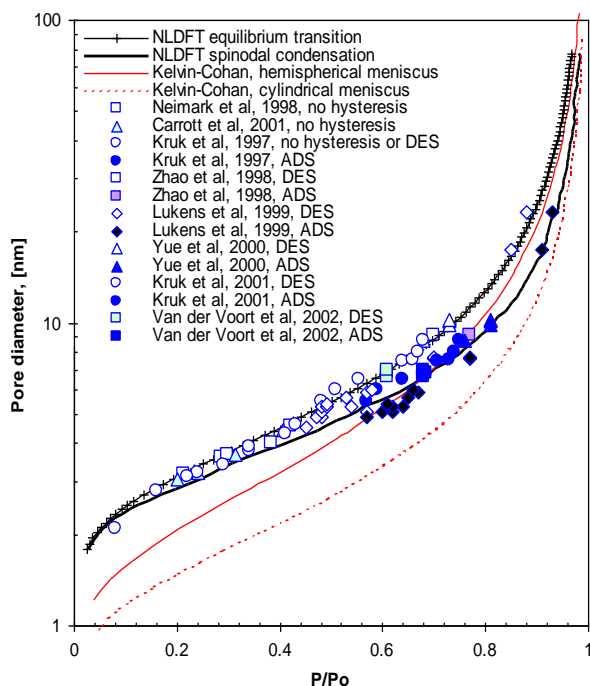


Figure 2-3. Relative pressures of the adsorption and desorption for N₂ (at 77 K) in open cylindrical pores in comparison with the experimental data [14, 27, 30-34] on ordered MCM-41 and SBA-15 nanoporous materials with cylindrical pores. Predictions of the macroscopic Kelvin-Cohan equation are also shown. Reproduced from ref. [29]

The mechanisms of capillary condensation hysteresis in cage-like pore networks are different from those in cylindrical pores due to the presence of the connecting channels (necks) or openings. The NLDFT method was extended to the spherical shape pore geometry to model adsorption in cage-like mesoporous materials [23]. Experimental observations with specially designed ordered materials and respective theoretical analysis revealed three different mechanisms of evaporation from cage-like mesopores [35]: (i) pore blocking controlled desorption, (ii) spontaneous evaporation due to cavitation, and (iii) near-equilibrium desorption. A typical example of experimental and NLDFT isotherms for a material with cage-like pores is given in Figure 4. The prevalence of a given mechanism, and thus the pressure p_d at which desorption occurs, depends mainly on the relation between the size of the cavity and the size of the necks. Near-equilibrium

desorption is possible from the cavities that have immediate access to the vapor phase through relatively wide openings, and thus are effectively unblocked. Once the vapor pressure reaches the vapor-liquid equilibrium (VLE) pressure p_e , desorption from the main cavity proceeds via a receding meniscus; therefore $p_d \approx p_e$. However, if wide cavities are connected with narrower necks, so that the fluid in the neck has a lower VLE pressure than that of the fluid in the cavity, the neck effectively “blocks” desorption from the cavity. Emptying of the pores occurs at the pressure of equilibrium desorption of the neck, and as such becomes a function of the neck size. Finally, if the connecting necks are even narrower, fluid in the cavity becomes substantially metastable, and the vapor pressure may reach the spinodal point of the confined liquid before the equilibrium meniscus can be formed in the neck. Thus, the fluid desorbs from the pore by the cavitation mechanism, which involves fluctuation-driven formation and growth of a bubble. In this scenario, $p_d \ll p_e$, and p_d has little or no dependence on the size of the necks. Due to these peculiarities of adsorption hysteresis in the cage-like pores NLDFT methods should be applied carefully, taking into account the physical origin of the desorption branch of experimental isotherm.

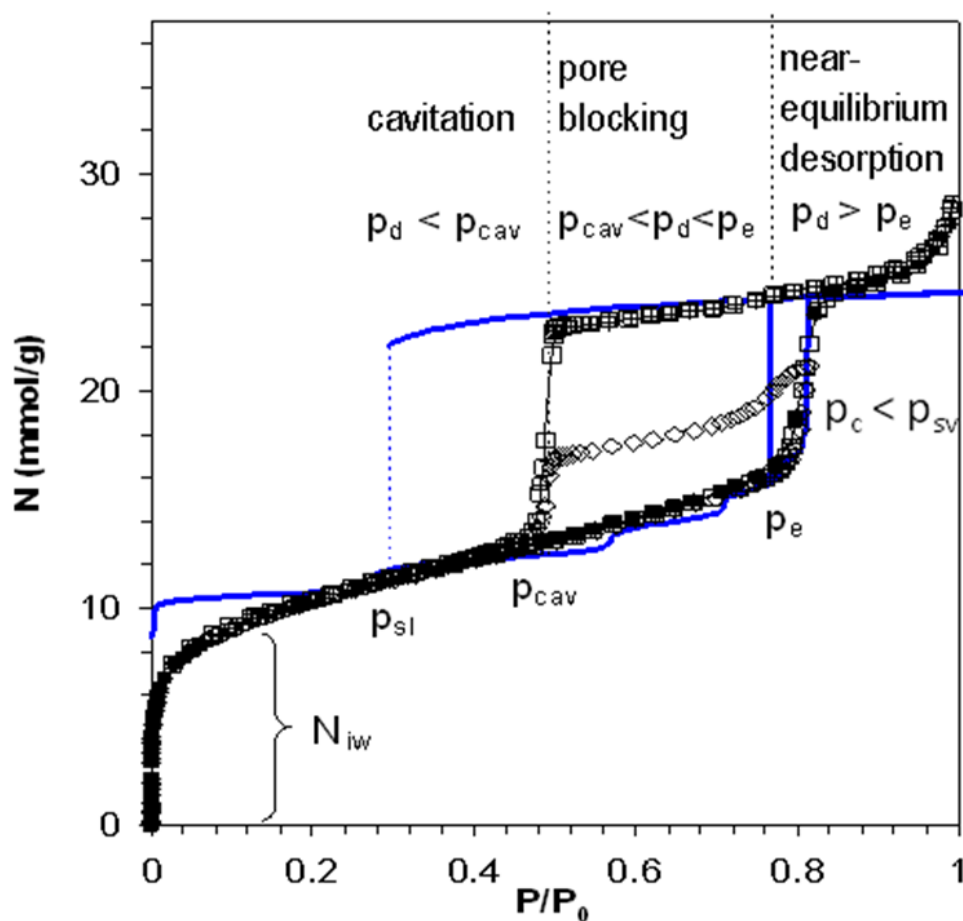


Figure 2-4. NLDFT N_2 adsorption-desorption isotherm (at 77 K) in 15.5 nm spherical cavity (thick solid line) and experimental data on a FDU-1 silica sample (points). The theoretical pressures of liquid like spinodal, equilibrium, and vapor like spinodal are denoted, respectively, as p_{sl} , p_e , and p_{sv} . Experimentally observed pressures of spontaneous capillary condensation and cavitation are denoted as p_c and p_{cav} , respectively ($p_c \approx p_{sv}$ and $p_{sl} < p_{cav} < p_e$). Three possible regimes of evaporation from the cavity are classified with respect to the pressure p_d of desorption from the neighboring pores or from the pore neck. Reproduced from ref. [35]

Further, the hybrid NLDFT methods, which combine the theoretical isotherms in pores of different shapes (slit, cylindrical, and spherical) in different diapasons of pore sizes have been developed for the characterization of a variety of ordered and hierarchically structured micro-mesoporous materials [36]; the latter are discussed in sections 4.4 and 5.5.

2.2.2 Drawbacks of NLDFT and Paths to Improvement

Most of the adsorbents have molecularly rough microporous surface. A drawback to the standard NLDFT method is that it does not take into account chemical and geometrical heterogeneity of the pore walls, instead assuming a structureless, chemically and geometrically smooth surface model. The consequence of this mismatch between the theoretical assumption of smooth and homogeneous surfaces and the inherent molecular scale heterogeneity of real adsorbents is that the theoretical NLDFT adsorption isotherms exhibit multiple steps, these steps are associated with a layering transition related to the formation of a monolayer, second adsorbed layer, and so on (see examples in Figures 1, 2, 4). The problem is enhanced in microporous carbon materials, which exhibit broad PSDs, where the artificial layering steps inherent to the theoretical isotherms cause artificial gaps on the calculated pore size distributions around 1 and 2 nm [15, 37] (see discussion in section 4.4). There were multiple attempts to improve the NLDFT method to avoid artificial layering on theoretical isotherms.

Olivier [38] introduced a modification to the mean field approximation, which allowed him to obtain good agreement with experimental isotherms for argon and nitrogen adsorption on non-porous surface and in slit pores. He further suggested to use a combination of modified DFT isotherms to mimic the real heterogeneous surface [37]. A different extension of NLDFT for carbons was suggested by Nguyen and Bhatia [39]. This approach was based on a model of carbon wall heterogeneity, assuming the varying thickness of the pore walls [40]. While such an approach smoothened the NLDFT adsorption isotherms, making them closer to the experimental ones, it required, along with the unknown pore size distribution, the introduction of an unknown distribution of

the pore wall thickness. The latter can be hardly verified against experimental data for disordered materials, and so to some extent is arbitrary. Another modification of the Tarazona's NLDFT capable of generating smooth isotherms in the region of mono- and polymolecular adsorption was further developed by Ustinov et al. [41-44]. The authors used the WCA scheme (Eq. 3) for solid–fluid attractive interactions and reduced the contribution from the HS repulsive interactions in the vicinity of the solid surface, which decreased the layered structure of the fluid. The parameters of the model were fitted to obtain good agreement with experimental N₂ and Ar adsorption data on MCM-41[43], nonporous amorphous silica[42], and carbon[44]. An alternative method was suggested by Jagiello and Olivier [45], who reached a better agreement between NLDFT and experimental isotherms for nitrogen adsorption on porous carbons by introducing the two-dimensional finite pore model instead of standard one dimensional model that assumes infinite graphite-like pores. This record of literature is not comprehensive and is limited to the most prominent modifications.

Recently, the NLDFT method was advanced to take into account the molecular level surface roughness that is typical to most carbonaceous and siliceous materials as well as other materials including hybrid organic-inorganic hierarchical structures [46]. This technique, named the quenched solid density functional theory (QSDFT), was shown to be more practical than NLDFT for the analysis of microporous and mesoporous silicas [46, 47] and carbons [20, 48].

2.2.3 Quenched Solid Density Functional Theory

Within the framework of QSDFT, the grand potential of both the solid and fluid are considered. Unlike the conventional NLDFT, QSDFT implies a two-component density functional, where the solid is modeled as a compound of hardcore spheres interacting with the fluid molecules via a pairwise attractive potential. From Eqs. (1) and (2), the grand potential of the solid-fluid system Ω_{sf} is written as

$$\begin{aligned} \Omega_{sf}[\rho_s(\mathbf{r}), \rho_f(\mathbf{r})] = & F_{id}[\rho_f(\mathbf{r})] + F_{id}[\rho_s(\mathbf{r})] + F_{ex}[\rho_s(\mathbf{r}), \rho_f(\mathbf{r})] \\ & + \frac{1}{2} \iint d\mathbf{r} d\mathbf{r}' \rho_f(\mathbf{r}) \rho_f(\mathbf{r}') u_{ff}(|\mathbf{r} - \mathbf{r}'|) + \frac{1}{2} \iint d\mathbf{r} d\mathbf{r}' \rho_s(\mathbf{r}) \rho_s(\mathbf{r}') u_{ss}(|\mathbf{r} - \mathbf{r}'|) \\ & + \iint d\mathbf{r} d\mathbf{r}' \rho_f(\mathbf{r}) \rho_s(\mathbf{r}') u_{sf}(|\mathbf{r} - \mathbf{r}'|) - \mu_f \int d\mathbf{r} \rho_f(\mathbf{r}) - \mu_s \int d\mathbf{r} \rho_s(\mathbf{r}) \end{aligned} \quad (4)$$

where $\rho_s(\mathbf{r})$ is the density profile of the solid component, $F_{id}[\rho_s(\mathbf{r})]$ is the ideal contribution of hard-sphere free energy of the solid, $F_{ex}[\rho_s(\mathbf{r}), \rho_f(\mathbf{r})]$ is the excess HS free energy term for both the solid and fluid components, $u_{ss}(r)$ and $u_{sf}(r)$ are the attractive parts of the solid-solid and solid-fluid potentials respectively, and μ_s is the chemical potential of the solid. The key component in the QSDFT approach displayed in Eq. (4) is the $F_{ex}[\rho_s(\mathbf{r}), \rho_f(\mathbf{r})]$ term, known as the excess free energy of the solid-fluid HS mixture. To calculate this term, Rosenfeld's fundamental measure theory, the so called RLST approximation [18, 19] was employed, which is consistent with the Percus-Yevick equation of state for bulk HS fluids (see details in [20]).

The essence of QSDFT model is related to the “quenched” state of the solid. While the authors take into account the density of the solid component, $\rho_s(\mathbf{r})$, they do not vary it while optimizing the grand potential Ω_{sf} . Thus only those terms that are

related to the fluid in Eq. (4) are subject to minimization. The final density profile is found from the condition

$$\left. \frac{\delta \Omega[\rho_s(\mathbf{r}), \rho_f(\mathbf{r})]}{\delta \rho_f(\mathbf{r})} \right|_{\rho_s(\mathbf{r})} = 0, \quad (5)$$

which finally leads to the solution of the Euler-Lagrange equation

$$\rho_f(\mathbf{r}) = \Lambda_f^{-3} \exp \left\{ c^{(1)}(\mathbf{r}, [\rho_s, \rho_f]) - \beta \int d\mathbf{r}' \rho_f(\mathbf{r}') u_{ff}(|\mathbf{r} - \mathbf{r}'|) + \beta \mu_f - \beta \int d\mathbf{r}' \rho_s(\mathbf{r}') u_{sf}(|\mathbf{r} - \mathbf{r}'|) \right\} \quad (6)$$

where $c^{(1)}(\mathbf{r}, [\rho_s, \rho_f]) = -\beta \delta F_{ex}[\rho_s(\mathbf{r}), \rho_f(\mathbf{r})] / \delta \rho_f(\mathbf{r})$ is the one-particle direct correlation function expressed as the functional derivative of the excess Helmholtz free energy of the two-component HS fluid, which depends on both solid and fluid densities. Here $\beta = 1/k_B T$, k_B is the Boltzmann constant, T is the absolute temperature, $\Lambda_f = h / (2\pi m k T)^{1/2}$ is the thermal de Broigle wavelength, h is the Planck constant, and m is the molecular mass of the fluid molecule.

The solid density profile $\rho_s(\mathbf{r})$ takes into account the molecular level geometrical heterogeneity of pore walls, known as “corona” in XRD studies of mesoporous crystals of SBA-15 type [49]. The solid density profile for mesoporous crystals can be calculated from the reconstruction of XRD patterns [50, 51] or from the molecular dynamics simulations of real surface of amorphous solids [52-54]. For the practical calculations the density profile for most of surfaces can be approximated by the simplest function with a linear gradient, varying from the density of solid to null. Thus, within the corona, the molecular level roughness is accounted by one main parameter δ equal to the half width of the corona. As such, the solid density profile is defined by

$$\rho_s(z) = \begin{cases} \rho_s^0 & 0 \leq z < h_0 \\ C\rho_s^0 \left(1 - \frac{z-h_0}{2\delta}\right) & h_0 \leq z < h_0 + 2\delta \\ 0 & h_0 + 2\delta \leq z \end{cases} \quad (7)$$

Here z is the distance from the pore wall, ρ_s^0 is the bulk density of the adsorbent, C is the constant (which is set to 1 for most of the surfaces, including silica), h_0 is the thickness of the solid wall, and δ is the roughness parameter, which represents the half-width of the region of variable solid density. The position of the edge of the solid, which is responsible for the pore size D discussed in section 3, is determined from the condition of zero solid excess. The values of these parameters for silica and carbon are given in Table 2. Note that for silica $C = 1$, i.e. the simple linear ramp is used; the roughness parameter is determined from the XRD [55]. For carbons, based on the properties of the reference material (Cabot BP-280 carbon black with a partial degree of graphitization) the solid density has a more complex profile [20]. Fluid-fluid and solid-fluid molecular interactions parameters for characteristic systems are summarized in Table 3.

An example of QSDFT calculation of adsorption-desorption cycle of Kr at 119 K on SBA-15 sample is given in Fig. 5a, showing excellent agreement with the experimental adsorption data without any adjustable parameters. The roughness parameter was defined from XRD data. Fig. 5b shows solid and fluid density profiles at different pressure values.

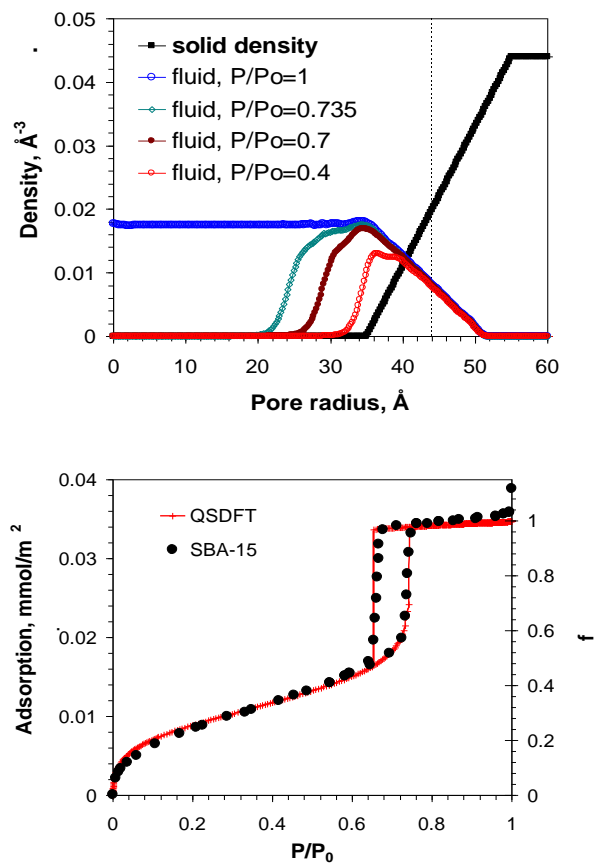


Figure 2-5. (a) Density profiles of solid (squares) and fluid at different pressures along the adsorption branch. Thin vertical line at $r = 43.9 \text{\AA}$ indicates the pore radius at which the excess fluid density is zero. The solid excess mass is zero at $r = 45 \text{\AA}$. (b) Prediction of krypton adsorption on SBA-15 silica at 119 K. Experimental data are from ref. [55] Reproduced from ref. [46]

QSDFT solid density distribution parameters					
adsorbent	$\rho_s^0 (\text{m}^{-3})$	C	$h_0 (\text{nm})$	$\delta (\text{nm})$	d_{HS}
silica	4.4×10^{28}	1.0	2×0.34	0.4	0.3
carbon	1.14×10^{29}	0.75	2×0.34	0.13	0.2217

Table 2. Parameters of the solid density distribution.

QSDFT interaction parameters					
QSDFT		fluid-fluid parameters		solid-fluid parameters	
adsorbent	adsorbate	ε_{ff}/k_B (K)	$\sigma_{ff} = d_{hs}$ (Å)	ε_{sf}/k_B (K)	σ_{sf} (Å)
silica/zeolite	N ₂ at 77.4 K	95.77	3.549	148.45	3.17
	Ar at 87.3 K	111.95	3.358	160.5	3.104
	Kr at 119 K	155.9	3.589	189.4	3.22
carbon	N ₂ at 77.4 K	95.77	3.549	150	2.69
	Ar at 87.3 K	111.95	3.358	162.18	2.595

Table 3. Parameters of nitrogen [47] [Alex, this paper is missing on your website and I can't get it through Princeton subscription, I guess parameters for QSDFT for nitrogen first appeared there.], argon and krypton adsorption on silica [46], nitrogen and argon on carbon [20] surface used in QSDFT method. Usually the fluid-fluid interactions are truncated at $5\sigma_{ff}$.

2.3 Recovering the pore size distribution (PSD) using DFT methods; DFT Kernels

2.3.1 Recovering the PSD using DFT methods

PSD's are calculated from the experimental adsorption isotherm $N_{\text{exp}}(P/P_0)$ by solving the integral adsorption equation [8]. The experimental isotherm is represented as the convolution of the DFT kernel (set of the theoretical isotherms $N_{QSDFT}(P/P_0, D)$ in a series of pores within a given range of pore sizes D) and the unknown PSD function $f(D)$,

$$N_{\text{exp}}(P/P_0) = \int_{D_{\min}}^{D_{\max}} N_{QSDFT}(P/P_0, D) f(D) dD. \quad (8)$$

Here D_{\min} and D_{\max} are the minimum and maximum pore sizes in the kernel, respectively. Two kernels of the selected DFT adsorption isotherms for the slit geometry are presented in the Figure 6, (a) NLDFIT and (b) QSDFT. In contrast to the NLDFIT kernels, the QSDFT isotherms are smooth prior to the capillary condensation step, which is characteristic of mesopores ($D > 2$ nm), and thus do not exhibit stepwise inflections caused by artificial layering transitions.

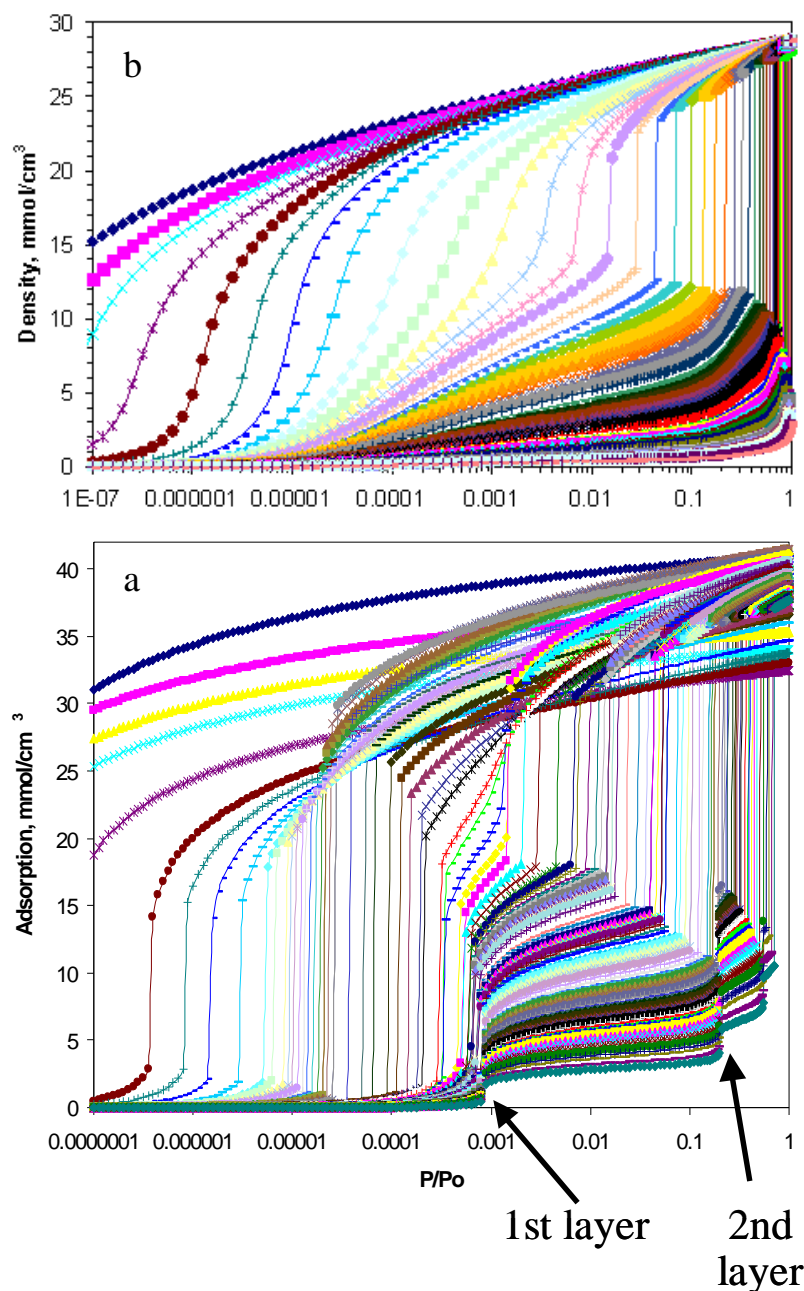


Figure 2-6. Kernels of selected equilibrium adsorption isotherms in slit-shaped pores, calculated using (a) NLDFT nitrogen at 77.4 K (smooth pore walls) and (b) QSDFT Ar at 77.4K (molecularly rough surface).

Solution of Eq. (8) can be obtained using the quick non-negative least square method [56]. In this method Eq. (8) is represented as a matrix equation, which is solved using the discrete Tikhonov regularization method combined with the non-negative least

square algorithm [57]. All examples of PSDs presented below were calculated by using this efficient scheme. At the same time, it is worth noting that in the literature one can find several alternative techniques for the solution of Eq. 8, and the results obtained with different regularization techniques may deviate (see e.g. [58] and references therein).

2.3.2 *DFT Kernels for Characterization of Various Systems*

Over the years a library of NLDFT [14, 15, 23, 26, 36, 50] and more recently QSDFT [20, 46-48, 51, 59] kernels were developed for calculating pore size distributions in carbonaceous and silica micro- mesoporous materials of different origin from nitrogen and argon adsorption isotherms, as well as for microporous carbons from carbon dioxide adsorption [15]. For a DFT kernel of a given adsorbate-adsorbent pair, the parameters should not only represent the specifics of adsorbent-adsorbate interactions, but also take into account the pore structure morphology. The latter is accounted by the choice of the characteristic pore geometry represented by cylindrical, spherical, and slit model pores. Hybrid kernels, which use different pore geometries within different ranges of pore sizes, were developed to characterize hierarchical structures that combine different type pores over a wide range of scales [23,35]. The kernels were verified on the well-characterized materials like mesoporous crystals, zeolites, and active carbons with independently determined pore sizes. To treat hysteretic adsorption-desorption isotherms, two kernels were developed for adsorption and desorption branches. These kernels imply different physical mechanisms for capillary condensation and evaporation. Adsorption kernels are composed of theoretical adsorption isotherms accounting for the delayed condensation effect. Equilibrium kernels are composed of theoretical adsorption isotherms with the

position of vapor-liquid phase transition determined from the condition of phase equilibrium. While the adsorption kernels should be applied only for adsorption branches of hysteretic isotherms, the equilibrium kernels can be used for both desorption and adsorption branch depending on the system and the pore range. Some hybrid kernels combine equilibrium isotherms in the range of micropores and small mesopores ($< \sim 4$ nm), in which hysteresis is not experimentally observed due to inherent thermal and mechanical fluctuations that disturb metastable states. The desire of the developers was to design the kernels, which would provide consistent results while calculating the pore size distributions using different adsorbates and, in the case of hysteresis, using different branches of the isotherm. It is worth noting that at this moment all DFT methods rely upon the models of independent pores and do not take into account cooperative adsorption and desorption mechanism, which may be important for pore networks. At the same time, customization of characterization methods based on different adsorption-desorption mechanisms and different pore geometries is a big step forward compared to conventional BJH method. Moreover, since the DFT models provide important corrections for the Kelvin equation at the nanoscale, the results of PSD calculations are more reliable as confirmed by the broad experimental validation.

A brief overview of the available DFT kernels and basic recommendation for their applicability are given in Section 4 and Section 5 with typical examples of application of these kernels to different types of carbonaceous and silica materials, respectively.

2.3.3 *Role of the adsorptive for characterization*

Conventional adsorptive for PSD calculation using DFT methods is done with nitrogen at 77.4 K. However, argon and carbon dioxide are more suitable in some cases. Argon at 87 K shows better adsorption behavior when compared to nitrogen; ~~argon~~ as it does not give rise to specific interactions with a variety of surface functional groups, which can lead to enhanced adsorption/specific interactions caused by quadrupole moment characteristic inherent to non-symmetric molecules. As a consequence of this factor and a slightly higher temperature, argon at 87 K fills micropores of dimensions 0.5-1 nm at higher relative pressures compared to nitrogen at 77 K, leading to accelerated diffusion and faster equilibration times. This effect is very pronounced, for zeolites [60] and metal-organic frameworks [61].

When using either argon or nitrogen pore filling of ultramicropores still occurs at very low pressures. Associated with the low pressures is the well-known problem of restricted diffusion, which prevents nitrogen and also argon molecules from entering the narrowest micropores pores of width <0.45 nm. In order to address this, the use of CO_2 as the adsorbate at temperatures close to room temperature has been suggested. Despite the fact that the dimensions of N_2 , Ar, and CO_2 are similar, CO_2 molecules are able to easily access the ultramicropores. Because of these experimental advantages, CO_2 adsorption has become a standard tool for the assessment of microporous carbons [62]. Due to the complex interaction of CO_2 with SiO_2 , the carbon dioxide is not used for characterization of silica and other oxides.

2.4 Applications of DFT Kernels for carbonaceous and organic materials

2.4.1 Microporous carbons: NLDFIT model of slit-shaped pores

Historically, the first DFT kernels were developed for carbon slit pores [8, 10]. Ravikovitch et al. [15] designed the consistent equilibrium NLDFIT kernels for nitrogen, argon, carbon dioxide isotherms, which is applicable for disordered micro-mesoporous carbons of various origin, including activated carbons, and carbon fibers, charcoal, and carbon black. These kernels are composed of equilibrium isotherms and they should be applied to reversible isotherms and desorption branches of hysteretic isotherms. The exception is the case of hysteretic isotherms with a sharp desorption step at $p/p_0 \sim 0.4-0.5$, which may indicate the cavitation mechanism of desorption. In this case the adsorption branch should be used and the adsorption kernels are recommended. This is a general recommendation applicable to all systems with the sharp desorption branch in the region of cavitation, which is discussed in details in section 5.6.

2.4.1.1 Activated Carbons (AC)

Activated carbons (AC) are some of the first materials to be characterized by NLDFIT. It is a fair assumption to model pores found in activated carbons and activated carbon fibers as graphitic slabs separated by slit like pores.

Due to the abundant micropore volume and corresponding high internal surface area activated carbons have found wide usage in a range of applications which include separation, gas purification, removal of pollutants and odors, gas storage, catalysis as

well as catalyst supports. Current routes to synthesize activated carbons typically are done through the use of natural materials as a precursor and include coal petroleum, vegetable and polymeric precursors [63]. The nature of which, along with the activation procedure and means of carbonization, effect the pore structure and surface chemistry, which determine the adsorption capabilities and thus applicability as adsorbents for gas and liquid separation and purification [63], electrodes, supercapacitors, etc to name a few. However, there is an ever growing need to find new and cheaper precursors in the form of industrial and agricultural residues which can exhibit great valorization potential.

The following studies used the NLDFT method as a tool for AC characterization. Nabais et al. synthesized activated carbons by using vine shoot as a biomass precursor as seen in Figure 7[64]. They evaluated that a greater amount of porosity was achieved at higher activation temperatures when the burn-off is kept constant. Rios et al. prepared samples of activated carbon using coconut shells as a precursor [65]. They were able to show that their synthesis procedure produced pores within the range of 8-15 Å regardless of the activation protocol chosen, the ideal range for methane storage. Meanwhile Zhang et al. increased the microporosity of already made AC by depositing fine carbon particles onto the AC from pyrolyzing methanol and by heating the AC in an inert atmosphere [66]. Although neither approach changed the trend of the PSD, it did significantly increase the pores within the range of 4-20 Å. Almarri et al. evaluated the performance of 7 commercial AC for the removal of nitrogen compounds [67]. By invoking the NLDFT method Rios et al. were capable of identifying the optimal AC structures for the removal of propanethiol from the liquid phase[68]. Burrell et al. used NLDFT as one of the tools to compare the structure of different activated carbon derived from corncob for

the hydrogen storage. Their samples were shown to have storage capacities of up to 100 g H₂/kg (90 bar, 83 K) and 20 g H₂/kg (90 bar, 303K) [69].

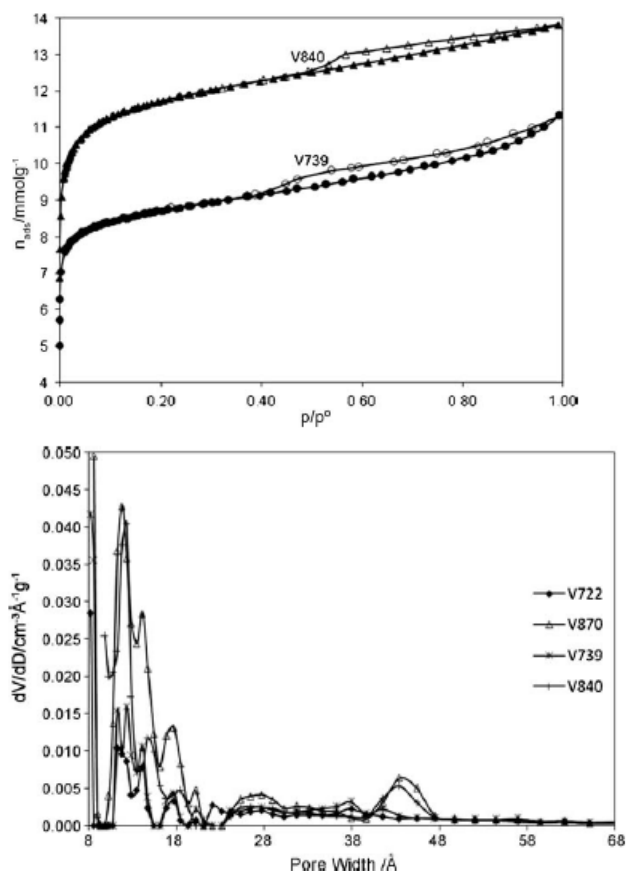


Figure 2-7: (a) Nitrogen adsorption isotherms at 77 K obtained for activated carbons derived from vine shoot designated as V739 and V840. (b) Pore size distribution obtained by NLDFT for samples designated as V722, V870, V739 and V860. Example of the labeling scheme is V840, where V stands for vine, 8 stands for an activation temperature of 800 °C, and 60 implies the percentage that is burned off.

2.4.1.2 Activated Carbon Fibers

Activated carbon fibers (ACF) exhibit a type I isotherm and possess a very high adsorption capacity with BET surface areas up to 3000 m²/g [70]. This results in rapid adsorption and desorption rates with over 90% of the total surface area belonging to micropores of 2 nm or less [71]. And like their granular counterparts, ACF are finding a foot hole in a broad range of applications including gas and liquid phase adsorption,

carbon molecular sieves, catalysis, gas storage, and supercapacitors [71]. The advantages of ACF are multi-fold and are primarily due to its ability to be drawn into lightweight fibers or cloth with a fiber diameter ranging between 10 and 40 microns. Their fibrous design is advantageous in applications where settling and channeling becomes an issue [72] or when higher packing density is required [73]. In addition, ACF tend to possess a narrow and uniform pore distribution, thus eliminating mass transfer limitations. Nevertheless, the implementation of ACF are inhibited by the relatively high unit cost [74-76] and thus requires a detailed elucidation of the synthesis conditions that can comply to different applications [77].

The factors that greatly affect the ACF properties (precursor source, temperature, time, gas flow activating agents and the use of catalysts) are the ones that most influence the pore structure. ACF prepared by a physical activation process will be dependent on a controlled gasification process at temperature ranging from 800 to 1000° C. In their activation procedure Shiratori et al. [77] applied the NLDFT method and showed that a greater degree of activation led to a widening of the pore size distribution from 2.8 to 7.0 nm. They contribute this broadening to the decrease in the number of microdomains. This phenomena was coupled with an increase in the peak pore size (from 0.44 nm to 1.86). The adsorption data and subsequential pore size analysis was confirmed by ^{129}Xe NMR [77]. The chemical activation process on the other hand involves the mixing of a carbon precursor with a chemical activating agent typically KOH, NaOH, H_3PO_4 or ZnCl_2 [71]. Overall the chemical route does have some advantages over the physical one, primarily due to the fact that it can be run at lower temperatures and shorter pyrolysis times and the resultant fibers are high in yield.

Additional species can be added in order to steer the activation process. Mushrif et al. studied the effect of adding an organometallic salt to the fiber precursor [78]. They synthesized ACF prepared from isotropic petroleum pitch, with and without palladium acetylacetonate. They conclude that the presence of the palladium led to an increase in micropores that widened at very high activation values, a trend not observed with the BJH method. In contrast, Wu et al. concluded that activation at high levels of burn off did contribute to the overall increase of the BET surface area, it did not contribute much to the increase of micropores which they defined being less than 7 Å [79]. Donnaperna et al. used the NLDFT CO₂ kernel [15] to study the extent of adsorption of the two dyes Remazol Black B and Acidol Red on ACF [70]. Since ACF possesses a microporosity defined almost entirely by ultramicropores (< 1 nm) the uptake in adsorption of the dyes were defined by interparticle diffusion.

Figure 8 gives differential and cumulative pore volume distributions of CFCMS carbon fiber calculated from N₂ and Ar adsorption isotherms at 77 K using NLDFT model, and from sub atmospheric CO₂ adsorption isotherm at 273 K using NLDFT and three-center GCMC models [15]. Since the considered sample had ultra-microporosity, the PSD obtained using CO₂ provides more complete information on the structure (see section 3.3).

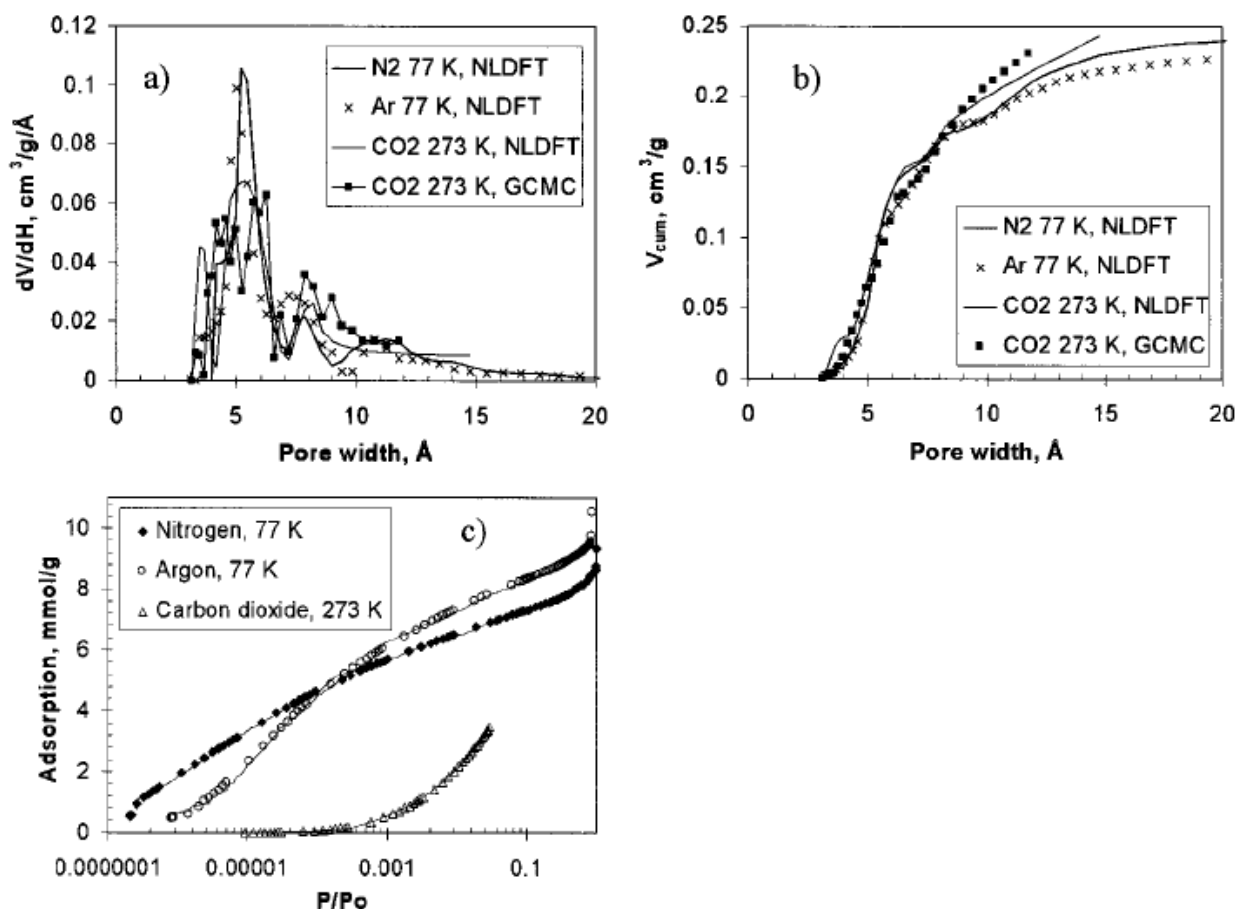


Figure 2-8: (a) Differential and (b) cumulative pore volume distributions of carbon fiber calculated from N₂ and Ar adsorption isotherms at 77 K using NLDFT model, and from sub atmospheric CO₂ adsorption isotherm at 273 K using NLDFT and three-center GCMC models. (c) N₂ and Ar adsorption isotherms at 77 K, and CO₂ isotherm at 273 K on carbon fiber. Experimental isotherms (points). Theoretical fits (lines) (Adapted from ref [15]).

2.4.1.3 Carbon Black, Deposits and Charcoal

Carbon black possess a surface area up to $\sim 100 \text{ m}^2/\text{g}$, displaying a reversible type II isotherm [80] and is the result of an incomplete combustion of fossil fuel derived from petroleum in the fluid catalytic cracking process and includes coal, tar as well as some biomass materials. Although carbon black does not possess the same high surface area to volume ratio that is inherent to AC, its porosity is still significant enough where it can be utilized in the sorption of organic compounds such as pesticides and polycyclic aromatic

hydrocarbons. Fifteen commercial grades of carbon black were utilized to study its capability as a carbon support in the preparation of Fe/N/C electrocatalysts in polymer electrolyte membrane (PEM) fuel cells [81]. It is well known that the presence of micropores in carbon black serve as catalytic sites and therefore are essential to catalytic activity [82]. These authors reaffirm this by studying the development of the pore structure as a function of pyrolysis and with the further development of microposity (< 22 Å) leading to an increase in catalytic activity. These results were concluded with the NLDFT N_2 77 K kernel and correlated with XRD results. Another class of carbon black, commonly known as charcoal, typically has a heterogeneous micropore structure which includes pores less than 4 Å. Braida et al. investigated the sorption hysteresis of benzene in charcoal particles and proposed the occurrence of irreversible pore deformation [83]. NLDFT analysis of pore-size distribution from both N_2 and Ar at 77 K allowed them to conclude that swelling occurs within the charcoal by the solute which in turn opens up previously inaccessible pores. Their results can be seen in Fig 9.

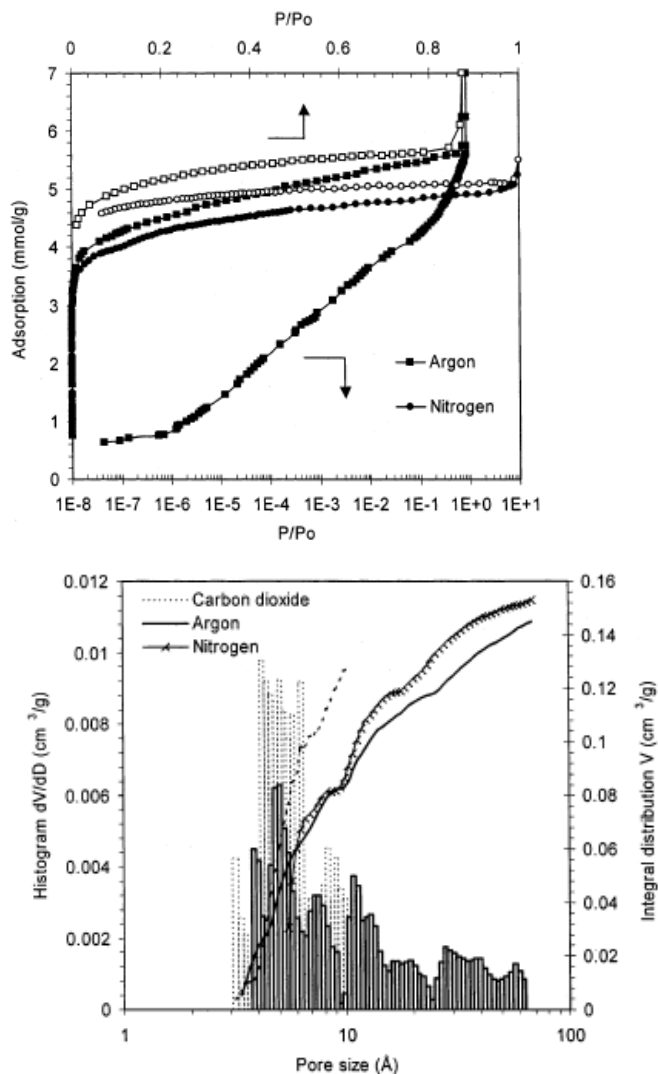


Figure 2-9: (Left) Nitrogen (circles) and argon (squares) isotherms at 77.4 K on charcoal outgassed at 573 K. Adsorption and desorption points are depicted by closed and open symbols respectively. Both linear and logarithmic pressure scales are shown for argon. The isotherm for N₂ contains 150 points collected over 50 h, whereas the Ar isotherm was performed over a combination of 60 then 70 h with 3 and 132 data points respectively. (Right) Pore size distributions calculated from the N₂, Ar and CO₂ adsorption branch of the isotherm. The NLDFT method was applied for Ar and N₂ whereas Monte Carlo models were applied for CO₂. (Ref: Braida et al. #83)

An interesting field where porous carbons exert an influence is in the area of tokamaks, a device that utilizes a magnetic field in order to bound plasma and commonly found in nuclear reactors. Richou et al. studied the carbon deposits collected on the neutralizers of a Tore Supra tokamak by N₂ and CO₂ at 77 K and 303 K respectively.

Using NLDFT analysis they found that the adsorption capacity reversibly increases up to 40% when outgassed [84]. The authors surmised that the latter is most likely the consequence of re-opening of ultra-micropores. It should be noted that porosity is the most critical aspect in modeling and estimating the degree of hydrogen diffusion into tokamak walls[85].

2.4.1.4 Carbon nanotubes

With a high aspect ratio, tensile strength, electrical and thermal conductivity, carbon nanotubes (CNT) represents a class of nanomaterials that is being employed extensively in a wide array of fields. In particular, there has been growing interest on the adsorption capabilities of CNT for various applications [86, 87] . CNT typically display a type II isotherm [88, 89] with no hysteresis due to the smooth inner walls of the CNT. While CNT have apparent cylindrical structure, the NLDFT kernel for slit pores is conventionally used for characterization, which is well suited due to the microporous nature akin to activated carbons. However due to the limited size and high propensity to bundle, current methods are underway to increase the porosity of CNT. One current route is to etch the carbon nanotubes with acid or ozone [90, 91]. In the latter Byl et al. utilized ozone as an oxidative agent in order to expose more pore volume. They concluded that extensive O₃ induced etching resulted in pore wall destruction of the nanotubes with diameters less than 20 Å. Their results are displayed in Figure 10. The Kaneko group studied the effect of oxidation after treatment with HCl[91]. They showed an increase from 524 m²/g for pristine HiPco nanotubes to 861m²/g for the HCl treated and air

oxidized nanotubes. Porosity also plays a significant factor is in the field of hydrogen storage where thus far the optimal storage conditions are still ill-defined. Anson et al. deduced from NLDFT pore size distributions done at both CO₂ at 273 K and N₂ at 77 K[15], that CNT pores with a maximum width between 0.5 and 0.7 nm was optimal for hydrogen to be adsorbed at room temperature[92]. Byl et al. investigated the porosity as a function of already adsorbed n-nonane to determine the existence of blocking effects within the CNT [93]. In relation to polymer composites fabricated with CNT, Neimark et al. showed that single-wall CNT fibers produced by a particle-coagulation spinning process possessed a well-developed hierarchical pore structure [94].

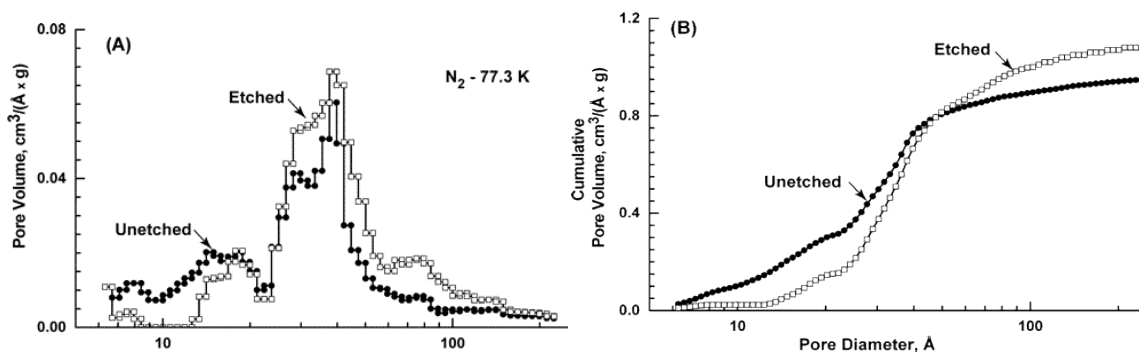


Figure 2-10: (a) Pore size distribution calculated using the NLDFT slit pore model for etched and unetched CNT samples; (b) Comparison of the cumulative pore volume increase versus pore size. (Adapted from ref [90])

2.4.1.5 Additional Applications

The NLDFT method for carbon has been applied to molecular sieves and membranes resulting in their detailed characterization, critical for applications in gas separation, chromatography and storage. Katsaros et al. produced membranes through a carbonization and subsequent activation of phenolic resins. When they applied the NLDFT method they deduced that the majority of the pore volume lies below 7.5 Å [95].

Jagiello et al. applied the NLDFT method to Ar and H₂ adsorption data, demonstrating it as an effective and sensitive tool to characterize carbon molecular sieves [96]. NLDFT was also utilized by Drozdov et al. who modified a mesoporous carbon substrate with activated carbon capable of adsorbing CO₂ and CH₄ [97].

2.4.2 Improvement of pore structure characterization with QSDFT model

QSDFT method significantly improves the pore size characterization of carbons. Due to the mismatch between the theoretical assumption of a smooth and homogeneous surface and the real molecularly heterogeneous surfaces of porous carbons the theoretical NLDFT adsorption isotherms exhibit multiple steps associated with layering transitions related to the formation of a monolayer, second adsorbed layer, and so on (see Figure 6). The problem is enhanced in many porous carbon materials, which exhibit broad PSDs, where artificial layering steps inherent to the theoretical isotherms cause artificial gaps on the calculated pore size distributions [20]. Figure 11 A gives the experimental adsorption isotherm of N₂ on ACF along with the fitting from NLDFT and QSDFT methods. Figure 10B gives the PSDs obtain using these methods. The gap in the NLDF PSD corresponds precisely to the pressure at which the first layer of adsorbed fluid forms.

Further examples of QSDFT kernel applications include activated carbons derived from pecan shells [98], biochars [99] and activated chars derived from poultry manure [100, 101]. Polymer systems have included carbon aerogels [102] and various polymer networks [103]. Commercial versions of granular activated carbons commonly used in water treatment applications were studied in accordance with water sorption

measurements [104]. In the case of activated carbon produced by KOH, Romanos et al. showed the capability of tailoring the pore size and distribution by precise control of the carbon consumption and amount of potassium intercalated between the graphitic layers [105]. Likewise, Hu et al. examined the effect of activation temperature and the KOH treatment ratio on the outcomes of the pore size distribution and mean sizes [106]. These samples were used for CO₂ adsorption at atmospheric pressures, with the pores < 1 nm filling with the high density CO₂. Yang et al. used the QSDFT model to study CO₂ adsorption on coal under geological conditions [107]. Nanostructured carbons template using zeolite NaY and two commercial silica gels (SG60, Fluka and ZK, POCh) were investigated with the QSDFT method to yield a mean pore size of 1.1 nm in the micropore range [108]. Another material whose microporosity plays a critical role in its applications is that of carbon derived carbide (CDC). In the work of Gogosti et al. the authors transformed TiC by a chlorination technique to that of CDC [109]. The resultant material possessed a significant amount of carbon microporosity characterized by the QSDFT method [20]. The authors show that this material has little macroporosity and demonstrates a significantly enhanced gas storage capacity compared to their powder counterparts. Another paper by the same group shows that the method accurately portrays pores comprised of a slit geometry at higher chlorination temperatures where the pores becomes more elongated [110]. Supercapacitors represent one field where the interplay between the porosity and underlying carbon substrate contribute to the overall capacitance. The Ruoff group demonstrated an activation procedure to produced mesoporous single layer graphene comprised primarily of sp² carbon with low overall oxygen content [111]. Their material, which possesses a surface area of 3100 m²/g and a

high electrical conductivity, was characterized by both NLDFT[15] and QSDFT[20] assuming a hybrid slit and cylindrical model. Jaramillo et al. employed QSDFT analysis to determine textural properties of various activated carbons used as electrodes for supercapacitors [112]. QSDFT also served for characterization of flexible supercapacitors fabricated with activated carbon impregnated into woven cotton and polyester fabrics [113].

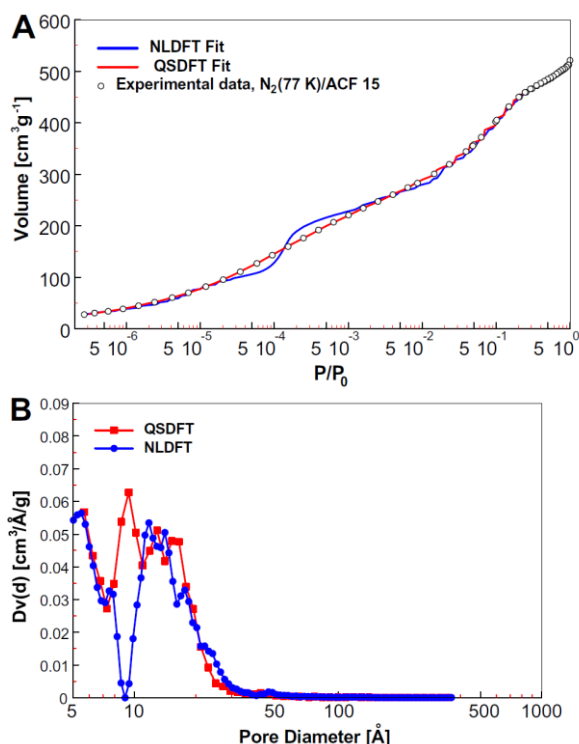


Figure 2-11: Comparison of the QSDFT and NLDFT methods for nitrogen adsorption for activated carbons. (a) Experimental isotherms with the NLDFT and QSDFT theoretical isotherms on a semi-logarithmic scale. (b) Differential pore size distributions obtained from the NLDFT and QSDFT methods. (Adapted from ref [20])

2.4.3 Designer mesoporous carbons: hybrid QSDFT kernels

For ordered/templated carbons where the morphology is a system of cylindrical rods or cylindrical channels (CMK-1, CMK-3, CMK-5, MWCMK-3, FDU-14, FDU-15, FDU-16) the cylindrical kernel is recommended [48]. If such materials have a high

degree of activation, leading to significant microporosity, than the hybrid slit-cylindrical kernel is more suitable. Equilibrium NLDFT or QSDFT kernels can be recommended for pore size analysis from either the reversible experimental isotherm, or from the desorption branch of the hysteretic isotherm of type H1. Adsorption QSDFT kernels are recommended for treating the adsorption branch of the hysteretic isotherm of H2 type. It should be noted that the criterion for choosing a particular DFT kernel is the fitting of the PSD to the experimental isotherm. Choosing the wrong pore geometry will lead to poor fitting results.

2.4.3.1 Structures with mesopore channels: cylindrical pore model

One class of carbons whose mesoporosity consists of a network of aligned cylindrical rods connected by crossbars is known as CMK-3 [114]. These materials are synthesized by inverse replication of mesoporous silica SBA-15, therefore possessing 2-D hexagonal symmetry ($p6mm$). Having a number of unique properties these materials attracted much attention for energy and biological applications. As such Zhou et al. showed that CMK-3, having high negative redox potential and high electrical double-layer capacitance, can serve as a material for negative electrode for rechargeable lithium batteries [115]. Vinu et al. [116] showed that CMK-3 is an excellent adsorbent for biomaterials, since it is thermally and mechanically stable, and, unlike silica, it is water stable and does not have charges on a surface. Since CMK-3 is microporous, as opposed to many other carbon materials, it is capable to adsorb large molecules, like enzymes and vitamins. Despite the addition of these crossbar pores which possess a complex shape, the cylindrical model is typically assumed for characterization [117].

CMK-3 usually shows the type IV adsorption isotherms with a pronounced hysteresis loop. If the hysteresis is of H1 type, the PSD can be obtained both from adsorption and desorption branches using adsorption and equilibrium kernels correspondingly; the resulting PSD give good agreement [48]. However, if hysteresis has features of H2, evidence of the pore-blocking effects upon desorption, only the adsorption branch of an isotherm should be used for analysis. This is the case for the example shown in Figure 12. For this sample the pore size distribution obtained from the desorption branch of the isotherm (using equilibrium kernel) noticeably deviates from that of the adsorption branch and gives an incorrect pore size distribution because this kernel assumes that desorption occurs via equilibrium evaporation from the pore, which is not the case for this sample. These pore size distributions are shown in Figure 12b and the fit for the adsorption kernel is shown on the isotherm in Figure 12a.

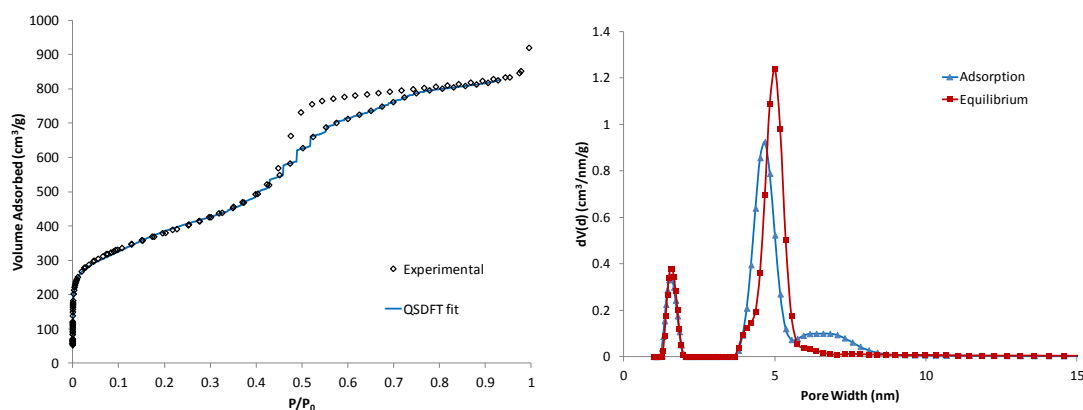


Fig 2-12: Isotherm (left) and corresponding pore size distribution (right) for CMK-3 materials of varying pore sizes. (Adapted from ref [48])

2.4.3.2 Structures with cage-like mesopores: spherical pore model

For materials in which the mesopore system is comprised of large cage-like pores connected by smaller mesopores and/or embedded in microporous matrix, such as carbons prepared from 3D colloidal templates (3DOm), the cylindrical-spherical adsorption kernel is recommended [59]. Use of cylindrical or slit model for micropores mesopores, smaller than ca. 5 nm is reasonable, since such pores (if present) are not affected by templating.

Materials with cage-like mesopores typically have H2 hysteresis type due to the pore-blocking effects (see section 5.5). However, both N₂ [118] and Ar [59] adsorption isotherms show H1 type of hysteresis. This is due to the unconventional mechanism of pore-blocking, specific for 3DOm carbons, where upon desorption the fluid in the cage-like pores is blocked not by channels [119] but by the openings between the pores [120]. Irrespective of the pore-blocking mechanism, the desorption branch of an isotherm for a 3DOm carbon sample is not suitable for calculating PSD.

In general there are two approaches to synthesizing 3DOm's, both of which includes a templating procedure. These two routes include the filling of either a mesoporous matrix or the filling of voids, typically between silica spheres in the latter, with a carbon precursor that is polymerized then carbonized [121]. The final step involves the removal of the original templating matrix commonly by etching. These two approaches have become commonplace especially with the abundance of mesoporous silicas, where there is a large variety, owing to their high structural order, large diversity in structure, controlled tunability of the wall thickness [122], and cost efficiency [123, 124]. As such, 3DOm's are ideal candidates for several applications in adsorption,

separation of bulky molecules [125] as well as supercapacitors [126]. In the latter, the advantages are clear in cases where the electrolyte solution contains bulky ions, as is the case for ionic liquids, and are too large to enter into micropores.

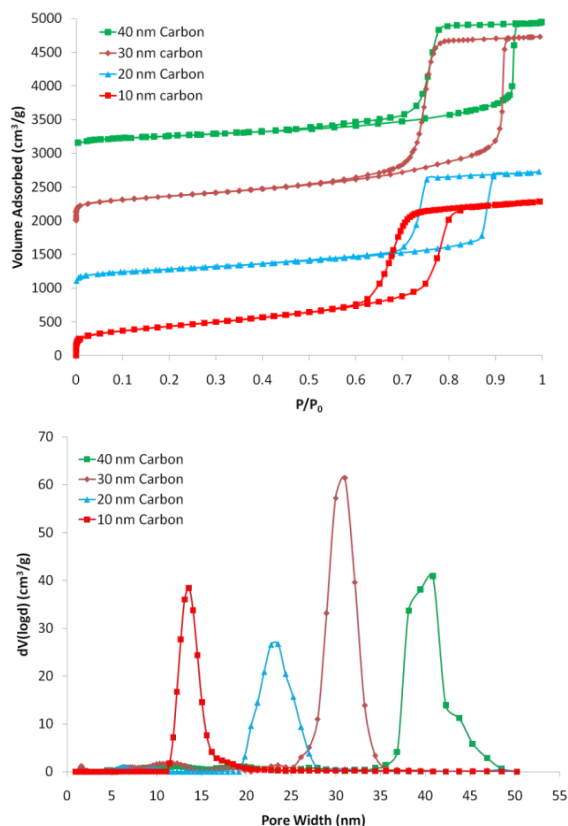


Fig 2-13: Isotherm (left) and corresponding pore size distribution (right) for 3DOM materials of varying pore sizes.

Wilke et al. applied the QSDFT model for spherical carbons in their replication of the commercially available Ludox™-50 glass yielding poly(divinyl benzene)-TM50 (PDVB-TM50) as seen in Fig. 14[127]. Pore size analysis obtained from the adsorption branch shows three pore sizes. Within the micropore range, they attributed the presence of 5% of the pore volume due to a polymerization induced phase separation. They support this argument with SAXS data. This pore fraction was followed by mesopores constituting about 10% pore volume likely due to partially collapsed larger pores or voids. Lastly the third and largest fraction, of which 85% of the total porosity is

represented, contains diameters of about 28 nm corresponding to the original silica particles. Like the 3DOm carbons explained before, this example whose hysteresis exhibits a Type H1 hysteresis originated from the pore-blocking effects. This is substantiated by the fact that the desorption branch occurs at a relative pressure of about ~ 0.6 .

Spherical QSDFT kernel was shown also to give good predictions for the pore sizes in mesoporous the poly(ionic liquid) network [128], templated using the same recipe as polymers in ref. [127].

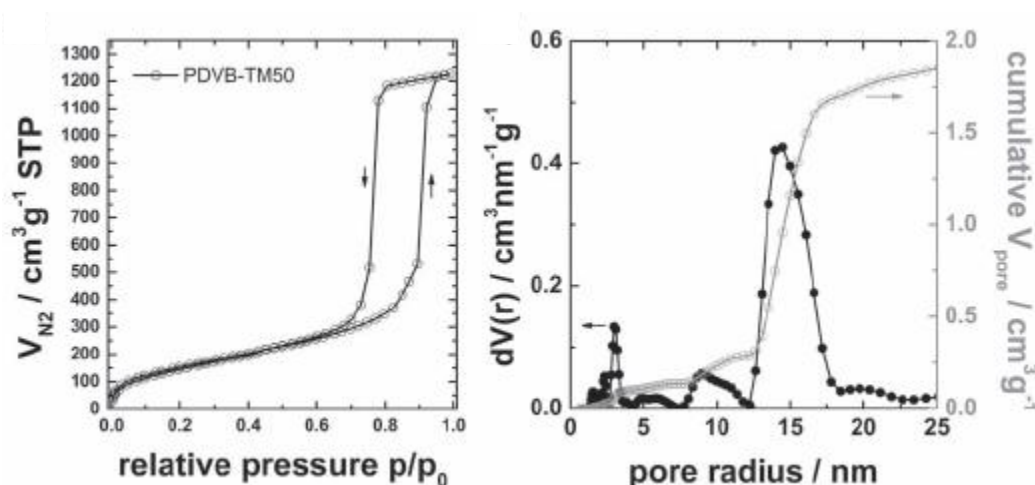


Figure 2-14: Hard templating from silica spheres to produce mesoporous carbons. (Right) N_2 at 77.3 K adsorption/desorption isotherm of PDVB-TM50; (Left) pore size distribution (black) and cumulative pore volume (grey) as obtained by QSDFT analysis (carbon, spherical pores, adsorption branch) from the adsorption isotherm. (Adapted from ref [127])

2.5 Applications of DFT Kernels for silica and other inorganic materials

For silica materials with assumed channel-like pores resulting in a H1 type hysteresis on the adsorption-desorption isotherm (MCM-41, SBA-15), a cylindrical kernel is recommended. Pore size distributions can be obtained from the adsorption branch by means of the adsorption kernel and from the desorption branch using the

equilibrium kernel. The agreement between the two PSDs obtained testifies to the absence of any pore blocking or cavitation effects.

For silica with cage-like pores connected by channels (i.e. SBA-16) spherical-cylindrical adsorption kernel should be used. Such systems tend to reveal a wide H2 hysteresis loop with the desorption branch, which is governed by cavitation [129]. As such, only the adsorption branch can be employed for PSD calculations.

5.1. MCM-41 as the reference materials for pore structure characterization.

Verification of DFT kernel of cylindrical pore model. Agreement with XRD and TEM, agreement between adsorption and desorption, agreement between different adsorbates.

The appearance of MCM-41 on the scientific landscape provided investigators for the first time a well ordered mesoporous material for which they could test their theoretical models for capillary condensation in pores in order to obtain accurate pore size distributions. Prior to the introduction of MCM-41, meso and microporous substances consisted of disordered entities where the correlation between different characterization techniques were poorly understood. However with the development of MCM-41, NLDFT methods were developed and applied in tandem with other experimental techniques such as XRD and TEM[14, 24]. The range of samples that were first tested were within 3.2 to 4.5 nm, with an example given in Figure 15. XRD results confirmed regular hexagonal arrays of pores that were correlated to NDLFT by accounting for the pore wall thickness and thereby the pore sizes themselves. This was validated against independent means to calculate the pore wall thickness by XRD [130-133] as well as TEM [131, 133]. Furthermore, both Ar and N2 adsorbates were tested for MCM-41 accounting for the consistent nature of the NLDFT approach.

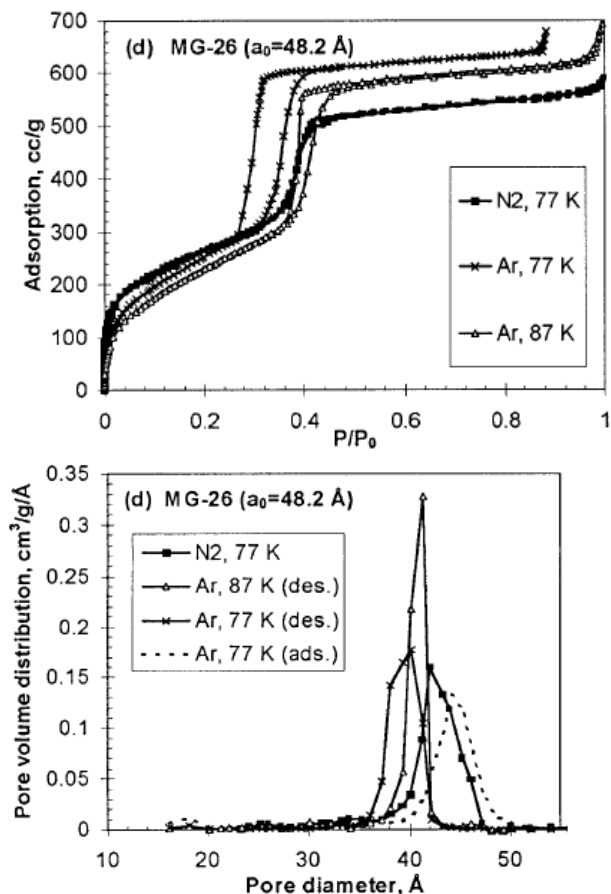


Figure 2-15: (Left) Isotherms for MCM-41 at N₂ (77 K) and Ar at both 77 K and 87 K. (Right) Corresponding pore size distributions calculated using the NLDFT method. (Adapted from Ref 14)

2.5.1 Accounting for microporosity.

Two critical problems can arise when properly taking into account the surface roughness and microporosity inherent to many polymer-templated silicas such as SBA-15, as well as many other organosilica materials. Past efforts to correctly account for the microporosity involved the standard comparison or t-plot methods [135]. However, the volume of micropores obtained by this method cannot reliably decipher between the two mechanisms of micropore filling and multilayer adsorption on a rough surface of a low-density “corona” [46]. As will be shown in the following section, using SBA-15 as a case example, the comparison method greatly underestimates the total amount of

micropores residing in the intrawall pores and the NLDFT method is revealed to be an exceedingly better approach.

2.5.2 SBA-15 as the case study system

In 1994 a seminal class of silica compounds were created from the Stucky group in Santa Barbara denoted as SBA-n [136-138]. The most widespread being SBA-15. Templated from triblock copolymers, this material possessed cylindrical mesoporous channels much like MCM-41. However SBA-15 differs from MCM-41 in the sense that due to the templating procedure it contained an appreciable amount of intrawall pores, amounting up to 30% of the total porosity. Previous methods to accurately describe the microporosity, such as the comparison plot, erroneously assumed that the micropore and mesopore range did not overlap. Doing so results in a significantly lower micropore volume. This was resolved with the application of the NLDFT method [26] which showed that pore diameters were in accord with the pore diameters obtained from quantitative modeling of XRD patterns [139]. The cumulative pore size distribution curves are displayed in Figure 16 where a prominent step corresponds to the primary mesoporous channel between 6-7 nm. In addition a tail in the curve is also representing the intrawall pores. However, it should be noted that calculating the micropore distribution is impeded by the typically smooth nature of the isotherm at low pressures [26].

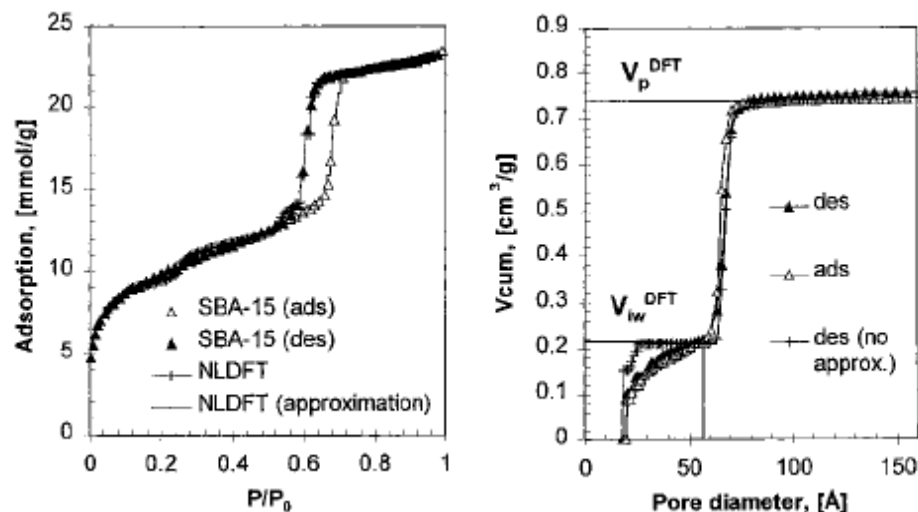


Figure 2-16: (Left) Nitrogen isotherms for SBA-15 material (triangles) with the fitted NLDFT isotherms obtained without approximation (crosses) and with approximation for the multilayer adsorption (lines). (Right) Cumulative pore volume distributions calculated from adsorption (open triangles) and desorption (closed triangles) branches. NLDFT pore volume distribution obtained from the desorption branch without approximation for the multilayer adsorption (crosses). V_p^{DFT} and V_{iw}^{DFT} are the total and intrawall pore volumes, respectively. (Adapted from ref [26])

A variety of groups have chosen the NLDFT kernel for validation of their synthesis procedure of SBA-15. Bao et al. used the nonionic surfactant P123 as a template under acidic conditions to produce ethylene-bridged SBA-15[140]. They demonstrated that as the SiO₂/P123 ratio is increased so does the microporosity. As a result the pores slowly transition from open channels to a cage like structure. Hsu et al. synthesized SBA-15 using the carboxylate-terminated triblock copolymer Pluronic P123[141]. They concluded that the use of a carboxyl terminated polymer leads to a larger pore diameter and thicker walls compared to a polymer terminated with a hydroxyl group.

Recently Pollock et al. [142] used NLDFT together with diffraction intensity analysis of small-angle neutron scattering measurements of dry SBA-15 samples to characterize the micropore, secondary mesopore, and primary mesopore structure. Based

on the agreement between the minimum pore size with the onset of the micropore size distribution, they concluded that the shape of the smallest micropores is cylinderlike, which is consistent with the unraveling of the polymer template.

2.5.2.1 Grafting of additional species on SBA-15

The emergence of SBA-15 has also led to the development of post synthesis grafting techniques that enables enhanced catalytic behavior. Despite the introduction of species into the silica that do not share the same fluid-solid interactions of the designed kernel, this does not adversely affect the application of the NLDFT methods. Yue et al demonstrated this by synthesizing Al grafted SBA-15 (Figure 17) where the resulting materials retain the hexagonal order and physical properties of purely siliceous SBA-15 [33]. Their material displays the same hysteretic isotherm behavior typical of capillary condensation in mesopores before and after grafting. Another popular species for grafting is the use of Ti. This is owed to its better activities compared to microporous zeolites, in particular when bulky molecules are involved[143]. Berube et al. utilized a chelated titanium alkoxide precursor for the grafting of Ti to SBA-15[144]. Characterization by NLDFT method allowed them to reveal that the hydrothermal treatment and calcination temperatures greatly influence the extent of epoxidation of the grafted Ti-SBA-15 structures. They further explored the conditions of the SBA-15 synthesis conditions and discovered that the density of silanol groups determines the properties of the grafted Ti both in terms of retention and coordination number [145]. Overall they concluded that the best supports for epoxidation were those SBA-15 materials that were aged at elevated

temperatures of 140 C°. The same group also demonstrated a one-step synthesis of Ti substituted silica SBA-15 by a co-condensation and demonstrated the influence of synthesis conditions (acid concentration, silicon concentration, hydrothermal treatment temperature, time) on the incorporation ratio of Ti and its subsequential chemical reactivity[146]. Along similar lines, Berube et al. grafted a titaniumalkoxide precursor onto the surface of a P123/SBA-15 composite by first modifying the precursor with a chelating agent, in this case acetyl acetone (acac) [147]. They demonstrated that the presence of acac is critical in preventing the formation of anatase TiO₂.

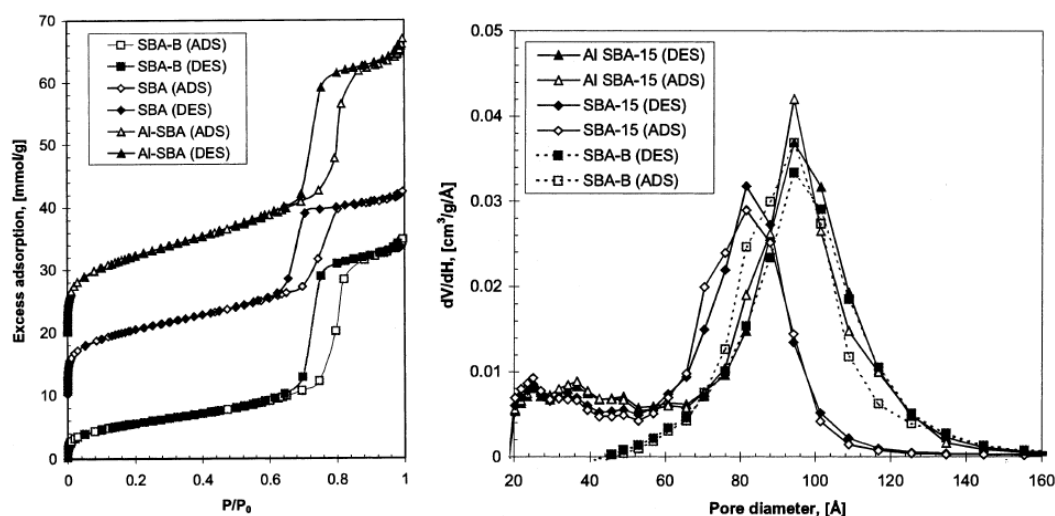


Figure 2-17: (Left) Nitrogen adsorption at 77.4 K on SBA-15 materials[33] displaying the corresponding Al grafted SBA-15 isotherms. The scale is shifted by 10 and 20 mmol g⁻¹. (Right) The pore size distributions of SBA-15 and Al-SBA-15 materials [33] calculated from the adsorption (open symbols) and desorption (filled symbols) branches of nitrogen isotherms by the NLDFT method. (Adapted from [148])

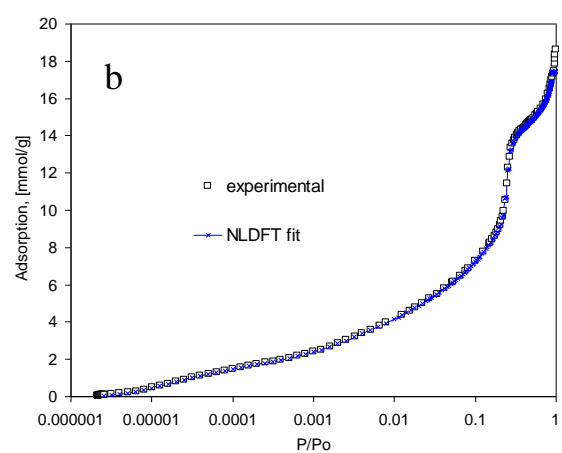
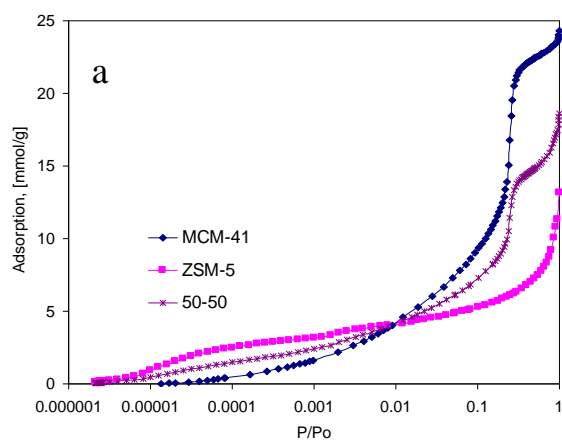
Additional species grafted to SBA-15 have included transition metals other than Ti as well as some polymers. Szegedi et al. grafted Co to SBA-15 for the oxidation of toluene [149]. Tsoncheva et al. administered a post solid state reduction technique with V₂O₅ verified by the oxidation of ethyl acetate [150]. It was concluded that the distribution of vanadium was dependent on the peculiarities of the pores structure. The result is a

consistent pore diameter after modification, albeit the surface area and pore volume are slightly diminished.

Polymer–silica composites have become appealing candidates for catalysis due to its ability to combine highly porous structures such as SBA-15 with the diverse functionality of organic polymers [151]. Wainer et al. used a surface-confined polymerization technique with two separate polymers, poly(styrene) and poly(2-hydroxyethyl methacrylate), grafted onto SBA-15 for the purposes of liquid-phase heterogeneous catalysis [151]. SBA-15 has also been shown to be a viable support for the immobilization of proteins [152]. Lin et al. deposited magnetic iron nanoparticles into the pores of SBA-15 with the intent of a facile recovery and separation process. In a separate study a metalorgano complex ferrocenyl Fischer chromium carbene complex was grafted onto the surface of SBA-15 for improved catalysis [153]. Using N₂ sorption NLDFT analysis they elucidated a diminishing effect of the pore properties after functionalization, which in turn they used to interpret the thickness of the grafted molecule layer. Likewise, the same group grafted tungsten carbene molecules onto the walls of the silica with the surprising result that a decrease of 0.30 nm in the pore size occurs when the ethoxysilane bridging units are anchored onto the SiO₂ surface, a result that was independent of the pore size [154].

2.5.2.2 Application of DFT methods to microporous materials: zeolites and MOFs.

The NLDFT model for cylindrical pores that was verified on mesoporous MCM-41 materials[14] was extended by Ravikovitch and Neimark to the micropore region for application to zeolites and zeolite containing materials [60]. The NLDFT method was tested using different standard zeolites, including ZSM-5, AlPO4-5, and VPI-5. Figure 18 presents the results of the test of the NLDFT model on high-resolution Ar adsorption isotherms at 87K (Fig. 18, a) on three reference samples: mesoporous MCM-41 material, zeolite catalyst ZSM-5, and model adsorbent, containing 50% of ZSM-5 and 50% of MCM-41 [60]. NLDFT provided an excellent fit to all samples as shown in Fig. 18 b for the isotherm on the combined adsorbent. Figs. 18 c-e present the pore size distributions. The reported average pore diameter of ZSM-5 zeolites obtained from structural considerations is 0.51-0.55 nm that agrees well with the pore size distribution obtained from Ar adsorption by the NLDFT method. It is seen that this particular sample of ZSM-5 material contained not only micropores, but also mesopores. The reference MCM-41 material is non-microporous and its pore size obtained by independent methods is 3.2 nm, in excellent agreement with the NLDFT method. The pore size distribution of the combined adsorbent exhibits two distinct groups of pores: micropores of the same size as in ZSM-5 and mesopores of the size as in MCM-41.



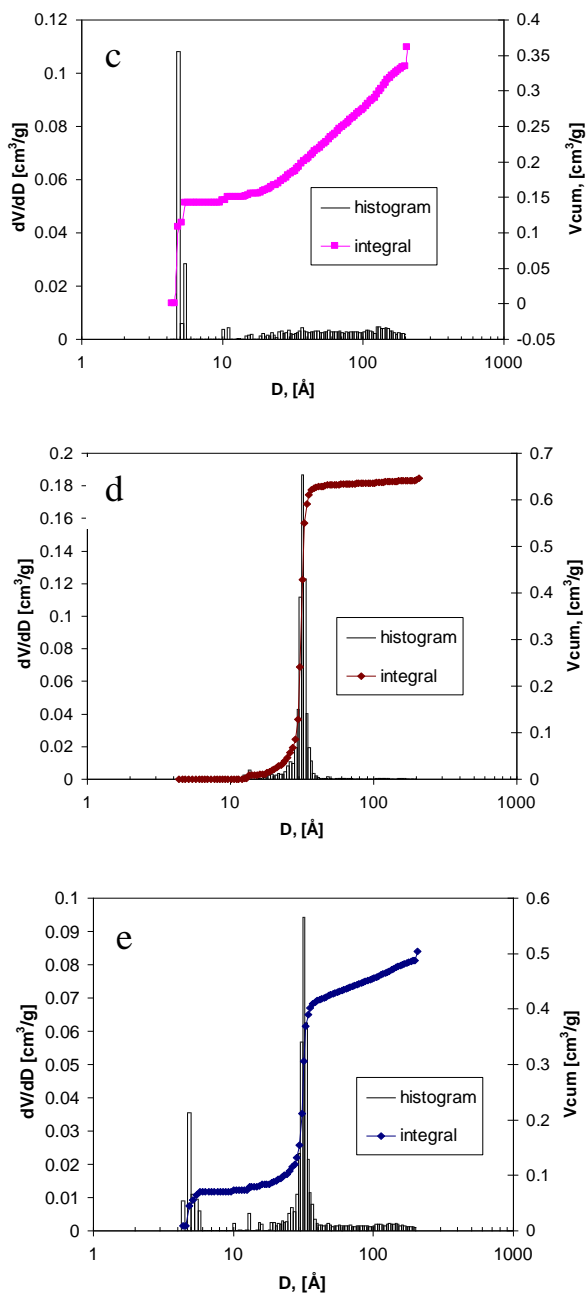


Figure. 2-18. Test of the NLDFT model for zeolite-containing materials. (a) Argon adsorption isotherms at 87 K on MCM-41, ZSM-5 and their 50-50 mixture. (b) NLDFT fit of the isotherm on combined sample. (c-e) NLDFT pore size distributions for ZSM-5, MCM-41, and combined sample. The pore size distribution of the combined sample perfectly agrees with the sum of the pore size distributions of its constitutive parts. (Adapted from ref [60])

Another example of the NLDFT analysis of ZSM-5 zeolite materials of hierarchical structure was performed by Serrano et al[155]. It is worth noting that the range of pore

sizes that can be captured by the NLDFT method in these samples extends from 0.5 to 50 nm.

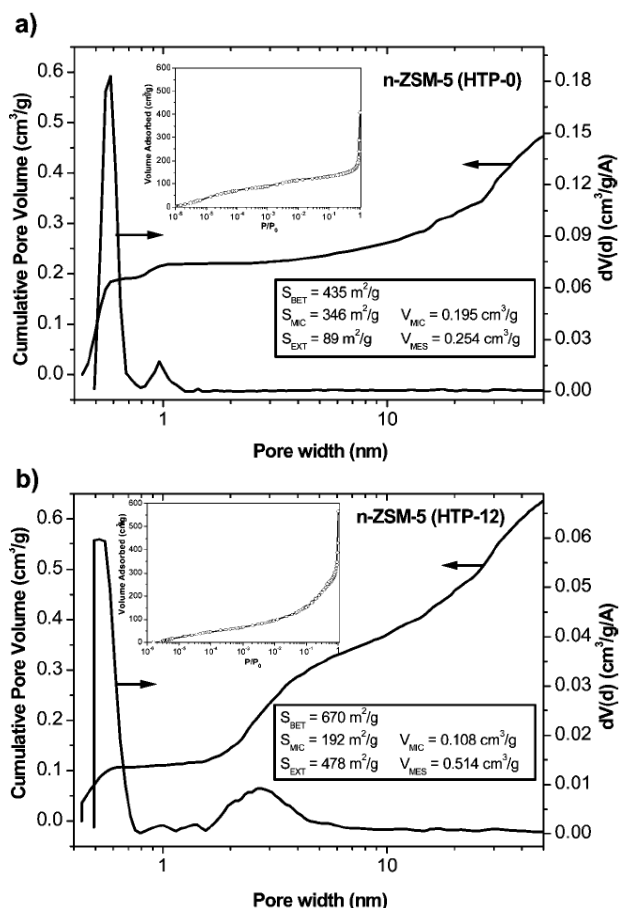


Figure 2-19. Pore size distributions and cumulative pore volumes for calcined nanocrystalline *n*-ZSM-5 materials prepared under high-temperature precrystallization (HTP) at 90 °C. Conditions include both (a) 0% and (b) 12% PHAPTMS surface-silanization agent. The NLDFT method was applied to obtain the pore size distributions assuming a cylindrical pore model and using the adsorption branch of the Ar isotherm at 87 K plotted on logarithmic scales (insets). Nomenclature corresponds to the following: BET surface area (S_{BET}); micropore surface area (S_{MIC}); external surface area (S_{EXT}) estimated as the difference $S_{\text{BET}} - S_{\text{MIC}}$; micropore volume (V_{MIC}) determined for pore sizes below 1.6 nm; and mesopore volume (V_{MES}) determined for pore sizes ranging from 1.6 to 50 nm. (Adapted from ref [155])

The NLDFT method is applicable to various micro-mesoporous materials, including adsorbents, catalysts, separation membranes, sensors, and other zeolite-based systems[156]. Recently, the NLDFT method was used for analysis of Ar isotherms on indium base metal-organic frameworks of soc topology (soc MOF) with channel pore structures[157]. This example is presented in Figure 20. Since the parameters for Ar-

socMOF interactions are not developed, the authors used two existing kernels with Ar-silica and Ar-carbon interaction parameters, and found that the pore size determined from the Ar-silica kernel produced the pore size in agreement with the crystallographic data.

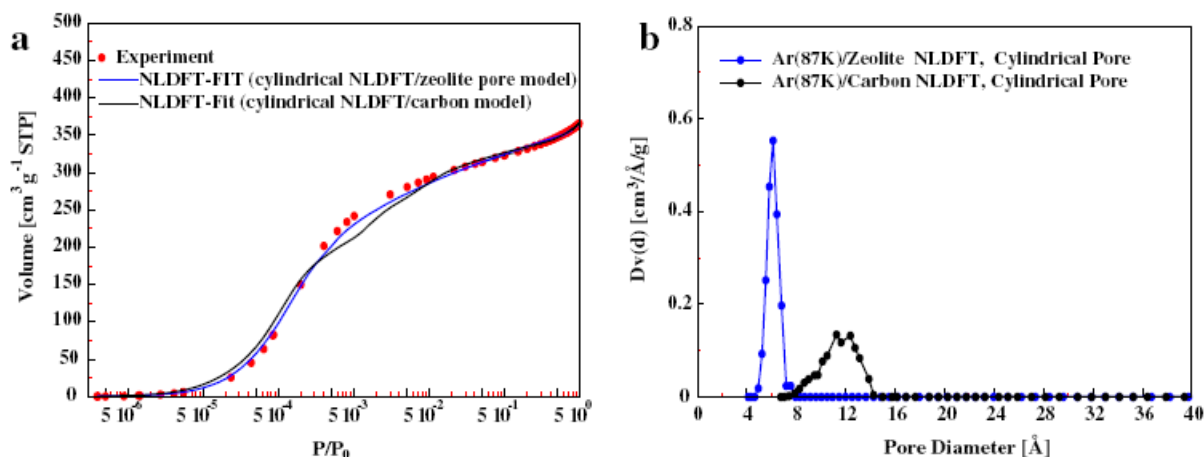


Fig. 2-20 a) Experimental Argon (87.3 K) isotherm on socMOF and NLDFT fit for Argon adsorption at 87.3 K in cylindrical pores with either Ar- silica/zeolite or Ar-carbon interaction parameters. **(b)** Differential NLDFT pore size distribution curves. Pore size of 6.1 Å obtained from the NLDFT kernel with Ar-silica/zeolite parameters agrees well with the expected accessible pore diameter of the cylindrical-like main channels in soc-MOF. (Adapted from ref [157])

2.5.3 Oxides other than silica.

Although originally developed for silicas, the NLDFT kernel can be applied to disordered systems and other inorganic porous materials without further modification. In the case of disordered materials such as porous glass, the adsorbate wall interaction remains the same. Kullmann et al. studied nanoporous glass monoliths with pore sizes under 5 nm and compared the characterization results of NDLFT and positron lifetime spectroscopy (PALS), the latter being a technique to study voids and defects [158]. The authors obtained a type I isotherm, typical of microporous materials and applied the NLDFT equilibrium model for silicas. It can be seen from Figure 21 that the authors

produced a porous glass with a bimodal distribution consisting primarily of micropores confirmed by the two independent methods.

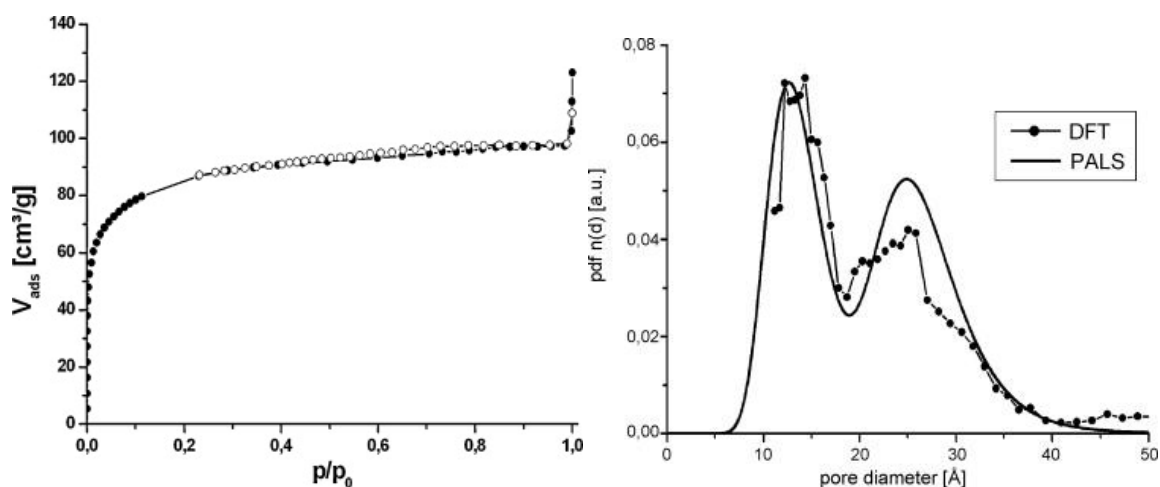


Figure 2-21: (Left) N₂ isotherm at 77 K for nanoporous glass monoliths. (Right) Overlay of NLDFT equilibrium model for cylindrical pores and PALS pore size distributions (distribution curves were normalized for the same maximum) (Adapted from ref [158])

The application of the NLDFT silica model can also hold true for a variety of oxides. Chavez et al. applied the NLDFT technique to characterize the synthesis of tungsten oxide (WO_3) films that displayed pore size distributions in both the meso and microporous ranges [159]. Likewise Zhou et al. developed a hard templating technique using mesoporous silica to fabricate mesoporous WO_3 [160]. The application of the NLDFT adsorption kernel for cylindrical silica pores indicated highly ordered pores with crystalline walls. Their results were validated against both TEM and XRD. Chandra et al synthesized zinc oxide (ZnO) by a templated method and the corresponding NLDFT characterization proved to be in good agreement with TEM results[161]. In the case of alumina, Landers et al. utilized the NLDFT kernel to show the evolution of a bimodal

distribution as a function of mixing time of alumina pastes, a change reflected in both the desorption isotherms and pore size distribution (Figure 22) [162].

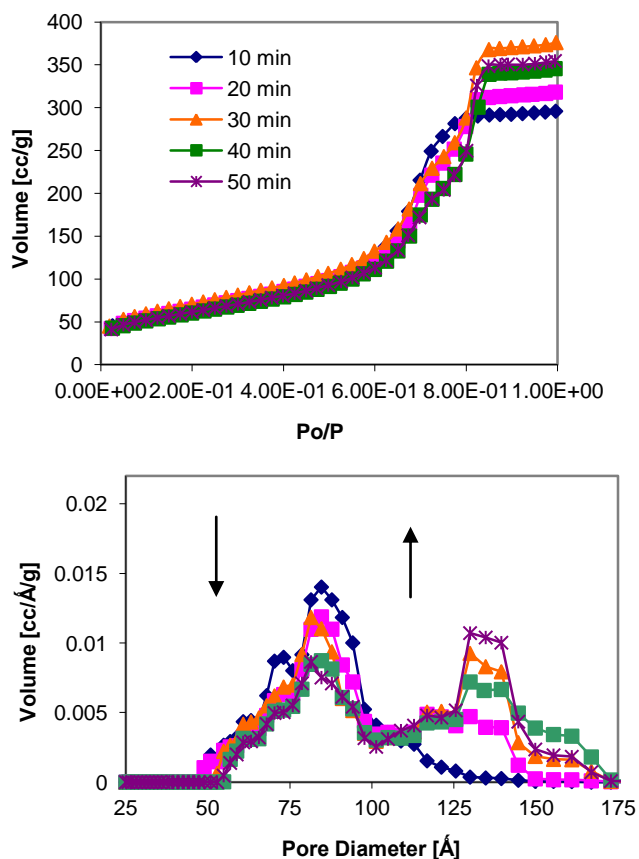


Figure 2-22: (a) N₂ Desorption isotherms 77 K on extruded and calcined alumina pastes mixed with 1% acid displayed as function of mixing time. (b) Pore size distribution calculated using NLDFT as a function of mixing time for 1% acid. (Adapted from ref [162])

2.5.4 QSDFT model for silica materials.

Application of NLDFT method for characterization of silica materials did not reveal artifacts in PSDs related to the layered structure of the theoretical isotherms as it was observed in carbons (see section 4.2). QSDFT predictions in the region of film adsorption (prior to the capillary condensation) provide excellent agreement to the

experimental adsorption data on SBA-15 silica (Fig 5 b) [46], which could not be achieved having a NLDFT isotherm with layering steps. Giving more advanced and realistic model for silica surface QSDFT tends to replace NLDFT for characterization of silicas, including MCM-41 [163], SBA-16 [164] and other.

2.5.5 Materials with cage-like structure: spherical pore model

The characterization of cage like silica structures (SBA-1, SBA-6, SBA-16, FDU-1, KIT-5, and FDU-12) has been impeded by the use of traditional kernels. First the accurate description of the transport pores via N₂ adsorption-desorption becomes invalid as they go past the lower limit of 5 nm. Matters are further complicated by mechanisms previously mentioned involving pore blocking and cavitation. These issues were resolved with the advent of a new NLDFT kernel tailored for silica pores constituting of both spherical and cylindrical geometries [23, 35]. Tailored for hierarchical ordered porous materials, this kernel should be applied for systems containing cylindrical pores less than 5 nm and spherical pores greater than 5 nm. These materials also typically exhibit a H2 hysteresis type loop resulting from pore blocking. It is thus recommended that the pore size analysis be based solely on the adsorption branch.

2.5.5.1 SBA-1 and SBA-16 cage-like structures

SBA-1 represented the first class of materials resulting from the templating of supramolecular surfactant aggregates to form uniform spherical pores connected by smaller transport pores [136]. Moreover, these pores had the ability to be tailored to

different sizes and specifications by merely altering the synthesis conditions (pH, temperature, concentration). Of the new materials that emerged SBA-1 and SBA-16 were notable in terms of their uniform and large cage like cavities with cubic ($Im\bar{3}m$) symmetry. The arrival of new NLDFT kernels capable of addressing hybrid pore structures led to the better characterization of such porous materials as SBA-1 and SBA-16. The kernel developed for the latter was recently validated with XRD results stemming from the work of Miyasaka et al. [164]. Several groups have employed the use of the NLDFT kernel in order to confirm their pore size distribution resulting from various synthesis conditions. Vinu et al. investigated the influence of acid to surfactant concentration as well as synthesis time on the pore size and stability of SBA-1 structures. They concluded that SBA-1 is mechanically more stable compared to mesoporous silica materials such as MCM-41 and SBA-15, but is mechanically comparable to the cubic structure of MCM-48 [165]. Ting et al. were capable of synthesizing SBA-1 across a wide temperature range and composition range by using the template dodecyl trimethyl ammonium chloride ($C_{12}TMACl$) under strongly acidic conditions as opposed to the more conventional $C_{16}TMABr$ [166]. Kao was able to synthesize SBA-1 with the aid of D-fructose as an auxiliary agent [167]. Likewise, the same group was able to functionalize SBA-1 through several means. First with vinyl groups via a room temperature condensation reaction with tetraethoxysilane (TEOS) and trimethoxyvinylsilane (TMVS) templated by cetyltriethylammonium bromide (CTEABr) under acidic conditions [168]. In a proceeding paper the same group functionalized SBA-1 with phenyl groups via co-condensation of tetraethoxysilane (TEOS) and phenyltriethoxysilane (PhTES) [169]. In

both cases the pore size distribution were confirmed with the aid of the hybrid NLDFT kernel and the presence of the functional groups with the aid of NMR.

SBA-16 was first synthesized in a low acidic medium (0.5 M HCl) using a silica source of either TEOS or TMOS [170]. Like SBA-15, SBA-16 can be synthesized by using triblock copolymers to produce large 3-dimensional mesoporous silicas. Typically these triblock polymers are relatively large PEO chains, the most common being F127, F108, and F98. The first example of the NLDFT applied to SBA-16 showed it to have a spherical cage size of 8.5 nm and a minimum wall thickness of 5.9 nm[23].

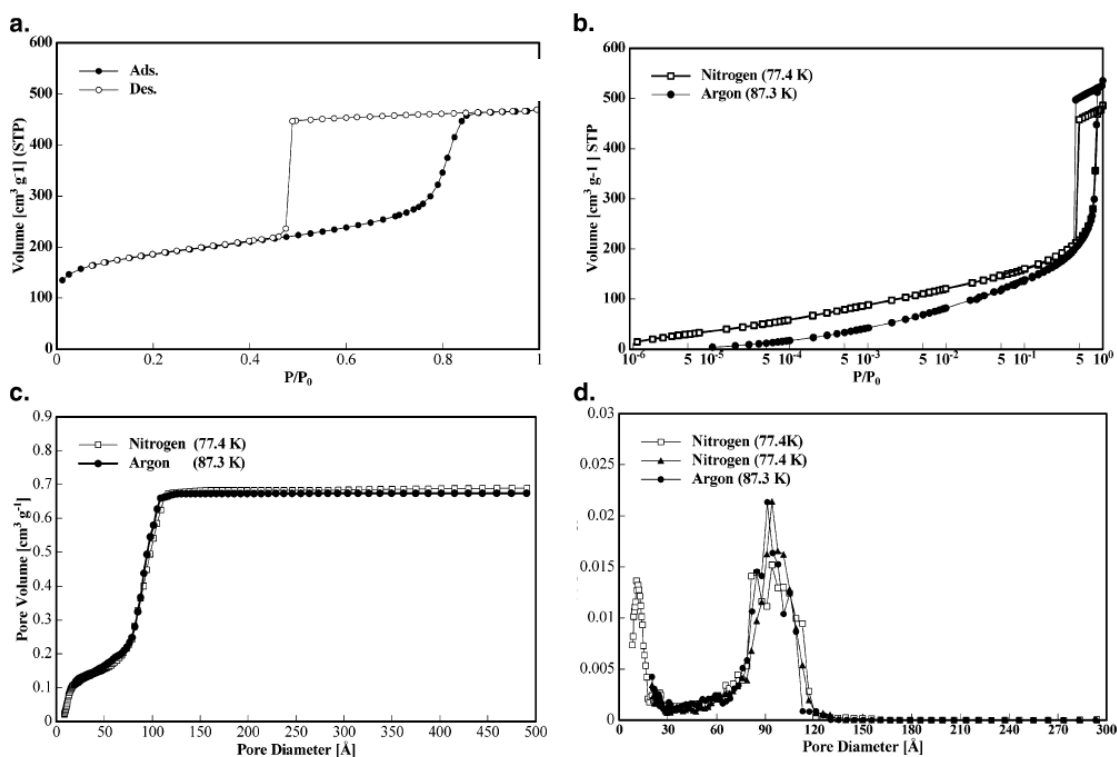


Figure 2-23: (a) High-resolution nitrogen (77.4 K) adsorption/desorption isotherm on SE3030 silica. (b) Comparison of nitrogen (77.4 K) and argon (87.3K) adsorption/desorption on SE3030 silica plotted on a semi logarithmic scale. (c) NLDFT cumulative pore volume plots calculated from the adsorption branch by applying the kernel of metastable adsorption isotherms based on a cylindrical pore model for silica. Both nitrogen at 77.4 K and argon at 87.3 K are displayed. (d) NLDFT pore size distributions from nitrogen at 77.4 K and argon at 87.3 K respectively. Distributions were calculated from the adsorption branch of the isotherm (see b and c) (Adapted from ref [36])

Esparza et al. synthesized a variety of SBA-16 through a common micelle templating technique ranging in pore sizes from 7.59-7.90 nm verified by the NLDFT technique[171]. Kleitz et al. were capable of producing SBA-16 materials synthesized in a EO106PO70EO106 (F127)-butanol-H₂O system under mildly acidic conditions[172]. They could fine tune the pore diameter by altering the hydrothermal treatment temperature producing cage dimensions varying between 6 to 12 nm. From these results they concluded that the NLDFT kernel was in excellent agreement with XRD modeling results. In a similar system, the authors demonstrated that they could tune the pore size between 4 and 7 nm by varying the initial mixture composition [173].

2.5.5.2 FDU-1, FDU-2, and FDU-12 Spherical Structures

FDU materials derive its name from Fudan University in Shanghai [174, 175]. Like SBA-16, the unique pore structures of these FDU materials elicited the need for methods to accurately take into account their hybrid structure[35]. The pores in these materials consist of geometries similar to ink bottles, and gives rise to the challenges outlined in section 2.1 relating to the phenomena of pore blocking and cavitation. The synthesis involves three components, namely block copolymers, an organic solvent, and inorganic salts, which when combined properly and polymerized forms a template. Two routes can then be employed to attain either mesoporous silica or carbon. In the former a source of silica can be introduced in order to fill the voids of the mesoporous material with the polymer template being removed later in the process. In the latter, no further carbon source is required, as the material can be merely carbonized under nitrogen gas to form a sturdy carbon framework. Several groups have validated the existence of spherical

pores using the NLDFT kernels. The Zhao group first showed that FDU-1 exhibits Im3m symmetry[176]. They have studied the pore variations that arises during the synthesis of FDU-12 structures, most notably the effect of temperature on the cage like spherical pores and the cage entrances[177]. Ersen et al. coupled electron tomography with nitrogen adsorption measurements in order to study the stacking faults residing in the silica material FDU-12[178].

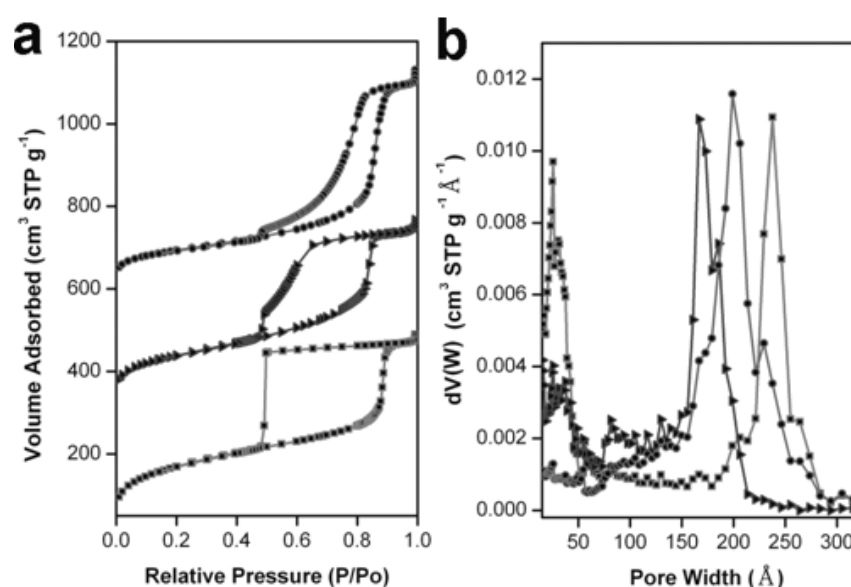


Figure 2-24: (a) Nitrogen sorption isotherms and (b) pore size distribution of calcined mesoporous silica FDU-12 samples. The plotted lines of L-FDU-12 and R-FDU-12 hydrothermally treated at 100 °C, and R-FDU-12 treated at 120 °C are denoted as solid squares, triangles, and circles, respectively. L and R refer to different amounts of salt in the synthesis procedure. The scale of adsorption volume in panel is shifted by 300 cm³/g for R-FDU-12 at 100 °C and 600 cm³/g for R-FDU-12 at 120 °C.

2.5.5.3 KIT-5 cage like pore structures.

An advantage of the NLDFT method is the ability to characterize 3-D structures with interconnecting geometries. A case example is the silica KIT-5. First reported by Kleitz et al., KIT-5 is defined by a Fm3m symmetry with a spherical pore geometry interconnected by smaller pores [179]. The adsorption isotherm features a type IV

classification with a sharp capillary condensation step at high relative pressures. KIT-5 is further defined by a H2 hysteresis loop, indicative of uniform spherical pores. Several investigators have applied the NLDFT method in determining the effect of synthesis modulation on these 3D spherical structures. Yang et al. attempted a post synthesis technique on KIT-5 samples treated with H_2SO_4 [180]. They used Ar at 87 K in order to reduce any interaction which may arise with the different surface chemistry related to either the calcined or acid treated samples. From NLDFT analysis it was demonstrated that the acid treated KIT-5 samples exhibited a much larger pore volume compared to their calcined counterparts. However, the largest surface areas were obtained from the calcined samples due mostly in part to the contribution of intrawall microporosity from the block copolymer templates. These results were confirmed by Wu et al. who studied the post-synthesis structural modulation of KIT-5 [181]. On one hand, they were able to show that treatment with NH_4OH in general gave smaller mesopore cage sizes and lower micropore volume. On the other hand, treatment with H_2SO_4 produced mesopores with larger cage-like structures containing larger pore entrances but a decrease in the ultramicro pore volume. Their acid treated KIT-5 samples are displayed in Fig. 24 where the as synthesized samples of KIT-5 are treated with a fixed concentration of acid at various times. The evolution of the hysteresis loop corresponds to a change from a H2 to a H1 hysteresis loop. This in turn implies a change in the pore morphology. This is displayed in the NLDFT calculated PSD results which show a decrease in microporosity with increased acid treatment duration.

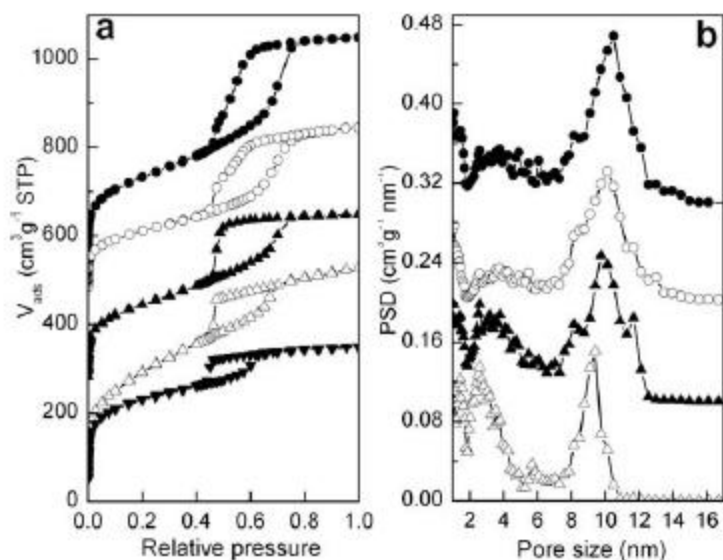


Figure 2-25:(a) Nitrogen isotherms of KIT-5 treated with acid for various durations. KIT-5-0h (\blacktriangledown), KIT-5-1h (\triangle), KIT-5-5h (\blacktriangle), KIT-5-10h (\circ) and KIT-5-24h (\bullet). The isotherms are shifted by 40, 260, 460 and 510 $\text{cm}^3 \text{g}^{-1} \text{STP}$, respectively. (b) Pore size distributions of the acid-treated materials calculated from the adsorption branches by using the NLDFT method. The offset between each PSD is 0.1 $\text{cm}^3 \text{g}^{-1} \text{nm}^{-1}$.

2.5.5.4 Silica's with gyroidal pore structure: KIT-6, MCM-48

The application of NLDFT is not limited to pore structures that are defined by an array of pores. In the case of KIT-6, the structure is defined by two intertwining mesopores, forming a gyroidal structure. The interconnected pores can give rise to a hysteresis relating to pore blocking effects. Kleitz et al investigated the hysteresis mechanism within KIT-6 materials aged at different temperatures seen in Figure 25 using both NLDFT for N_2 at 77 K and Ar at 87 K [184]. They observed a narrower hysteresis loop for KIT-6 when compared to SBA-15 of the same pore size, thus indicating a characteristic feature of the hysteresis when going from a pseudo-one-dimensional material such as SBA-15 to that of a 3-D structure such as KIT-6. The authors validate their NLDFT finding with the use of TEM and XRD modeling. In a related paper Guo et

al. probed phenylene-bridged periodic mesoporous organosilicas produced via synthesis materials containing Pluronic P123 triblock copolymer, butanol and water[185]. This led to a bicontinuous cubic Ia3d KIT-6 structure produced in high yields and purity. In this case 1,4-bis(triethoxysilyl)benzene was used as the organosilica source where the ageing temperature allowed for precise control over the pore characteristics such as mesopore size, volume and specific surface area. The authors suggested that the resultant 3-D structure would be beneficial for applications of host-guest chemistry, where concerns of pore blocking may arise. Post synthesis grafting techniques [186-191] for mesoporous silicas have gained traction in recent years for the development and application of highly selective sorbents, solid catalysts or drug delivery systems[192-196]. One such approach is the pore surface-confined polymerization technique developed by Choi et al.[197]. In a two step process Guillet-Nicolas et al. modified the walls of KIT-6 with the polymer polychloromethylstyrene (PCMS) followed by the attachment of amine groups to the polymer[198].

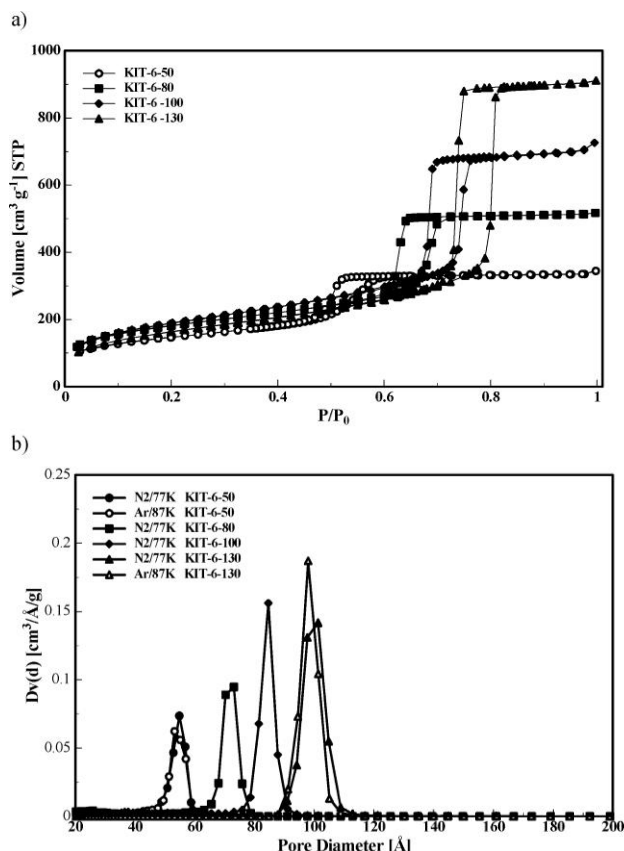


Figure 2-26: (a) Nitrogen isotherms (at 77.4 K) in KIT-6 samples aged at temperatures varying from 50 to 130 °C. The desorption branch is used for the NLDFT pore size distributions for nitrogen at 77.4 K and argon at 87.3 K respectively. (b) Selected KIT-6 samples aged at different temperatures are displayed. The NLDFT pore sizes (equilibrium) are 5.5, 7.3, 8.4, and 10.1 nm, for 50, 80, 100, and 130 °C, respectively. (Adapted from ref [184])

2.5.6 Cavitation as a negative factor in pore size analysis

Complexity can arise in hierarchical systems comprised of both micro-mesopores that creates a wider variety in the observed hysteretic behavior. This complexity is inherent to the adsorbed fluid and surrounding pore system and can mask phenomena such as pore blocking and cavitation resulting from desorption. From a characterization stand point this can complicate matters. However if the hysteresis loop is interpreted correctly it can provide a myriad of information about the pore network morphology. For

the case of cavitation the pore size is obscured as the point of desorption is weakly correlated with the pore size. Cavitation occurs during the desorption process resulting from the spontaneous nucleation and growth of gas bubbles in the metastable fluid confined in the pores[129]. The process leading up to this spontaneous act involves a prolonged metastable state of the condensed fluid which is overstretched by capillary pressure. It is typically inherent to spherical pore systems connected by smaller necks seen in Figure 26. Both theoretical and experimental [23, 36] studies have shown that if this neck diameter is smaller than some critical size than cavitation will occur. In the case of nitrogen at 77.4 K this is estimated to be 5 nm.

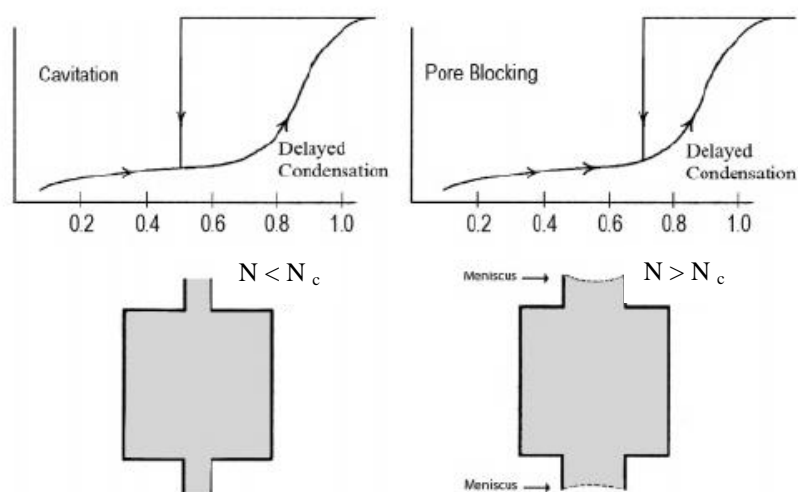


Figure 2-27: Schematic illustration of cavitation and pore blocking where the variable N indicates the neck size of the pore [36]

2.5.6.1 How to distinguish cavitation effects with DFT?

Desorption isotherms of the materials having spherical pore geometry are always affected by either pore blocking [119] or cavitation effects [129]. Therefore the size of the primary cage-like pores cannot be derived from the desorption branch using one of the NLDFT/QSDFT spherical kernels. For the case of pore-blocking, the desorption

isotherm may have information on the distribution of the pore necks (connecting channels), which can be derived applying a hybrid cylindrical-spherical kernel [36]. How to distinguish the cavitation mechanism of evaporation from the classical pore-blocking? First criterion is the pressure. It has been shown that homogeneous cavitation of nitrogen in pores takes place at the relative pressures 0.4-0.5 almost irrespective of the pore size [129]. However, this rule is not strict; recently several experimental [199-201] and theoretical [202] papers reported cavitation events in the pores at a substantially higher pressure values ($> 0.6-0.7$), when not homogeneous, but heterogeneous nucleation takes place.

On the basis of DFT method Thommes et al. proposed a simple criteria to distinguish, whether the desorption branch of an isotherm is affected by pore blocking or cavitation [36]. They used experimental data from two adsorptives, nitrogen (77.4 K) and argon (87.3 K), and calculated PSDs by means of applying the N₂ and Ar hybrid NLDFT kernels to the desorption branches of the corresponding isotherms. For Vycor glass, where desorption is affected by pore blocking, the resulting PSDs were close (Fig. 27 a), since they were determined by the pressure of equilibrium desorption from the connecting throats. For SE3030 silica, where desorption was affected by cavitation, on the contrary, resulting PSDs were noticeably different. The cavitation pressure depends weakly on the pore size, and mainly determined by the properties of the fluid. This method was employed recently to determine the mechanism of desorption in the 3DOM carbons [59], discussed in section 2.4.4.3.

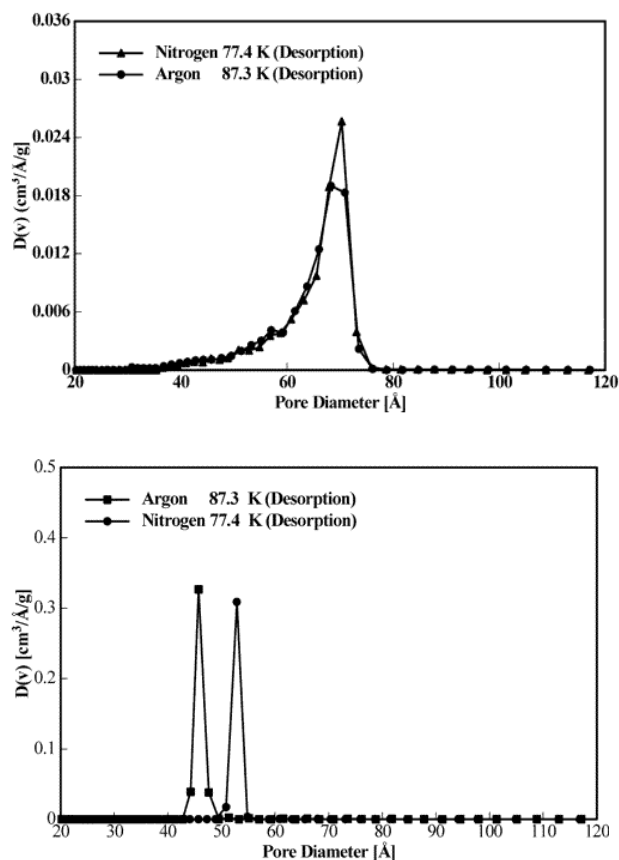


Figure 2-28. Distinguishing between cavitation effects in materials. NLDFT pore size distribution curves obtained from the desorption branches of the sorption data by applying the NLDFT equilibrium transition kernel (on the basis of a cylindrical pore model) for the systems nitrogen (77.4 K)/silica and argon (87.3K) /silica. (a) for Vycor glass (b) for SE3030 silica. (Adapted from ref. [36])

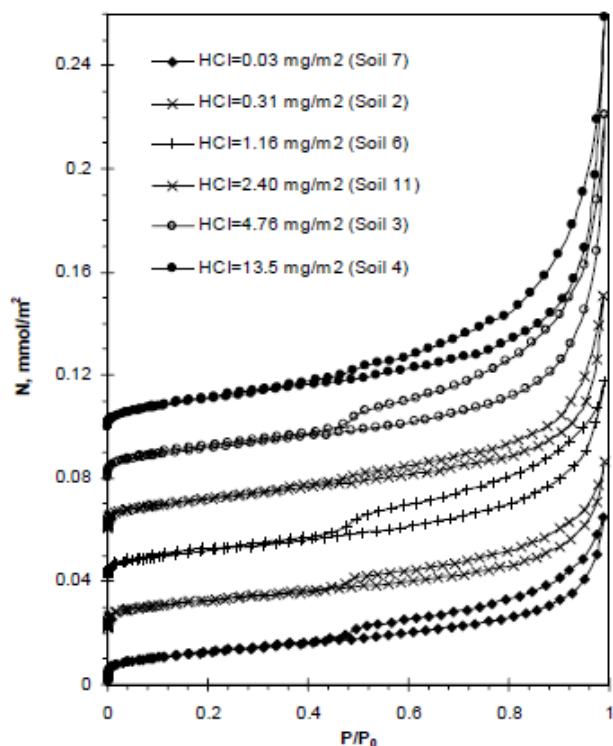


Figure 2-29: N_2 adsorption/desorption isotherms at 77.4 K reduced per unit of BET surface area. The isotherms are shifted on the vertical scale by 0.02, 0.04, 0.06, 0.08 and 0.1 mol/m^2 for soils 2, 6, 11, 3 and 4, respectively. (Ref: Nitrogen and Carbon Dioxide Adsorption by Soils, Ravikovitch et al.)

2.5.6.2 Characteristic examples. Plugged SBA-15 open and blocked cylindrical channels. Cage-like materials – SBA-16, etc.

One advantage to silica materials such as SBA-15 is the inherent microporosity. It would be advantageous to be able to tailor the ratio of the micro and meso pores in these materials. Miyazawa and Inagaki improved on the work of Stucky and Zhao by being able to optimize this ratio [203]. Van Der Voort et al. [28] showed further improvement both in the thermal and mechanical stability by synthesizing a plugged hexagonal templated silica (PHTS). This material exhibited a typical XRD pattern commonly found for SBA-15 and shared similar features, but differed in several regards. Like SBA-15, the PHTS displays a one-step capillary condensation signifying uniform mesopores (Figure

29). In addition to this is the presence of a two-step desorption branch with the second step occurring at a relative pressure of 0.45. This delayed desorption is representative of pore blocking effects and is consistent with a structure that has both open and blocked cylindrical pores.

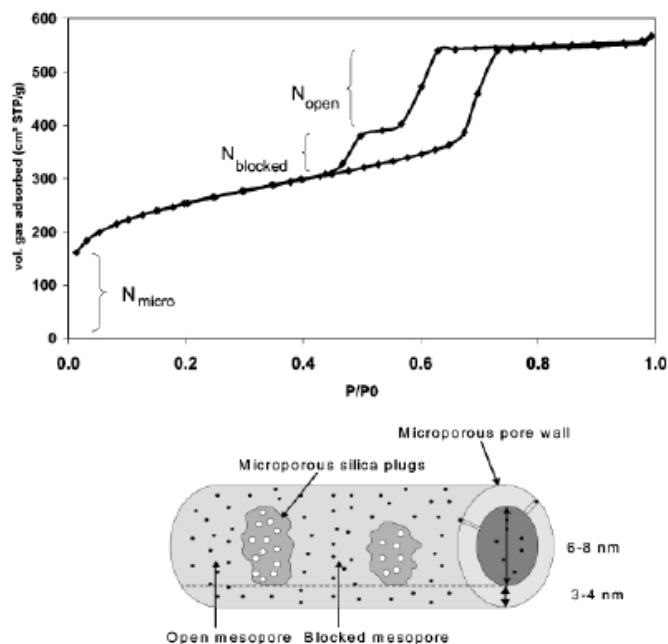


Figure 2-30: Nitrogen 77 K isotherm of a typical PHTS material exhibiting a 2-step desorption demonstrating two mechanisms of evaporation and cavitation. (Adapted from ref [28])

2.6 DFT models for interpretation of in-situ XDR data

In a series of papers [51, 163, 164], the QSDFT method was extended to describe the observations of the in-situ XDR measurements on mesoporous crystals of MCM-41 and SBA-16 types. The strategy for the QSDFT approach for modeling of diffraction patterns is as follows. The parameters of fluid-solid interactions are taken from the literature, see Table 3. The parameters for the solid density distribution, solid density and roughness parameter, are taken from the reconstruction of the XRD patterns on the dry sample. The temperature of the XRD experiments, which is maintained by liquid nitrogen

and is not measured directly at the adsorbent, is determined from the agreement of the measured by XRD pressure of capillary condensation pressure and predicted by the QSDFT model with adopted energetic and structural parameters. Then, the calculation of the density profiles of adsorbed fluid is performed at a series of gas pressures and the predicted XDR patterns are obtained by the Fourier transform converting the fluid and solid densities into the electron density.

An example of such approach is illustrated in Figures 30 and 31 for the Ar adsorption on an MCM-41 sample with the mean pore diameter of 36.8 Å[51]. From the comparison with the QSDFT predictions for the hexagonal array of cylindrical silica pores with the roughness parameter of $\delta=4\text{\AA}$, the XRD experiment temperature was determined as 83 K. The calculated fluid density profiles (DP) in pores are in agreement with the reconstructed from the XRD patterns electron density profiles, Fig. 30. Note that the QSDFT model correctly predicts the increase of adsorption in the pore wall corona and the growth of the adsorption film. In Fig. 31, the calculations by the Fourier transform diffraction intensity are compared with the experimental XRD data for 10, 11, and 20 reflections. An analogous study was performed [164] for cubic cage-like structures of SBA-16 crystals. Almost quantitative correspondence of theoretical and experimental data suggests that the QSDFT method correctly captures the main physical mechanisms of physical adsorption on mesoporous crystals with minimum additional structural and energetic parameters, which can be determined from the independent measurements.

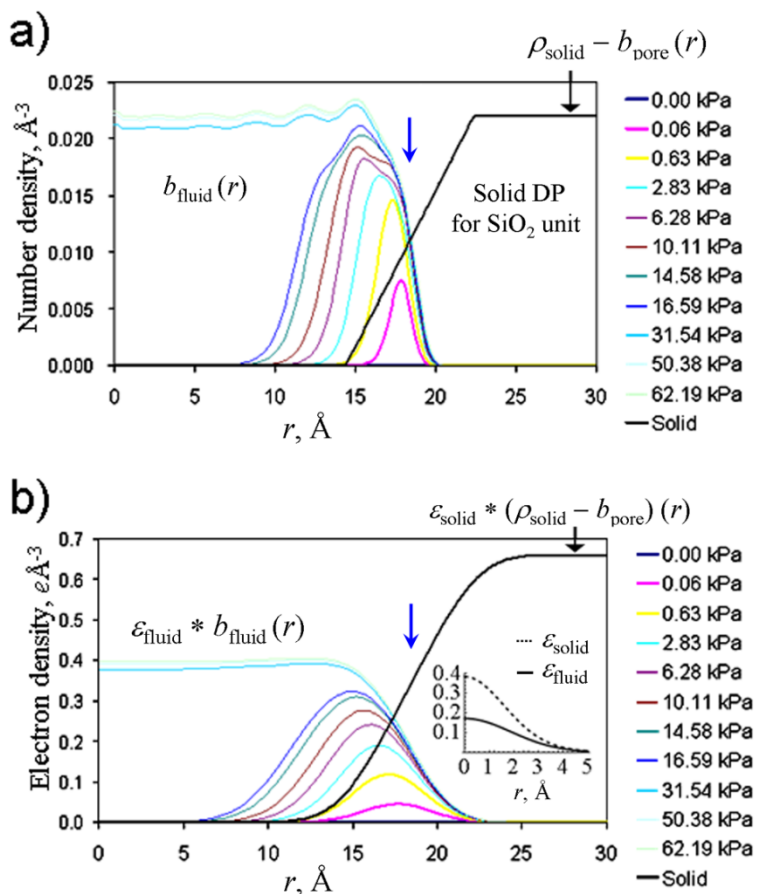


Figure 2-31. Evolution of the mass and electron density profiles of adsorbed fluid in the process of adsorption. Ar adsorption at T=83K in cylindrical pores of MCM-41 sample at different Ar pressures in the gas phase (the pressure values are shown in the left column). a) – QSDFT fluid density profiles in the silica pore of diameter $D=36.8\text{\AA}$ with the roughness parameter $\delta=4\text{\AA}$, the color corresponds to the pressure shown on the left, solid density is plotted in black; b) – reconstructed electron density profiles for fluid and solid from in-situ XRD measurements (kernel for the electron spread of solid and fluid shown in the insert), the color corresponds to the pressure shown on the left, solid density is plotted in black. Blue arrows indicate the position of the mean pore radius, 18.4 \AA . (Adapted from ref [51])

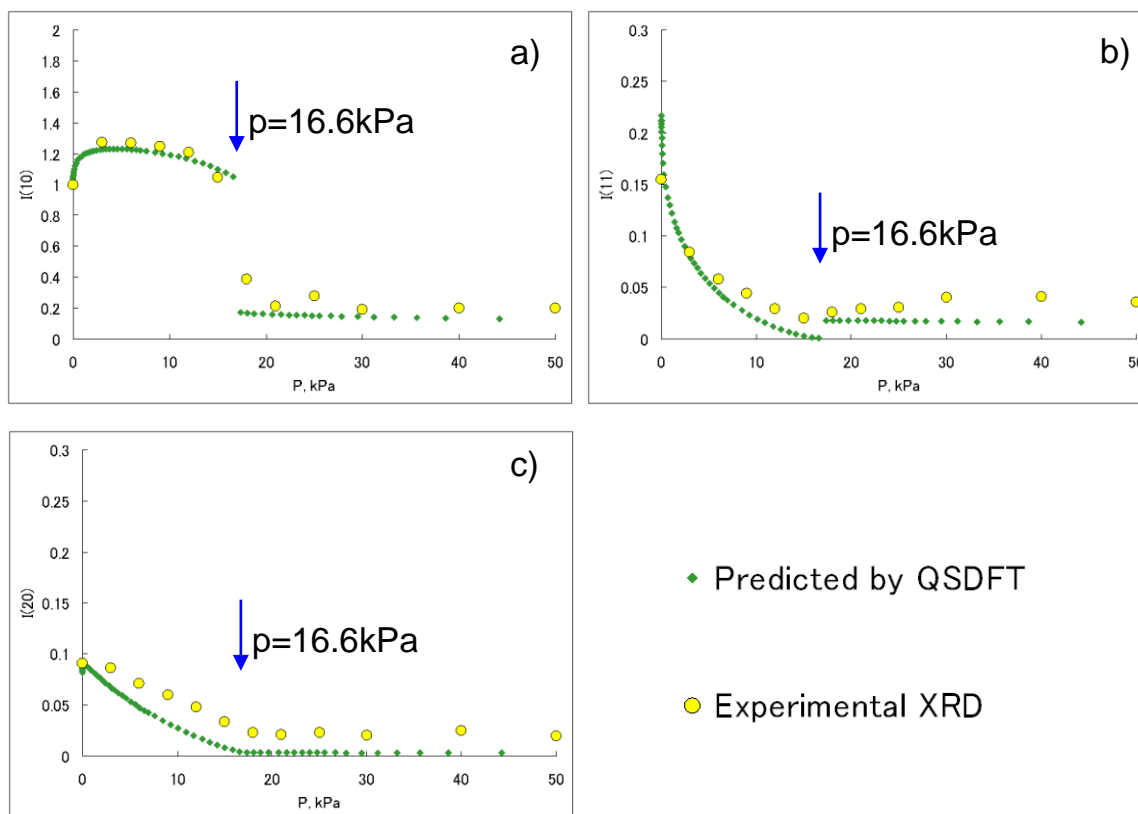


Figure 2-32. QSDFT prediction of the XRD intensities. Comparison of the theoretical diffraction intensities calculated from DPs of QSDFT and the experimental diffraction intensities measured during in situ powder XRD for Ar adsorption on MCM-41 mesoporous crystal. (a) 10, (b) 11, and (c) 20 reflections are presented. The capillary condensation takes place at 16.6 kPa at $T = 83$ K. (Adapted from ref [51])

2.7 Concluding Remarks

The intent of this review was to introduce the reader to the several years of intense and over layering effort that has been put into the study of gas adsorption for porous materials. This said effort has accumulated with the introduction of density functional methods. In the beginning of the review, emphasis was placed on the NLDFT methods, explaining its strength and weakness all the while slowly transitioning to QSDFT. This detailed explanation was followed by an in depth look at the materials commonly characterized (i.e. different synthesis techniques, applications) by the aforementioned methods in order to glean insight for the reader which method to choose.

While there exists an endless list of materials that can be considered, each with its own countless permutations, several stand out more than others. In the first group that was examined we took a look at activated carbons, a material studied early and often by the NLDFT models. These models evolved over the years, each considering the pore geometry as slit-like, eventually leading to a unified approach that allowed for the characterization of these materials with a range of adsorbates to include N_2 , Ar and CO_2 . For the latter of the three, its application has been deemed instrumental in characterizing materials consisting primarily of micropores due to the slow diffusion kinetics associated with N_2 and Ar at their respective boiling point temperatures. In addition to activated carbons, more novel materials were shown to be good candidates for the application of NLDFT methods for accurate characterization. These materials included carbon nanotubes and different molecular sieves. A new class of kernels were then introduced designated QSDFT, which were designed to take into account heterogeneity of the pores. Thus materials such as activated carbons, carbon black, and activated fibers that contained heterogeneity in their structures, along with various other examples, were visited. In doing so, it was clearly seen that the artifacts associated with many of the NLDFT methods that are due to a layering assumption in the model, are removed. A new hybrid QSDFT pore model was also presented capable of accurately depicting mesoporous carbons, most notably those derived from a templating procedure. The review then shifted focus to include silica materials based around SBA-15 whose pore properties are very similar to that of MCM-41, identified by its array of cylindrical pores. Soon more intricate constructs were being investigated that possessed complexity in their isotherms that could not be easily deduced. This complexity arose from the various

effects due to cavitation, metastability of the confined fluid, and pore blocking or network effects. These issues were addressed with the advent of newer kernels that considered hybrid pore structures accurately obtaining pore size distributions from experimental isotherms. Additional inorganic materials were also examined, including zeolites, MOF's and some alumina, where the application of the described DFT methods are valid. Finally the DFT methods were validated against other experimental techniques, TEM and XRD to name a few, in order to ensure the reader of its accuracy.

This review has been prepared for publication to Colloid & Surfaces Special CMP-6 issue.

Chapter 3 Fabrication of Nanocarbon Composites

3.1 *Properties of Carbon Nanotubes*

Single walled carbon nanotubes (SWNT) were first synthesized in 1991 by Iijima and since then has experienced a barrage of research in a broad range of applications and fields[1]. The uniqueness of this molecule can be attributed to its long aspect ratio, high thermal conductance, inert characteristic and high conductivity. CNT can be envisioned as a rolled up sheet of one atom thick graphene. Graphene, which is comprised of hexagonally bonded sp^2 carbon atoms, has pi-pi orbital interactions that account for its incredibly conductive and relatively inert structural properties. A consequence of having a network of overlapping pi-pi bonds is the accumulation of van der Waals forces. Traditionally, these forces account for weak short range interactions. However, due to the total number that is present, the summation of these forces imposes a deep energetic well for these individual tubes to bundle and aggregate. As a result, carbon nanotubes are notoriously difficult to separate within any dispersive medium, and further action is needed to take advantage of their exceptional properties. One such procedure is to disrupt the pi-pi network and covalently attach a molecule to the surface of the CNT. This however leads to degradation of the mechanical and conducting properties of the CNT. Another course is to use a surfactant or polymer to intercalate between the carbon nanotube aggregates and hence debundle them. This non covalent route allows for fine dispersions of CNT, without sacrificing the inherent conductive and mechanical properties that would result upon functionalization. However, from a kinetics standpoint this process is usually slow and generally ultra sonication is required

Sonication inflicts a shear force that can exfoliate the SWNT bundles during the sonication process in the form of cavitation, which enables bubble formation, growth and collapse[183]. The resultant collapse creates enough energy to debundle the aggregates and allow the intercalation of the surfactant or polymer. This process is dependent on a multitude of variables not limited to solvent viscosity, surface tension, vapor pressure, gas solubility, nature and type of radical formed, liquid temperature and pressure. In addition, several process parameters can be controlled that will influence the degree of dispersion which include ultrasound frequency, acoustic amplitude and sonication time. The compilation of the above variables leads to an high level of interplay and complexity. To further complicate matters, carbon nanotubes that undergo intense sonication can succumb to defects and even scission of the tubes leading to degradation of the unique properties associated with carbon nanotubes[184].

3.2 Apparatus Construction

In order to reduce the number of experimental variables, a new spinning and extraction device has been implemented. A moveable laser mounting stage, a rotating platform, a variable speed motor, and a digital syringe pump work in concert to limit experimental variation. The recording platform allows for three speeds, and the injection speed consists of a wide range of pump speeds which can be programmed digitally. Meanwhile, the pullup or extraction speed is assisted by a mechanical stable support (laser stage) which prevents jarring and possible fiber breakup.

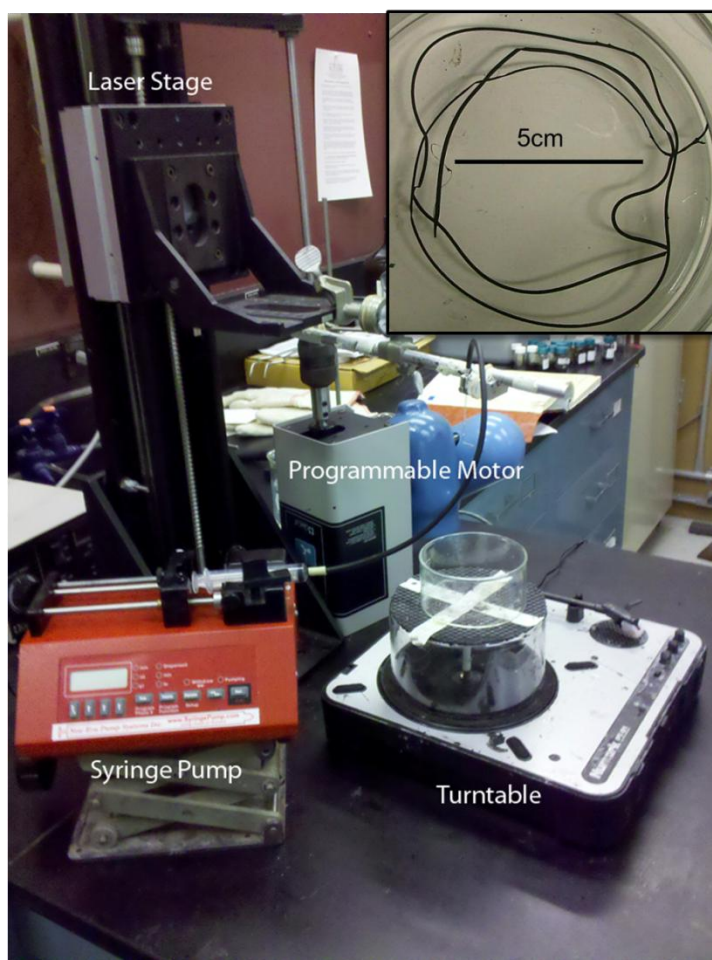


Figure 3-1: Apparatus construction of the wet spinning device. Includes a syringe pump, laser stage, programmable motor, rotating platform with adjustable speeds and coagulation bath. Inlet: CNT fiber produced by the particle coagulation process.

3.3 Fiber Fabrication

Considered one of the easiest processes to scale, particle coagulation spinning has long been utilized in polymer science [3, 4, 185, 186]. Prior to spinning the CNF, a solution of CNT is dispersed with the help of surfactants such as Sodium Dodecyl Sulfate (SDS). SDS, like other surfactants, help stabilize the CNT by disrupting the strong van der Waals forces and hydrophobic interaction which make them notoriously difficult to disperse. However, the presence of surfactants poses a problem, as the body possesses a biological threshold for them. This issue will need to be circumvented if incorporation of

CNT into composite materials destined for biomedical applications is desired. This can be achieved by extensive washing of the fiber, but there is no assurance that the fiber will become surfactant free.

Typically a coagulating bath comprised of a polymer solution is used to help form the fiber. As the dispersion is injected into the bath, the nanotubes are bonded by the polymer in the shearing flow to form a ribbon. After the polymer has exchanged with the surfactant and formed a sheath around the ribbon, the ribbon is transferred to a rinse bath typically containing deionized water. This bath helps remove the excess polymer that may be present. Several authors have applied this method using a variety of surfactants, polymers, and biological molecules to prepare these fibers and their variation on the process along with fiber properties are listed below.

Polymer	SWNT (wt %)	Young Modulus (GPa)	Tensile Strength (MPa)	Conductivity (S cm ⁻¹)	Comments	Year	Source
CS/POSS	1-9			Not Stated		2011	[187]
Alginate	0.6-23	3.6-7.0	141-250	Varied		2011	[188]
Ppy/ Alginate	0.01	11.8 & 3.7	95 & 65	0.5-10.0		2011	[189]
Agarose	1				Spun into either DI or ethanol	2011	[190]
PVA (10)	0.3	36 ± 3	2.2 GPa	Not Stated	Gel spun into cold methanol	2010	[191]
None	0.5	120	50-150, >320	120 μΩ cm	Acid spun	2010	[192]
PVA	1.0	70	2.6 GPa	Not Stated	Gel spun	2009	[193]
PEDOT					Razdan, come back	2009	[194]

HA	0.6	8 ± 1 5 ± 1	120 ± 32 , 51 ± 10	8 ± 1 186 ± 23	Spun into PEI or Acetone	2009	[195]
CHIT	0.3	8 ± 1 14	40 ± 18 60 ± 15	23 ± 5 0.04	Spun into PEI or Acetone	2009	[195]
GG	0.075	6.0 ± 1.3 MPa	176 ± 21	9.0 (mS cm ⁻¹)	Spun into CHIT, took most conductive fiber	2008	[196]
CHIT	0.075	4.7 ± 1.3 MPa	98 ± 20	18.0 (mS cm ⁻¹)	Spun into GG, took most conductive fiber	2008	[196]
None	1-3	69 ± 41 142 ± 70	Not Stated	800 3000	MWNT, N- MWNT; dispersed in ethylene glycol & spun into ether	2008	[197]
DNA	0.6	1.25 (in 2 M NaCl solution)	Not Stated	560	Resistant to torison, knot forming HNO ₃ /EtOH as bath. Crosslinked	2008	[198]
HA	0.4	12 ± 5	123 ± 28	270 ± 44	5 % Acetic Acid	2008	[199]
HA	0.4	12 ± 1	105 ± 15	158 ± 18	0.3 M H ₂ SO ₄	2008	[199]
HA	0.4	17 ± 5	111 ± 24	229 ± 46	0.3 M HCl	2008	[199]
HA	0.4	13 ± 1	110 ± 3	537 ± 56	0.3 M HNO ₃	2008	[199]
HA	0.4	14 ± 4	115 ± 17	66 ± 7	5 % CaCl ₂ in 70% Methanol	2008	[199]

HA	0.4	12 ± 4	89 ± 15	199 ± 37	Ethanol	2008	[199]
DNA	1	Not Stated	85	150		2008	[199]
CHI	0.3	Not Stated	155	21	Spun into 0.1 wt % NaOH in 90 vol % ethanol	2008	[199]
					Reactive Spinning	2008	[200]
PVA	0.4	78	1.8 GPa	Not Stated	1.2% LDS, Coaxial Spinning	2007	[201]
PVA	Not Stated	7	220	0.25 Ω m	PVA 5% in water, dispersed with [Na(THF)]n/DMSO	2007	[202]
PVA	Not Stated	5	115	0.053 Ω m	PVA 3% in water/DMSO (25/75), dispersed with [Na(THF)]n/DMSO	2007	[202]
PVA	Not Stated	0.7	160	0.006 Ω m	PVA 5% in deoxygenated water, dispersed with [Na(THF)]n/DMSO	2007	[202]
PVA	Not Stated	0.35	27	0.014 Ω m	PVA 5% NaCl 2.5% in water, dispersed with [Na(THF)]n/DMSO	2007	[202]

PVA	Not Stated	5	50	0.003-0.01 Ω m	PVA 5% in water, dispersed with SDS	2007	[202]
PVA	0.9	Not Stated	Not Stated	Not Stated	MWNT, dispersed with SDS; measured R as a fn of annealing T	2007	[203]
DNA	0.4	65 \pm 43	135 \pm 8	30 \pm 4	Coagulant: CHIT	2007	[204]
HA	0.4	4 \pm 1	20 \pm 8	135 \pm 35	Coagulant: CHIT	2007	[204]
CHIT	0.3	145 \pm 30	170 \pm 46	2 \pm 0.02	Coagulant: chondroitin sulfate	2007	[204]
CHIT	0.3	146 \pm 10	118 \pm 17	1 \pm 0.04	Coagulant: heparin	2007	[204]
CHIT	5	10.25 (w/ removal of aggregates)	Not Stated	Not Stated	aqueous solution of 2 wt % acetic acid, spun into ethanol/ NaOH (30:70), crosslinked with 25% glutaraldehyde	2006	[205]
PVA		5-10	Not Stated	3-8 Ω cm	o-MWNT	2006	[186]
None	0.8	2	Not Stated	1.5 \cdot 10 ⁻³ Ω m	Dispersed with 1% SDS, coagulating flow: ethanol, glycerol or ethanol/ glycol	2005	[206]

PEI	0.4	7-11	100-130	100-200, 10-30	1.2% LDS PEI/methanol is coagulant	2005	[207]
PVA	0.35	45	1.8 GPa	Not Stated	1% SDS, Hot Drawn	2005	[185]
PVA	0.6	12; 8.9 (after soaking in PVA)	770 (after soaking in PVA)	15 (as spun) 140(annealed)	1.2 LDS, 37% HCl used as flocculation agent	2005	[208]
None	8	120	116	0.2 mΩ/cm	102% sulphuric acid	2004	[209]
PVA	Not Stated	Not Stated	3.2 GPa	Not Stated	SDS	2004	[210]
DNA	1	14.5	101	166.7	Selected from 15 fibers done in general, higher conductivity lower mechanical strength	2004	[211]
PVA	Not Stated	80	1.8 GPa	Not Stated	LDS used as surfactant	2003	[4]

Table 4: CNF listed found in the literature. Abbreviations: Poly(p-phenylene terephthalamide) (PPTA), Hyaluronic Acid (HA), Chitosan (CHI), Polyacrylonitrile (PAN), Polyethyleneimine (PEI), Lithium Dodecyl Sulfate (LDS), Polyvinyl Alcohol (PVA), Sodium Dodecyl Sulfate (SDS), Polyaniline (PANI), Chondroitin Sulphate (SC), Salmon Sperm DNA (DNA).

Included in the above table is the use of polymeric hydrogels. The distinct advantage of using polymeric hydrogels is their ability to mimic the natural ECM, thus promoting cell growth[212, 213]. This concept has been previously invoked where a polymer, such as PVA, is utilized as either the bath component or as the dispersant. In the former, this leads to several shortcomings which makes the process difficult to scale commercially. The primary concern arises when the gel ribbon becomes suspended at the

spinning position. Thus it is necessary to continually raise the tip of the spinning bath to prevent the ribbon from clashing into itself. However, with the removal of the polymer from the bath there is a reduction in several degrees of freedom and the process becomes less complex. Several authors have demonstrated this practicality by using the polymer as the dispersant. This provides several advantages, including the fact that the spun ribbon can be reeled up onto a spool. Lastly, deciphering the composition of the fiber becomes easier as it is only dependent on the initial concentrations of the dispersion. This is contrary to analyzing the fiber post facto when it is spun into a polymer bath which will be dependent on the polymer concentration and adsorption kinetics.

During the drying stage the gel ribbon will begin to shrink due to the creation of a dry region in the gel possessing a higher interfacial energy than its wet counterpart[214, 215]. As a result, the gel has an incentive to contract which is dependent on the difference in the elastic strain experienced in the wet and dry regions[214, 215]. Choosing a solvent with a lower surface tension than water will contribute to a lower interfacial energy and corresponding strain. This in turn will lead to less contraction. By doing so a degree of mechanical strength is sacrificed as it inhibits the hydroxyl groups from coming in close proximity to each other and forming crosslinked chains. However, by preventing the gel contraction, the structure of the fiber will possess a greater surface area and volume. This fact is significant when a high porosity is desired, such is the case for drug delivery and absorption of toxins[2]. Therefore, by modifying the solvent, one is able to control the morphology of the dried fiber in terms of width, mechanical strength, and internal volume and surface area.

How the interplay of different forces can dictate the morphology of the fiber is presented in the following example. From figures 3-2 and 3-3 a coiling mechanism develops for fibers made from CNT with a dispersant consisting of the protein bovine serum albumin (BSA) and ascorbic acid spun into an aqueous polyvinyl alcohol (PVA) solution consisting of 10% by weight. The stability of the fiber is strong enough to withstand the capillary forces at the interface of the wash bath upon extraction that typically results in a compression force that forces the ribbon to collapse in an accordion like manner[216]. This results in a ribbon with a high width to thickness aspect ratio in the drying stage. As the flat ribbon dries from the top to the bottom, a contraction of the gel proceeds. But due to the flat morphology of the ribbon, the fiber reaches a critical point where the ability to contract inward is overcome by the instability due to the fibers aspect ratio. This results in the fiber folding onto itself, a phenomena that propagates down the fiber resulting in a coiled like fiber.

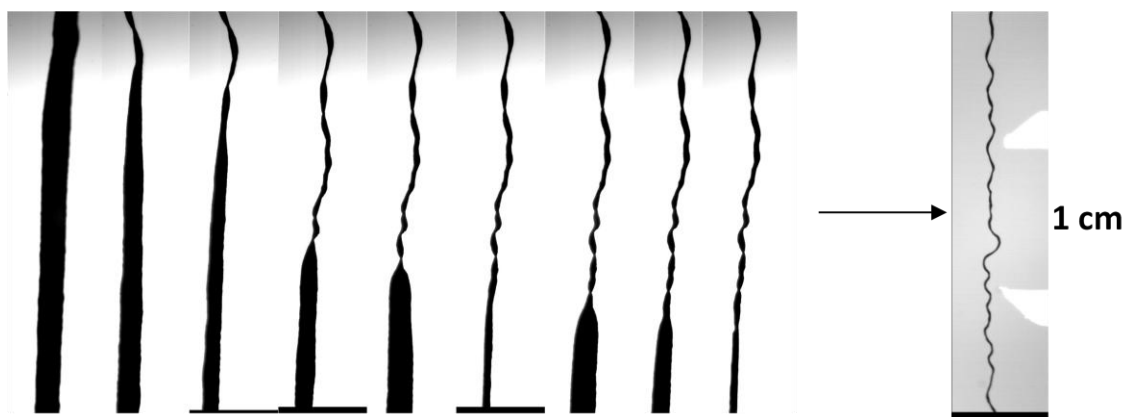


Figure 3-2: Coiling mechanism of the PVA/CNT/BSA/Ascorbic Acid fibers upon drying.

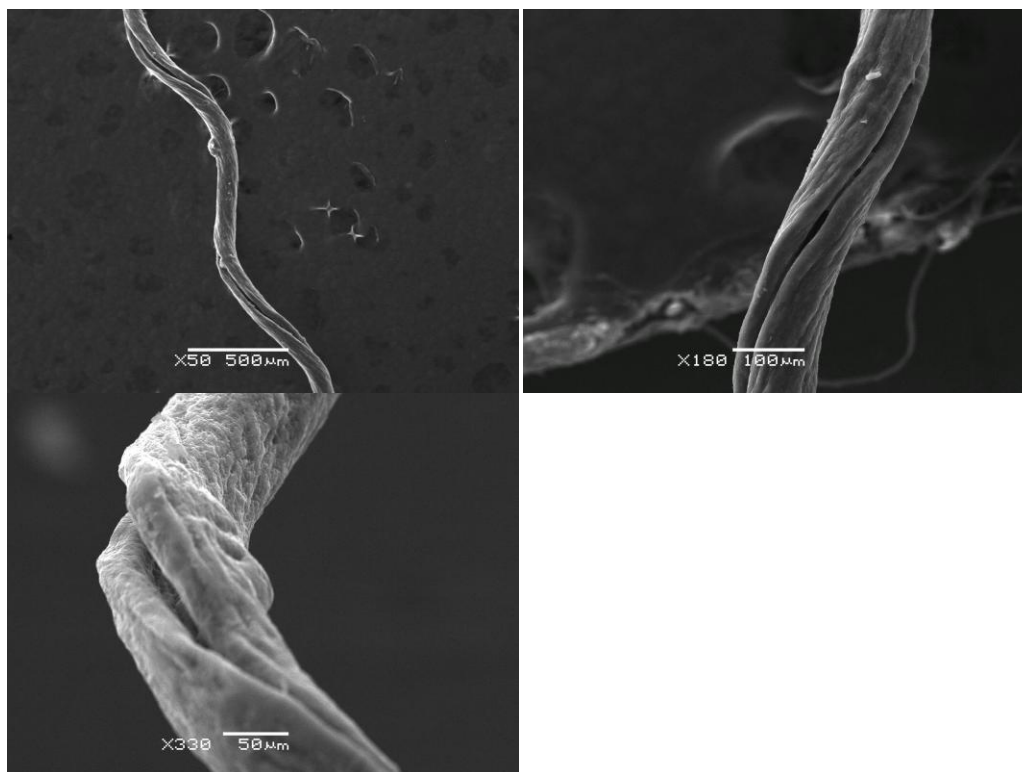


Figure 3-3: Scanning electron microscopy images of folded PVA/CNT/BSA/Ascorbic Acid fibers.

3.4 Fiber Fabrication with Agarose

Agarose is a natural linear polysaccharide hydrogel possessing a sub-micron pore structure derived from algae. It is a poly(1→4)-3,6-anhydro- α -l-galactopyranosyl-(1→3)- β -d-galactopyranose) with thermoreversible properties. Although it is a non cell adherent, due to its benign and biocompatible nature, it is commonly used as a substrate for in vitro cell studies[77-80]. Its unique hydrogel properties allows it to be malleable into different shapes and forms. Fibers were fabricated by two methods, wet spinning and molding the fiber in a hollow tube. In the former the liquid dispersion used to make the fibers was injected into a rotating bath, with the rotation velocity larger than the injecting velocity. Upon entering the bath, the dispersion displays an axial diffusion which is inhibited by two factors. First, the stretching imposed by the rotating velocity field and

second by the gelation of the agarose/CNT composite. By controlling the speed, the rheology of the injecting dispersion and the rotating solution, the width and morphology of the fiber precursor can be controlled. Therefore, a greater rotation speed may result in better alignment of the single walled carbon nanotubes (SWNTs) encapsulated in the agarose gel matrix.

SEM images of molded fibers are presented in Figure 3-5 a, b and c. This fabrication technique results in a smooth and nearly flat morphology. However, fibers fabricated by the wet spinning method (Figure 3-5 d, e and f) resulted in round circular fibers with a rough outer surface. This is the result of the extraction process from the bath where capillary forces fold the fiber precursor.[216] This ability to control the surface roughness has been determined to be a key parameter that affects the quality of cellular interfacing between CNT's and cultured neurons.[217] For both types of fibers, a close inspection of the cross section will show the exposure of carbon nanotube bundles depicted in Figure 3-5 c and f evident by the long overlapping strands. A degree of alignment, which is critical to improvements in mechanical and electrical properties[218], is still obtained when molding is used. This is most likely induced when the dispersion is first injected into the tube. The TEM images shown in Figure 3-4 support this assumption, where longitudinal cross sections of CNT fibers demonstrate general orientation in the direction of the fiber.

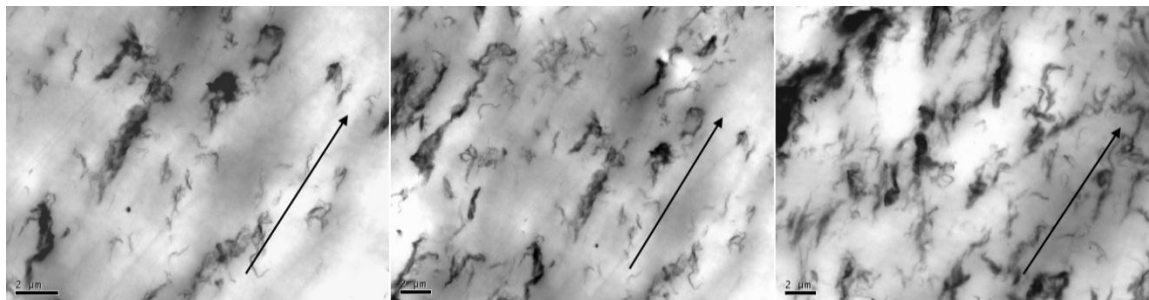


Figure 3-4. TEM images of molded fibers demonstrating fiber orientation in the direction of molding indicated by the arrows.

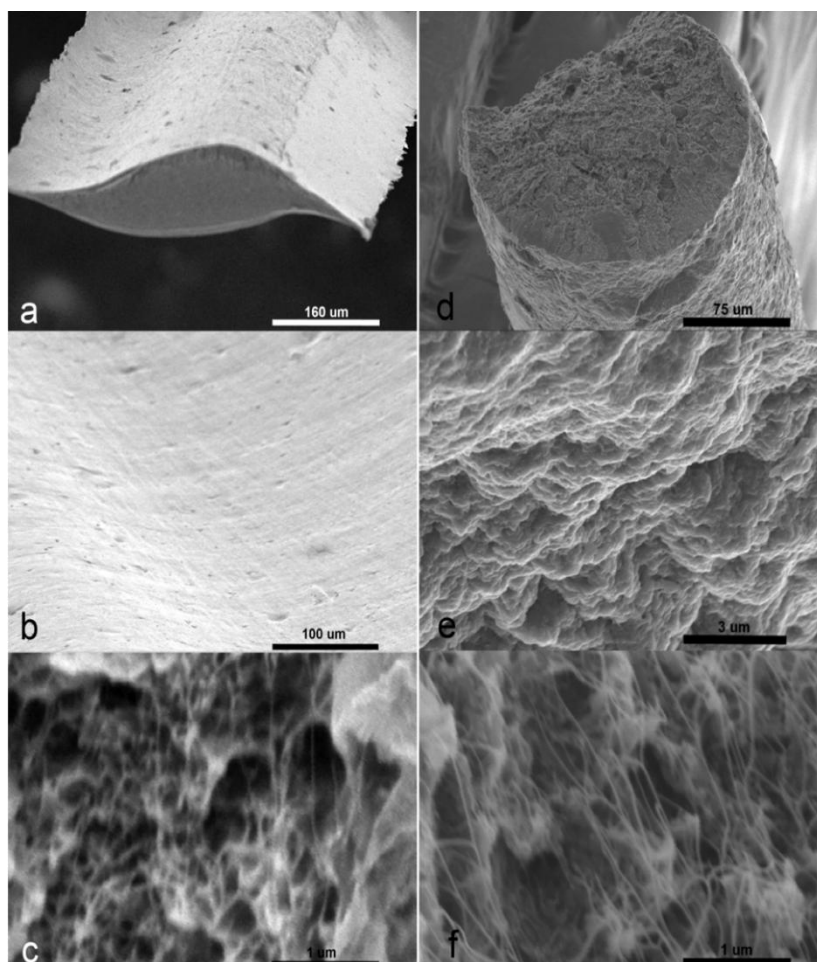


Figure 3-5. Scanning Electron Microscopy images of CNT agarose fibers. Left, molded fibers a) cross section of the fiber, b) close up of the fiber body depicting the smooth morphology of the surface, c) Close up of the cross section depicting the carbon nanotube bundles. Right, wet spun agarose fibers d) cross section of the fiber, e) close up of the fiber body depicting the rough morphology f) close up of the cross section depicting the carbon nanotube bundles.

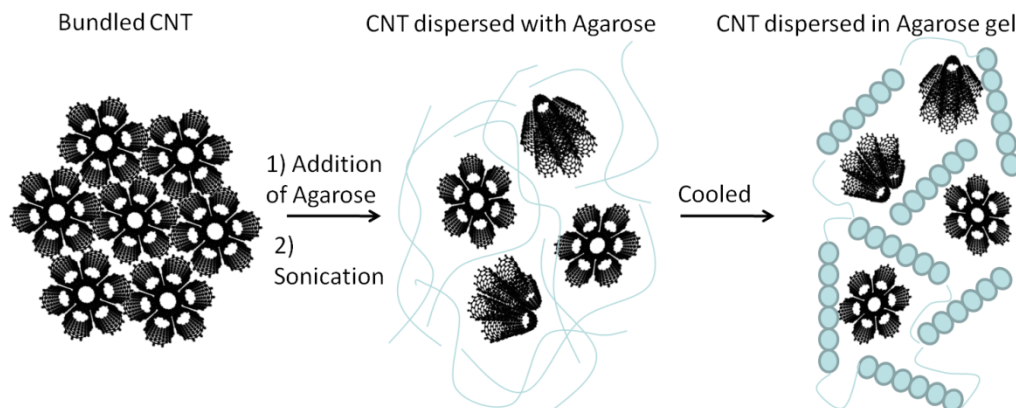


Figure 3-6: Schematic of dispersion mechanism for aggregates of carbon nanotube bundles separated by the polysachride agarose. Upon sonication, there is enough shear to be imparted to the aggregated bundles to separate them. The now soluble agarose polymer intercalates between the bundles and upon cooling the bundles are entrapped in the agarose matrix.

3.5 Graphene Fibers

Graphene oxide was synthesized by the improved modified hummers method[219] and by an alternative route[220], and fibers were produced in a similar manner as those obtained with carbon nanotubes and agarose[190]. 10 ml of a concentrated dispersion of graphene oxide was added to a vial containing agarose 2 wt%. The solution was heated up and wet spun into a rotating bath containing ethanol with the same spinning parameters as established before[190]. The ribbons were extracted from the bath, rested on a towel to soak up excess ethanol then hung to dry. The fibers were then annealed at various times and temperatures under the flow of argon in order to yield conductive fibers (See Table 3-2). Alternatively, fibers were also produced by the previously mentioned molding technique and allowed to dry on a flat surface.

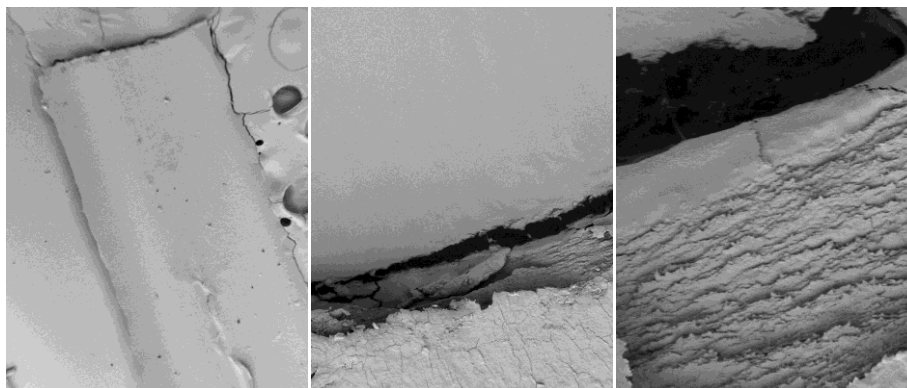


Figure 3-7: Molded fibers of graphene oxide and agarose.

Method	Components	Tensile Strength	Conductivity	Year	Ref
Wet spinning	RGO/SWNT/PVA	-----	-----	2012	[221]
Gel Drawing	GONR	-----	370 S/m^{-1}	2012	[222]
Wet spinning	Alginate/GO	4.3 GPa	-----	2012	[223]
Hydrothermal Treatment	GO	420 MPa	$\sim 1 \times 10^{-4} \text{ S/m}$	2012	[224]
Wet spinning	GO in NaOH	140 MPa	$2.5 \times 10^{-4} \text{ S/m}^{-1}$	2011	[225]
Drawing	Graphene	-----	$1 \times 10^{-3} \text{ S/m}^{-1}$	2011	[226]

Table 5: Review of the literature of already produced graphene fibers.

(Abbreviations: RGO(Reduced Graphene Oxide), SWNT (Single-walled carbon nanotubes), PVA (Polyvinyl alcohol), GONR (Graphene oxide nano ribbon).

3.6 Conclusion

Fibers consisting of either graphene or SWNT were easily produced when included in a dispersion of agarose. The ease of gelation and malleability that agarose provides allows for a robust technique in producing fibers in different shapes and sizes.

Furthermore, the technique allows the method of producing fibers to be scalable with future implications in industrial applications. Several fields of interest includes neural tissue engineering, catalysis where brittle activated carbon fibers are employed, wearable electronics, and aeronautics which requires a low weight to volume ratio would benefit by utilizing these composite fibers.

Further research in these carbon nanotube fiber composites will depend on the application in mind. For the field of neural tissue engineering focus should be emphasized on increasing the charge storage capacity of the fibers and the obtaining smaller dimensions in order to prevent glial damage upon insertion into neural tissue. In the field of catalysis, the porosity of the fibers should be optimized in order to facilitate mass transfer and fast kinetics. As for wearable electronics, a bottom up approach will need to be adopted in order to have the fibers act as integrated circuits. This will include tailoring the fiber at different regions in order for it to act as a conductors, a transistor with semiconductor properties, as well as resistors. A great amount of work is expected for this goal to be achieved.

The results described in this chapter were reported in the journal *Advanced Functional Materials* [227]. A US patent was also filed regarding this work.

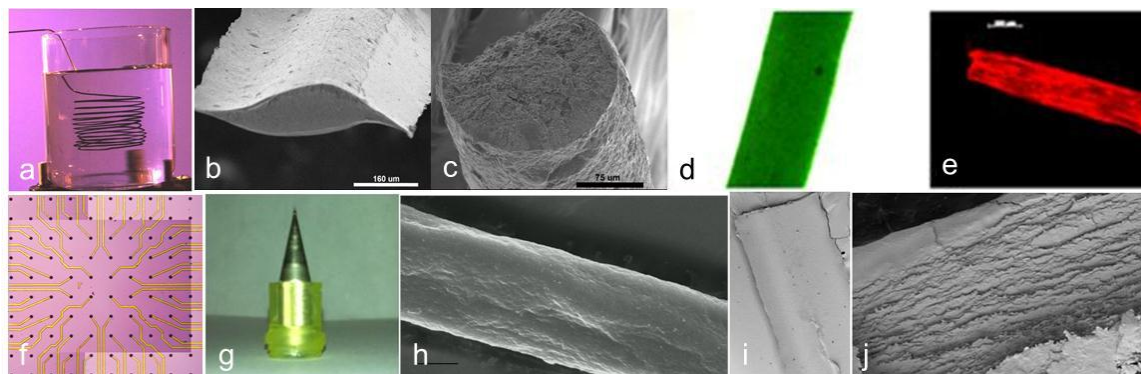


Figure 3-8: (a) Wet spinning process. (b& c) Two examples of variation in size, shape and morphology of NCAC wire-like fibers as shown by SEM. Both fibers are 200 μm wide at their largest point. (d& e) Bioactivation using fluorescent bovine serum albumin (green) and laminin (red) [227, 228]. (f) CNT based MAE[229]. (g) Microbore with 50 μm tapered opening used to produce ultrathin fibers. (h) Ultrathin NCAC electrode produced by wet spinning being approximately 26 μm in width. (i) Body image of a graphene/agarose produced electrode and (j) cross section of the same displaying the platelets of the graphene stacks.

Chapter 4 Nano carbon fiber composites for biological applications

4.1 Introduction

The inherent electrically conductive nature of carbon nanotubes and graphene make them appealing candidates in biological applications over the use of metals due to the liability of the latter to produce unwanted byproducts in the body. Over the years the use of these nano carbon materials have generally focused around drug delivery[230, 231], incorporation into composites[232, 233], as well as biosensors[234, 235]. Recent applications developed here have focused on the producing materials whose composition includes carbon nanotubes towards the purposes of neural tissue engineering and stem cell differentiation. On one hand neural prosthetic devices are commonly employed but suffer from drawbacks such as mechanical mismatch, size and inducing a glial response. Stem cells on the other hand provides an interesting route for degenerative disease, however are attached with challenges of controlling the cell lineage, differentiation time and cell viability. Resolution to both fields are explored by the incorporation of carbon nanotubes into composite materials. This chapter is thus apportioned accordingly: section 4.2 will bring to light the fabrication and use of carbon nanotube in fiber composites as described in the previous chapter. Emphasis will be placed on the electronic and mechanical properties of these fibers before and after chemical functionalization as well as in vivo and in vitro studies performed in collaboration with the Kohn laboratory. In sections 4.3 and 4.4 will investigate two novel approaches incorporating carbon nanotubes into electrospun polymeric scaffolds for the purposes of stem differentiation

with and without electrical stimuli. Section 4.5 will address conclusions and future work that will ultimately be needed in order to overcome the limitations outlined in the previous sections.

4.2 *Applications in Neural Tissue Engineering*

It is generally recognized that cortical neural prosthetic devices are limited to 12 months or less before their recording performance deteriorates substantially.[236, 237] This limitation lies with the fact that a sustained reactive response develops upon insertion of the probe. This response, known as gliosis, diminishes the long-term performance of devices.[236, 238-240] Control of the brain cell response to the inserted device could lead to improvement of its long-term performance. A number of approaches have been considered, both in terms of biochemistry and design. Examples include the addition of anti-inflammatory agents [240-244] or cell cycle-inhibiting drugs,[244, 245] as well as surface modification of silicon substrates.[244, 246-248] Nevertheless, these approaches are burdened by the large stiff constructs that will be present in the tissue throughout its lifetime. To circumvent this, an approach has recently emerged relying on two principals. First, these devices should be made of flexible materials. This will reduce the mechanical disparity between the device and the brain and possibly reduce development of the chronic glial response,[244, 249-253] Second, devices smaller in size, comparable to the neuronal soma, could lead to a reduction in the chronic glial response through the restoration of neuronal and astroglial synapses.[252, 254, 255] Therefore, smaller and more flexible devices may reduce reactive responses and improve long-term performance, e.g. recording of neural signals.

In this work, a new material comprised of carbon nanotubes (CNT) and agarose is suggested as promising candidate for the fabrication of neural probes that may reduce the limitations stated above. CNT display unique characteristics of superior conductivity, tremendous stiffness and a high aspect ratio. As such, they have been extensively employed in novel materials[2-4] stemming from their ability to absorb strain and induce conductivity. In addition, it has been shown that macroscopic materials made out of CNT are in fact biocompatible,[6, 7] making their inclusion into materials destined for medical applications that much more promising. Indeed, this coincides with reports that the incorporation of carbon nanotubes maintains a material's structural stability during cell growth.[256] This attribute is coupled with the fact that CNT can support neuron cell growth and differentiation,[7, 257] a decisive factor for any device that hopes to induce electrical stimulation with neurons in vivo. The evolving interest in natural polymers destined for drug delivery and tissue engineering has led to the emergence of new hybrid materials. So far a popular method to fabricate CNT/polymer hybrids is through the technique of wet spinning.[3, 7, 186, 196, 199, 204, 213, 258, 259] Wet spinning has been utilized in producing CNT/polymer composite fibers for the last 10 years.[3, 4, 186] Despite its inherent advantage, the ability to scale up the production of CNT fibers, specifically those intended for biomedical applications, incurs some drawbacks. This concept has been previously invoked where a polymer, such as PVA, is utilized as either the bath component or the dispersant. The former leads to several shortcomings which make the process difficult to scale commercially. The primary concern arises when the gel ribbon becomes suspended at the spinning position. Thus it is necessary to continually raise the tip of the spinning bath to prevent the ribbon from clashing into itself. However,

with the removal of the polymer from the bath there is a reduction in several degrees of freedom inherent to how the polymer solution is prepared. Several authors have demonstrated this practicality by using the polymer as the dispersant.[186, 196, 199, 259] This provides several technical advantages, including the fact that the spun ribbon can be reeled up onto a spool. Alternative methods have been proposed, which lead to a cleaner product and less expensive process.[186] The use of polymeric hydrogels has a certain advantage due in part to their ability to imitate the natural extra cellular matrix (ECM), thus promoting cell growth.[212, 213] Lastly, deciphering the composition of the fiber becomes easier as it is dependent only on the initial concentrations of the dispersion. This is contrary to analyzing the fiber *post facto* when it is spun into a polymer bath which will be dependent on the polymer concentration and adsorption kinetics.

In this process, CNT are dispersed with the aid of a surfactant or polymer by non-covalent means. The literature is scattered with examples of polymers which aid in this process.[258, 259] Some of these materials are based on the use of natural polymers or naturally based dispersant that are known to be biocompatible, such as chitosan, hyaluronic acid, DNA and chondroitin sulfate.[199, 204] However, both chitosan and hyaluronic acid are biodegradable and are undesirable for long-term indwelling recording electrodes. One alternative which is absent from the current list of proposed polymers is the naturally occurring polysaccharide agarose.

Agarose is an algae derived linear polysaccharide hydrogel possessing a sub-micron pore structure. It is a poly(1→4)-3,6-anhydro- α -l-galactopyranosyl-(1→3)- β -d-galactopyranose) with thermoreversible properties. Although it is a non cell adherent, due to its benign and biocompatible nature, it is commonly used as a non adhesive substrate

for in vitro cell studies[260]. In addition, agarose has several distinct advantages over other natural polymers: (A) its thermal dependant hydrogel properties allow it to be easily malleable into different shapes and forms without the use of additional reagents or organic solvents. (B) Unlike extracellular matrix based polymers, specific proteins or DNA, it lacks native ligands and is thus inert to mammalian cells.[261] (C) Through available primary and secondary hydroxyl groups, agarose can be chemically modified. This leads to a functionalization through grafting of proteins, peptides and glycogens to the polysaccharide backbone, allowing it to be specifically tailored for various biorelevant applications.[262-264] (D) The addition of such molecules can alter not only its biocompatible properties, but its mechanical properties as well. (E) Its high surface to volume ratio and porosity[261, 265] combined with its hydrophilic nature allows for a more effective penetration of cells during seeding while supporting delivery of nutrients and metabolites to these cells.[262, 263] Carrying out such modifications will result in a substantial increase in cell attachment, continuous support of 3D neural cell cultures, the ability to orient cell migration, and specifically enhance neurite extension with the grafting of neuron conductive constituents such as laminin or various oligopeptides.[262, 263] (F) Unlike other biopolymers, it is non-biodegradable, therefore will allow for long term performance and integration of the carbon nanotubes and avoid disintegration of the fabricated structures.[261] (G) Agarose is a cheap and abundant polysaccharide, sourced from plants (algae) and can be grown in highly controlled environments. This is compared with the prohibitive cost associated with making fibers with either DNA or hyaluronic acid. Due to these reasons, agarose has found use in the field of neural

engineering and nerve regeneration where it has been suggested as the primary support construct in nerve guide conduits.[261, 266]

In this work, we aim to combine three elements that have not yet been adjoined, the ease of wet spinning as a fabrication technique, with the reinforcing and conductance properties of CNT's, along with the gelation and functionalization potential of agarose, to create a continuous, electro and neuron conductive biohybrid nanocomposite fiber. The consequence of which is a fiber that is stiff when dry yet flexible when hydrated. We believe the impact of this work will provide a foundation for long-term neural recording devices as an alternative to silicone/metal based electrodes in the quest to evade gliosis and performance degradation.

4.2.1 Fiber fabrication

All chemicals were of reagent grade or higher. Fibers were produced from a dispersion containing 1 wt. % of SWNTs (Unidym or Nanoledge), 2 wt. % agarose (15517-014, Invitrogen,) and 97 wt. % distilled water. The dispersion was prepared with the aid of a horn sonicator (Mixonix S400) for 10 minutes at a pulsed rate of one second on and one second off. The sonicator was operated at 40 A. During the sonication process, enough heat is generated to invoke the transition of the agarose from an insoluble powder to a viscous liquid. This allows the agarose present in the liquid state to form random coils and physically wrap around and disperse the SWNT without the use of additional dispersant such as a surfactant. While the dispersion is still a liquid, it is injected through a 1 mm diameter tip into a bath of ethanol at room temperature rotating at a rate of 33 rpm, at which time it becomes a pre-fiber. The second approach produces 200 μ m fibers fabricated by injecting the dispersion into a 1 mm diameter tube and

allowing it to gel. The subsequential molds are then flushed out with lukewarm water. Upon drying, these fibers shrink to ribbons 200 μm wide. The characterization studies were performed mainly with the molded samples. Morphology of the fibers was evaluated using a Hitachi S-4500 Field emission SEM. Fresh cut sections were obtained by breaking the fibers after immersion for one 1 minute in liquid nitrogen. This process avoid smearing of the polymer/CNT nanostructures. The orientation of CNT in molded fibers was visualized using transmission electron microscopy. Fibers were embedded in embedding media (Electron Microscopy Sciences) and sectioned longitudinally with a diamond knife (Ultracut E ultramicrotome) at room temperature. Thin sections were applied on a copper Formavar / carbon coated grids (Electron Microscopy Sciences). Electron micrographs were taken using a model JEM 100 CX transmission electron microscope (JEOL).

4.2.2 Agarose fiber functionalization

4.2.2.1 Agarose fiber activation

CDAP activation of agarose and protein attachment was based on methods published by Kohn and Wilchek [264] with slight modifications: Agarose CNT ribbons were weighed (approximately 4 mg) and placed in a 20 mL glass scintillation vial (Fisher). 10 mL of each of the following solutions were added to the vials; each for 15 min followed by aspiration and replacement with the next solution under gentle agitation. (1) Deionized water (twice), (2) 30% acetone (twice), (3) 60% acetone (twice). The last solution was then replaced with 3 mL of ice-cold 60% acetone. Under agitation, 300 μL of 100 mg/mL of CDAP (Sigma) in dry acetonitrile (Sigma) was added. After one min,

250 μ L of 0.2 M Et₃N (Sigma) solution was added drop wise over one min. After five minutes of mixing, the solution from the vial was aspirated and transferred to a clean vial for activation verification. 5 mL of ice cold 0.05 N HCl was added to the fibers for five min mixing, followed by five min in 5 mL cold deionized water.

4.2.2.2 Protein attachment

Functionalized fibers were added with 5mL of 20 ug/mL of either laminin (LN) from Engelbreth-Holm-Swarm murine sarcoma basement membrane (L2020, Invitrogen) or fluorescein conjugated bovine serum albumin (BSAC, A23015, Invitrogen) both in 0.1 M NaHCO₃ for at least 16 hours. Remaining active groups were quenched by adding 150 μ L of ethanolamine (Sigma) per 100 μ L of attachment solution then stirring for 4 h. Fibers that underwent the full reaction were designated either “LN+” or “BSAC+”. Control fibers designated “LN-” or “BSA-” did not undergo the CDAP addition step but were added with the proteins. Another control group that was not added with any proteins and was designated “CDAP+”, while the pristine fibers were designated as such.

4.3.1 *Washing*: Fibers were washed in 10 mL for 15-20 minutes in each of the following solutions: (1) deionized water (twice), (2) 0.5 M NaCl (twice) (3) deionized water (twice). Fibers were then dried in nitrogen, sealed in airtight bags and refrigerated until use.

4.2.2.3 Activation verification

Qualitative verification of the activation of the agarose was performed as described by Kohn and Wilchek. [264] 0.15 g of 1,3-dimethylbarbituric acid (Sigma)

were dissolved in 9 mL of pyridine and 1 mL of deionized water. 2 mL of the resulting solution was added with 100 μ L of the activation solution.

4.3.3 Protein attachment verification: Visualization of the fibers using a fluorescent microscope can be performed. Fibers functionalized with BSAC, control fibers, and pristine fibers (those that did not undergo any reaction) were placed in either a clear or a black 96 well multi-well plate. The clear plate was placed within an inverted fluorescent microscope (Axio Observer-D1, Carl Zeiss MicroImaging GmbH) and imaged using a 10x objective. All fluorescent images were taken with similar exposure time to provide a true reflection of the intensity of the fluorescence. Fluorescent intensity recording from the black plate was taken using a well plate reader (M 200, Tecan). To allow background subtraction from the polypropylene, the fluorescence intensity of empty wells was measured and their average was subtracted from the readings of the fiber containing wells. The mean and standard deviations of fluorescent intensity (FI) measured using constant gains are presented in arbitrary units. To ensure laminin activation, 5 mm pieces of each type of fiber were placed in a 48 well plate (4 fibers per condition). Wells were added with 300 μ L of phosphate buffer saline (PBS, Sigma Aldrich) containing 1% w/v of non-specific blocking serum (BSA, Sigma Aldrich) then gently shaken for 30 minutes. The solution was aspirated followed by 3 washes of the plates with 500 μ L of PBS. 300 μ L of 1:100 dilution of rabbit polyclonal to laminin primary antibody (ab11575, Abcam) in PBS containing 1% BSA was added to each plate and incubated in room temperature overnight under gentle agitation. Wells were washed three times with 500 μ L of PBS, and 300 μ L of 1:50 dilution of secondary antibody, Tetramethylrhodamine goat anti-rabbit IgG (T-2769, Invitrogen) was added to each well and incubated in room temperature for

4 hours under gentle agitation followed by 5 washing steps and a final aspiration. The plate was kept in a dark and dry environment to allow evaporation of excess moisture. Fluorescent images and intensity reading of the fibers were taken as described for the BSAC functionalized fibers.

4.2.2.4 Results of Activation

Functionalized and control fibers were qualitatively evaluated by both fluorescent microscopy and fluorescent intensity reading. Representative fluorescent and phase contrast images of functionalized (“protein”+) and control fibers (“protein”-) are shown in Figure 4-1. Fluorescein conjugated bovine serum albumin (BSAC) allows for direct attachment verification. Since the protein has a fluorescent marker conjugated, its covalent attachment will result in fibers with inherent fluorescence. Indeed functionalized fibers demonstrate high fluorescence, compared to the control fiber (Figures 4-1 A & B). The validation of laminin attachment to the agarose carbon nanotube fibers was performed using an immunohistochemical (IHC) technique as shown in Figure 4-1 C. This method allowed not only validation of the attachment, but also to some extent confirmed the retention of the protein conformation, as the primary antibody used is specific for laminin. Moreover, the immunofluorescence of the fibers reveals that the agarose orientates itself longitudinally with the fiber. This feature is most likely due to the elongation of the dispersion when it experiences the rotating velocity field during the fabrication process. Fibers placed in a black 96 well plate were tested for fluorescence intensity using a plate reader. Results for LN and BSAC functionalized fibers and their prospective controls are shown in Figure 4-1 D and Figure 4-1 E respectively. The

control and pristine fibers exhibited low values of fluorescence intensity (FI) with no statistical difference between them ($P>0.05$). The functionalized fibers FI values were 2 orders of magnitude higher than those of the other two types ($P<0.05$), indicating successful functionalization. The actual quantification of the functionalized sites by the CDAP chemical reaction and amount of bound proteins was not performed, though could be possible based on the barbituric acid assay.[264] These findings emphasize the advantage of using agarose. It is a “clean slate” for biochemical manipulation. This allows for specific cellular cues and even several different cues to be covalently conjugated to the fibers, resulting in functionalized material thus allowing for specific use and application.

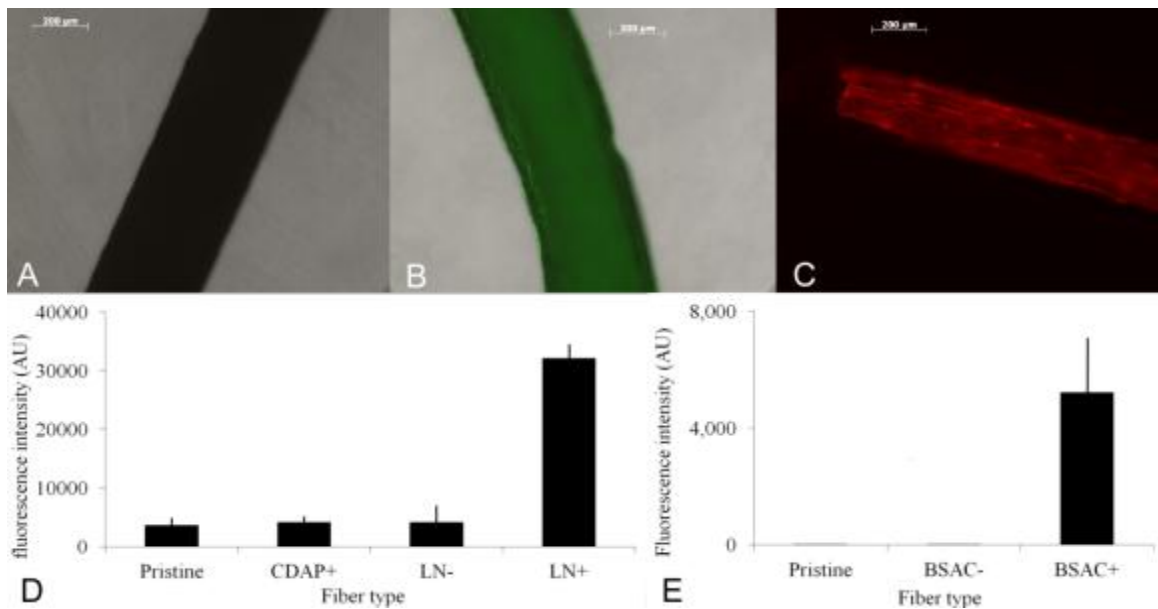


Figure 4-1. (A) Merged fluorescent and phase contrast image of BSAC- conjugate control fiber (B) Merged fluorescent and phase contrast image of BSAC+ conjugate functionalized fiber. (C) Fluorescent image LN+ Laminin functionalized fiber. The exposure time to the fluorescent channels were kept constant to eliminate gain variability and false images. Fluorescent intensity (FI) reading from fibers placed in a well plate then scanned through a plate reader. D) LN reactions E) BSAC. [190]

4.2.3 Mechanical Properties

4.2.3.1 Mechanical testing

Tensile properties of the CNT fibers were tested using an MTS model Sintech 5/D tension machine, fitted with the 100N load cell at room temperature with 50% relative humidity. A minimum of 5 fibers per sample were tested. To evaluate the effect of the activation on the agarose, samples were hydrated by immersing individual fibers in PBS at 50°C (close to the agarose melting temperature) under gentle agitation for one hour. The mechanical testing was terminated when fibers reached their breakpoint. The mean and standard deviation of the secant modulus, yield stress and strain, and the maximal stress and strain are reported.

4.2.3.2 Results of Mechanical Testing

The results of the mechanical tensile testing are shown in Table 4-1. Fiber stability was evaluated through hydration at a temperature close to the agarose melting point (50 °C). The dry fibers exhibited stiffness close to over 1 GPa, with the pristine fibers being the stiffest. All fibers exhibited a rigid and tough behavior, with none of them failing through a brittle manner, but rather maintaining their strength past the yield point until complete failure. Such intrinsic strength in the dry state surpasses the critical strength required for pial penetration, reported to be 0.3-1.3 MPa. Moreover, the low strain values allow for minimal collateral damage during insertion process[267]. Once hydrated, only the CDAP functionalized fibers (LN+ and CDAP+) exhibited enough mechanical integrity to be evaluated and studied for their tensile properties). A 90% and

80% drop in the elastic modulus for the LN+ and CDAP+ respectively was observed for hydrated fibers accompanied with a decrease in yield and maximal strain. These reduced strength values in the kPa range bring the fiber's properties closer (if still higher) to that of inherent brain tissue.[268]

Sample [190]		Modulus (MPa)	Yield Stress (MPa)	Yield Strain (%)	Max Strain (%)
Pristine	Dry	1280 ± 386	17.3 ± 5.1	1.8 ± 0.8	8.3 ± 2.0
	Hydrated	0	0	0	0
LN+	Dry	867 ± 247	14.3 ± 4.8	1.9 ± 0.7	6.2 ± 2.5
	Hydrated	85.6 ± 12.8	0.1 ± 0	4.7 ± 2	4.8 ± 1.8
CDAP+	Dry	1060 ± 698	5.2 ± 0.6	0.7 ± 0.5	8.9 ± 0.3
	Hydrated	220 ± 120	0.6 ± 0	4.2 ± 2.8	10.5 ± 4.2

Table 6: Mechanical properties of fibers, both wet and hydrated, after functionalization.

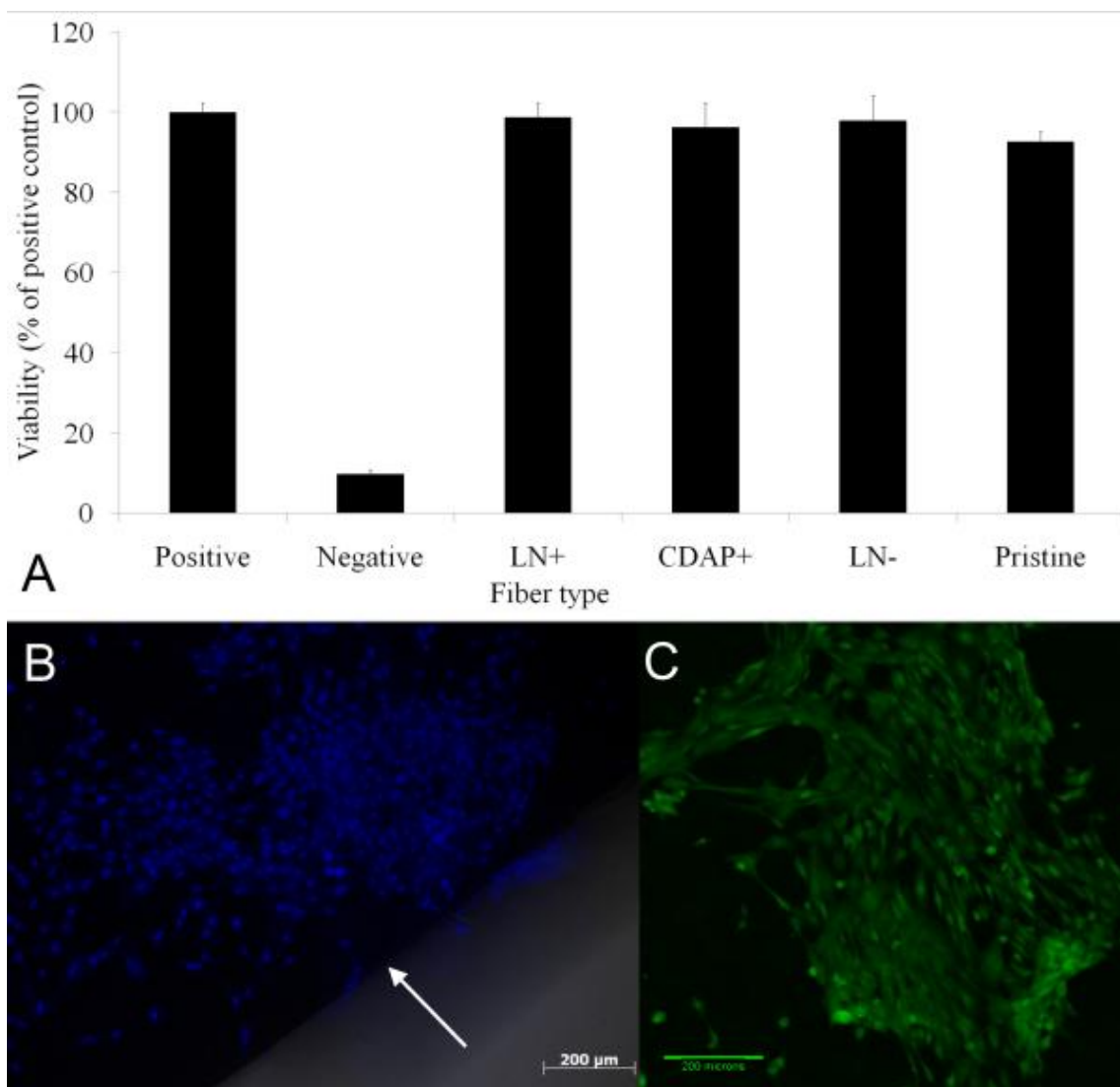


Figure 4-2. A) Cell viability after exposure to four types of fibers. Data is plotted against positive control. B) Projected phase contrast and fluorescent images of DAPI stained fixed astrocytes grown on LN+ disc. Edge of disc is marked by white arrows. Cells are solidly attached to only the agar disc. C) Projected confocal image of live astrocytes grown on LN+ stained with Calcein AM. [190]

When CDAP is added to the agarose, cyano-ester termini results, and is available to react with free amide groups in the reaction. Competing reaction exists, where either a carbamate or an imidocarbonate can be formed from the cyanate ester.[264] The latter forms either a cyclic bond within an agarose backbone or a crosslink between adjacent polymer chains, thus resulting in a slightly crosslinked and more stable CNT fiber

(CDAP+). When laminin, a high molecular weight protein is added to the reaction (LN+), there is increased coupling, principally due to the available ϵ -amines of surface lysine. This in turn creates the formation of an isourea bond resulting in the observed CNF stability.[269] The late addition of the quenching ethanolamine to the functionalization reaction possibly leads to elevated density of the crosslinking imidocarbonate in the CDAP+ fibers. Moreover, we expect that the crosslinking density of the CDAP+ fibers would be higher than the LN+ samples since the distance between formed cross-linking junctions is shorter. We designed these fibers to be biological viable, conductive and supportive for soft tissue rather than applicable for load bearing applications. This plasticization process occurring due to water absorption brings the fiber's strength and modulus much closer to that of inherent brain tissue, thus they become more compliant compared to silicon neural devices.[236] We do suspect that using a higher melting point agarose, with a higher molecular weight, could increase the strength of the composite fibers.[270] The chemical reaction itself through changes in reagent stoichiometry can be used to further modify the mechanical stability of the fibers in a biological environment.

4.2.4 Electrical properties

4.2.4.1 Conductivity Measurements

Fibers were partitioned into three batches based on whether either CDAP and / or LN were added to the reaction. Within each batch, three fibers were tested. Prior to testing, each end of the fiber was dipped in liquid nitrogen and clipped to expose a rigid cross section. Droplets of gallium/indium eutectic (liquid metal) was placed on each end of the fiber and the resistance was measured with a circuit-test DMR-5200 handheld

multimeter. Eight measurements were taken and a statistical analysis was performed to compare the variance within each group and between groups. To test the fibers in buffer, the same procedure was used. However, in order to do so, a basin of vacuum grease was placed around the body of the fiber leaving the two fiber ends protruding out and untouched by the grease. Then the basin was filled with PBS. Resistance measurements were taken one hour after filling the basin with PBS and 48 h after. This was repeated three times with batches of three different fibers.

4.2.4.2 Results of Conductivity Measurements

The results of the different fiber conductivities are presented in Table 4-2. The dual mechanical and conductive effect of having carbon nanotubes present in a material is essential for any composite. Electrical conductivity has been shown to support the growth of a variety of tissues such as cardiac muscle and neural tissue.[271] Furthermore, it is key for neurite extension, where electrical propagation assists in the growth of neurons on carbon nanotube deposited planar substrates.[272-274] The effect of which can be attributed to the carbon nanotubes acting as excellent free radical inhibitors.[275] This is due in part to their ability to either donate or accept electrons. As such, free radicals which are considered detrimental to cell viability, will be absent from the agarose fibers.

Dry samples of CNF prepared in this paper were shown to be electro-conductive with a specific conductivity of approximately $130\text{-}160\text{ S cm}^{-1}$ (depending on the fiber batch). These values fall near the range of our previously reported results which used the polymer PVA.[7] Likewise, these values are comparable with those for boron doped silicon, a material commonly used for fabrication of neural prosthetic devices.[276] In

addition, we set out to test the fibers in buffer. The specific conductivity dramatically decreases in the pristine fiber when immersed in buffer (indeed almost 2 order of magnitudes), while the functionalized fibers show much less variation (LN+) and even no deterioration at all for the CDAP+. This implies that the cross-linking effect of the functionalization reaction impedes the swelling of the fiber, which then leads to a decrease in conductivity, possibly through disconnection of CNT bundles, affecting electrical paths.

Specific Conductivity $S\ cm^{-1}$ [190]					
Fiber type	Dry	1 h wet	Retention	48 h wet	retention
Pristine	191 ± 14	6 ± 1	3 %	3 ± 0	2 %
LN+	145 ± 0	64 ± 4	44 %	67 ± 1	46 %
CDAP+	131 ± 1	131 ± 4	100 %	135 ± 55	103 %

Table 7: Conductivity measurements of dry and wet fibers before and after functionalization.

4.2.5 Cytotoxicity and cell attachment

4.2.5.1 Cytotoxicity and cell attachment

Fibers were cut into 5mm pieces with a razorblade and placed into the wells of a Costar 96-well tissue-culture treated polystyrene plate. The plate was sterilized for 1 h in UV. Four types of fibers were used: CDAP+, LN-, LN+, and pristine fibers. Rat astrocytes, kindly provided by John Frampton of the Wadsworth Center, were cultured in DMEM (Invitrogen), 10%FBS (Atlanta Biologicals), 1% Penicillin/Streptomycin at 37 °C, 5% CO₂. The cells were cultured to 90% confluence and then trypsinized, centrifuged, and the pellet re-suspended in media and the cells counted. 15,000 astrocytes were seeded into each well containing fiber and incubated for 18 hours at 37 °C. 15,000 astrocytes were added to the positive and negative control wells. After 18 hours, the

media was aspirated from each well and washed with PBS. A 1:10 dilution of Alamar Blue (ABD Serotec) to regular media was prepared and 100ul of this mixture was added to each well. The cells were incubated for 5 hours at 37 °C and then a fluorescence measurement was recorded at 560 excitation and 590 emission using a Tecan Infinite M200 Fluorescent Plate Reader. The data obtained was normalized to the positive controls. To allow for the evaluation of cell attachment on functionalized agarose CNT composites, dispersion films were prepared in the following manner: After sonication, 90 μ L of CNT/agarose was sandwiched between two 12mm glass cover slips. Once cooled, flat gel capsule were formed. These capsules, with a composition similar to that of the fibers, underwent chemical modification in the same manner described for the fibers. Discs were placed in a 24 well plate, sterilized under UV for 15 minutes, then washed with serum free culture media. 20 μ l containing 100,000 primary rat astrocytes were seeded onto the disks and incubated for two hours to allow for cell attachment. Regular media was added to the wells containing the disks and the plates were incubated for three days. Afterward, the astrocyte-seeded disks were either (1) stained with Calcein AM (Invitrogen) followed by imaging using in the form of 3D data sets using a Leica SP2 confocal laser scanning inverted microscope with a 10x dry objective, or (2) fixed with 4% PFA for 15 minutes at 4 degrees Celsius. Following fixation, the cells were stained with 1:500 v/v Hoechst 33258 (Anaspec) and imaged using a Zeiss Axio Observer Fluorescent Microscope

4.2.5.2 Results of Cytotoxicity

The metabolic activity of the cells exposed to different types of fibers was compared to positive-control cells kept in culture media. The effect of fiber presence on

primary astrocyte culture viability is presented in Figure 4-2a. Tests revealed that the fibers had no effect on the cell viability ($p > 0.05$). An exception would be the pristine fibers, where a slight (10%) statistically different reduction in viability was observed ($p < 0.01$). This reduction is possibly due to presence of some catalyst residue in the CNT raw material. It is possible that the process of functionalization, involving multiple washing steps, redeemed the processed fibers from these toxic residues. It has also been reported that unpurified CNT containing a large amount of iron induces a inflammatory response in vivo by stimulating the production of reactive oxygen species (ROS).[277] When the CNT were purified to contain no impurities and subjected to a macrophage cell line, it was reported that no ROS production occurred.[278]

Cells attachment studies performed on molded composite discs revealed that only the LN functionalized composites, seen in Figures 4b and 4c, allowed for cell attachment while the control discs did not permit cell attachment. The agarose based materials maintain their biocompatibility properties, but are not permissive for cell attachment without the addition of cell adhesion moieties.[262, 263]

The process of conjugating peptides to the fabricated fibers was repeated several times successfully. It is a simple and safe process that does not require the use of a chemical hood or special safety measures.[264] Moreover, the cytotoxicity and cell attachment studies performed on primary brain cells prove the process to be non-toxic to mammalian cells.

4.2.6 In vivo evaluation

4.2.6.1 In vivo characterization: fiber sterilization and implantation

To allow accurate placement and smooth insertion of the fibers, a new insertion method was used. First a 24G x 3/4" catheter (Terumo, Somerset, NJ) was clipped. This allows the cannula and needle to be at the same length. The needle was withdrawn from the tip, and then the fiber was manually threaded into the now empty lumen tip. To insert the fibers into live tissue, the catheter was held above the insertion site using a mechanical arm, and a push of the needle drove the fiber into the required area without the needle penetrating the tissue. Prior to use, catheters with fibers were placed in self-sealing sterilizable pouches and sterilized with ethylene oxide gas (Anprolene; Anderson Products, Chapel Hill, NC) followed by 10 days aeration. Animal procedures were performed under the approval of the Wadsworth Center Institutional Animal Care and Use Committee (IACUC). Insertions were performed in a manner previously described with slight modifications[240]. Briefly, a 360 g male Sprague–Dawley rat was anesthetized with 2.5% isoflurane with oxygen (1 l/min) for 5 min in a pre-exposed chamber, and then maintained with 2% isoflurane with oxygen for the duration of the procedure (60 min) in a stereotaxic holder. Four holes were drilled using electric drill (two on each side of midline, one anterior to bregma and one posterior to lambda). The dura was transected from the area of interest. Using a stereotactic holder, catheters were accurately placed above the insertion area, and a manual push of the needle allowed for smooth insertion of the fibers. Cellulose dialysis film (Fisher Scientific) was cut to 5 x 5 mm squares and applied over the exposed tissue, adhered to the skull and the skin was closed using staples.

4.2.6.2 Tissue Processing and immunohistochemistry

14 days after implantation animal was sacrificed by first anesthetizing with a ketamine/xylazine mixture, followed by transcardial perfusion[279] . Tissue processing was performed based on standard immunohistochemistry (IHC) procedures[280]. Horizontal 80- μ m-thick tissue slices were cut using a vibratory microtome (Vibratom®, model 1000). Sections 900–1100 μ m down from the dorsal surface of the brain were used. Once sectioning was completed, fibers remaining in the intact tissue were gently removed and processed similarly to the brain slices. Histochemistry was performed on tissue slices and fibers labeling 3 cell types using the following reagents: Primary antibodies: (1) Astrocytes, rat anti-GFAP (Invitrogen, 13-0300, dilution 1:200) (2) Microglia, rabbit anti-Iba1 (019-19741, dilution 1:800, Wako, Richmond, VA. Secondary antibodies and added stain: (1) Goat anti-rabbit (Alexa Flour 488 A11008, dilution 1:200, Invitrogen) (2) Goat anti-rat (Alexa Flour 546 A110081, dilution 1:200, Invitrogen) (3) NeuroTrace stain for Nissl substance (530/615 N21482, Invitrogen). Sections were mounted on glass slides with ProLong Gold (Invitrogen) for confocal imaging. Histological images were collected in the form of 3D data sets using a Leica SP2 confocal laser scanning inverted microscope with a 10x dry objective. Images were stacked into X, Y projections of the entire Z dimension of the sample to allow for evaluation of cellular populations surrounding insertion sites. Images of the insertion site and two adjacent lateral fields were collected. Composite images were formed by aligning and superimposing through-focused projections of individual images using image-processing software (ImageJ, NIH). This allowed for observation of changes in immunohistochemistry immediately around the insertion sites and in control regions farther away. Fiber samples were imaged

on both sides of the mounting slide since the black opaque nature of the fibers did not allow imaging of the full fiber thickness. One or two fields were collected for each side.

4.2.6.3 Image quantification

Using ImageJ, individual channels were converted to 8 bit, followed by correction of the background and intensity. The radial profile plugin (by Paul Baggethun) was used to produce a profile plot of normalized integrated intensities around the implant site as a function of distance from the fiber center. The averaged intensity gradient maximized at the fibers edge is plotted along with the standard deviation in Figure 4-3.

The insertion of fibers into a rat cerebral cortex was performed to allow preliminary evaluation of the insertion ability of the fibers into live tissue. This in turn permitted the acquisition of data with regard to the foreign body response inflicted by the presence of fibers in the tissue. Brain tissue inflammatory response to implanted materials is materialized through the presence of activated microglia and astrocytes at the vicinity of the implant site.[236, 280] Representative immunohistochemical images from sites where LN+ and LN- fibers were inserted into rat cortex are shown in Figure 4-3A and 4-3B. The intensities of astrocyte, microglia and neural expression measured for two of each fiber are shown in Figure 4-3C, 4-3D and 4-3E respectively.

4.2.7 Results of *in vivo* characterization

The *in vivo* evaluation as to the effect of the inserted fibers on brain tissue reveals a slight effect to the functionalization with laminin on the formation of the glial response (gliosis). In both cases activation of microglia and astrocytes is observed corresponding to the formation of mild gliosis.[236, 280] The resulting extent of glia activation

(approximately 100 μm of glial sheath formation) is similar in extent to data reported for other biocompatible materials such as silicon.[280] It has been reported that LN can reduce the extent of glial response when tethered to silicone devices and implanted for four weeks.[281] It is possible that an extended period of implantation may have revealed a greater reduction in the response as a result of the presence of the laminin functionalized nanofibers.

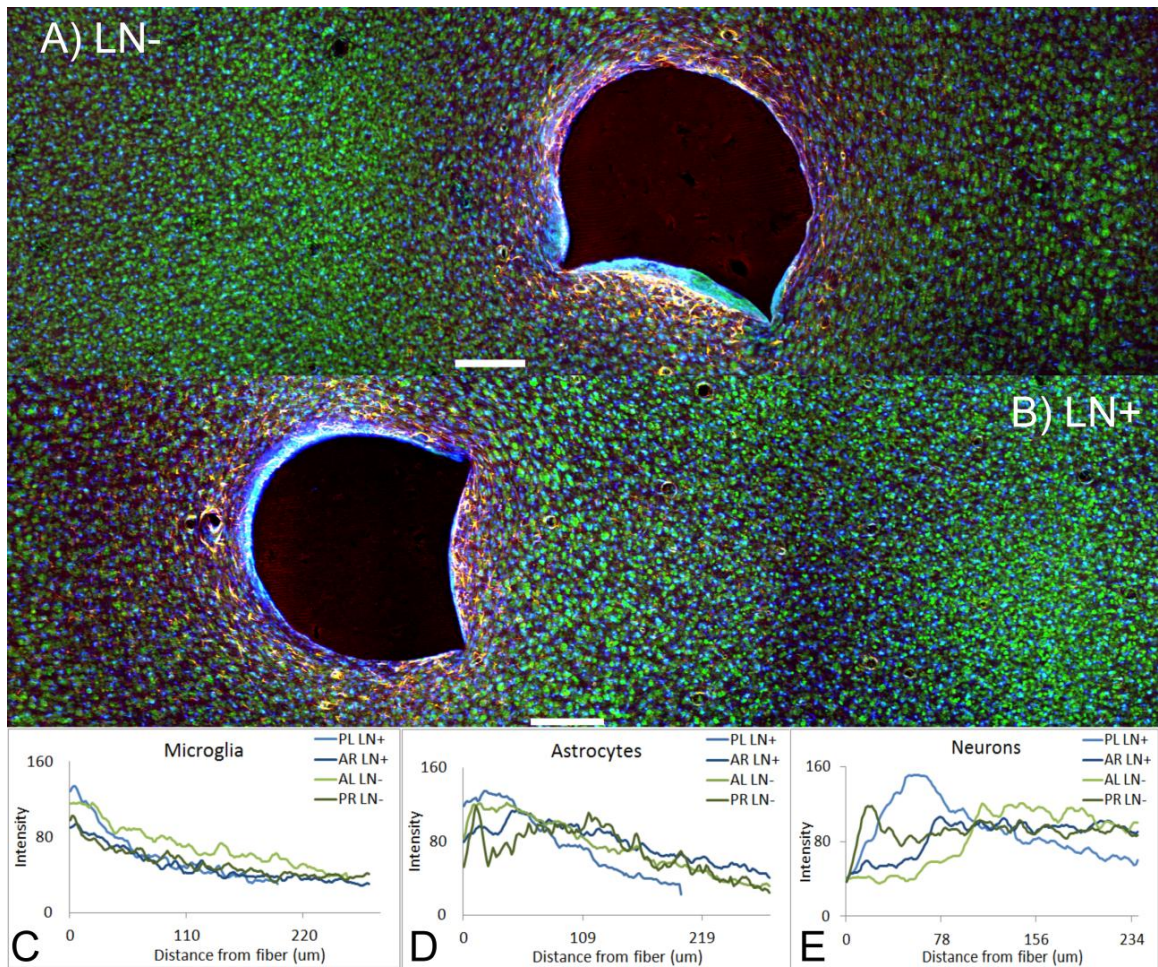


Figure 4-3. Representative immunohistochemical images of fibers inserted into rat cortex. No qualitative observation can be made regarding the nature of glial response and its extent towards the different fiber types. Yellow – astrocytes (GFAP). Blue – microglia (Iba-1). Green- neurons (Nissl). Scale bar 200 μm . A) CDAP+ fiber. B) LN+ fiber. C,D,E) Normalized intensity of cell expression at the fiber vicinity for microglia, astrocyte, and neuron respectively. [190]

Representative images of fibers extracted from brain tissue are shown in Figure 4-4. A difference between the fiber types could be observed once they were explanted. The laminin functionalized fibers seem to promote more cell adhesion compared to the non-functionalized ones. Laminin is an ECM protein that is known to enhance neural growth both *in vitro* and *in vivo*. [247, 281] Naturally, the attachment enhancement properties of such constituent will have effect on all cell types, as it is non-specific. [247] Finer manipulation of the foreign body response to the fibers can be achieved by the addition of more specific adhesion molecules to the fibers. Examples would be inflammatory response reducing agent such as alpha melanocyte stimulating hormone or neuron specific adhesion molecules such as L1 molecule. L1 has been shown not only to induce neurite outgrowth, but also to reduce astrocytic attachment. [247, 281, 282] Moreover, the explanted fibers demonstrated mechanical and dimensional stability. They became soft and pliable, in a trend similar to that shown with the mechanical tests.

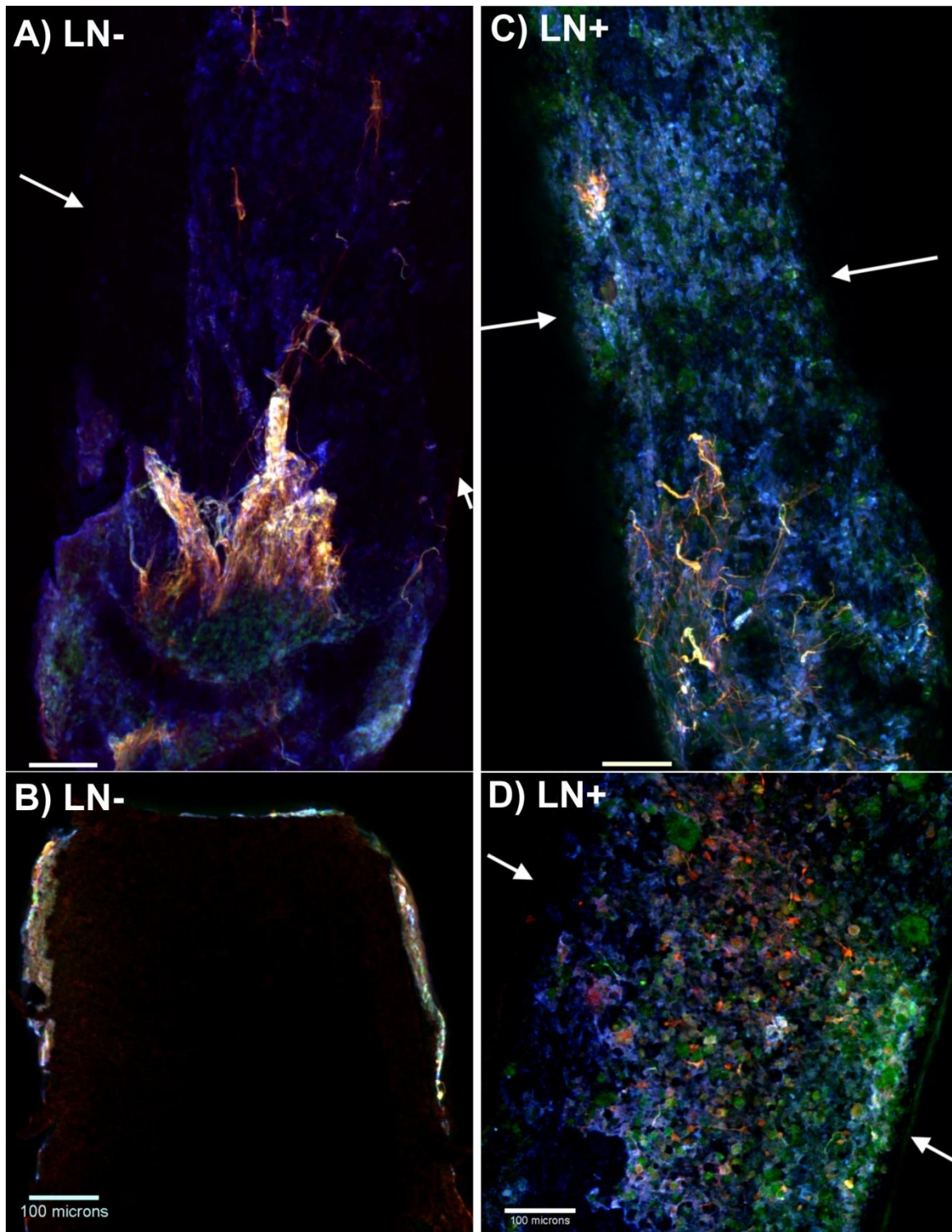


Figure 4-4. Projection confocal images of fibers extracted from brains. Images are of two sides of each fiber mounted on the glass slide (designated as LN- and LN+). Yellow – astrocytes (GFAP). Blue – microglia (Iba-1). Green – Neurons (Nissl). The micrograph of the laminin functionalized fiber (LN+, C and D) demonstrates a greater attachment of all cell types when compared to non-functionalized (LN-, A and B) fiber. Non-specific cell attachment is more evident with the LN+ fibers. [190]

In the central nervous system (CNS), such inherently conductive fibers could be developed into microscale neural recording devices. They can advance the field of neural prosthetics through long-term biocompatibility and performance by allowing the recording devices to interface with brain tissue. This in turn would allow for the enhancement of neural integration and the reduction of gliosis formation.[281] The materials characterized in this work could potentially function in the peripheral nervous system (PNS) as well. These fibers can be developed into intrafascicular electrodes, thus allowing for neural interfacing with the advantage of being both mechanically compliant and biologically attractive for long-term recording.[281] Additionally, in the PNS, nerve guidance conduits could be prepared either through molding of agarose/CNT dispersions,[266] or as fibers braided into nerve guide conduits. In the latter, their potential to support nerve growth and regeneration through electrical stimulation, porosity, and biochemical cues could prove advantageous.[283]

4.2.8 Conclusions

We have successfully fabricated agarose CNT hybrid fibers by taking advantage of agarose's ability to disperse and accommodate CNT's, its thermo responsive hydrogelation and its functionalization potential. These fibers are rigid and tough when dry, but exhibit mechanical properties compliant with brain tissue once hydrated. They prove to be not just non-toxic, but biocompatible, and biologically modifiable. These properties, along with their stable electrical conductance, provide a novel material with solid potential in future neurophysiologic applications. Although it was the scope of this paper to produce fibers for implantable electrodes, the gelling properties of agarose

allows it to be easily molded into other shapes with alternative applications such as directed nerve repair and nerve guidance conduit.

4.3 *Applications in Stem Cell Differentiation*

The pluripotent capabilities of human embryonic stem cells (hESC) enables the differentiation into a wide array of cell types[284-286]. As a result they are being considered one of the most promising avenues to combat diseases resulting in degenerative tissue damage. Of particular interest is the differentiation into neural stem cells. One current approach is the use of electrical stimulation (see Table 9), which has been found to promote neuron growth[287-289] and the differentiation of hESC into neurons[6, 8, 256, 290]. Because of carbon nanotubes inherent conductivity they are being implemented in the fabrication of biomedical scaffolds. This coincides with reports that the inclusion of carbon nanotubes into scaffolds maintains their structural stability during cell growth. This ability of CNT to support growth and differentiation arises from the enhanced signal transmission that is present. This in turn is the consequence of electrical shortcuts resulting from the tight contacts formed between the CNTs and the neuron membranes[217, 256, 274]. To this extent then, the conductive properties of CNT are regarded as a decisive factor for any support that expects to induce electrical stimulation with neurons in vivo.

Conductive scaffolds	DC/AC current; potential	Duration	Cells	Ref.
PANI/PG	DC: 100 mV	1 h	C17.2	[291]
PANI/PLACL	DC: 0–200 mA	2 days	NIH-3T3 fibroblasts	[292]
PPy	DC: 100 mV	2 h	PC12	[293]
PLGA coated with PPy	DC: 10 mV/cm	2 h	PC12	[294]
PPy/PLLA	DC: 100 mV/mm	2, 24 h	Fibroblasts	
PDLLA/CL coated with PPy	DC: 0, 2, 8 and 20 μ A/mm	—	PC12	[295]
PPy	AC: 50 μ A at 0.05, 5 and 500 Hz	—	VSMC	[296]
PPy/PLLA	DC: 50 mV/mm	24 h	Fibroblasts	[297]
ITO	AC: 100 mV (100 Hz)	30 min/day (3 days)	PC12	[298]
PLLA/CNT	AC: 10 mA (10 Hz)	6 h/day	Osteoblasts	[299]
PCL/PPy	DC: 10 V	4 h/day	DRG	[300]
PPy	Biphasic 100 μ s pulses of ± 1 mA/cm ² at 250 Hz	8 h/day	Cochlear neural explants	[301]
PLAAP	Electric potential of 0.1 V (1 Hz)	1 h/day	PC12	[302]
PPy/chitosan	DC: 100 mV	4 h	Schwann cells	[303]
Collagen			Mesenchymal SC	[304]

Table 8: Electrical stimulation parameters found in the literature. PANI, polyaniline; PG, PCL/gelatin; PDLLA/CL, poly(d,l-lactide-co- ϵ -caprolactone); PLLA, poly(l-lactic acid); PLGA, poly(d,l-lactide-co-glycolide); CNT, carbon nanotubes; PLACL, poly(l-lactide-co- ϵ -caprolactone); ITO, indium–tin oxide; PLAAP, copolymer of hydroxyl-capped poly(l-lactide) (PLA) and carboxyl-capped aniline pentamer (AP); PC12, rat neuronal pheochromocytoma cells; PPy, polypyrrole; VSMC, vascular smooth muscle cells; DRG, dorsal root ganglia; C17.2, mouse neuronal cerebellum stem cells; PC12, rat neuronal pheochromocytoma cells.

4.3.1 Electrowetting of Scaffolds

Currently a popular route to fabricate polymeric scaffolds is through the process of electrospinning[305-308]. In this process a polymer solution is injected by a syringe towards a charged plate or charged rotating mandrel separated by some distance. When a

difference in voltage is applied on the scale of the kilovolt range, a charge separation occurs within the polymer solution causing it to extrude out of the syringe in a fiber form. Once this fiber lands on the charged plate, the polymer solvent quickly evaporates and the fiber solidifies. After sometime this process creates a polymeric and porous scaffold. Attempts have been made to repeat this process with conductive materials, such as CNT, within the polymeric solution. However the presence of conductive materials within the solution will cause a shorting to occur and prevent the formation of the fiber extruding from the syringe. This is indeed the case as a review of the literature reveals only a few instances[309-313] where the electrospinning of a trace amount of CNT did not proceed without the need for either multi walled carbon nanotubes (MWNT) or functionalized single walled carbon nanotubes (f-SWNT). This is a critical concern because in both cases the conductivity is hindered compared to their non functionalized SWNT counterpart. While this decrease resulting from the use of MWNT can be explained by their decrease in curvature, the f-SWNT conductivity is reduced by a covalent disruption on its highly overlapped π - π orbital surface. Therefore the purpose of this work is to demonstrate a post fabrication technique that enables the integration of non functionalized SWNT into polymeric scaffolds. This is facilitated first by electrowetting the scaffolds with dispersions of SWNT, then by a forced impregnation approach. Electrowetting has long been utilized to permit the impregnation of a non-wetting fluid into a porous substrate. As is the case here, the hydrophobic nature of the polymer scaffold inhibits the spreading of the aqueous based SWNT dispersion. Upon applying a voltage difference at the droplet, the contact angle decreases indicating a change in the interfacial properties. Continuation of the applied voltage results in the impregnation of

the scaffold, evident by the fact that the dispersion has penetrated to the opposite side. Several theories have been described to explain this phenomena and the reader is referred to the fundamental Lippmann equation, which takes into account the parallel capacitor approximation for the droplet-dielectric interface[314].

In addition the dispersant will be essential in both the electrowetting process and its effect on the ability of the scaffold to support growth and differentiation. Traditionally, surfactants are used to disperse CNT. However, due to a surfactants ability to intercalate into the cell membrane, the protein bovine serum albumin (BSA) has been chosen instead. The advantages of which is several fold. First proteins are known to disperse CNT by physically wrapping around them leading to strong electrostatic and nonspecific adsorption[315, 316]. Second BSA is commercially available and abundantly cheap. Lastly the structure of BSA is quite similar to the human equivalent which is one of the most prolific proteins in the body. As such, materials incorporating BSA would be less likely to be recognized by the host's immune system[316-318]. This choice is further validated by the fact that a large portion of proteins adsorbed onto a thin film scaffold will help promote hESC differentiation and is considered a controlling factor for cell adhesion. Therefore, it is with these concepts in mind that we aim to adjoin the ability of CNT to enhance stem cell differentiation with the means to incorporate SWNT into electrospun polymeric scaffolds by either two routes: electrowetting or forced impregnation.

4.3.2 Physics of Electrowetting

To force the droplets of a nonwetting fluid to penetrate into the porous scaffold it was suggested to use an electric field (see review [314]). The droplet is held under an

electric potential by placing the electrode into the droplet. Another electrode is placed underneath the scaffold, the electrodes being separated against electric breakdown by a thin dielectric layer. Applying the voltage, one forces the droplet to move in order to minimize the electrostatic energy of the system. The liquid is assumed to be conductive, as is the case for the aqueous solutions of carbon nanotubes. Under the voltage V , the fluid is forced to move inwards to the scaffold. The effect is explained as follows. Since the liquid is conductive, the application of the voltage transforms the scaffold into a parallel plate capacitor. The charges at the interface of this parallel plate capacitor is on the order of the Debye-Huckel thickness which allows for the polarization of the current to occur as long as it remains between the boundaries of oxidizing and reducing the scaffold. The interfacial tension of the scaffold-liquid system thus evolves as the following:

$$\frac{d\gamma_{SL}}{dV} = -\sigma \quad (\text{Eq. 4.1})$$

Where γ_{SL} is the interfacial tension, V is the voltage and σ is the surface charge density. Wetting of the surface occurs when a second derivative of Eq 1 is taken and is combined with the Young's equation to obtain the following:

$$\frac{d^2 \cos \theta}{dV} = \frac{c}{\gamma} \quad (\text{Eq. 4.2})$$

Where c is the capacitance of the solid-liquid interface per unit surface area. Given the assumption that the liquid is much more conductive than the underlying insulating surface and surrounding gas, the change in the contact angle is given by:

$$\cos \theta = \cos \theta_0 + \frac{c}{2\gamma} V^2 \quad (\text{Eq. 4.3})$$

Where θ_0 is the contact angle in absence of an electrical field. The voltage required to affect the contact angle is thus:

$$V \approx \sqrt{\frac{\gamma}{c}} \approx \sqrt{\frac{e\gamma}{\epsilon\epsilon_0}} \quad (\text{Eq. 4.4})$$

Where ϵ and ϵ_0 is the dielectric constant with and without an applied electrostatic field, respectively. The energy of the capacitor is given by the following:

$$E = \frac{CV^2}{2} = \frac{\epsilon\epsilon_0 A}{2d} \quad (\text{Eq. 4.5})$$

Here d is the distance of the front of penetrating fluid and A is the area of the scaffold.

The work needed to move the dispersion into the dry scaffold by the distance d is equal to the change of the free energy. Thus, we find the electrical force per unit area as:

$$P_e = \frac{\epsilon_0\epsilon}{d} V^2 \quad (\text{Eq. 4.6})$$

At the front of the liquid invading the pore space we have the balance of stresses as

$$-P_a + P_e = -P_l \quad (\text{Eq. 4.7})$$

where P_l and P_a are the pressures in the liquid and dry zone of the scaffold, respectively.

Thus, the front moves if and only if the capillary pressure $P_a - P_l$ is smaller than the electrical pressure P_e . The critical condition for onset of front propagation corresponds to the equality (4.7), in which d is the scaffold depth. The thickness of the absorbed droplet can be altered by the variation of the applied voltage. In order to start wetting, the voltage must be higher compared to that needed to keep the front a bit inside the scaffold.

4.3.3 Electrowetting Setup

The electrowetting setup is quite simple and constitutes of a power source, wires connected to a ground source/sink, and a wire connected to a aluminum foil support on a non conductive platform (seen in figure 4.5). The hydrophobic scaffold, which the CNT dispersion will be driven into, sits upon the aluminum foil support separated by a layer of plastic in order to prevent a short. Upon applying a current, a difference in voltage is

maintained which acts as a driving force for the CNT dispersion to penetrate into the scaffold. Immediately it can be seen that the dispersion begins to wet the surface evident by the change in contact area. The current is gradually increased until a dielectric breakdown occurs of the air/liquid interface evident by a continuous spark.

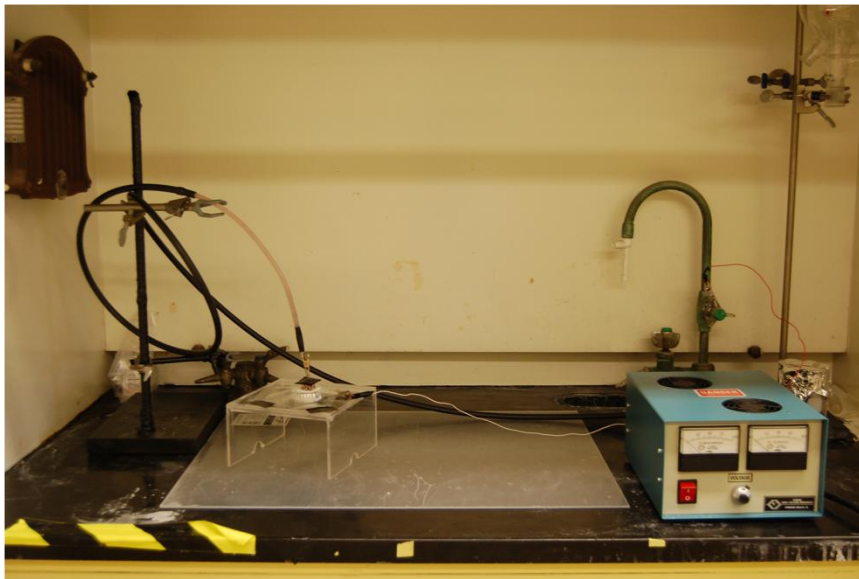


Figure 4-5: Electrowetting set up consisting of a power source, conductive platform and a dielectric layer separating the platform and the scaffold.

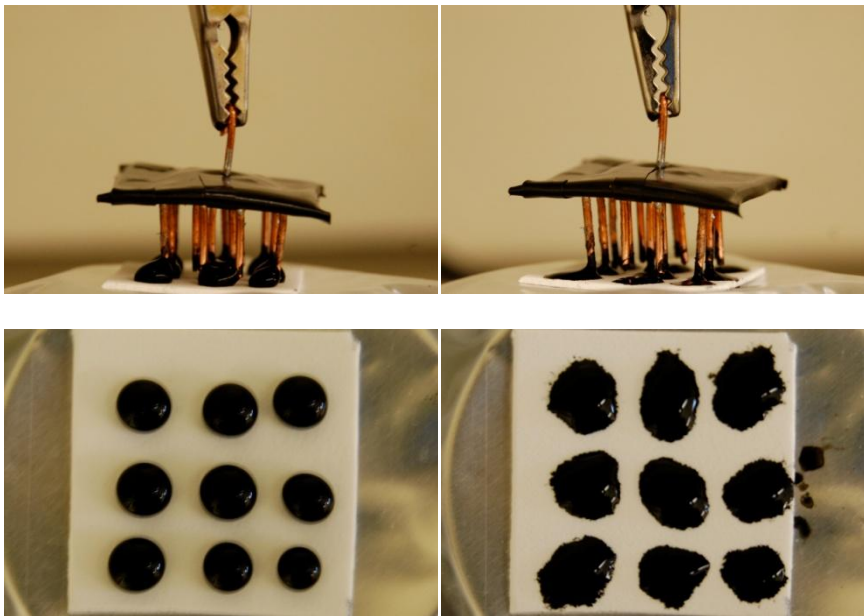


Figure 4-6: Earlier prototype of multi pin electrode used to electrowet and corresponding top view image of droplets prior to electrowetting (left) and after electrowetting (right). Substrate consists of porous Teflon as a test model for the scaffolds.

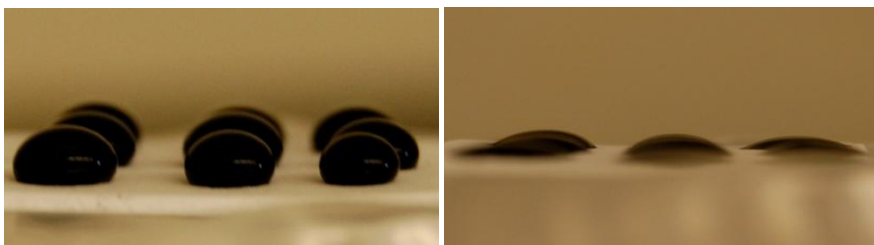


Figure 4-7: Side view of droplets prior to electrowetting (left) and after electrowetting (right).

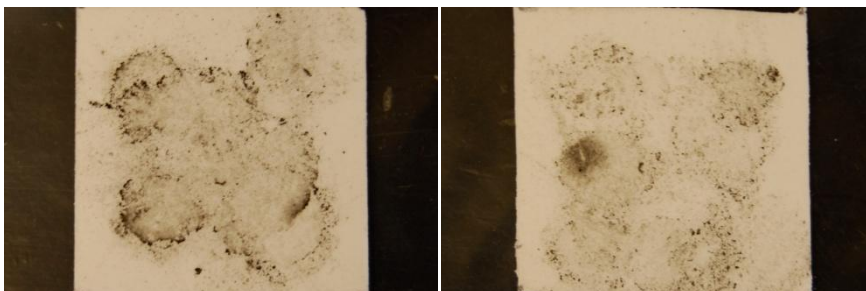


Figure 4-8: Effects of electrowetting.

4.4 Forced Impregnation

Due to the inhomogeneous nature and thus ineffective method of electrowetting another external driving force was invoked in order to impregnate the hydrophobic pores by the aqueous based CNT dispersion. Although vacuum filtration methods have been tried in house in the past, they failed to successfully impregnate the pores. This may be on account of the underlying pore size of the filter which dictates the distributive negative pressure across the scaffold. While using a 0.2 micron pore filter (Nalgene Analytical Filter, 150 ml) successful trials of wetting was accomplished.



Figure 4-9: Pressure induced wetting set up. Apparatus includes a 0.2 micron filter connected to a flow gauge and vacuum line.

After allowing the scaffold to dry, scanning electron microscopy images (SEM) were taken of the scaffold before and after impregnation (Figure 4-10 b & c respectively). It can be seen that the morphology of the scaffold changes upon impregnation going from smooth overlapping fibers to those with a rougher morphology. This can be attributed to the presence of aggregated carbon nanotubes strongly adsorbed onto the fibers of the scaffold via van der Waals forces. In addition there is a change in contrast with the scaffolds impregnated with CNT opposed to those without. This can be attributed to the charging that occurs on the bare polymeric scaffolds, a phenomena consistent with insulators.

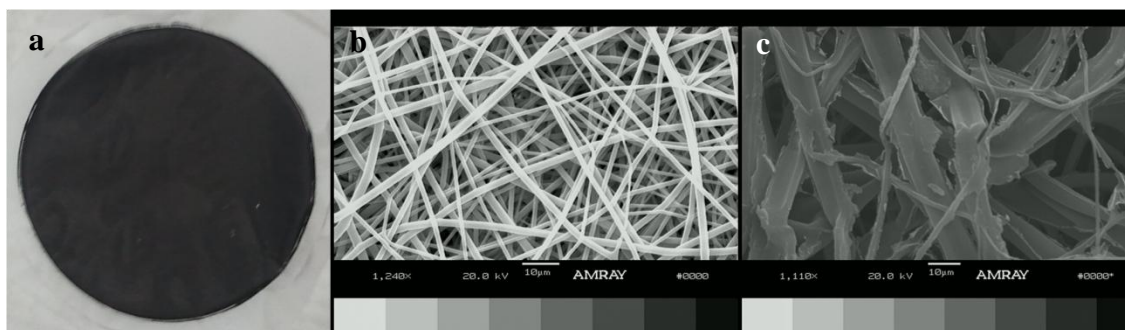


Figure 4-10: (Left) Impregnated polymeric scaffold with an aqueous solution of CNT via vacuum filtration. (Middle) SEM of an un-impregnated scaffold. (Right) SEM of an impregnated scaffold.

Further studies looked at the morphology of the scaffolds both on the top and the bottom.

Visual inspection indicates that the CNT have penetrated through the scaffold to the bottom. This was validated by SEM both sides where there appears to be a lack of brightness associated with the bare scaffold. Differences that arise appear to be the amount of coating, with the top of the scaffold experience a greater degree of coating than the top. This observation also manifests itself when inspecting the bottom of the scaffold by SEM where there appear to be less uniformity, albeit only slightly.

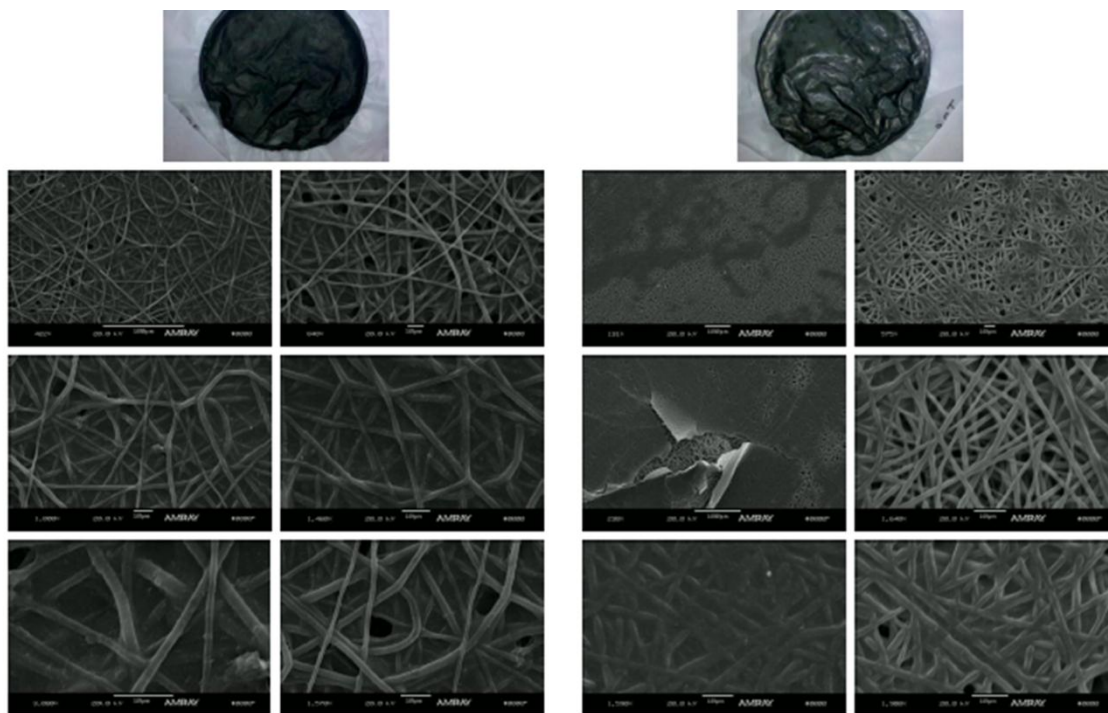


Figure 4-11: Scanning electron microscopy images of pressure induced wetted scaffolds.

4.5 Cell Differentiation Results

Both human embryonic stem cells (hESC) and human induced pluripotent stem cells (hiPSC) were deposited onto impregnated carbon nanotube scaffolds and their two respective controls (Figures 4-14 & 4-15). Cells were tagged with a marker for fluorescence studies. Initially it appeared that the cells on the CNT impregnated scaffolds were not present putting their viability into question. This can be attributed to the CNT quenching the fluoresce signal of the cells, an artifact that dissipates after 14 days. In fact, it can be seen that after 14 days of incubation, there is greater amount of differentiation from the cells deposited onto the PLGA/CNT scaffolds indicative of the bright green fluorescence.

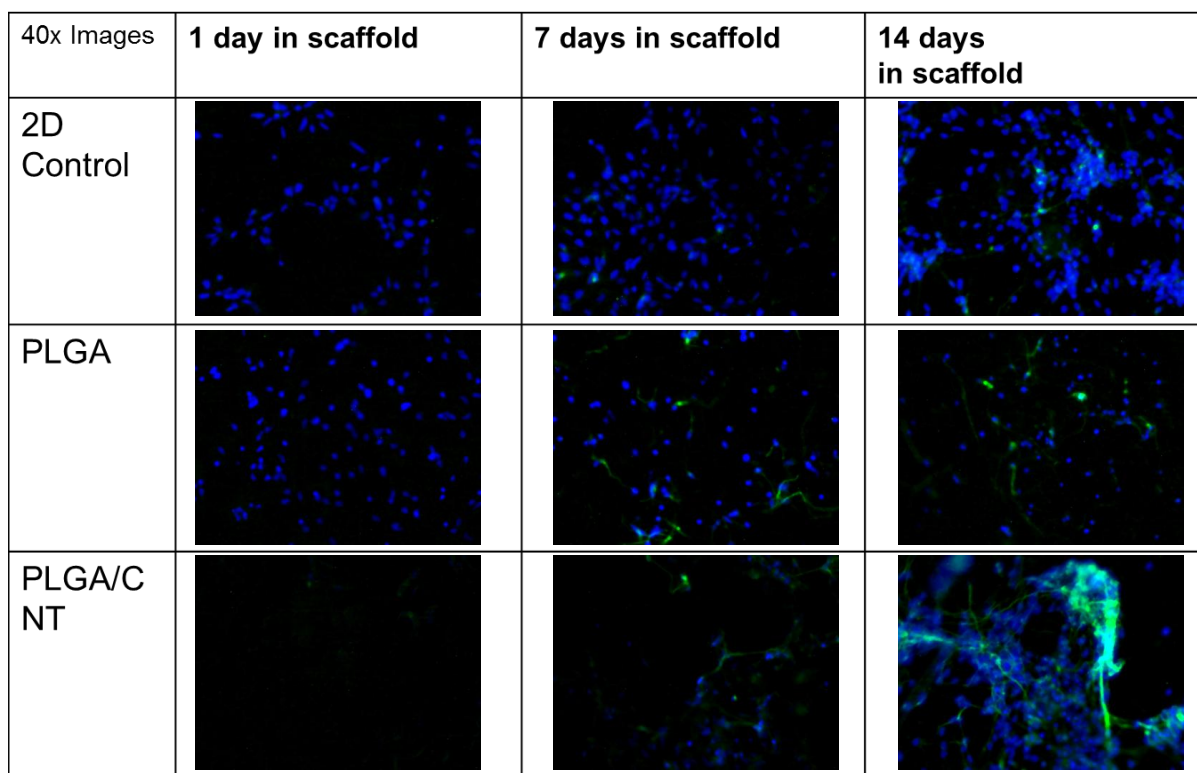


Figure 4-12: hESC Derived NSC differentiated in 2D, PLGA Scaffolds, or PLGA/CNT Scaffolds.

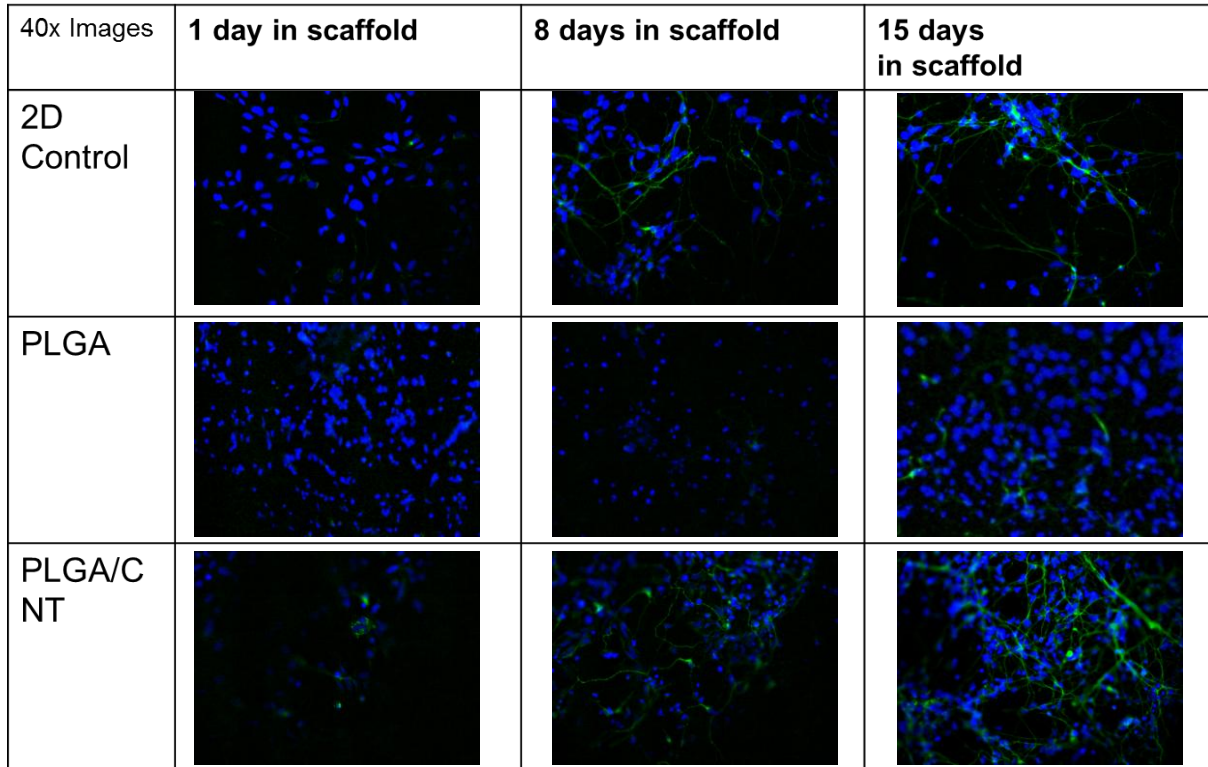


Figure 4-13: hiPSC Derived NSC differentiated in 2D, PLGA Scaffolds, or PLGA/CNT Scaffolds.

4.6 Electrical Stimulation

A circuit board was fabricated so that an external electrical stimuli could be applied simultaneously to eight electrodes. Each electrode was made within the following manner: The middle portion of a indium tin oxide (ITO) covered glass slides is etched with solution of 20% HCl and 5%t HNO₃ in order to create a non-conductive gap, forming two electrodes[319]. This is to ensure that the applied current is transferred from the ITO electrode to the CNT scaffold, and not directly to the solution within the cloning cylinder. CNT scaffold samples are fitted with cell culture rings to house the cells. In order to ensure uniform current applied to each slide and thus statistical significance, the board was wired in series. The power source consisted of a 1 V watch battery. The ITO glass slides had a resistance of 200 Ω (+/- 50 Ω) whereas the scaffold contained a

resistance of $5\text{ k}\Omega$ ($\pm 2.5\text{ k}\Omega$) on the top and $15\text{ k}\Omega$ ($\pm 5\text{ k}\Omega$) on the bottom, respectively.

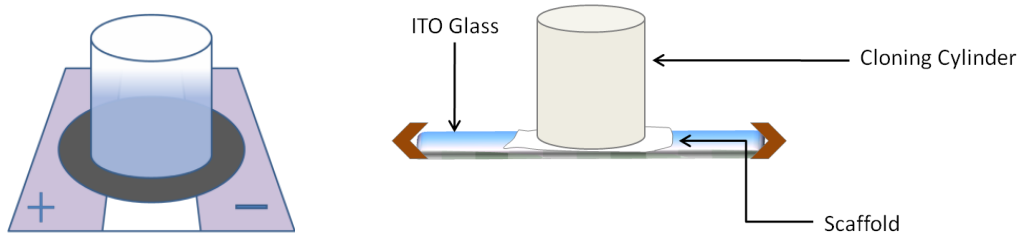


Figure 4-14: (Left) Schematic of the etched ITO glass (purple region) with an etched non-conductive gap (white). On top of the ITO glass is the electrospun polymeric scaffold impregnated with CNT. Lying on top is the cloning cylinder housing the differentiation process. (Right) Schematic of the same set up from a side view. Brown triangles represent the alligator clips on the fabricated circuit board where the current flows through.

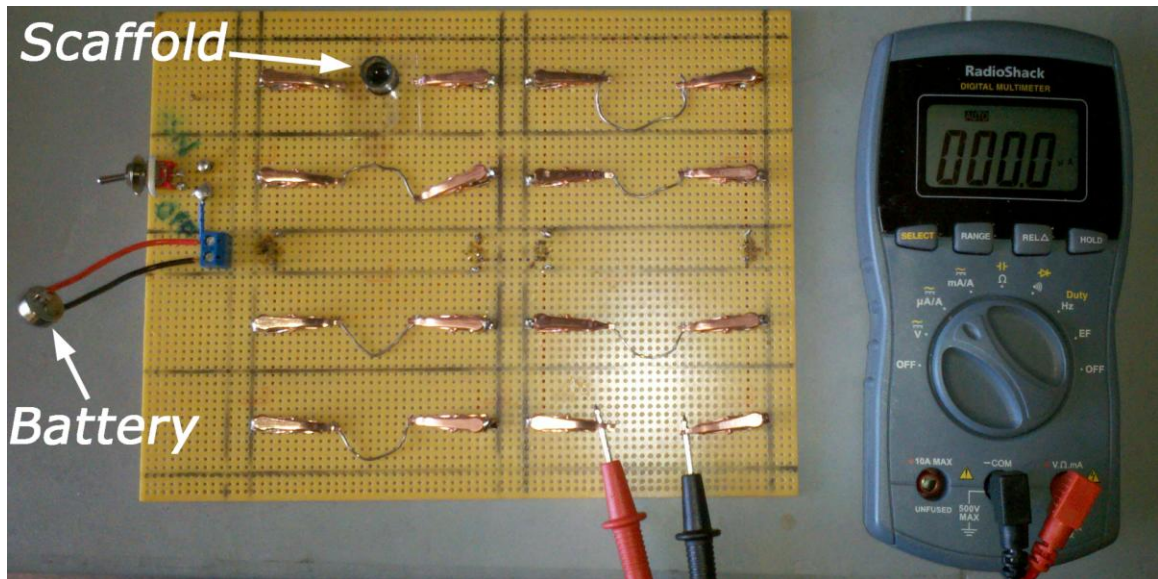


Figure 4-15: Electrical stimulation board with 8 slots for application of constant current or voltage.

Electrical stimulation of the cells was applied for a duration of 10 minutes. The results of which can be seen in figure 4-16. A greater density of differentiated stem cells can be seen in the cells where stimulation had been applied opposed to the unstimulated cells.

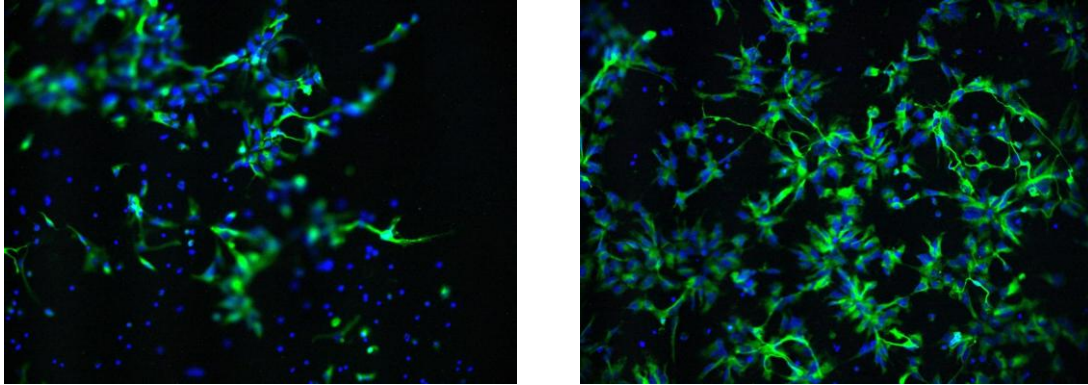


Figure 4-16: Differentiated hESC on the PGLA scaffold (left) and on the PGLA scaffold impregnated with carbon nanotubes.

4.6.1 Tilted Scaffolds

One of the primary goals in stem cell therapy, and therefore regeneration medicine, is the enlistment of nearby matured cells and stem cells to damaged tissue by a guided approach[320]. How these cells migrate will depend on the *in vivo* microenvironment, comprised of various physical, chemical and biological cues that provide signals to guide the adhesion, migration, proliferation, differentiation and apoptosis of cells at certain locations and times[321]. The use of gradient materials may lead to the enhancement of desired cell mechanisms in addition to gaining insight in how these cells behave *in vivo*. Gradient materials were first proposed over a century ago by Ramon et al. who suggested that attractive molecules could be used to assist growing axons to their desired targets[322]. However, it has not been until the past few decades that investigators began to implement a gradient into biomaterials [322]. Doing so has proceeded through several means including top down approaches (plasma[323], corona discharge[324], ultra-violet irradiation[325], chemical degradation[326]) as well as bottom-up approaches (infusion[327], diffusion[328], microcontact printing[329], microfluidic lithography[330], electrochemical method[331]). However, there are

insufficient number of studies, if any that has explored the use of electrical stimuli applied in a gradient fashion.

Here we employ a top down approach whereby a gradient is created by tilting the scaffolds at an angle during impregnation. In doing so, a concentration gradient of the carbon nanotubes is created that runs axial across the impregnated scaffold. This concentration gradient then in turn will allow for the resistance to vary across the scaffold therefore imparting in effect a voltage/current gradient. This differs from previous attempts where a external electrical field was used to create a concentration gradient with no benefits of a varying electrical potential (Electrochemical method). The extent of the gradient is characterized by thermal gravimetric analysis (TGA), Raman spectroscopy and liquid porosimetry. This allows one to identify which region of the scaffold enjoys the greatest cell viability, differentiation and neurite outgrowth, and therefore better optimization of the impregnated materials.

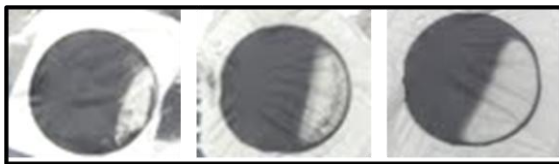


Figure 4-17: Tilted scaffolds impregnated at 5.5 °, 11 ° and 15 °.

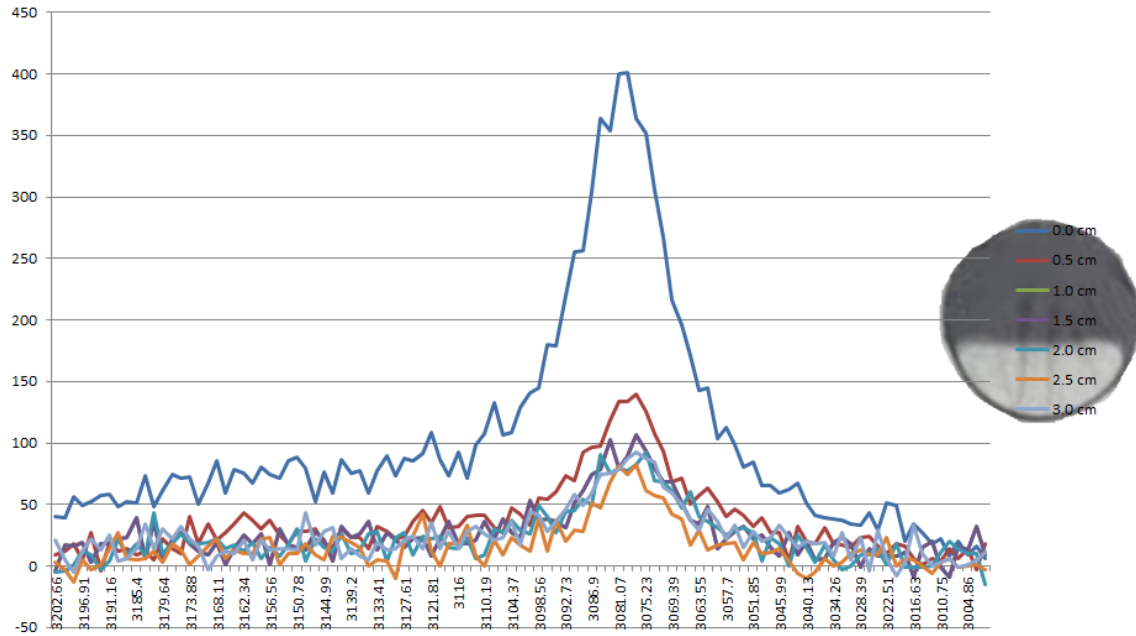


Figure 4-18: Raman spectroscopy of tilted scaffold.

4.7 Conclusion and Future Work

This chapter presented two examples where carbon nanotube composites have been successfully fabricated and applied for biological purposes. The lack of glial response when inserting carbon nanotube agarose fiber composites into neural tissue makes them promising candidates to be incorporated in future electrodes for neural recording. This can be attributed to the softness of the composite providing a better match with the neural tissue, opposed to stiffer materials such as silicon and metals. Future testing of the fiber should account for electrical stimuli, both in vitro and in vivo, and the reaction of the cells when a voltage is applied. In addition, fabricating fibers below 10 μm (below cellular dimensions) will need to be achieved that is capable of stiff penetration of the neural tissue but relaxed mechanical properties once situated inside the tissue. This presents a challenge on several fronts. First the flexibility of any material increases with decreasing size thereby making it more difficult to insert the fibers. Second, the charge

storage capacity (CSC) and the electrical impedance will change as we approach smaller dimensions thereby affecting the reliability of the recording electrode. Lastly, any functioning electrode should include components that act as capacitors, resistors and transistors in order to obtain a fully functional electrode. This is difficult to achieve with silicon and other metals, as already mentioned, but may be achievable by including defective graphene whose band gap has been manipulated to include semi-conducting properties.

Early research on the carbon nanotube scaffold composite implemented an external voltage as the driving force for the inclusion of carbon nanotubes into the polymeric scaffold. However, with the inconsistent wetting, a different and simpler approach was adopted that forcibly impregnated the scaffolds by an external pressure. With the adoption of the latter, consistent scaffolds were produced suitable for the differentiation of stem cells with and without electrical stimuli. The impregnation of the scaffolds soon diverged to include a concentration gradient that allowed for a variable resistance. As previously mentioned, inducing a gradient in biomaterials holds great promise in manipulating and understanding cell mechanics. Future work in this area will need to focus on the type of electrical stimuli to be considered for the cells, both for a particular mechanism as well as different stages of cell growth.

A patent disclosure has been made to the Office of Commercialization and technology at Rutgers University relating to the CNT/scaffold composite material in addition the circuit board designed for simultaneous application of either current or voltage. In addition, a manuscript is in preparation regarding this subject.

Chapter 5 Alumina Catalyst Supports

In designing a catalyst several factors need to be considered. Ideally a catalyst should have excellent fluid flow properties, activity and stability. More common, however, is the fact that concessions are usually made by one in order to accommodate the others. This weighted emphasis on one factor as opposed to another depends on the issues relating to the reaction, reactor design, process conditions and economics. The interplay and dependence of these properties are highlighted in figure 6-1.

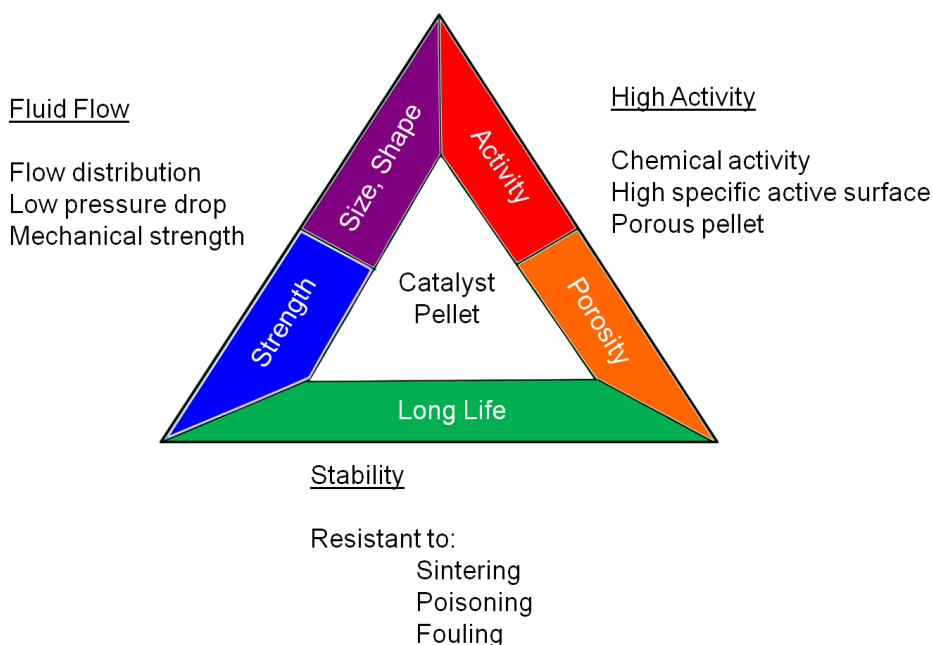


Figure 5-1: Ideal properties of a catalyst support. (Revised and adapted [332])

Although materials such as zeolites and activated carbons have been explored in catalysis, their domain of porosity typically consists only of the microporous range, thereby sacrificing fluid flow properties. An attractive alternative is the use of mesoporous materials. Interest in the structural modification of mesoporous materials has garnered a tremendous amount of attention in recent years for its applications in catalysis, sorption and separation processes[23, 333-336]. The ideal qualities of such materials

include large surface areas for deposition, durability, and fast diffusion times for rapid molecular transport. However, the materials possessing high surface areas produced on a large scale generally lack the larger mesopores required for short diffusion times. It is therefore imperative in fields such as catalysis to provide for both large pores as pathways for swift diffusion as well as smaller ones to serve as deposition sites[337, 338]. It is especially important in the petrochemical and petroleum industries where reactions typically occur with metals supported on porous metal oxides, the morphology of which will dictate the catalytic activity and product selectivity of the catalyst. However, the material typically chosen for these supports exist in a powder form and it is therefore necessary to impart some plasticity to the material in order to utilize it for the appropriate application[339]. This is accomplished by mixing the powder with a liquid binder in a process known as granulation[340, 341]. During this process a paste with sufficient plasticity must be formed which can be deemed adequate for extrusion, where in some cases a minimal amount of acid (peptization) is required[341]. The advantage of extrusion is that it allows for the formation of pellets or spheres with a highly uniform cross-section[342, 343]. It is these two processes that will ultimately determine the interplay between porosity and the susceptibility of an extrudate to fracture, properties that tend to be orthogonal to each other. The former of these two properties will determine the amount of catalyst that can be loaded and its corresponding efficiency. As a result, generating pores that maximize the loading capabilities without sacrificing extrudate strength serves as a major goal in catalysis.

One such metal oxide that has long been utilized as a support is alumina[344, 345]. The predominance of its use is owed to its low relative cost, long stability, and its

tunable surface area and porosity. The latter of these enables it to be used in a broad range of applications as previously mentioned[346, 347]. By knowing which experimental parameters determine porosity, one can tailor porosity during manufacture and match it to a specific need, thus improving efficiency. To date, however, any effort to manipulate a distribution to include a bimodal mesoporous distribution is accomplished by either a synthetic route[348-353], or the mixing of different phases of alumina consisting of various crystallite sizes. The former of these typically includes a template model using surfactants[348-353], ionic liquids[353], and in some cases microemulsions[338]. In lieu of these approaches, we present a simple method for producing a bimodal mesoporous alumina support via high shear mixer (granulator). It was revealed that with granulation time there emerges a bimodal distribution in the mesoporous range that can be controlled simply by time.

5.1 Experimental

5.1.1 Materials

CATAPAL[®] B boehmite (Sasol) was used as alumina (AlOOH) source in the catalyst preparation. Distilled water was used as the wetting agent. 1M HNO_3 was purchased from Sigma Aldrich and was used as the peptizing agent.

5.1.2 Granulation and Extrusion

A laboratory high shear mixer (granulator) was used in the preparation of the catalyst. A high-shear granulator (Fukae Powtec) was used to granulate the alumina. It has an impeller, which is attached to the bottom of the vessel and a chopper, which is

attached at the side of the vessel. Both the impeller and chopper rotate in clockwise direction. The total capacity of the mixing vessel, is about 200~500 g of solids in each experimental batch. The reaction temperature was recorded from the thermocouple which is installed in the mixer along the periphery, so the indicated temperature may not be a quantitative characterization of the whole mass, but it does act as a qualitative indicator. Granulation was done by mixing alumina with the addition of distilled water (wetting agent). The mixture ratio was 45:55 (solid:water). Before adding the distilled water, alumina was mixed by keeping the impeller speed ~ 100 rpm and chopper speed ~ 500 rpm. This is done in order to deagglomerate the alumina. After a few minutes, when homogeneity in the mixture is obtained, the wetting agent is added with the help of a burette in order to have a more constant flow rate ($0.0039 \text{ m}^3/\text{h}$). During the addition of distilled water the impeller and chopper speed is not increased. After the addition of all the water the rotation rate was increased to 500 rpm for the impeller and 1500 rpm for the chopper. Samples were then taken at 10 minutes intervals for extrusion and for characterization. The granulated sample is then extruded using a press (Carver, Inc.) and die whereby about 2 grams of sample was used and extruded through a 1/16" circular nozzle located at the base of the die.

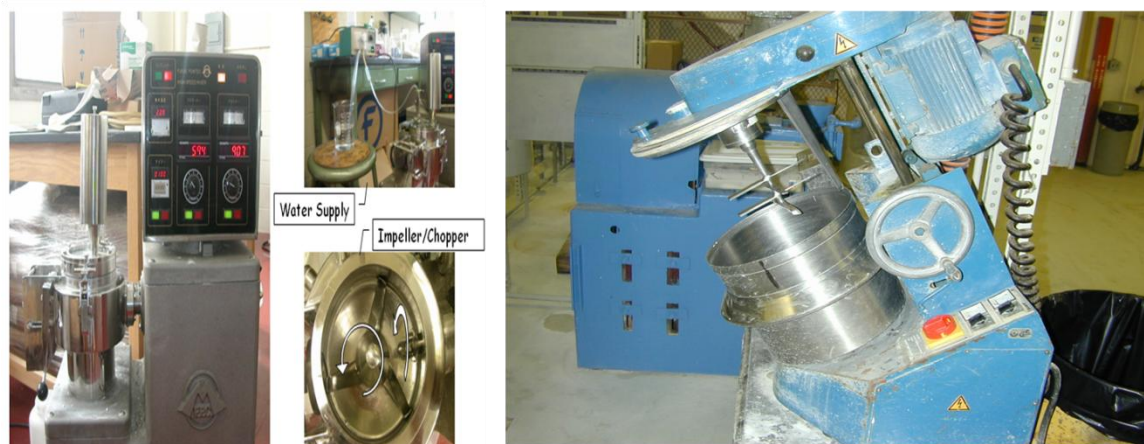


Figure 5-2: (Left) A laboratory Fukae granulation apparatus with an impeller and chopper blade and (Right) a Eirich mixer used in pilot plant operations.



Figure 5-3: View of the Fukae granulation as a function of time. (a) powder only (b) 0 minutes (c) 15 minutes (d) 30 minutes (e) 60 minutes.

5.1.3 Characterization

Nitrogen porosimetry analysis was measured using an AUTOSORB-1 series analyzer (Quantachrome). The resultant pore size distributions were calculated from the desorption isotherms using the Non-Local Density Functional Theory (NLDFT)[34, 354]. Prior to the analysis, the samples were calcined at 500° C and degassed at 300° C for 3 hrs. Particle size analysis was carried out in a LS-230 laser diffraction particle size

analyzer (Beckmann-Coulter GmbH). Trace amounts of the sample was placed in a cell filled with distilled water and sonicated at an amplitude of 14 until the polarization intensity differential scattering reached a range between 45 and 55 %. The measurements were then allowed to run. Scattering of the light is converted to particle size using the Mie theory and a particle size distribution based on an alumina model. Crush Strength measurements were measured using a DR. SCHLEUNIGER[®] model-6D tablet friability tester (Dr. Schleuniger Pharmatron AG). Between 25-50 extrudates were prepared of the same diameter and similar length to be crushed. Each sample was placed in the tester and two blocks applied a force until the sample fractured at which time a force in Newtons was registered.

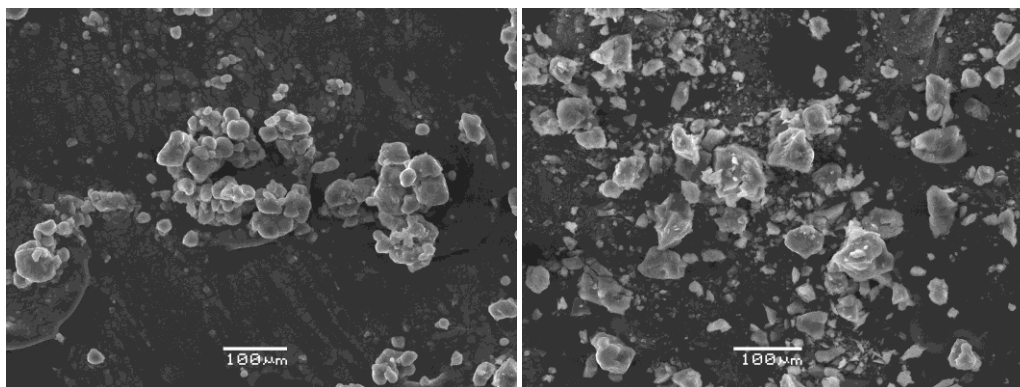


Figure 5-4: Scanning electron microscopy of granulated particles.

5.2 Results and Discussion

5.2.1 Extrudate Characterization

Surface area and pore volume serve as an indicator to the loading capabilities of a support. Figure 5-5 shows the single point BET surface area while figure 5-6 displays the total pore volume, of the extruded samples. With increasing granulation time, there is considerable increase in the BET surface area and in the total pore volume. This increase

starts to become less pronounced towards the end of the mixing time. By the addition of acid there is a considerable increase in the total pore volume over the entire mixing time. When calcined, the water is removed from the system, hence allowing adjacent particles to fuse together perhaps *via* neck formation. This allows for an increase in porosity and therefore an increase in surface area. With increasing acid concentration there was a decrease in surface area as well as a decrease in the total pore volume. This is attributed to an increase in concentration of aluminum soluble species that fill the interstices between the particles[355]. Upon calcination of the extrudates from wet pellets, there is considerable amount of shrinkage taking place; thereby an increase in the strength of interparticle bonds is observed[356].

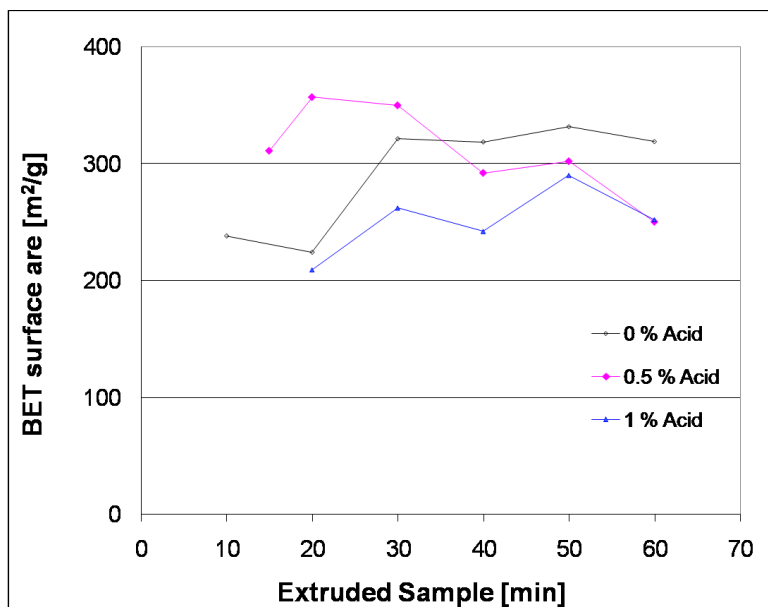


Figure 5-5: BET surface areas results for the extruded samples as a function of mixing time.

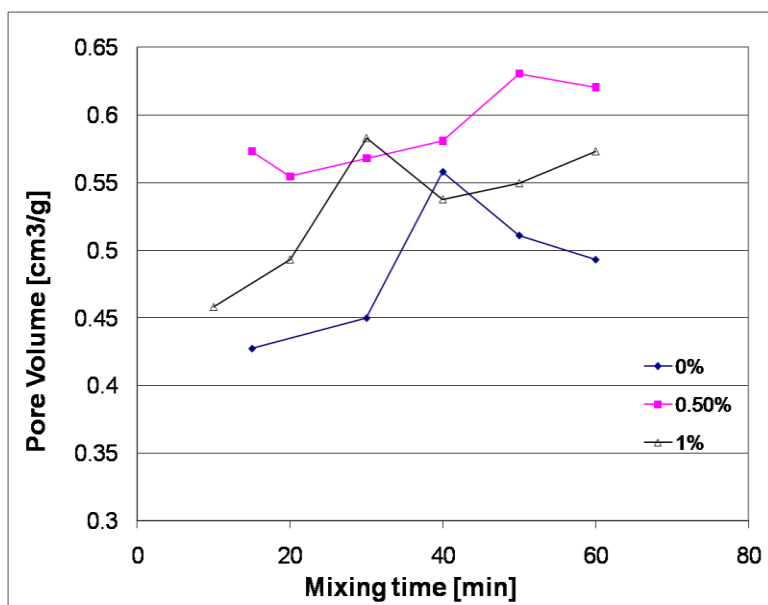


Figure 5-6: Total pore volume results for the extruded samples as a function of mixing time.

The NLDFT method allows for the calculation of the pore size distribution. This method is preferred to the traditional Barrett-Joyner-Halenda (BJH) model for pore size analysis which relies on the Kelvin equation, that is a macroscopic relationship that progressively becomes inaccurate for pores smaller than 100 \AA [357]. The sequential pore size distribution exhibits a bimodal nature that is clearly dependent on mixing time. Initially, the distribution is dominated by one peak. As granulation time is allowed to increase, the resultant extrudates reveal a second peak at a higher pore size. The emergence of this second peak evolves over the course of mixing whereby the first peak slowly dissipates at the expense of second one. Furthermore, the addition of acid imparts three effects. The first is that there is a shift to higher pore sizes for both the initial peak and the secondary peak. Secondly, the emergence of the secondary peak occurs more rapidly and surpasses the first in height in less time. Lastly, the more peptized systems show a height increase for both peaks at all stages of mixing.

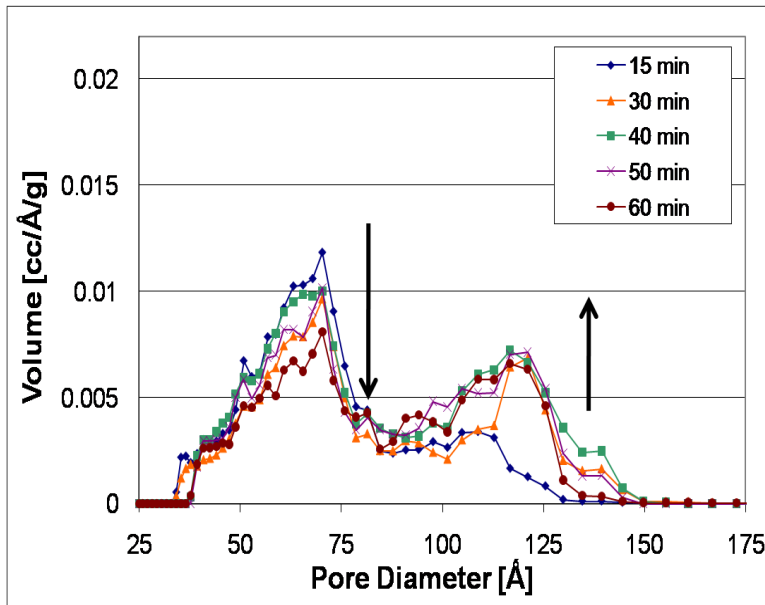


Figure 5-7: Pore size distribution as a function of mixing time for 0% acid .

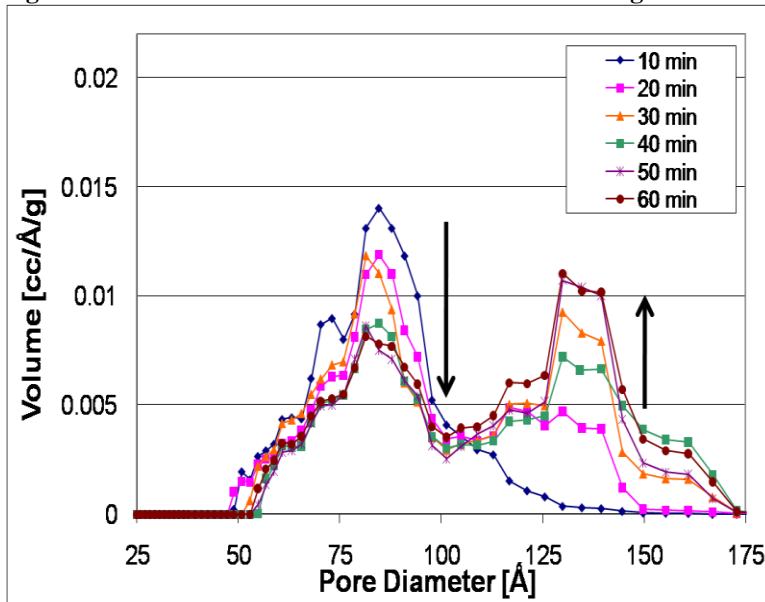


Figure 5-8: Pore size distribution as a function of mixing time for 1% acid.

The failure of catalyst strength in a fixed bed converter causes maldistribution of fluid flow. This in turn can lead to a large pressure drop through the bed which can result in a low efficiency of catalysis and in extreme cases plant shut down. The typical culprit for strength failure in these catalysts are brittle fractures. For porous catalysts containing defects, dislocations and discontinuations, the expending of the micro cracks under

tensile stress concentrated around the edges of flaws is the primary reason for fracture^[33]. It is thus necessary to have extrudates that are both porous for adsorption as well as durable. Crush strength measurements were taken as a function of time and displayed in 5-9. It can be seen that there is an overall increase in the strength of the extrudate with mixing time irrespective of acid concentration.

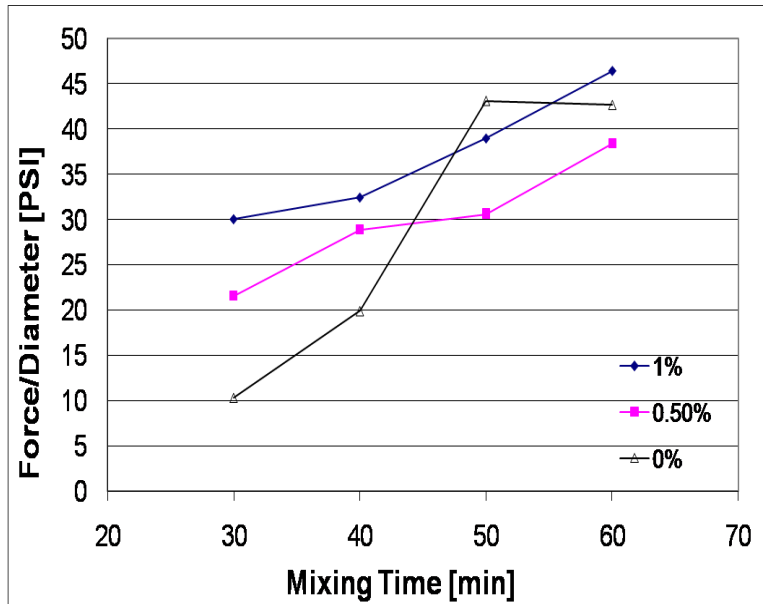


Figure 5-9: Crush strength as a function of mixing time.

5.2.2 Paste Characterization

The properties of the paste will ultimately decide the characteristics of the calcined extrudate. One property that plays a significant role in the pore size distribution will be the particle size. Upon calcination the water present in the extrudates will begin to evaporate. This induces the particles to form inter particle bridges via neck formation thereby creating a pore network[340]. It can be seen from figure 5-10 that as granulation time increases, there is a decrease in the overall particle size despite acid concentration.

This shift to smaller particle sizes is coupled with a broadening effect in the particle size distribution.

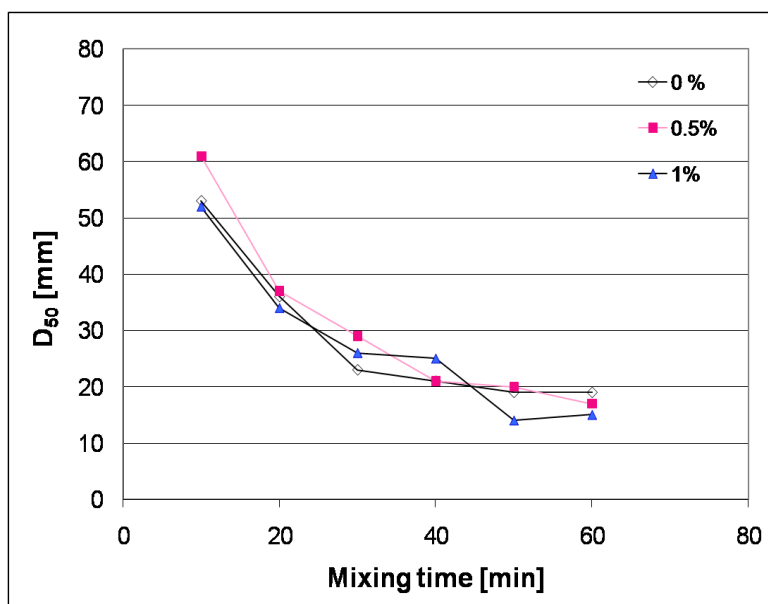


Figure 5-10: D₅₀ particle size values for the granulated samples as a function of mixing time for 0%, 0.5% and 1% acid case.

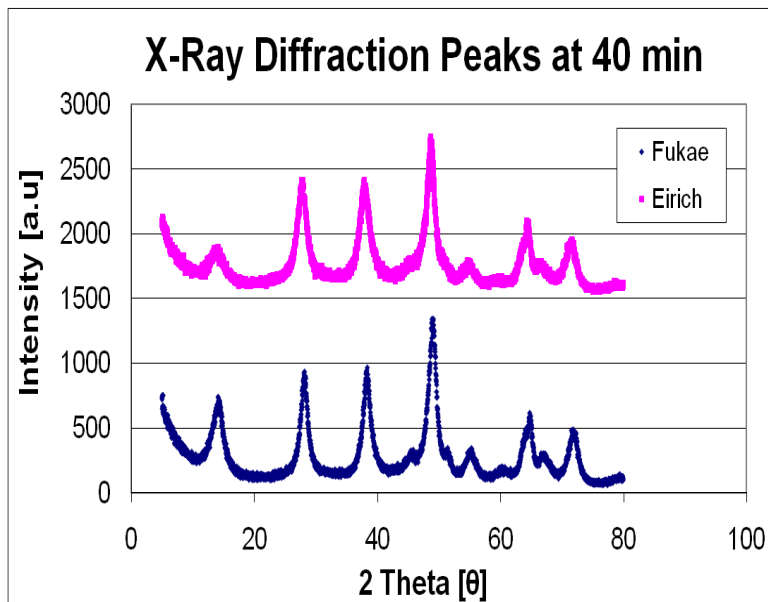


Figure 5-11: X-ray diffraction patterns of uncalcined alumina pastes processed in a Fukae mixer and Eirich. Choice of mixer does not affect the crystallinity of the paste.

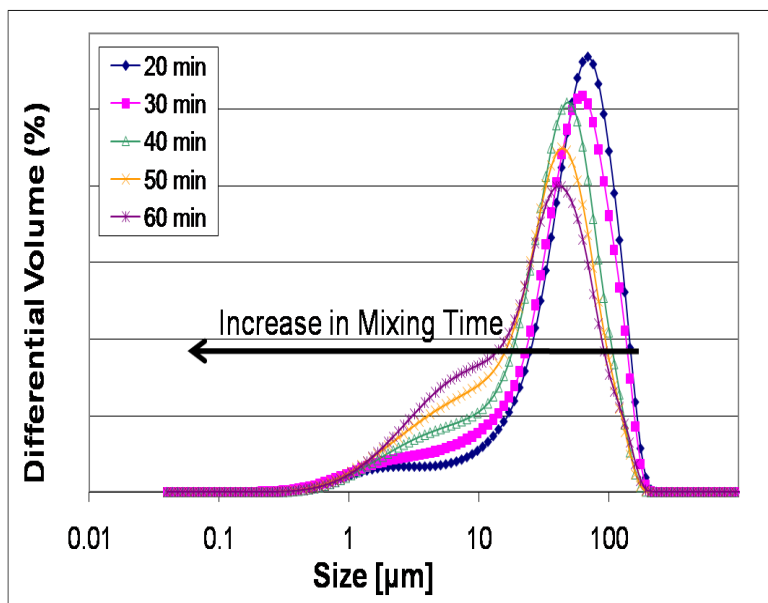


Figure 5-12: Particle size distribution as a function of time for 1% acid.

5.2.3 Comparative investigation of extrudates of different mixers

The bimodal distribution is thought to be the result of a higher severity inherent to the Fukae mixer. To verify this samples were produced in an Eirich mixer, a larger but less severe mixer whose (larger) blades operate at a sustained rate of 68 rpm, and is generally used in plant and pilot plant operations. At the conclusion of the mixing process, the batch was extruded with both a 2.25 inch single screw extruder (The Bonnet Company) and the 1/16th die. This provided data through two avenues. First it allowed for the resultant pastes to be characterized by their respective particle size distribution. Second, by extruding the raw pastes with both the Bonnot extruder and the Carver press, two different extrusion techniques could be compared via N₂ porosimetry. These results are summarized in figure 5-13 and table 1. The particle size distributions are shown in figure 5-14.

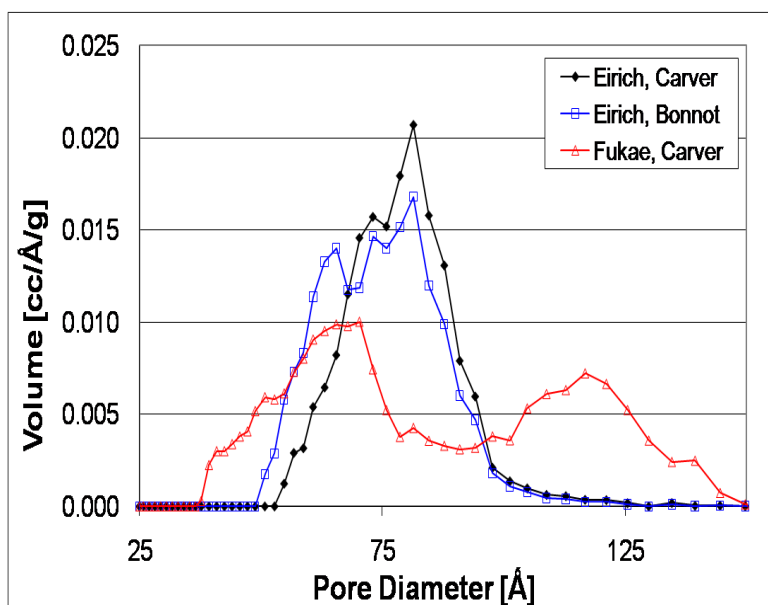


Figure 5-13: Pore size distribution for pastes mixed and extruded by two different methods. The first term in parentheses signifies the type of mixer used, while the second term signifies the type of extruder used.

Solids:Binder (45:55) 0% Acid	Granulated: Fukae mixer Extruded: Carver press	Granulated: Eirich mixer Extruded: Carver press	Granulated: Eirich mixer Extruded: Bonnot extruder
Multipoint Specific Surface Area (m ² /g)	304	260	289
Total Pore Volume at Po (0.990-0.998) (cm ³ /g)	0.56	0.49	0.50
Single Point Specific Surface Area (m ² /g)	300	254	282
Average Pore Diameter (Å)	73*	76	70

Table 9: Summary of the surface area and pore volume for pastes prepared under different instrumental conditions. Results show the 0% acid case mixed up to 40 minutes. * Denotes the fact that the value is not truly representative of the average pore diameter but the average of the two peaks.

Unlike the Fukae mixer which produces a bimodal pore size distribution, the Eirich mixer shows only one peak. The difference between the two is further reflected in the particle size distribution seen in figure 5-13 for pastes mixed with the Eirich mixer which show

an almost identical distribution with granulation time. But the overall properties- SA and PV- while higher for the more severe mixer, are not that dramatically different.

In addition, the crush strengths were measured to evaluate the extrudates resistance to fracture. These results show that it takes on average a force of 28.3 PSI to fracture the extrudates prepared by the Fukae mixer. This is compared to the 15.3 PSI that it takes to fracture those prepared by the Eirich mixer.

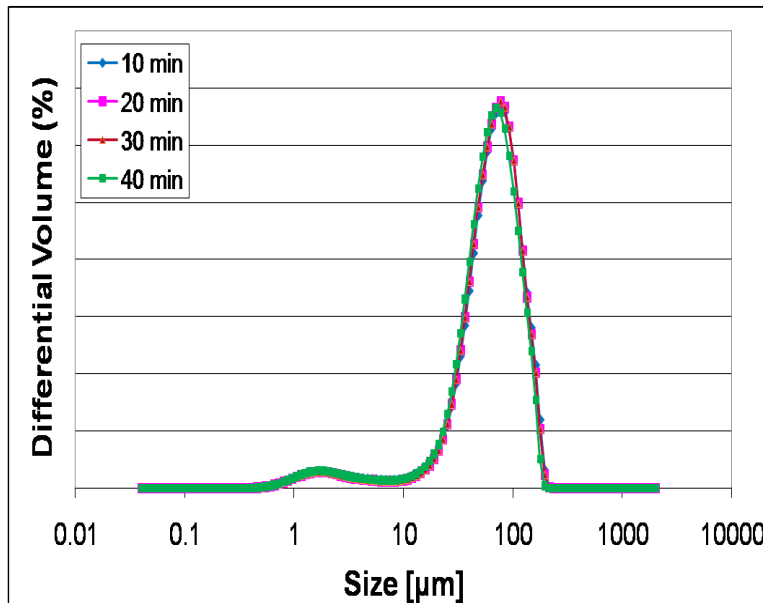


Figure 5-14: Particle size distribution as a function of time for pastes prepared via Eirich mixer.

To date there has not been a report of a bimodal mesoporous size distribution using alumina without the need of a multi component alumina mixture. In order to see if the bimodal distribution that is presented here is inherent to the granules or manifests itself in the extrusion process, nitrogen porosimetry analysis was performed on the pre extruded pastes. Although not shown, these results demonstrate that there is a slight downshift to smaller pore sizes after extrusion, with the bimodal distribution still persisting. This is to be expected because the force required to extrude will in the process

break down particles^[14]. It can thus be determined that the bimodal distribution, although slightly affected by extrusion, is inherent to the granulation process itself.

5.3 Conclusion

It was revealed that a bimodal pore distribution develops as a function of alumina granulation time in a more severe mixer. Severity increases as a function of both higher blade speed and size. This higher severity is thought to be due to the high speed chopper present in the Fukae mixer, which ran at 1500 rpm in our experiments. This was tested against the apparently less severe Eirich mixer which showed only one peak in the pore size distribution. The values of pore size and pore volumes obtained in this study were found to be higher for the most part than those found in the synthesis of boehmite sol-gels^[31]. The higher severity mixer produces a greater concentration of smaller particle sizes, which contributes to the formation of the bimodal pore size distribution at higher mixing times. Implementation of higher severity in larger scale mixers, perhaps by use of higher speed and larger choppers than now in use, could produce these bimodal distributions within the mesoporous range, if indeed that distribution actually produces improved catalysts.

One publication has resulted from the results described in this chapter. It regards the granulation and extrusion of alumina pastes and can be found in the journal *Particle & Particle Systems Characterization* [168].

Chapter 6 Nanocarbon and Alumina Composites for Energy

Applications

6.1 Part I: Characterization and Application to Catalysis

Graphene has reaped enormous praise in the past decade owing to its excellent electronic[358], mechanical[359] and thermal[360] properties. Particular interest has been paid to the former where it has been shown that electrons can behave like massless fermions. The ultrarelativistic nature of which has opened up an array of prospective applications ranging from ultra-high frequency transistors to gas sensors and transparent flexible electrode materials[361]. However, graphene's use in these applications has been limited due to the presence of defects that have been shown to greatly affect the electronic properties. Such defects include mono and divacancies, Stone-Wales defects, and adsorbed species. These defects strongly influence the electronic states near the Dirac point from which graphene derives many of its unique properties [362-364]. Nevertheless, some have sought to take advantage of this fact by intentionally introducing defects, via ion bombardment [348, 365-368], adsorbed species or by chemical synthesis, thereby allowing for the ability to precisely tailor the band gap. In addition, defects in graphene and its chemically synthesized derivative graphene oxide have the ability to stabilize what would be otherwise thermodynamically unstable nanoparticles[369]. The ability to do so is critical in terms of both dispersion quality and reaction efficiency in heterogeneous catalysis which is dependent on the shape of the nanoparticle and the exposed face. Table 7-1 highlights some graphene-nanoparticle structures that have been synthesized in the literature for catalysis and the reader is referred to a recent review on graphene based materials for catalysis by Machado et al.

[370]. It is the purpose of this work to adjoin the ability of graphene oxide to stabilize metal nanoparticles with the desired catalyst support properties of alumina to produce a new hybrid material for heterogeneous catalysis. We proceed by peptizing a powder of gamma alumina and mixing it with a known concentration of chemically exfoliated graphene oxide. The hybrid material is then impregnated with a solution of K_2PdCl_4 and reduced to form stable nanoparticles on the surface of the graphene sheets. Finally the material is characterized through various means (Raman, XPS, N_2 porosimetry, SEM and TEM) and the kinetics of the reaction is tested using the hydrogenation reaction of styrene in a pressure reactor.

Nanoparticle	Reaction	Comments	Ref
TiO(2) , and Pd@Pt	-----	Electrocatalysis	[371]
FePt	ORR		[372]
Pd	Carbon-Carbon Coupling Cross Reactions		[373]
CdS or TiO(2)	Photocatalytic hydrogen evolution		[374]
Ru	Hydrogenation of benzene		[375]
Au	Electrochemical catalyst of phenol		[376]
MnCoO	ORR		[377]
Au	Reduction of p-NA to p-PDA with $NaBH_4$		[378]
Ni	-----	DSSC	[379]
Pt/ITO	-----	Electrocatalysis	[380]
Pt	ORR	Fuel Cells	[381]
Pt/Au	Formic acid oxidation		[382]
Pt	ORR		[383]
Pt, Pd, CoO and Pd-CoO	CO oxidation		[384]
PtRu	Methanol Oxidation	Fuel Cells	[385]
MnO	Electrocatalysis of Zn		[386]
Pd	Formic acid/Ethanol oxidation		[387]
Au	Reduction of Nitroarenes		[388]
Pd	Hydrogenation of alkenes, nitro- aromatics		[389]
Pt	Methanol Oxidation	Electrochemistry	[390]

Pd	Suzuki Coupling		[391]
PdO	Reduction of 4-nitrophenol	Het. Cat.	[392]
Pt	Hydrogen	Fuel Cells	[393]

Table 10: Examples in the literature where graphene has been combined with metal nanoparticles for catalysis.

6.1.1 Synthesis of Graphene Oxide

5 g of graphite was placed in a flask with a 9:1 ratio of sulfuric acid to phosphoric acid (360ml:40ml). 30 g of KMnO_4 (oxidizing agent) was added to the flask and the reaction was stirred for 12 hrs at 50°C . After 12 h, the reaction was cooled to RT and quenched with 30% H_2O_2 . The resultant slurry was then filtered through 300 micron mesh, washed with deionized water and centrifuged 5X to remove the excess acid and metal ions.

6.1.2 Characterization and Validation of Graphene Oxide

Presently there does not exist a single instrumental tool capable of fully characterizing graphene or its oxide. Verification of the graphene oxide synthesis thus proceeded through three techniques. First Raman spectroscopy was used to identify graphene oxide. Considered a compliment to infrared spectroscopy, Raman spectroscopy is capable of identifying vibrational peaks associated with limited movement by a non-destructive manner. This is exemplified by the bulk movement of structures such as expanding and contracting of carbon nanotubes. For a pristine single layer of graphene, there are two prominent peaks, one at 1580 and one at approximately 2700. These peaks represent the G and G' bands respectively and are always present in graphitic materials. In addition graphene oxide has a prominent peak at 1340 (D-band) which corresponds to structural imperfections created by the attachment of functional groups or defects in the graphene

lattice. This differs from the Raman spectra of graphite which shares prominent peak positions with graphene but with different relative intensities. Measured spectras of graphene oxide and graphite are shown in figure 6-2(a).

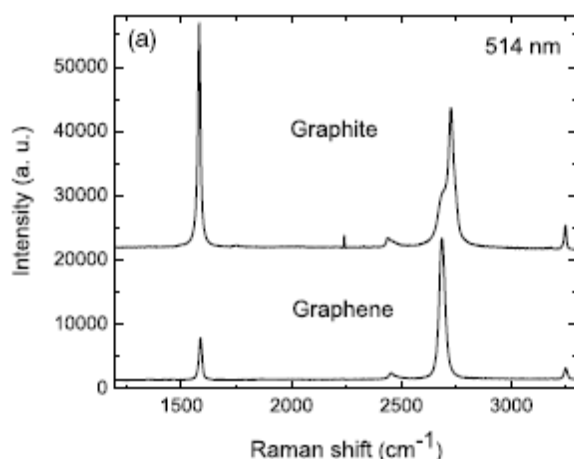


Figure 6-1: Raman spectra of graphite and graphene (Adapted from ref [394]).

X-ray photoelectron spectroscopy was performed using a Thermo Scientific K-Alpha instrument, and the data was analyzed using CasaXPS 2.3.15 software. To do so, a thin dispersion was deposited onto a gold film (a 100 nm gold layer was sputter-coated on silicon with a 10 nm Ti adhesion layer). It can be seen from figure 6-2 (b) that there exists two curves. The blue curve represents graphene oxide with two prominent peaks at 285 and 287 eV which corresponds to sp^3 and sp^2 hybridization of the carbon atoms in the basal plane, respectively. This was compared to results where graphene oxide was partially reduced with Fe powder[395]. After partial reduction with Fe powder, the peak representing sp^3 hybridization is reduced signifying a residual presence of oxygen containing functional groups remaining on the surface. Meanwhile, the degree of sp^2 hybridization is increased. In both cases there is an overall shift to the right.

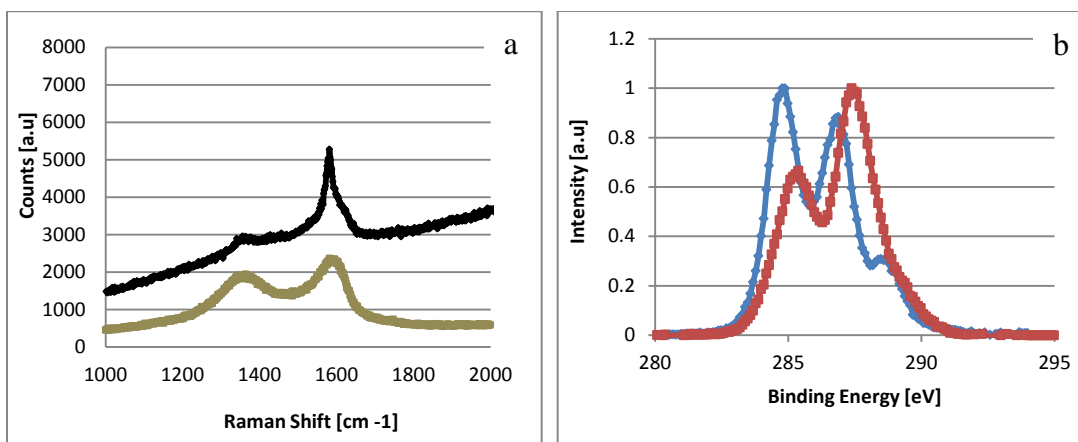


Figure 6-2: (a) Raman spectroscopy of graphene oxide (brown) and graphite (black). (b) X-ray photospectroscopy of graphene oxide (blue) and graphene oxide reduced via Fe nanoparticles (red).

Transmission electron spectroscopy of the exfoliated graphene was performed using a model JEM 100 CX transmission electron microscope (JEOL). Single to a few layers of graphene oxide can be identified in by the presence of ripples and folds displayed in figure 6-3. This is a common signature of graphene sheets where the central part of the sheet tends to display wrinkles and the edges tend to roll up. The origin of these ripples may be attributed to either intrinsic features, such as the instability of two-dimensional crystals, or that of an extrinsic nature, namely defects created by the synthesis process[396]. These features also tend to reveal themselves as dark lines thus making it possible to count the number of sheets. The assumption for figure 7-3 is the presence of one layer whose edge has been rolled over.

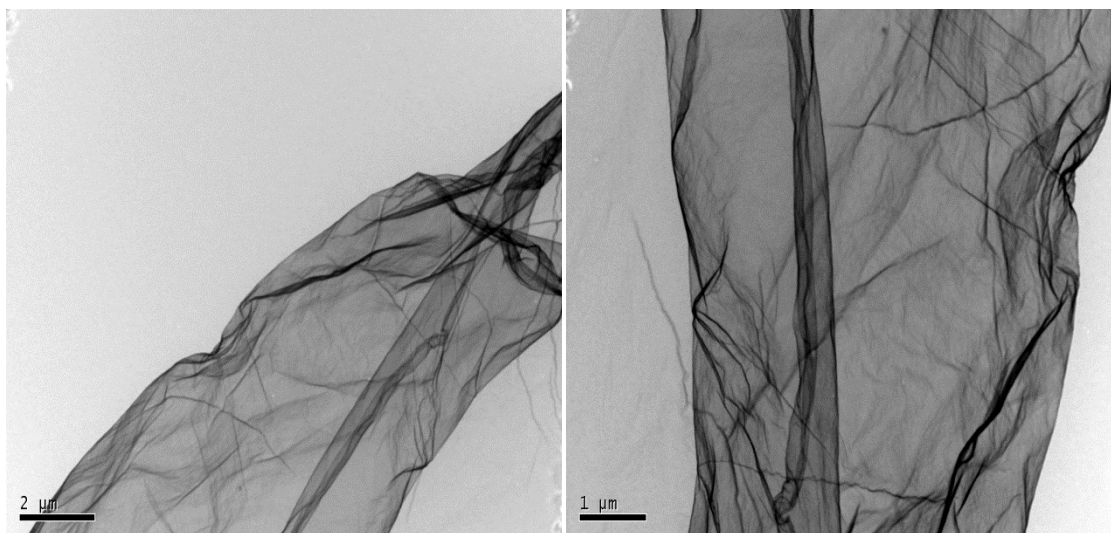


Figure 6-3: Transmission electron microscopy of single to a few layers of graphene oxide chemically exfoliated.

6.1.3 Graphene Oxide Alumina Support Synthesis

Alumina sol gels were produced by measuring out 916 ml of DI water and adding approximately 83 ml of 12 M HCl to produce a 1M solution of HCl. 40 g of alumina was added to the mixture and allowed to stir overnight until a milky suspension was reached as seen in the left image of figure 6-4. 20 ml of various concentrations of graphene oxide was added to this mixture and stirred overnight. After which time the sol gel displayed a creamy tan appearance as evident in the right image of figure 6-4. Approximately 100 ml of the GO/Al sol gel mixture was filtered using a Nalgene filter with a corresponding 100 ml of a Al sol gel prepared in parallel for later comparisons. After filtering, both GO/Al and Al were placed in the oven under air at 60 ° C for 24 h. Prior to calcination, portions of each filtered product was set aside for characterization. The remaining portions were calcined in a tubular furnace under the flow of argon at 450 ° C for 2 h.



Figure 6-4: Sol-gel of alumina (left) and after mixing with graphene oxide (right).

SEM images of the granular composites of the various sol gels are displayed in figure 6-5. It can be seen that the addition of the graphene oxide does not alter the morphology to a great extent of the alumina. This holds true for both prior to calcination under argon and afterwards. Figure 6-6 shows TEM images of the calcined alumina particles. This morphology is seen in TEM images of calcined GO/Al composites impregnated with Pd nanoparticles. The upper two images of 6-6 show the nanoparticles supported on alumina, whereas the bottom two images show nanoparticles supported on alumina supported on the sheets of graphene oxide.

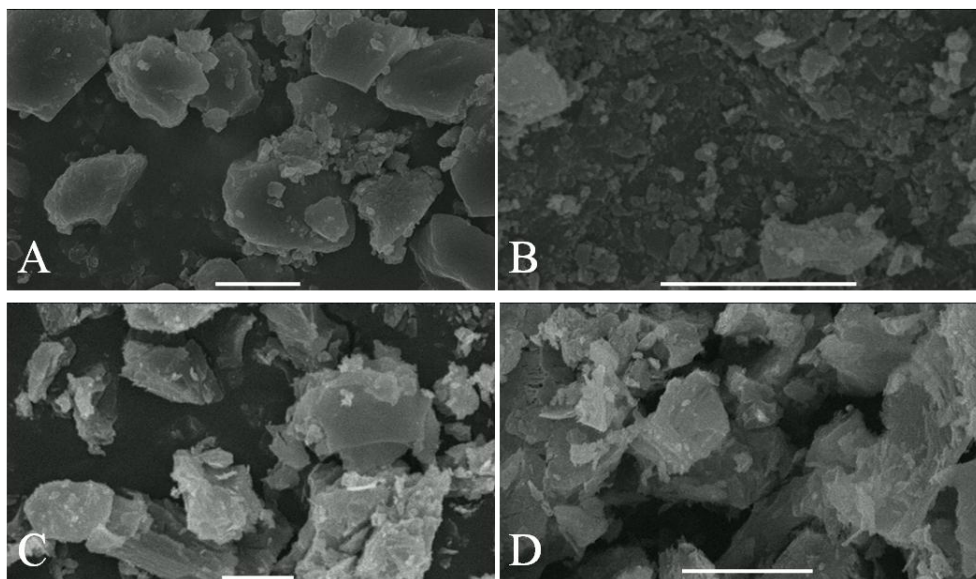


Figure 6-5. SEM images of granular dried sol-gels A) Uncalcined Al B) Calcined Al C) Uncalcined GO/Al D) Calcined GO/Al

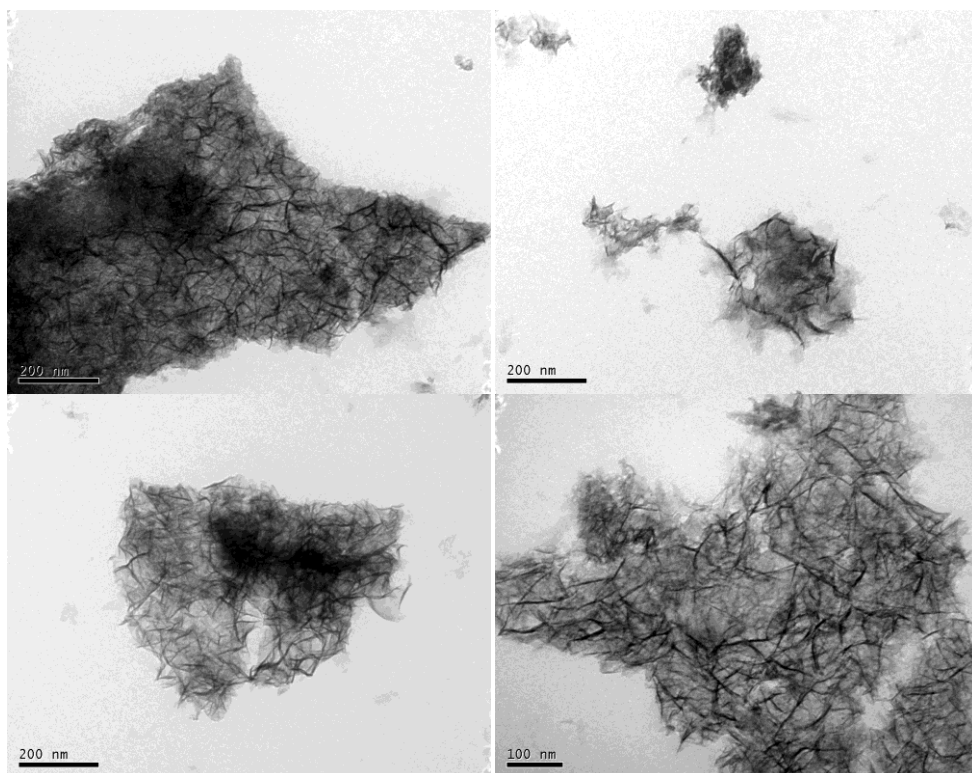


Figure 6-6. TEM images of calcined alumina.

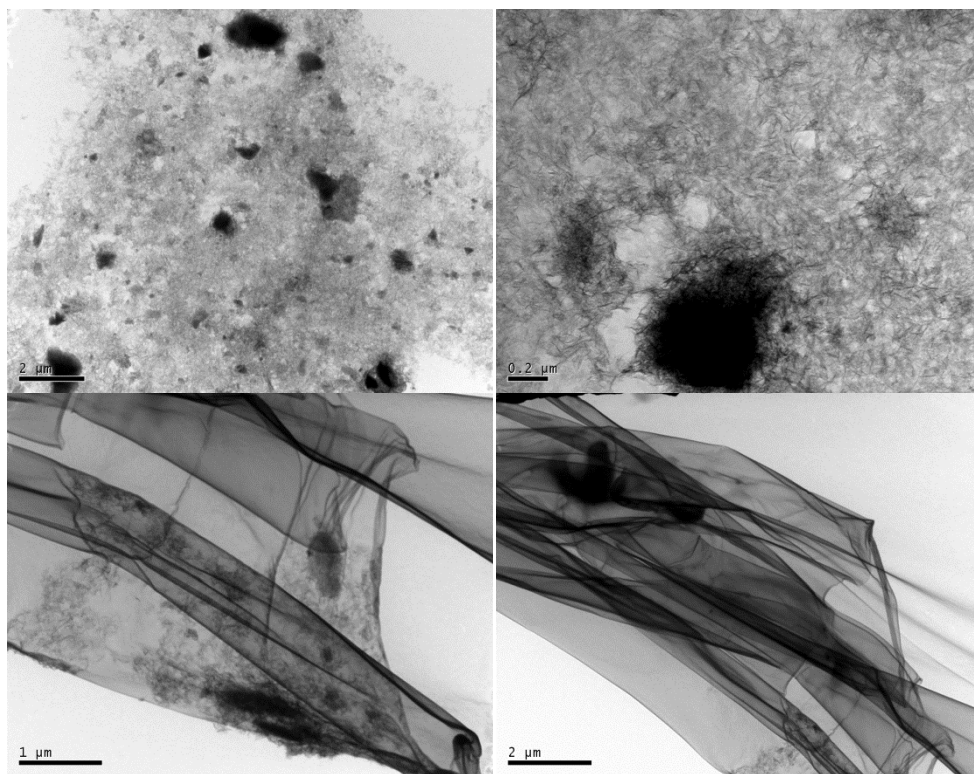


Figure 6-7. TEM images of on Pd nanoparticles on calcined GO/alumina.

Nitrogen porosimetry analysis was measured using an AUTOSORB-1 series analyzer (Quantachrome). The resultant pore size distributions were calculated from the desorption isotherms using the Non-Local Density Functional Theory (NLDFT). Samples were outgassed for 3 hours at 300 °C. The results indicates that the addition of graphene oxide does not alter the pore structure and therefore opens the possibility to pre-tailor the mesoporosity of the entire composite prior to the addition of the graphene oxide.

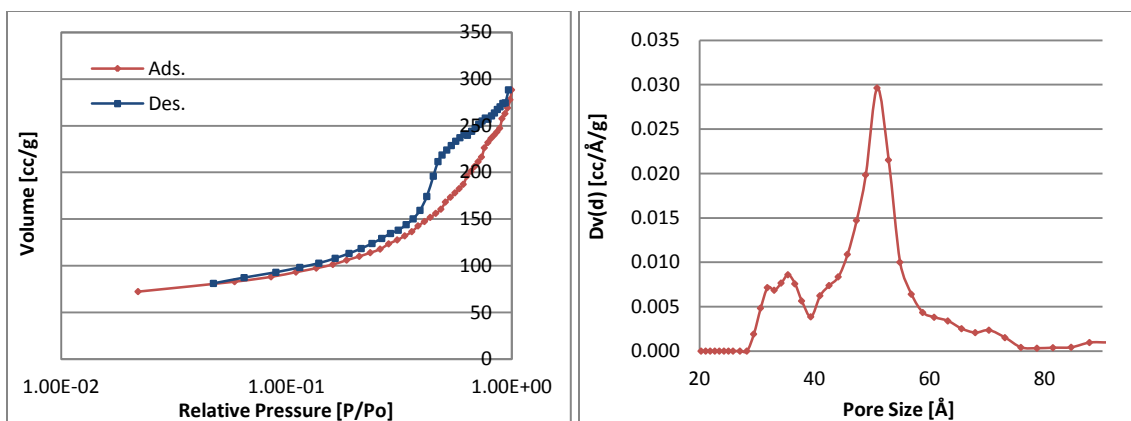


Figure 6-8: N₂ isotherms and corresponding pore size distribution for Alumina.

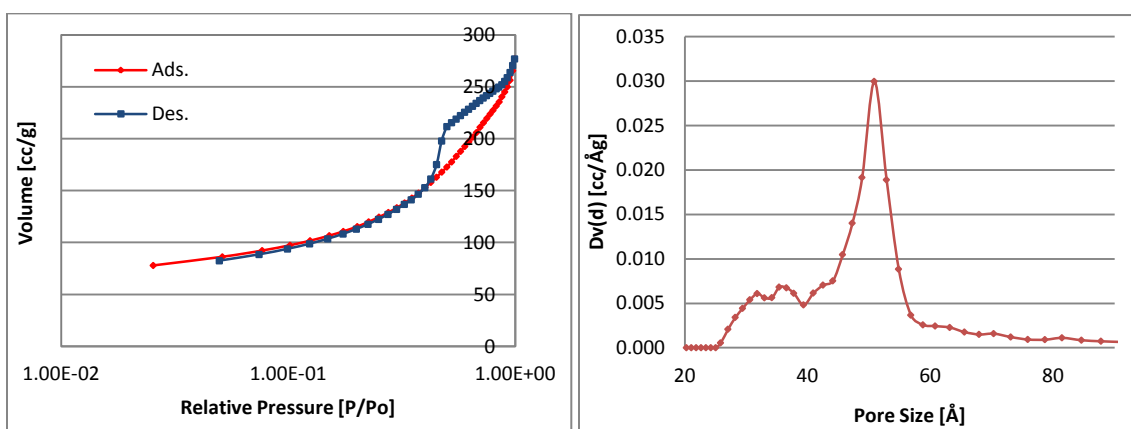


Figure 6-9: N₂ isotherms and corresponding pore size distribution for GO/Alumina.

Porosity Summary	Calcined Alumina	Calcined GO/alumina
Multipoint Specific Surface Area (m ² /g)	391	412
Total Pore Volume at (0.990- 0.998) (cm ³ /g)	0.44	0.42
Pore Diameter (Mode) (Å)	37	38

Table 11: Porosity summary of calcined alumina and calcined GO/alumina.

Samples of both alumina and the graphene oxide/alumina composite were characterized by powder X-ray diffraction (XRD) to see the extent of the phase change upon calcination. It can be seen from figure 7-11(a) that the uncalcined alumina displays a unique XRD pattern with peaks specific to α -alumina. Upon adding the graphene oxide to the sol gel mixture, there is broadening of the spectra that occurs which is displayed in figure 7-11(b). Although convoluted, the feature diffraction peak (002) of the chemically reduced GO occurs at 26.6° . The broadening of the spectra can be attributed to the non crystallinity of chemically exfoliated then reduced graphene oxide as compared to pristine graphite seen in figure 7-10. As previously mentioned, there is an abundance of defects in the form of vacancies but also in the form of line defects that contributes to the scattering of the incoming X-rays. Once the samples are annealed and calcined under a flow of argon at 450°C for 2 hours their respective XRD patterns are again measured to see the effect of calcination. It can be seen from figures 7-12(a-b) that structural changes occur that results in the reduction of all the peaks with a corresponding broadening of the entire spectra. This can be attributed to the reduction of crystallinity that accompanies a phase change from α -alumina to the γ -form.

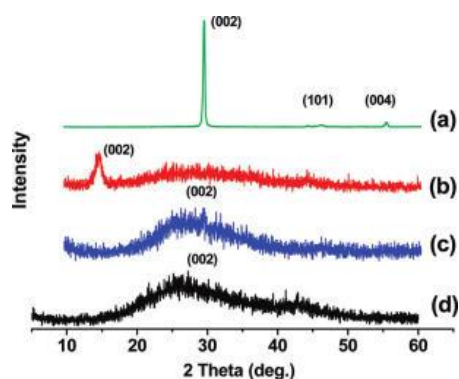


Figure 6-10: X-ray diffraction patterns of (a) pristine graphite (b) exfoliated GO), (c) electrochemically reduced GO and (d) chemically reduced GO. (Adapted from ref [397])

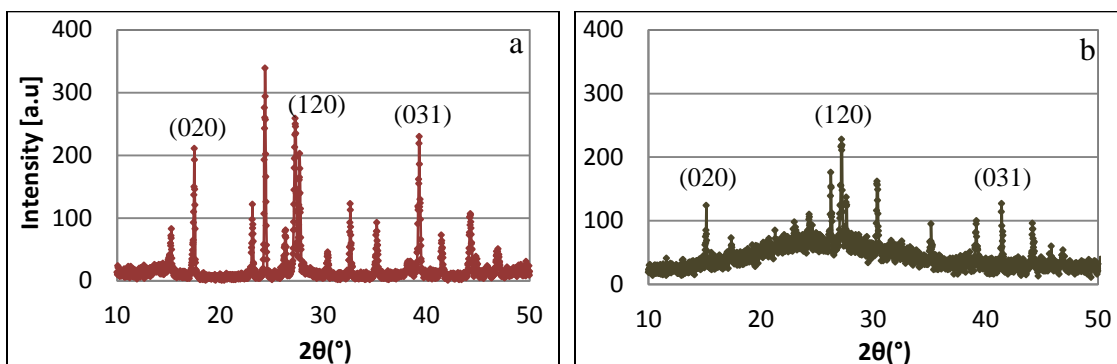


Figure 6-11: Powder x-ray diffraction patterns of uncalcined alumina (a) and uncalcined GO/alumina (b).

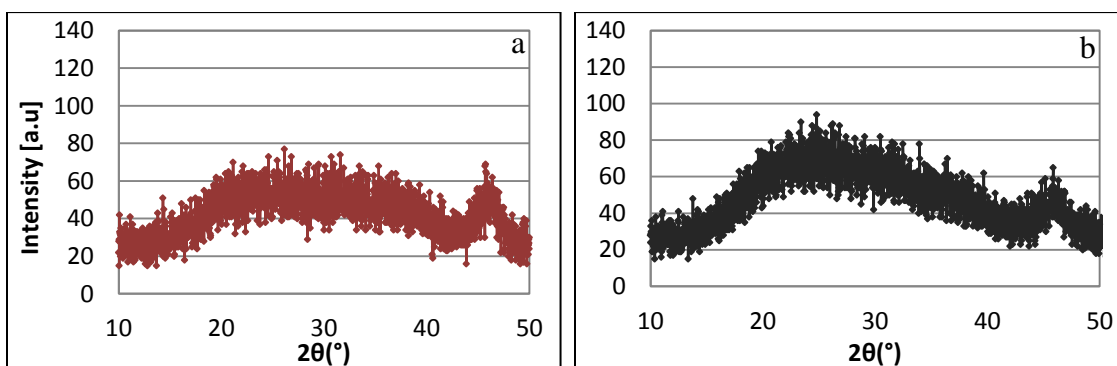


Figure 6-12: Powder x-ray diffraction patterns of calcined alumina (a) and calcined GO/alumina (b).

6.1.4 Impregnation and Catalysis

Supports were impregnated with a 0.05 M solution of K_2PdCl_4 and reduced with a 1 M solution of $NaBH_4$. Hydrogenation reactions were then performed using styrene in a pressure reactor and compared to the alumina control (reaction scheme 7.1). The hydrogenation of styrene towards ethyl benzene was chosen as the test reaction. Approximately 6-7 mg of impregnated catalyst was added to 20 ml of methanol with 1 ml of styrene. The starting reaction pressure is approximately 308 PSI, a stir rate of 500 rpm done at room temperature. Time pressure, temperature and their respective changes were recorded until the reaction was completed signified by a constant pressure reading. It was

observed that a decrease in pressure occurs proportional to the amount catalyst present. This decrease in pressure is attributed to the consumption of hydrogen gas in the reaction driving the conversion of styrene into ethyl benzene. A constant pressure signifies that the reaction has come to completion. Comparison of the impregnated catalyst and control are displayed in figure 6-13.

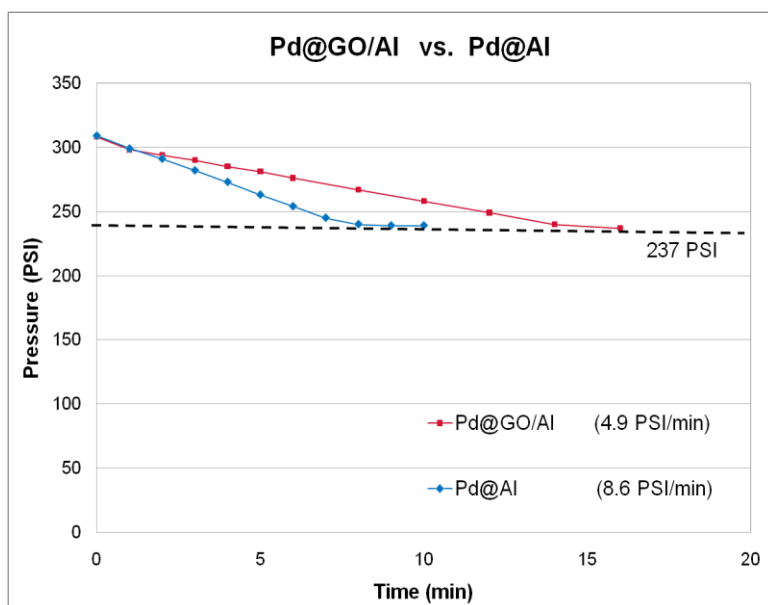
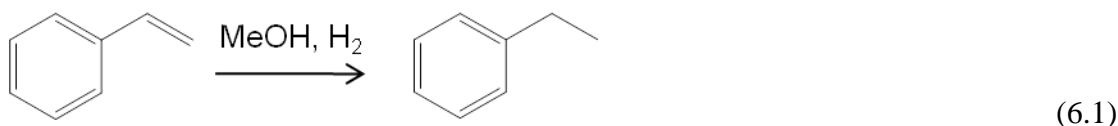


Figure 6-13: Hydrogenation reaction of the conversion of styrene to ethyl benzene with the impregnated GO/Al and Al (control) respectively.

6.1.5 Conclusions

Successful composites of graphene oxide and alumina were synthesized, characterized and impregnated with Pd nanoparticles. The new hybrid composite displays a pressure drop of 8.6 PSI/min. Although currently this value is within the same

magnitude of order of the control, it still suffers from an increase in reaction time compared to its alumina analogue. Further studies will need to be done to elucidate the nanoparticle distribution, via chemisorption, and the turn over frequency (TOF) of the catalyst. It is suspected that the latter will be the prominent factor in showing the superiority of the hybrid catalyst, indicative of the stability seen between graphene and various nanoparticles in the literature.

6.2 Part II: Applications in UltraCapacitors

Over the years there has been a gradual shift away from fossil fuels as a dependable energy source due to its rise in cost and diminishing availability. This has led to the rise of alternative energies that are clean, renewable and cost effective. So far the general public has been made aware of the prospects of wind and solar. However, these technologies are beholden to the development of large infrastructures, and there exists a need to create renewable energy storage devices which can be implemented in a versatile range of applications capable of delivering and storing large amounts of energy for a sustained duration of time. Among the most studied and used technology in everyday devices are Li ion batteries (LIB). LIBs were first introduced by Sony in 1990[398], and since then a great deal of research has gone into improving their performance. However, LIBs still suffer from the disadvantage of low power delivery. In order to circumvent the issues that plague LIBs, the field of ultracapacitors has emerged over the past decade, as a viable and competitive technology and is poised to supplant LIBs as the leading technology. Ultracapacitors are advantageous over their LIB counterparts in several regards; they have a much shorter charging time (a few minutes or seconds), longer life-cycle (10000 or more compared to only 500-2000 for LIB), larger power densities (10 to

100 times larger than LIB) and a wider working temperature range[398]. Comparisons between LIB and ultracapacitors are made in 6-15

Ultracapacitors are however not without their limitations. The most prominent is the fact that their energy densities lag behind values associated with LIB. Researchers have shown that it is theoretically possible to improve the energy density by using carbon based materials. The list of carbon candidates investigated to increase the energy density have included activated[398], templated, and carbide derived carbons[398], carbon fabrics[399], single walled carbon nanotubes (SWNT)[400], carbon onions[401], and carbon nanohorns[402]. Although these materials offer a high surface area, a requirement for ultracapacitors, they are limited by a narrow pore size. This undermines the performance by inhibiting access of the electrolyte to the entire surface area. Therefore, in order to reach the maximum theoretical capacitance, defined by equation 6.1, the material in question must possess a large internal surface area which can be accessible by the electrolyte.

$$C = \frac{A}{4\pi d} \quad (\text{Eq. 6.1})$$

$$E = \frac{1}{2}CV^2 \quad (\text{Eq. 6.2})$$

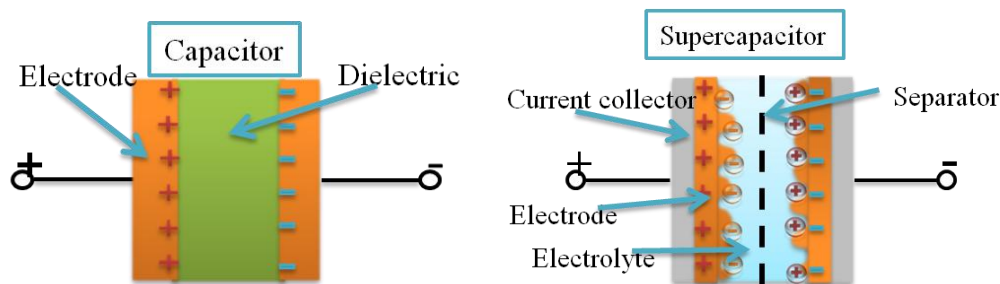
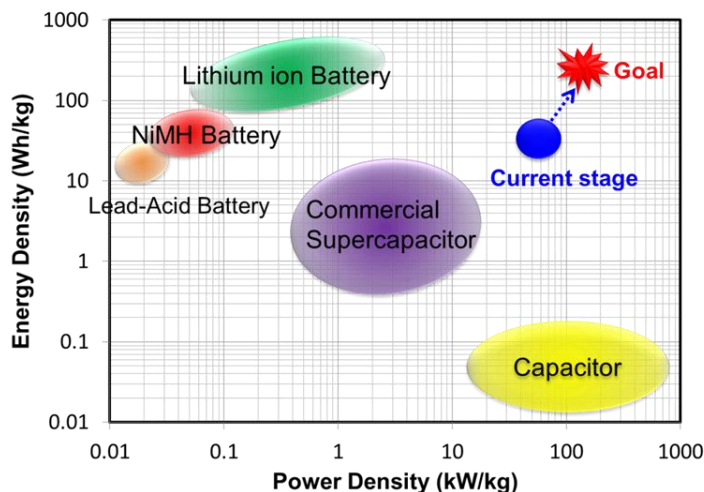


Figure 6-14: (Left) Schematic of a traditional capacitor separated by a dielectric layer. (Right) Schematic of an ultracapacitor and its reliance on the electrical double layer at the nanoscale.



	Ultra-capacitor	Battery
Life time	2000~500000	500~2000
Charging time	1~60s	1~8h
Temperature	-40~125°C	-20~60°C
Energy Density (Wh/kg)	1~100	20~300

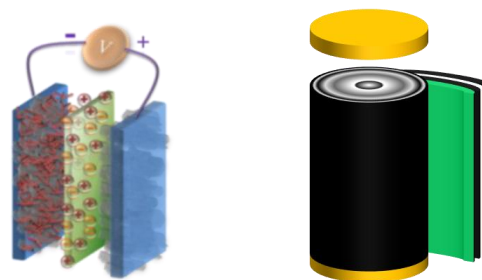


Figure 6-15: Comparison between ultracapacitors and batteries. Schematic ultracapacitor set up and (Right) multiple ultracapacitors rolled into a single device [403].

To accomplish this a promising routes is proposed. An alternative to the previously mentioned list is the 2-D carbon graphene. Graphene possesses attributes of both abundant surface area and a high conductivity making it ideal for ultracapacitors. Theoretical calculations show that an ideal graphene sheet with a surface area of 2630 m²/g yields a specific capacitance of 550F/g. Thus far, ultracapacitors made with just graphene have produced capacitances within the range of 30-210 (F/g)[404]. When graphene is combined with alumina, the latter acts as a spacer thereby allowing for a greater access by the electrolyte to both the sheets of graphene and the alumina[405]. The capacitance of both alumina and graphene can be further improved by functionalization

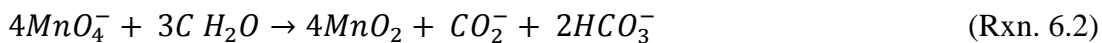
with metal oxide and metal hydroxide nanoparticles. Most notably Wang et al. deposited Nickel (II) hydroxide nano-crystals onto graphene nano sheets and has thus set the benchmark with a value of 1335 (F/g)[8].

Herein the fabrication composites of GO/alumina for ultracapacitor applications is partitioned into two parts. First, as previously described, composites of GO/alumina are produced and functionalized with MnO_2 nanoparticles. These nanoparticles are pseudocapacitance in nature and have been shown to dramatically increase the overall capacitance of devices required to compete with LIB. Second the cyclic-voltammetry tests are performed to measure the electrical properties and hence potential to be used as a ultracapacitor.

6.2.1 *Functionalization of GO with pseudocapacitance nanoparticles*

Graphene and carbon nanotubes provides an excellent platform for the growth of zero and one dimensional nanostructures. Possible candidates for nanoparticle growth includes compounds such as ZnO , MnO_2 , RuO_2 and TiO_2 [406]. These particles exhibit pseudocapacitance behavior through fast and reversible redox reactions at the surface of the nanoparticle. Among the available candidates, MnO_2 poses to be the most promising due to its low cost, abundance, high specific capacitance, and environmentally benign characteristics[407]. Since the contributing capacitance from the MnO_2 nanoparticles will depend on its size and shape, synthesis conditions will have to be taken into account. To date various morphologies of MnO_2 have been produced in the literature and they include plate-like[408, 409], nanorods[410, 411], rod-shaped[412, 413], nanowires[414], cubes[414], hollow spheres[415], spherical particles[416, 417], nanoflowers[418] and urchin-like particles[415, 419]. Synthesis conditions utilizing a dip coating method will

be preferred and the effect of the loading concentration on the SCF is explored. Formation of the nanoparticles proceeds by the following reaction:



6.2.2 *Electrical measurements*

In order to show the versatility of the graphene oxide alumina composite, cyclic voltammetry measurements were performed to see its ability to act as a capacitor. To do so, approximately 1 mg of graphene oxide/alumina calcined under argon was weighed. This was combined with a 3:1 mixture of water:isopropanol solution for a total of 20 μl for every 0.1 mg of the GO/Al support. Then Nafion was added at a ratio of 0.1 mg of support to 2.1 μl Nafion. The mixture was then bath sonicated for 10 minutes several times in order to break up the particles and expose the greatest amount of surface area. Between 1-3 μl was placed at the end of an electrode and allowed to dry. After drying, the electrode was placed into a 1 M solution of H_2SO_4 and current vs. voltage measurements were taken between 0.3 to 1 V. Cyclic voltammetry curves are measured at scan rates of 5, 10, 50, 100, 200 mV s^{-1} and 1 V s^{-1} . Maintaining the scan rates within this window of voltage is critical in order to prevent the electrolysis of water. Capacitance is measured by dividing by the scan rate of 1 V s^{-1} at the highest point in the plateau. It should be noted that ideal CV curves display rectangular geometries which indicate excellent charge propagation[403]. Any distortion of these curves towards narrower, more oblique loops indicates a higher resistance. Curves are identified for any pseudocapacitance behavior resulting from Faradaic reactions. The source of which can

be attributed to redox reactions happening at the surface of the nanoparticles functionalized onto GO, a schematic of which is seen in figure 6-18. Capacitance results of the GO/Al composite are displayed in figure 6-19, 6-20, and 6-21.

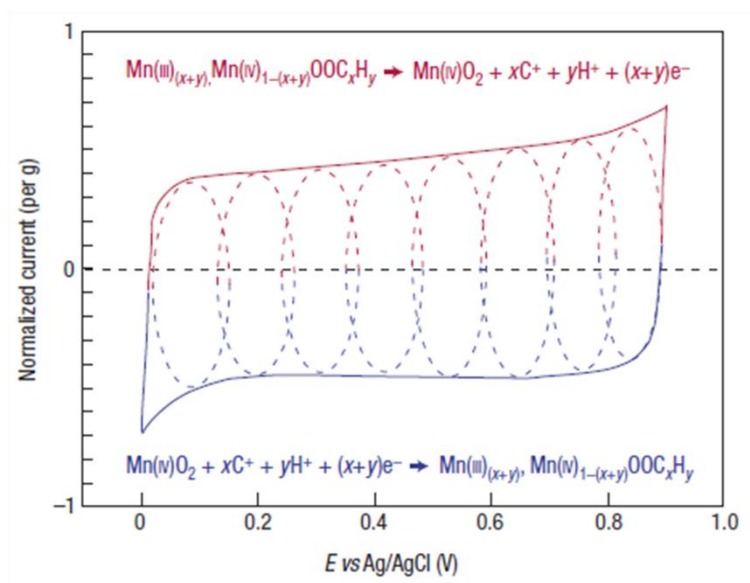


Figure 6-16: Schematic of cyclic voltammetry for a MnO_2 electrode cell in mild aqueous electrolyte (0.1 M K_2SO_4) shows the successive multiple surface redox reactions leading to the pseudo-capacitive charge storage mechanism. The red (upper) part is related to the oxidation from Mn(III) to Mn(IV) and the blue (lower) part refers to the reduction from Mn(IV) to Mn(III) [398].

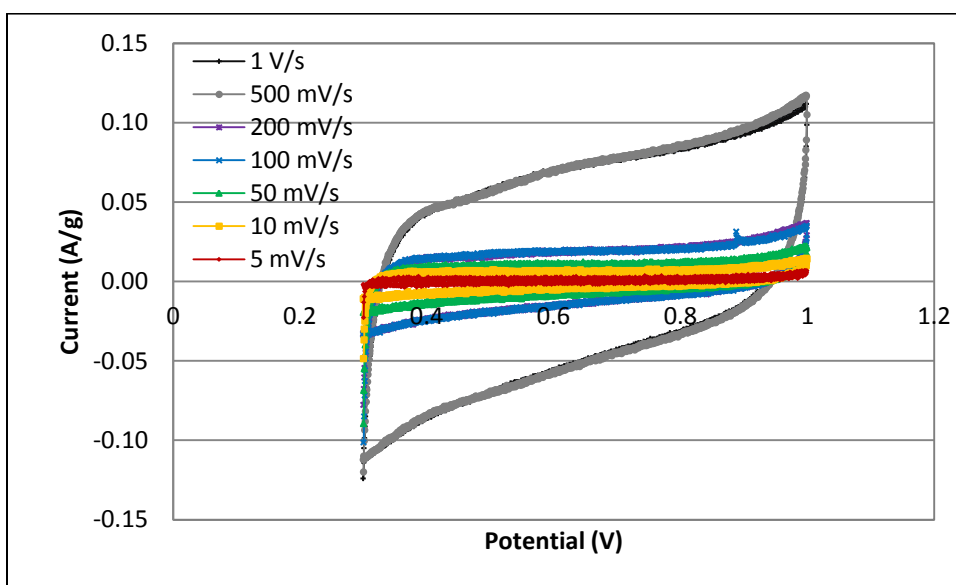


Figure 6-17: Cyclic-voltammetry measurements of GO/Al composite.

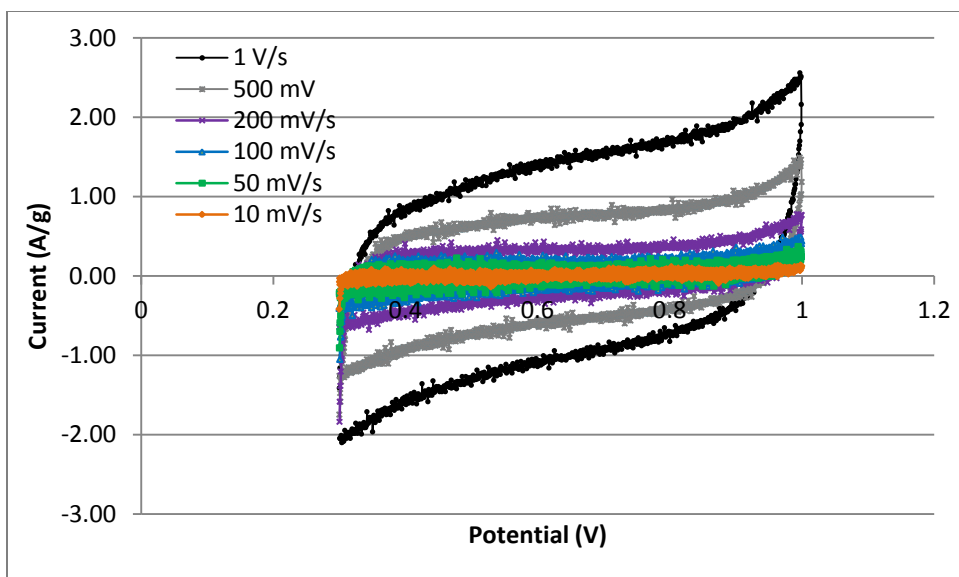


Figure 6-18: Cyclic-voltammetry measurements of GO/Al composite impregnated with KMnO_4 for 2 hours.

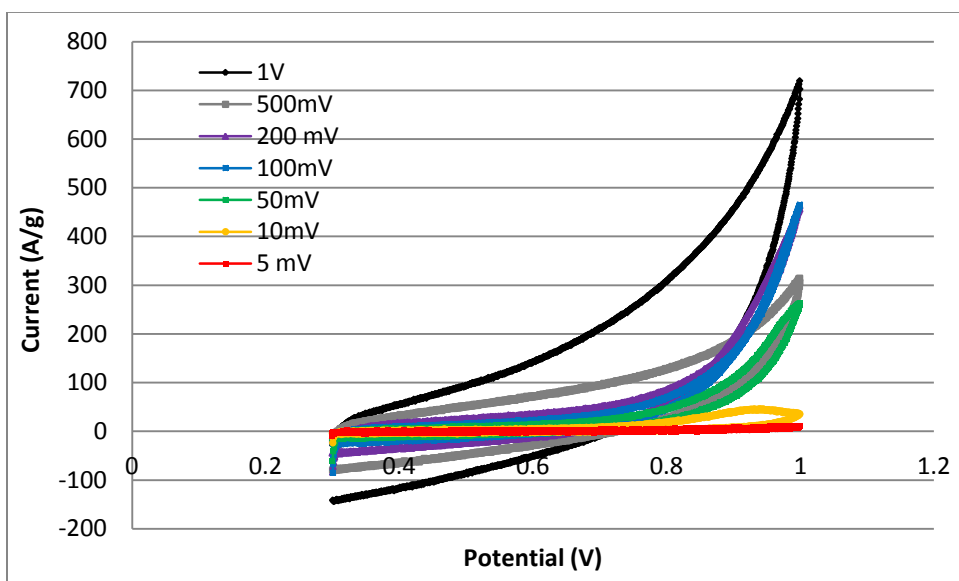


Figure 6-19: Cyclic-voltammetry measurements of GO/Al composite impregnated with KMnO_4 for 2 days.

In order to increase the capacitance of the GO/Al samples, a 0.5 mM solution of K_2MnO_4 was prepared and used to impregnate the GO/Al powder. To do so, 25 mg of the GO/Al was degassed at 130°C overnight and added to the impregnating solution. Impregnation times occurred for 2 h and 2 days. It can be seen that with increased impregnation time

there is a corresponding increase in the height and depth of cyclic voltammetry hysteresis loop which corresponds to a greater capacitance for the same voltage range. However with greater impregnation time for the 2 day sample there is change in the shape of the hysteresis loop from a square like hysteresis to one with more oblique characteristic. This change in shape indicates that additional reactions may be occurring that affects the reversibility of the voltage loop. This in turn affects the cyclicability of the material to act as a ultracapacitor, with an increase number of charging and discharging cycles leading to decreased performance. The capacitance for each sample taken as the highest point in the plateau of the curve and normalized to its mass. To obtain the specific capacitance, this value was divided by a scanning rate of 1 V/s. For the sample impregnated for 2 days, due to the oblique nature of the curve the capacitance was averaged out and divided by the same scanning rate. Results are displayed in Table13.

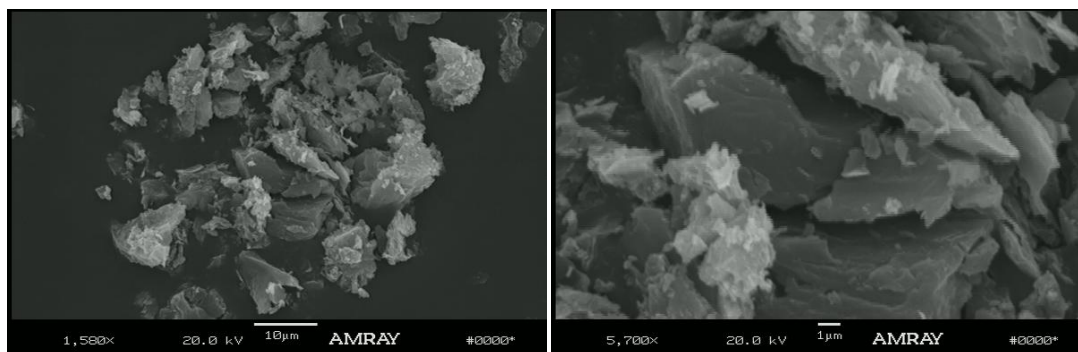


Figure 6-20: Scanning electron microscopy of impregnated GO/Al with KMnO_4 for 2 hours.

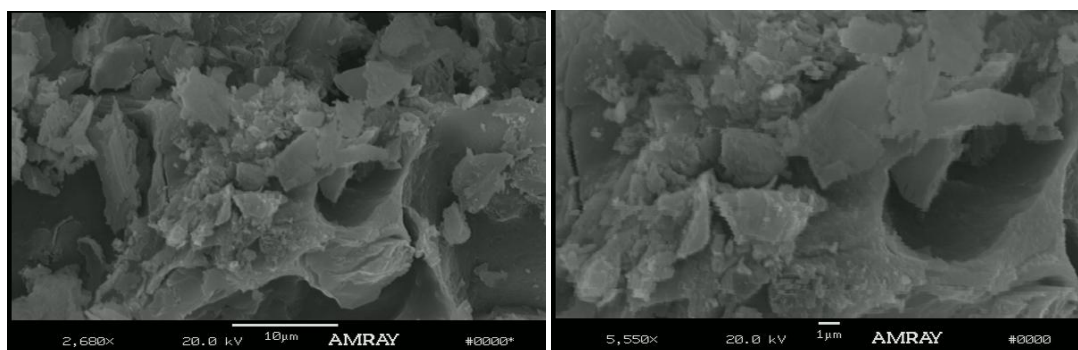


Figure 6-21: Scanning electron microscopy of impregnated GO/Al with KMnO_4 for 24 hours.

Sample	Specific Capacitance (F/g)
GO/Al	0.11
2 h	1.84
2 days	126

Table 12: Specific capacitance for GO/Al impregnated with KMnO_4 .

6.3 Conclusion and Future Work

Hybrid composites of graphene oxide and alumina were easily fabricated that were demonstrated to be versatile in two areas. The first was for the use in catalysis where these hybrid composites were capable of anchoring nanoparticles of Pd highlighted by the hydrogenation reaction of styrene. It was also demonstrated that the hybrid composite had a moderate level of capacitance, or ability to store charge. The capacitance could easily be increased by the impregnation of the composite in a solution of KMnO_4 in order to synthesize MnO_2 nanoparticles, which act as pseudocapacitors, onto the surface of the composite particles. As a result this hybrid impregnated material shows great promise in the field of ultracapacitors. Lastly it was shown that the addition of the graphene oxide did not affect the pore structure of the alumina thereby opening the possibility to pre-tailor the pore size of the hybrid composite material. This critical aspect is important not just for catalysis where mass transport is concerned, but also in the field of ultracapacitors where the pore size needs to be optimized relative to the chosen

electrolyte. Future work will focus on determining the particle size distribution through chemisorption.

Chapter 7 Conclusions and Future Perspectives

In the preceding chapters it was shown that the ability to incorporate nano carbon into porous materials greatly enhances their designed purpose. For neural engineering, the ability to make malleable fibers consisting of CNT or graphene showed promising results to act as neural recording devices. Furthermore, it was demonstrated that CNT could be forcibly impregnated into electrospun polymeric scaffolds by an external pressure. These scaffolds showed that they were not only capable of acting as a support for the differentiation of stem cells but showed indications that they could enhance the differentiation process. This was further improved by the fabrication of a device capable of applying an electrical stimuli. This too showed great promise, as what appears to be a greater amount of cell density and differentiation occurring on the impregnated scaffolds where an electrical stimuli had been applied.

It was later shown that these nano carbon materials could be combined with mesoporous materials, namely alumina. This metal oxide has great significance in the field of catalysis and the ability to tailor its pore size distribution is of great concern. The fact that composites of graphene and alumina does not alter the pore size of the latter is also a significant factor as it reduces the complexity required for catalysis design. As such, the resulting integration of graphene with alumina proved to be very versatile in the areas of catalysis and ultracapacitors, two fields where interest is heavily reliant on optimizing the pore structure.

Further work is always on the horizon in order achieve a conclusive ending. For fibers fabricated for neural tissue engineering, the fact that they induce a minor glial response is not enough. Fibers will need to be made that approach the cellular level, in

other words 10 μm . In addition these fibers will need to mimic the properties of components of any electrode to be placed in the brain. This calls for fibers that can act as transistors and resistors which in turn can send a wireless signal. Materials do so is so far lacking, and progress will need to be made in this area for any conclusive improvement. As for the scaffolds incorporating CNT, future work will need to center around maximizing the differentiation in vitro prior to any in vivo studies. This calls for an optimizing of the stimulation process, as cells at different stages of growth may respond differently to varying degrees of stimuli. For the hybrid structures discussed in chapter 6, future progress will rely on showing the turn over frequency (TOF) of these materials and that they do indeed stabilize the nanoparticles that might otherwise sinter and aggregate over the lifetime of a catalyst.

Preparations are in order for a manuscript summarizing the results discussed in this chapter. Furthermore, a provisional patent has been filed relating to graphene oxide/alumina composite materials for catalysis.

REFERENCES

1. Iijima, S. and T. Ichihashi, *SINGLE-SHELL CARBON NANOTUBES OF 1-NM DIAMETER*. Nature, 1993. **363**(6430): p. 603-605.
2. Neimark, A.V., et al., *Hierarchical pore structure and wetting properties of single-wall carbon nanotube fibers*. Nano Letters, 2003. **3**(3): p. 419-423.
3. Vigolo, B., et al., *Macroscopic fibers and ribbons of oriented carbon nanotubes*. Science, 2000. **290**(5495): p. 1331-1334.
4. Dalton, A.B., et al., *Super-tough carbon-nanotube fibres - These extraordinary composite fibres can be woven into electronic textiles*. Nature, 2003. **423**(6941): p. 703-703.
5. Ni, Y.C., et al., *Chemically functionalized water soluble single-walled carbon nanotubes modulate neurite outgrowth*. Journal of Nanoscience and Nanotechnology, 2005. **5**(10): p. 1707-1712.
6. Jan, E. and N.A. Kotov, *Successful differentiation of mouse neural stem cells on layer-by-layer assembled single-walled carbon nanotube composite*. Nano Letters, 2007. **7**(5): p. 1123-1128.
7. Dubin, R.A., et al., *Carbon nanotube fibers are compatible with mammalian cells and neurons*. Ieee Transactions on Nanobioscience, 2008. **7**(1): p. 11-14.
8. Sridharan, I., T. Kim, and R. Wang, *Adapting collagen/CNT matrix in directing hESC differentiation*. Biochemical and Biophysical Research Communications, 2009. **381**(4): p. 508-512.
9. Novoselov, K.S., et al., *Electric field effect in atomically thin carbon films*. Science, 2004. **306**(5696): p. 666-669.
10. Avouris, P., Z.H. Chen, and V. Perebeinos, *Carbon-based electronics*. Nature Nanotechnology, 2007. **2**(10): p. 605-615.
11. Brunauer S., Emmett P.H., and Teller E., *Adsorption of gases in multi-molecular layers*. Journal of American Chemical Society, 1938. **60**: p. 309-319.
12. Barrett, E.P., L.G. Joyner, and P.P. Halenda, *The Determination of Pore Volume and Area Distributions in Porous Substances. I. Computations from Nitrogen Isotherms*. Journal of the American Chemical Society, 1951. **73**(1): p. 373-380.
13. Evans, R., U.M.B. Marconi, and P. Tarazona, *Fluids in narrow pores: Adsorption, capillary condensation, and critical points*. The Journal of Chemical Physics, 1986. **84**(4): p. 2376-2399.
14. Evans, R., U.M.B. Marconi, and P. Tarazona, *Capillary Condensation and Adsorption in Cylindrical and Slit-Like Pores*. Journal of the Chemical Society-Faraday Transactions II, 1986. **82**: p. 1763-1787.
15. Evans, R. and P. Tarazona, *Theory of Condensation in Narrow Capillaries*. Physical Review Letters, 1984. **52**(7): p. 557-560.
16. Seaton, N.A., J. Walton, and N. Quirke, *A new analysis method for the determination of the pore-size distribution of porous carbons from nitrogen adsorption measurements*. Carbon, 1989. **27**(6): p. 853-861.
17. Cohan, L.H., *Sorption Hysteresis and the Vapor Pressure of Concave Surfaces*. Journal of the American Chemical Society, 1938. **60**(2): p. 433-435.
18. Lastoskie, C., K.E. Gubbins, and N. Quirke, *Pore-Size Distribution Analysis of Microporous Carbons - a Density-Functional Theory Approach*. Journal of Physical Chemistry, 1993. **97**(18): p. 4786-4796.
19. Olivier, J.P., W.B. Conklin, and M.v. Szombathely, *Determination of Pore Size Distribution from Density Functional Theory: A Comparison of Nitrogen and Argon Results*, in *Studies in Surface Science and Catalysis*, J. Rouquerol, et al., Editors. 1994, Elsevier. p. 81-89.
20. Ravikovitch, P.I., et al., *Unified approach to pore size characterization of microporous carbonaceous materials from N₂, Ar, and CO₂ adsorption isotherms*. Langmuir, 2000. **16**(5): p. 2311-2320.
21. Tarazona, P., *Free-Energy Density Functional for Hard-Spheres*. Physical Review A, 1985. **31**(4): p. 2672-2679.
22. Beck, J.S., et al., *A new family of mesoporous molecular-sieves prepared with liquid-crystal templates*. Journal of the American Chemical Society, 1992. **114**(27): p. 10834-10843.
23. Kresge, C.T., et al., *Ordered mesoporous molecular-sieves synthesized by a liquid-crystal template mechanism*. Nature, 1992. **359**(6397): p. 710-712.

24. Yanagisawa, T., et al., *THE PREPARATION OF ALKYLTRIMETHYLAMMONIUM-KANEMITE COMPLEXES AND THEIR CONVERSION TO MICROPOROUS MATERIALS*. Bulletin of the Chemical Society of Japan, 1990. **63**(4): p. 988-992.
25. Ravikovitch, P.I., et al., *Capillary hysteresis in nanopores: Theoretical and experimental studies of nitrogen adsorption on MCM-41*. Langmuir, 1995. **11**(12): p. 4765-4772.
26. ISO-15901-3, *Pore size distribution and porosity of solid materials by mercury porosimetry and gas adsorption*, in *Analysis of micropores by gas adsorption*. 2007.
27. Roland, R., *Fundamental measure theory for hard-sphere mixtures: a review*. Journal of Physics: Condensed Matter, 2010. **22**(6): p. 063102.
28. Rosenfeld, Y., *Free-Energy Model for the Inhomogeneous Hard-Sphere Fluid Mixture and Density-Functional Theory of Freezing*. Physical Review Letters, 1989. **63**(9): p. 980-983.
29. Rosenfeld, Y., et al., *Fundamental-measure free-energy density functional for hard spheres: Dimensional crossover and freezing*. Physical Review E, 1997. **55**(4): p. 4245.
30. Neimark, A.V., et al., *Quenched solid density functional theory and pore size analysis of micro-mesoporous carbons*. Carbon, 2009. **47**(7): p. 1617-1628.
31. Weeks, J.D., D. Chandler, and H.C. Andersen, *Role of Repulsive Forces in Determining Equilibrium Structure of Simple Liquids*. Journal of Chemical Physics, 1971. **54**(12): p. 5237-&.
32. Steele, W.A., *The Interactions of Gases with Solid Surfaces*. 1974, Oxford: Pergamon.
33. Ravikovitch, P.I. and A.V. Neimark, *Density functional theory of adsorption in spherical cavities and pore size characterization of templated nanoporous silicas with cubic and three-dimensional hexagonal structures*. Langmuir, 2002. **18**(5): p. 1550-1560.
34. Neimark, A.V. and P.I. Ravikovitch, *Capillary condensation in MMS and pore structure characterization*. Microporous and Mesoporous Materials, 2001. **44**: p. 697-707.
35. Ravikovitch, P.I. and A.V. Neimark, *Density Functional Theory Model of Adsorption Deformation*. Langmuir, 2006. **22**(26): p. 10864-10868.
36. Neimark, A.V., et al., *Pore size analysis of MCM-41 type adsorbents by means of nitrogen and argon adsorption*. Journal of Colloid and Interface Science, 1998. **207**(1): p. 159-169.
37. Ravikovitch, P.I. and A.V. Neimark, *Characterization of micro- and mesoporosity in SBA-15 materials from adsorption data by the NLDFT method*. Journal of Physical Chemistry B, 2001. **105**(29): p. 6817-6823.
38. Van Der Voort, P., et al., *A new templated ordered structure with combined micro- and mesopores and internal silica nanocapsules*. Journal of Physical Chemistry B, 2002. **106**(23): p. 5873-5877.
39. Van Der Voort, P., et al., *Plugged hexagonal templated silica: a unique micro- and mesoporous composite material with internal silica nanocapsules*. Chemical Communications, 2002(9): p. 1010-1011.
40. Kruk, M., M. Jaroniec, and A. Sayari, *Adsorption Study of Surface and Structural Properties of MCM-41 Materials of Different Pore Sizes*. The Journal of Physical Chemistry B, 1997. **101**(4): p. 583-589.
41. Neimark, A.V., P.I. Ravikovitch, and A. Vishnyakov, *Bridging scales from molecular simulations to classical thermodynamics: density functional theory of capillary condensation in nanopores*. Journal of Physics-Condensed Matter, 2003. **15**(3): p. 347-365.
42. Carrott, M., et al., *Adsorption of nitrogen, neopentane, n-hexane, benzene and methanol for the evaluation of pore sizes in silica grades of MCM-41*. Microporous and Mesoporous Materials, 2001. **47**(2-3): p. 323-337.
43. Lukens, W.W., et al., *Evaluating Pore Sizes in Mesoporous Materials: A Simplified Standard Adsorption Method and a Simplified Broekhoff-de Boer Method*. Langmuir, 1999. **15**(16): p. 5403-5409.
44. Yue, Y.-H., et al., *Direct incorporation of Al in SBA mesoporous materials: characterization, stability and catalytic activity*. Stud. Surf. Sci. Catal. , 2000. **129**: p. 209-218.
45. Sayari, A., et al., *Characterization of Large-Pore MCM-41 Molecular Sieves Obtained via Hydrothermal Restructuring*. Chemistry of Materials, 1997. **9**(11): p. 2499-2506.
46. Ravikovitch, P.I. and A.V. Neimark, *Experimental confirmation of different mechanisms of evaporation from ink-bottle type pores: Equilibrium, pore blocking, and cavitation*. Langmuir, 2002. **18**(25): p. 9830-9837.
47. Thommes, M., et al., *Adsorption hysteresis of nitrogen and argon in pore networks and characterization of novel micro- and mesoporous silicas*. Langmuir, 2006. **22**(2): p. 756-764.

48. Olivier, J.P., *Improving the models used for calculating the size distribution of micropore volume of activated carbons from adsorption data*. Carbon, 1998. **36**(10): p. 1469-1472.
49. Olivier, J.P., *Modeling Physical Adsorption on Porous and Nonporous Solids Using Density Functional Theory*. J. Porous Mater., 1995. **2**: p. 217.
50. Nguyen, T.X. and S.K. Bhatia, *Characterization of Pore Wall Heterogeneity in Nanoporous Carbons Using Adsorption: the Slit Pore Model Revisited*. The Journal of Physical Chemistry B, 2004. **108**(37): p. 14032-14042.
51. Nguyen, T.X. and S.K. Bhatia, *Probing the Pore Wall Structure of Nanoporous Carbons Using Adsorption*. Langmuir, 2004. **20**(9): p. 3532-3535.
52. Ustinov, E.A. and D.D. Do, *Modeling of adsorption in finite cylindrical pores by means of density functional theory*. Adsorption-Journal of the International Adsorption Society, 2005. **11**(5-6): p. 455-477.
53. Ustinov, E.A., D.D. Do, and M. Jaroniec, *Application of density functional theory to equilibrium adsorption of argon and nitrogen on amorphous silica surface*. Applied Surface Science, 2005. **252**(3): p. 548-561.
54. Ustinov, E.A., D.D. Do, and M. Jaroniec, *Adsorption of argon and nitrogen in cylindrical pores of MCM-41 materials: application of density functional theory*. Applied Surface Science, 2005. **252**(4): p. 1013-1028.
55. Ustinov, E.A., D.D. Do, and V.B. Fenelonov, *Pore size distribution analysis of activated carbons: Application of density functional theory using nongraphitized carbon black as a reference system*. Carbon, 2006. **44**(4): p. 653-663.
56. Jagiello, J. and J.P. Olivier, *A Simple Two-Dimensional NLDFT Model of Gas Adsorption in Finite Carbon Pores. Application to Pore Structure Analysis*. The Journal of Physical Chemistry C, 2009. **113**(45): p. 19382-19385.
57. Ravikovitch, P.I. and A.V. Neimark, *Density functional theory model of adsorption on amorphous and microporous silica materials*. Langmuir, 2006. **22**(26): p. 11171-11179.
58. Ravikovitch, P.I. and A.V. Neimark, *Density Functional Theory Model of Adsorption on Amorphous and Microporous Solids.*, in *Characterisation of Porous Solids VII*, P.L. Llewellyn, et al., Editors. 2006, Elsevier. p. 9-16.
59. Gor, G.Y., et al., *Quenched solid density functional theory method for characterization of mesoporous carbons by nitrogen adsorption*. Carbon, 2012. **50**(4): p. 1583-1590.
60. Zickler, G.A., et al., *Physisorbed films in periodic mesoporous silica studied by in situ synchrotron small-angle diffraction*. Physical Review B, 2006. **73**(18): p. 10.
61. Muroyama, N., et al., *An Analytical Approach to Determine the Pore Shape and Size of MCM-41 Materials from X-ray Diffraction Data*. The Journal of Physical Chemistry B, 2006. **110**(22): p. 10630-10635.
62. Miyasaka, K., A.V. Neimark, and O. Terasaki, *Density Functional Theory of in Situ Synchrotron Powder X-ray Diffraction on Mesoporous Crystals: Argon Adsorption on MCM-41*. Journal of Physical Chemistry C, 2009. **113**(3): p. 791-794.
63. Garofalini, S.H., *A molecular dynamics simulation of the vitreous silica surface*. The Journal of Chemical Physics, 1983. **78**(4): p. 2069-2072.
64. MacElroy, J.M.D. and K. Raghavan, *Adsorption and diffusion of a Lennard-Jones vapor in microporous silica*. The Journal of Chemical Physics, 1990. **93**(3): p. 2068-2079.
65. Roder, A., W. Kob, and K. Binder, *Structure and dynamics of amorphous silica surfaces*. The Journal of Chemical Physics, 2001. **114**(17): p. 7602-7614.
66. Hofmann, T., et al., *Small-angle x-ray diffraction of Kr in mesoporous silica: Effects of microporosity and surface roughness*. Physical Review B, 2005. **72**(6): p. 064122.
67. Ravikovitch, P.I. 1998, Yale University.
68. Lawson, C.L. and R.J. Hanson, *Solving least squares problems*. 1995, Philadelphia: SIAM.
69. Jagiello, J., *Stable Numerical Solution of the Adsorption Integral Equation Using Splines*. Langmuir, 1994. **10**(8): p. 2778-2785.
70. Cychosz, K.A., et al., *Characterization of the Pore Structure of Three-Dimensionally Ordered Mesoporous Carbons Using High Resolution Gas Sorption*. Langmuir, 2012. **submitted**: p. la-2012-02362h.R1.

71. Miyasaka, K., et al., *A Stand-Alone Mesoporous Crystal Structure Model from in situ X-ray Diffraction: Nitrogen Adsorption on 3 D Cagelike Mesoporous Silica SBA-16*. Chemistry – A European Journal, 2012: p. n/a-n/a.
72. Sircar, S., *Gas separation and storage by activated carbons*, in *Adsorption by carbons*, J.M.D.T. Eduardo J. Bottani, Editor. 2008, Elsevier: Oxford.
73. Nabais, J.M.V., et al., *Thermal conversion of a novel biomass agricultural residue (vine shoots) into activated carbon using activation with CO(2)*. Journal of Analytical and Applied Pyrolysis, 2010. **87**(1): p. 8-13.
74. Rios, R.B., et al., *Adsorption of methane in activated carbons obtained from coconut shells using H(3)PO(4) chemical activation*. Adsorption-Journal of the International Adsorption Society, 2009. **15**(3): p. 271-277.
75. Zhang, T.Y., W.P. Walawender, and L.T. Fan, *Increasing the microporosities of activated carbons*. Separation and Purification Technology, 2005. **44**(3): p. 247-249.
76. Almarri, M., X.L. Ma, and C.S. Song, *Selective Adsorption for Removal of Nitrogen Compounds from Liquid Hydrocarbon Streams over Carbon- and Alumina-Based Adsorbents*. Industrial & Engineering Chemistry Research, 2009. **48**(2): p. 951-960.
77. Rios, R., et al., *Liquid phase removal of propanethiol by activated carbon: Effect of porosity and functionality*. Colloids and Surfaces a-Physicochemical and Engineering Aspects, 2007. **300**(1-2): p. 180-190.
78. Burriss, J., et al., *Hydrogen storage in engineered carbon nanospaces*. Nanotechnology, 2009. **20**(20): p. 10.
79. Linares-Solano, A., Cazorla-Amoros, D., *Adsorption on activated carbon fibers*, in *Adsorption by carbons*, J.M.D.T. Eduardo J. Bottani, Editor. 2008, Elsevier: Oxford.
80. Donnet, J.B., Bansal, R.Ch., *Carbon Fibers*. 1990: Marcel Dekker.
81. Lozano-Castello, D., Cazorla-Amoros, D., Linares-Solano, A., *Powered activated carbons and activated carbon fibers for methane storage: a comparative study*. Energy Fuels, 2002. **16**: p. 1321-8.
82. Miyamoto, J., K. Kanoh, and K. Kaneko, *The addition of mesoporosity to activated carbon fibers by a simple reactivation process*. Carbon, 2005. **43**(4): p. 855-857.
83. Chen, Y.H., et al., *Rayon-based activated carbon fibers treated with both alkali metal salt and Lewis acid*. Microporous and Mesoporous Materials, 2008. **109**(1-3): p. 138-146.
84. Zhang, S.J., et al., *Structure evolution and optimization in the fabrication of PVA-based activated carbon fibers*. Journal of Colloid and Interface Science, 2008. **321**(1): p. 96-102.
85. Shiratori, N., et al., *Pore Structure Analysis of Activated Carbon Fiber by Microdomain-Based Model*. Langmuir, 2009. **25**(13): p. 7631-7637.
86. Mushrif, S.H., A.D. Rey, and H. Tekinalp, *Effect of metal salt on the pore structure evolution of pitch-based activated carbon microfibers*. Industrial & Engineering Chemistry Research, 2008. **47**(11): p. 3883-3890.
87. Wu, X., et al., *The effect of processing conditions on microstructure of Pd-containing activated carbon fibers*. Carbon, 2008. **46**(1): p. 54-61.
88. Donnaperna, L., et al., *Comparison of adsorption of Remazol Black B and Acidol Red on microporous activated carbon felt*. Journal of Colloid and Interface Science, 2009. **339**(2): p. 275-284.
89. Sing, K.S.W., *Overview of physical adsorption by carbons*, in *Adsorption by Carbons*, J.M.D.T. Eduardo J. Bottani, Editor. 2008, Elsevier: Oxford.
90. Charretier, F., et al., *Fe/N/C non-precious catalysts for PEM fuel cells: Influence of the structural parameters of pristine commercial carbon blacks on their activity for oxygen reduction*. Electrochimica Acta, 2008. **53**(6): p. 2925-2938.
91. Jaouen, F., et al., *Heat-treated Fe/N/C catalysts for O-2 electroreduction: Are active sites hosted in micropores?* Journal of Physical Chemistry B, 2006. **110**(11): p. 5553-5558.
92. Braida, W.J., et al., *Sorption hysteresis of benzene in charcoal particles*. Environmental Science & Technology, 2003. **37**(2): p. 409-417.
93. Richou, M., et al., *Microporosity of carbon deposits collected in the Tore Supra tokamak probed by nitrogen and carbon dioxide adsorption*. Carbon, 2009. **47**(1): p. 109-116.
94. Schneider, R., et al., *Dynamic Monte-Carlo modeling of hydrogen isotope reactive-diffusive transport in porous graphite*. Journal of Nuclear Materials, 2007. **367**: p. 1238-1242.

95. Calbi, M.M., et al., *Colloquium: Condensed phases of gases inside nanotube bundles*. Reviews of Modern Physics, 2001. **73**(4): p. 857-865.
96. Hallock, R.B. and Y.H. Kahng, *Adsorption of helium and other gases to carbon nanotubes and nanotube bundles*. Journal of Low Temperature Physics, 2004. **134**(1-2): p. 21-30.
97. Jiang, J.W. and S.I. Sandler, *Nitrogen adsorption on carbon nanotube bundles: Role of the external surface*. Physical Review B, 2003. **68**(24): p. 9.
98. Li, F.X., et al., *Characterization of single-wall carbon nanotubes by N-2 adsorption*. Carbon, 2004. **42**(12-13): p. 2375-2383.
99. Byl, O., J. Liu, and J.T. Yates, *Etching of carbon nanotubes by ozone - A surface area study*. Langmuir, 2005. **21**(9): p. 4200-4204.
100. Yang, C.M., et al., *Effect of purification on pore structure of HiPco single-walled carbon nanotube aggregates*. Nano Letters, 2002. **2**(4): p. 385-388.
101. Anson, A., et al., *Porosity, surface area, surface energy, and hydrogen adsorption in nanostructured carbons*. Journal of Physical Chemistry B, 2004. **108**(40): p. 15820-15826.
102. Byl, O., J. Liu, and J.T. Yates, *Characterization of single wall carbon nanotubes by nonane preadsorption*. Carbon, 2006. **44**(10): p. 2039-2044.
103. Katsaros, F.K., et al., *Preparation and characterisation of gas selective microporous carbon membranes*. Microporous and Mesoporous Materials, 2007. **99**(1-2): p. 181-189.
104. Jagiello, J. and W. Betz, *Characterization of pore structure of carbon molecular sieves using DFT analysis of Ar and H-2 adsorption data*. Microporous and Mesoporous Materials, 2008. **108**(1-3): p. 117-122.
105. Drozdov, V.A., et al., *Developing the Synthesis of Homogeneously Microporous Carbon Membranes for Selective Extraction and Accumulation of Organic Molecules with a Carbon Unit as a Carrier*. Protection of Metals and Physical Chemistry of Surfaces, 2009. **45**(2): p. 191-196.
106. Cheng, H.N., et al., *Solid-state NMR and ESR studies of activated carbons produced from pecan shells*. Carbon. **48**(9): p. 2455-2469.
107. Lima, I.M., A.A. Boateng, and K.T. Klasson, *Physicochemical and adsorptive properties of fast-pyrolysis bio-chars and their steam activated counterparts*. Journal of Chemical Technology and Biotechnology. **85**(11): p. 1515-1521.
108. Klasson, K.T., et al., *Feasibility of mercury removal from simulated flue gas by activated chars made from poultry manures*. Journal of Environmental Management. **91**(12): p. 2466-2470.
109. Klasson, K.T., I.M. Lima, and L.L. Boihem, *Poultry manure as raw material for mercury adsorbents in gas applications*. Journal of Applied Poultry Research, 2009. **18**(3): p. 562-569.
110. Carrott, P.J.M., L.M. Marques, and M. Carrott, *Characterisation of the porosity of polymer and carbon aerogels containing Fe, Ni or Cu prepared from 2,4-dihydroxybenzoic acid by n-nonane pre-adsorption and density functional theory*. Microporous and Mesoporous Materials. **131**(1-3): p. 75-81.
111. Weber, J., et al., *Micropore Analysis of Polymer Networks by Gas Sorption and (129)Xe NMR Spectroscopy: Toward a Better Understanding of Intrinsic Microporosity*. Langmuir. **26**(19): p. 15650-15656.
112. Thommes, M., et al., *Assessing surface chemistry and pore structure of active carbons by a combination of physisorption (H(2)O, Ar, N(2), CO(2)), XPS and TPD-MS*. Adsorption-Journal of the International Adsorption Society. **17**(3): p. 653-661.
113. Romanos, J., et al., *Nanospace engineering of KOH activated carbon*. Nanotechnology. **23**(1): p. 7.
114. Hu, X., et al., *CO(2)-Filling Capacity and Selectivity of Carbon Nanopores: Synthesis, Texture, and Pore-Size Distribution from Quenched-Solid Density Functional Theory (QSDFT)*. Environmental Science & Technology. **45**(16): p. 7068-7074.
115. Yang, K., et al., *Effects of CO(2) adsorption on coal deformation during geological sequestration*. Journal of Geophysical Research-Solid Earth, 2011. **116**: p. 11.
116. Puziy, A.M., et al., *Nanostructured carbons for solid phase extraction*. Applied Surface Science. **256**(17): p. 5216-5220.
117. Yeon, S.H., et al., *Enhanced volumetric hydrogen and methane storage capacity of monolithic carbide-derived carbon*. Microporous and Mesoporous Materials. **131**(1-3): p. 423-428.

118. He, L.L., et al., *Small-angle neutron scattering characterization of the structure of nanoporous carbons for energy-related applications*. Microporous and Mesoporous Materials. **149**(1): p. 46-54.
119. Zhu, Y.W., et al., *Carbon-Based Supercapacitors Produced by Activation of Graphene*. Science, 2011. **332**(6037): p. 1537-1541.
120. Jost, K., et al., *Carbon coated textiles for flexible energy storage*. Energy & Environmental Science. **4**(12): p. 5060-5067.
121. Darmstadt, H., Ryoo, R., *Adsorption on ordered porous carbons*, in *Adsorption by carbons*, J.M.D.T. Eduardo J. Bottani, Editor. 2008, Elsevier: Oxford.
122. Lee, K.T. and S.M. Oh, *Novel synthesis of porous carbons with tunable pore size by surfactant-templated sol-gel process and carbonisation*. Chemical Communications, 2002(22): p. 2722-2723.
123. Ryoo, R., S.H. Joo, and J.M. Kim, *Energetically favored formation of MCM-48 from cationic-neutral surfactant mixtures*. Journal of Physical Chemistry B, 1999. **103**(35): p. 7435-7440.
124. Kruk, M., et al., *Characterization of MCM-48 silicas with tailored pore sizes synthesized via a highly efficient procedure*. Chemistry of Materials, 2000. **12**(5): p. 1414-1421.
125. Vinu, A., et al., *Adsorption of cytochrome c on new mesoporous carbon molecular sieves*. Journal of Physical Chemistry B, 2003. **107**(33): p. 8297-8299.
126. Zhou, H.S., et al., *Electrochemical capacitance of self-ordered mesoporous carbon*. Journal of Power Sources, 2003. **122**(2): p. 219-223.
127. Enterría, M., et al., *Synthesis of ordered micro-mesoporous carbons by activation of SBA-15 carbon replicas*. Microporous and Mesoporous Materials. **151**: p. 390-396.
128. Wilke, A. and J. Weber, *Mesoporous Polymer Networks-Ultraporous DVB Resins by Hard-Templating of Close-Packed Silica Spheres*. Macromolecular Rapid Communications, 2012. **33**(9): p. 785-790.
129. Rasmussen, C.J., et al., *Cavitation in Metastable Liquid Nitrogen Confined to Nanoscale Pores*. Langmuir, 2010. **26**(12): p. 10147-10157.
130. Huo, Q.S., et al., *GENERALIZED SYNTHESIS OF PERIODIC SURFACTANT INORGANIC COMPOSITE-MATERIALS*. Nature, 1994. **368**(6469): p. 317-321.
131. Huo, Q.S., et al., *MESOSTRUCTURE DESIGN WITH GEMINI SURFACTANTS - SUPERCAGE FORMATION IN A 3-DIMENSIONAL HEXAGONAL ARRAY*. Science, 1995. **268**(5215): p. 1324-1327.
132. Huo, Q.S., D.I. Margolese, and G.D. Stucky, *Surfactant control of phases in the synthesis of mesoporous silica-based materials*. Chemistry of Materials, 1996. **8**(5): p. 1147-1160.
133. Bao, X.Y., et al., *Pore structure characterization of large-pore periodic mesoporous organosilicas synthesized with varying SiO₂/template ratios*. Applied Surface Science, 2004. **237**(1-4): p. 380-386.
134. Hsu, Y.C., et al., *Facile synthesis of mesoporous silica SBA-15 with additional intra-particle porosities*. Chemistry of Materials, 2007. **19**(5): p. 1120-1126.
135. Blasco, T., et al., *SYNTHESIS, CHARACTERIZATION, AND CATALYTIC ACTIVITY OF Ti-MCM-41 STRUCTURES*. Journal of Catalysis, 1995. **156**(1): p. 65-74.
136. Berube, F., et al., *Optimizing Silica Synthesis for the Preparation of Mesoporous Ti-SBA-15 Epoxidation Catalysts*. Industrial & Engineering Chemistry Research, 2010. **49**(15): p. 6977-6985.
137. Berube, F., F. Kleitz, and S. Kaliaguine, *Surface properties and epoxidation catalytic activity of Ti-SBA15 prepared by direct synthesis*. Journal of Materials Science, 2009. **44**(24): p. 6727-6735.
138. Berube, F., F. Kleitz, and S. Kaliaguine, *A comprehensive study of titanium-substituted SBA-15 mesoporous materials prepared by direct synthesis*. Journal of Physical Chemistry C, 2008. **112**(37): p. 14403-14411.
139. Berube, F., et al., *Controlled Postgrafting of Titanium Chelates for Improved Synthesis of Ti-SBA-15 Epoxidation Catalysts*. Chemistry of Materials, 2010. **22**(6): p. 1988-2000.
140. Ravikovitch, P.I. and A.V. Neimark, *Characterization of nanoporous materials from adsorption and desorption isotherms*. Colloids and Surfaces a-Physicochemical and Engineering Aspects, 2001. **187**: p. 11-21.
141. Szegedi, A., M. Popova, and C. Minchev, *Catalytic activity of Co/MCM-41 and Co/SBA-15 materials in toluene oxidation*. Journal of Materials Science, 2009. **44**(24): p. 6710-6716.
142. Tsoncheva, T., et al., *Physicochemical and catalytic properties of grafted vanadium species on different mesoporous silicas*. Journal of Colloid and Interface Science, 2008. **321**(2): p. 342-349.

143. Wainer, M., L. Marcoux, and F. Kleitz, *Organic solvent treatment and physicochemical properties of nanoporous polymer-SBA-15 composite materials*. Journal of Materials Science, 2009. **44**(24): p. 6538-6545.
144. Han, Y.J., G.D. Stucky, and A. Butler, *Mesoporous silicate sequestration and release of proteins*. Journal of the American Chemical Society, 1999. **121**(42): p. 9897-9898.
145. Ojeda, M.L., et al., *SBA-15 surface functionalization via ferrocenyl Fischer chromium carbene coatings: Technology and textural properties*. Surface & Coatings Technology, 2009. **203**(10-11): p. 1444-1451.
146. Ojeda, M.L., et al., *SBA-15 pore-width decrease via a one- or a two-step covalent bonding of a Fischer tungsten carbene as measured by N(2) sorption*. Surface and Interface Analysis, 2008. **40**(9): p. 1262-1269.
147. Vinu, A., V. Murugesan, and M. Hartmann, *Pore size engineering and mechanical stability of the cubic mesoporous molecular sieve SBA-1*. Chemistry of Materials, 2003. **15**(6): p. 1385-1393.
148. Ting, C.C., et al., *Facile synthesis and morphology control of highly ordered cubic mesoporous silica SBA-1 using short chain dodecyltrimethylammonium chloride as the structure-directing agent*. Microporous and Mesoporous Materials, 2008. **116**(1-3): p. 323-329.
149. Kao, H.M., et al., *Facile synthesis of stable cubic mesoporous silica SBA-1 over a broad temperature range with the aid of D-fructose*. Chemical Communications, 2005(8): p. 1058-1060.
150. Kao, H.M., et al., *Direct synthesis of vinyl-functionalized cubic mesoporous silica SBA-1*. Microporous and Mesoporous Materials, 2006. **88**(1-3): p. 319-328.
151. Kao, H.M., et al., *Direct synthesis and solid-state NMR characterization of cubic mesoporous silica SBA-1 functionalized with phenyl groups*. Chemistry of Materials, 2008. **20**(6): p. 2412-2422.
152. Zhao, D.Y., et al., *Nonionic triblock and star diblock copolymer and oligomeric surfactant syntheses of highly ordered, hydrothermally stable, mesoporous silica structures*. Journal of the American Chemical Society, 1998. **120**(24): p. 6024-6036.
153. Zhao, D., et al., *Continuous mesoporous silica films with highly ordered large pore structures*. Advanced Materials, 1998. **10**(16): p. 1380-+.
154. Esparza, J.M., et al., *Development and sorption characterization of some model mesoporous and microporous silica adsorbents*. Journal of Molecular Catalysis a-Chemical, 2005. **228**(1-2): p. 97-110.
155. Kleitz, F., et al., *X-ray structural modeling and gas adsorption analysis of cagelike SBA-16 silica mesophases prepared in a F127/butanol/H(2)O system*. Chemistry of Materials, 2006. **18**(21): p. 5070-5079.
156. Kleitz, F., T.W. Kim, and R. Ryoo, *Phase domain of the cubic im3m mesoporous silica in the EO106PO70EO106-butanol-H2O system*. Langmuir, 2006. **22**(1): p. 440-445.
157. Fan, J., et al., *Low-temperature strategy to synthesize highly ordered mesoporous silicas with very large pores*. Journal of the American Chemical Society, 2005. **127**(31): p. 10794-10795.
158. Meng, Y., et al., *Ordered mesoporous polymers and homologous carbon frameworks: Amphiphilic surfactant templating and direct transformation*. Angewandte Chemie-International Edition, 2005. **44**(43): p. 7053-7059.
159. Yu, C.Z., Y.H. Yu, and D.Y. Zhao, *Highly ordered large caged cubic mesoporous silica structures templated by triblock PEO-PBO-PEO copolymer*. Chemical Communications, 2000(7): p. 575-576.
160. Yu, T., et al., *Pore structures of ordered large cage-type mesoporous silica FDU-12s*. Journal of Physical Chemistry B, 2006. **110**(43): p. 21467-21472.
161. Ersen, O., et al., *Direct Observation of Stacking Faults and Pore Connections in Ordered Cage-Type Mesoporous Silica FDU-12 by Electron Tomography*. Journal of the American Chemical Society, 2008. **130**(49): p. 16800-16806.
162. Kleitz, F., S.H. Choi, and R. Ryoo, *Cubic Ia3d large mesoporous silica: synthesis and replication to platinum nanowires, carbon nanorods and carbon nanotubes*. Chemical Communications, 2003(17): p. 2136-2137.
163. Kleitz, F., et al., *Large cage face-centered-cubic Fm3m mesoporous silica: Synthesis and structure*. Journal of Physical Chemistry B, 2003. **107**(51): p. 14296-14300.
164. Yang, C.M., W. Schmidt, and F. Kleitz, *Pore topology control of three-dimensional large pore cubic silica mesophases*. Journal of Materials Chemistry, 2005. **15**(48): p. 5112-5114.

165. Wu, C.Y., Y.T. Hsu, and C.M. Yang, *Structural modulation of cage-like mesoporous KIT-5 silica by post-synthesis treatments with ammonia and/or sulfuric acid*. Microporous and Mesoporous Materials, 2009. **117**(1-2): p. 249-256.
166. Hsu, Y.T., W.L. Chen, and C.M. Yang, *Co-Condensation Synthesis of Aminopropyl-Functionalized KIT-5 Mesophases Using Carboxy-Terminated Triblock Copolymer*. Journal of Physical Chemistry C, 2009. **113**(7): p. 2777-2783.
167. Tsoncheva, T., et al., *Critical evaluation of the state of iron oxide nanoparticles on different mesoporous silicas prepared by an impregnation method*. Microporous and Mesoporous Materials, 2008. **112**(1-3): p. 327-337.
168. Kleitz, F., et al., *Probing Adsorption, Pore Condensation, and Hysteresis Behavior of Pure Fluids in Three-Dimensional Cubic Mesoporous KIT-6 Silica*. Journal of Physical Chemistry C, 2010. **114**(20): p. 9344-9355.
169. Guo, W., et al., *Large pore phenylene-bridged mesoporous organosilica with bicontinuous cubic Ia(3)over-bard (KIT-6) mesostructure*. Journal of Materials Chemistry. **20**(38): p. 8257-8265.
170. Clark, J.H. and D.J. Macquarrie, *Catalysis of liquid phase organic reactions using chemically modified mesoporous inorganic solids*. Chemical Communications, 1998(8): p. 853-860.
171. Wight, A.P. and M.E. Davis, *Design and preparation of organic-inorganic hybrid catalysts*. Chemical Reviews, 2002. **102**(10): p. 3589-3613.
172. Kickelbick, G., *Hybrid inorganic-organic mesoporous materials*. Angewandte Chemie-International Edition, 2004. **43**(24): p. 3102-3104.
173. Yoshitake, H., *Highly-controlled synthesis of organic layers on mesoporous silica: their structure and application to toxic ion adsorptions*. New Journal of Chemistry, 2005. **29**(9): p. 1107-1117.
174. Hoffmann, F., et al., *Silica-based mesoporous organic-inorganic hybrid materials*. Angewandte Chemie-International Edition, 2006. **45**(20): p. 3216-3251.
175. Ford, D.M., E.E. Simanek, and D.F. Shantz, *Engineering nanospaces: ordered mesoporous silicas as model substrates for building complex hybrid materials*. Nanotechnology, 2005. **16**(7): p. S458-S475.
176. Taguchi, A. and F. Schuth, *Ordered mesoporous materials in catalysis*. Microporous and Mesoporous Materials, 2005. **77**(1): p. 1-45.
177. Ying, J.Y., C.P. Mehnert, and M.S. Wong, *Synthesis and applications of supramolecular-templated mesoporous materials*. Angewandte Chemie-International Edition, 1999. **38**(1-2): p. 56-77.
178. Vallet-Regi, M., F. Balas, and D. Arcos, *Mesoporous materials for drug delivery*. Angewandte Chemie-International Edition, 2007. **46**(40): p. 7548-7558.
179. Tiemann, M., *Porous metal oxides as gas sensors*. Chemistry-a European Journal, 2007. **13**(30): p. 8376-8388.
180. Hartmann, M., *Ordered mesoporous materials for bioadsorption and biocatalysis*. Chemistry of Materials, 2005. **17**(18): p. 4577-4593.
181. Choi, M., et al., *Controlled polymerization in mesoporous silica toward the design of organic-inorganic composite nanoporous materials*. Journal of the American Chemical Society, 2005. **127**(6): p. 1924-1932.
182. Guillet-Nicolas, R., L. Marcoux, and F. Kleitz, *Insights into pore surface modification of mesoporous polymer-silica composites: introduction of reactive amines*. New Journal of Chemistry. **34**(2): p. 355-366.
183. Cheng, Q.H., et al., *Ultrasound-Assisted SWNTs Dispersion: Effects of Sonication Parameters and Solvent Properties*. Journal of Physical Chemistry C. **114**(19): p. 8821-8827.
184. Hennrich, F., et al., *The mechanism of cavitation-induced scission of single-walled carbon nanotubes*. Journal of Physical Chemistry B, 2007. **111**(8): p. 1932-1937.
185. Miaudet, P., et al., *Hot-drawing of single and multiwall carbon nanotube fibers for high toughness and alignment*. Nano Letters, 2005. **5**(11): p. 2212-2215.
186. Neri, W., et al., *Surfactant-free spinning of composite carbon nanotube fibers*. Macromolecular Rapid Communications, 2006. **27**(13): p. 1035-1038.
187. Chen, J.H., L.S. Loo, and K.A. Wang, *Enhanced mechanical properties of novel chitosan nanocomposite fibers*. Carbohydrate Polymers, 2011. **86**(3): p. 1151-1156.
188. Sa, V. and K.G. Kornev, *A method for wet spinning of alginate fibers with a high concentration of single-walled carbon nanotubes*. Carbon, 2011. **49**(6): p. 1859-1868.

189. Foroughi, J., G.M. Spinks, and G.G. Wallace, *A reactive wet spinning approach to polypyrrole fibres*. Journal of Materials Chemistry, 2011. **21**(17): p. 6421-6426.
190. Lewitus, D.Y., et al., *Biohybrid Carbon Nanotube/Agarose Fibers for Neural Tissue Engineering*. Advanced Functional Materials, 2011. **21**(14): p. 2624-2632.
191. Xu, X.Z., et al., *Fabrication of high strength PVA/SWCNT composite fibers by gel spinning*. Carbon. **48**(7): p. 1977-1984.
192. Davis, V.A., et al., *True solutions of single-walled carbon nanotubes for assembly into macroscopic materials*. Nature Nanotechnology, 2009. **4**(12): p. 830-834.
193. Minus, M.L., H.G. Chae, and S. Kumar, *Interfacial Crystallization in Gel-Spun Poly(vinyl alcohol)/Single-Wall Carbon Nanotube Composite Fibers*. Macromolecular Chemistry and Physics, 2009. **210**(21): p. 1799-1808.
194. Razdan, S., et al., *Ionically Self-Assembled Polyelectrolyte-Based Carbon Nanotube Fibers*. Chemistry of Materials, 2009. **21**(14): p. 3062-3071.
195. Lynam, C., W. Grosse, and G.G. Wallace, *Carbon-Nanotube Biofiber Microelectrodes*. Journal of the Electrochemical Society, 2009. **156**(7): p. P117-P121.
196. Granero, A.J., et al., *Spinning Carbon Nanotube-Gel Fibers Using Polyelectrolyte Complexation*. Advanced Functional Materials, 2008. **18**(23): p. 3759-3764.
197. Zhang, S.J., et al., *Macroscopic fibers of well-aligned carbon nanotubes by wet spinning*. Small, 2008. **4**(8): p. 1217-1222.
198. Shin, S.R., et al., *DNA-wrapped single-walled carbon nanotube hybrid fibers for supercapacitors and artificial muscles*. Advanced Materials, 2008. **20**(3): p. 466-+.
199. Razal, J.M., K.J. Gilmore, and G.G. Wallace, *Carbon nanotube biofiber formation in a polymer-free coagulation bath*. Advanced Functional Materials, 2008. **18**(1): p. 61-66.
200. Che, J.F. and M.B. Chan-Park, *Reactive spinning of cyanate aligned amino-functionalized ester fibers reinforced with single wall carbon nanotubes*. Advanced Functional Materials, 2008. **18**(6): p. 888-897.
201. Razal, J.M., et al., *Arbitrarily shaped fiber assemblies from spun carbon nanotube gel fibers*. Advanced Functional Materials, 2007. **17**(15): p. 2918-2924.
202. Penicaud, A., et al., *Mild dissolution of carbon nanotubes: Composite carbon nanotube fibres from polyelectrolyte solutions*. Composites Science and Technology, 2007. **67**(5): p. 795-797.
203. Miaudet, P., et al., *Thermo-electrical properties of PVA-nanotube composite fibers*. Polymer, 2007. **48**(14): p. 4068-4074.
204. Lynam, C., S.E. Moulton, and G.G. Wallace, *Carbon-nanotube biofibers*. Advanced Materials, 2007. **19**(9): p. 1244-+.
205. Spinks, G.M., et al., *Mechanical properties of chitosan/CNT microfibers obtained with improved dispersion*. Sensors and Actuators B-Chemical, 2006. **115**(2): p. 678-684.
206. Steinmetz, J., et al., *Production of pure nanotube fibers using a modified wet-spinning method*. Carbon, 2005. **43**(11): p. 2397-2400.
207. Munoz, E., et al., *Highly conducting carbon nanotube/polyethyleneimine composite fibers*. Advanced Materials, 2005. **17**(8): p. 1064-+.
208. Kozlov, M.E., et al., *Spinning solid and hollow polymer-free carbon nanotube fibers*. Advanced Materials, 2005. **17**(5): p. 614-+.
209. Ericson, L.M., et al., *Macroscopic, neat, single-walled carbon nanotube fibers*. Science, 2004. **305**(5689): p. 1447-1450.
210. Dalton, A.B., et al., *Continuous carbon nanotube composite fibers: properties, potential applications, and problems*. Journal of Materials Chemistry, 2004. **14**(1): p. 1-3.
211. Barisci, J.N., et al., *Properties of carbon nanotube fibers spun from DNA-stabilized dispersions*. Advanced Functional Materials, 2004. **14**(2): p. 133-138.
212. Hynd, M.R., et al., *Directed cell growth on protein-functionalized hydrogel surfaces*. Journal of Neuroscience Methods, 2007. **162**(1-2): p. 255-263.
213. Thompson, B.C., et al., *Carbon nanotube biogels*. Carbon, 2009. **47**(5): p. 1282-1291.
214. Scherer, G.W., *DRYING GELS .1. GENERAL-THEORY*. Journal of Non-Crystalline Solids, 1986. **87**(1-2): p. 199-225.
215. Scherer, G.W., *DRYING GELS .8. REVISION AND REVIEW*. Journal of Non-Crystalline Solids, 1989. **109**(2-3): p. 171-182.

216. Kornev, K.G., et al., *Ribbon-to-fiber transformation in the process of spinning of carbon-nanotube dispersion*. Physical Review Letters, 2006. **97**(18): p. 4.
217. Cellot, G., et al., *Carbon nanotubes might improve neuronal performance by favouring electrical shortcuts*. Nature Nanotechnology, 2009. **4**(2): p. 126-133.
218. Blighe, F.M., et al., *The Effect of Nanotube Content and Orientation on the Mechanical Properties of Polymer-Nanotube Composite Fibers: Separating Intrinsic Reinforcement from Orientational Effects*. Advanced Functional Materials. **21**(2): p. 364-371.
219. Marcano, D.C., et al., *Improved Synthesis of Graphene Oxide*. Acs Nano. **4**(8): p. 4806-4814.
220. Lee, S.W., et al., *Plasma-Assisted Reduction of Graphene Oxide at Low Temperature and Atmospheric Pressure for Flexible Conductor Applications*. Journal of Physical Chemistry Letters, 2012. **3**(6): p. 772-777.
221. Shin, M.K., et al., *Synergistic toughening of composite fibres by self-alignment of reduced graphene oxide and carbon nanotubes*. Nature Communications, 2012. **3**: p. 8.
222. Jang, E.Y., et al., *Fibers of reduced graphene oxide nanoribbons*. Nanotechnology, 2012. **23**(23): p. 235601.
223. He, Y.Q., et al., *Alginate/graphene oxide fibers with enhanced mechanical strength prepared by wet spinning*. Carbohydrate Polymers, 2012. **88**(3): p. 1100-1108.
224. Dong, Z.L., et al., *Facile Fabrication of Light, Flexible and Multifunctional Graphene Fibers*. Advanced Materials, 2012. **24**(14): p. 1856-1861.
225. Xu, Z. and C. Gao, *Graphene chiral liquid crystals and macroscopic assembled fibres*. Nature Communications, 2011. **2**: p. 9.
226. Li, X.M., et al., *Directly Drawing Self-Assembled, Porous, and Monolithic Graphene Fiber from Chemical Vapor Deposition Grown Graphene Film and Its Electrochemical Properties*. Langmuir, 2011. **27**(19): p. 12164-12171.
227. Lewitus, D., et al., *Biohybrid Carbon Nanotube/Agarose Fibers for Neural Tissue Engineering*. Under Review, Advanced Functional Materials.
228. Lewitus, D., et al., *BIOACTIVE CARBON-NANOTUBE AGAROSE FIBER COMPOSITES FOR NEURAL TISSUE ENGINEERING*. . U.S. Provisional Patent Application Serial No. 61/417,913, 2010.
229. Shoval, A., et al., *Carbon nanotube electrodes for effective interfacing with retinal tissue*. Frontiers in Neuroengineering, 2009. **2**.
230. Bianco, A., K. Kostarelos, and M. Prato, *Applications of carbon nanotubes in drug delivery*. Current Opinion in Chemical Biology, 2005. **9**(6): p. 674-679.
231. Liu, Z., et al., *PEGylated nanographene oxide for delivery of water-insoluble cancer drugs*. Journal of the American Chemical Society, 2008. **130**(33): p. 10876-+.
232. Sinha, N. and J.T.W. Yeow, *Carbon nanotubes for biomedical applications*. Ieee Transactions on Nanobioscience, 2005. **4**(2): p. 180-195.
233. Fan, H.L., et al., *Fabrication, Mechanical Properties, and Biocompatibility of Graphene-Reinforced Chitosan Composites*. Biomacromolecules, 2010. **11**(9): p. 2345-2351.
234. Shan, C.S., et al., *Direct Electrochemistry of Glucose Oxidase and Biosensing for Glucose Based on Graphene*. Analytical Chemistry, 2009. **81**(6): p. 2378-2382.
235. Lin, Y.H., et al., *Glucose biosensors based on carbon nanotube nanoelectrode ensembles*. Nano Letters, 2004. **4**(2): p. 191-195.
236. Leach, J., A.K.H. Achyuta, and S.K. Murthy, *Bridging the divide between neuroprosthetic design, tissue engineering and neurobiology*. Frontiers in Neuroengineering, 2010. **3**: p. 12.
237. Ryu, S.I. and K.V. Shenoy, *Human cortical prostheses: lost in translation?* Neurosurgical Focus, 2009. **27**(1).
238. Polikov, V.S., P.A. Tresco, and W.M. Reichert, *Response of brain tissue to chronically implanted neural electrodes*. J Neurosci Methods, 2005. **148**(1): p. 1-18.
239. Shain, W., et al. *Controlling cellular reactive responses around neural prosthetic devices using peripheral and local intervention strategies*. 2003.
240. Szarowski, D.H., et al., *Brain responses to micro-machined silicon devices*. Brain Res, 2003. **983**(1-2): p. 23-35.
241. Zhong, Y.H. and R.V. Bellamkonda, *Dexamethasone-coated neural probes elicit attenuated inflammatory response and neuronal loss compared to uncoated neural probes*. Brain Research, 2007. **1148**: p. 15-27.

242. Abidian, M.R. and D.C. Martin, *Multifunctional Nanobiomaterials for Neural Interfaces*. Advanced Functional Materials, 2009. **19**(4): p. 573-585.
243. Mercanzini, A., et al., *Controlled release nanoparticle-embedded coatings reduce the tissue reaction to neuroprostheses*. Journal of Controlled Release, 2010. **145**(3): p. 196-202.
244. Marin, C. and E. Fernandez, *Biocompatibility of intracortical microelectrodes: current status and future prospects*. Front Neuroengineering, 2010. **3**: p. 8.
245. Purcell, E.K., et al., *Flavopiridol reduces the impedance of neural prostheses in vivo without affecting recording quality*. Journal of Neuroscience Methods, 2009. **183**(2): p. 149-157.
246. He, W., et al., *A Novel Anti-inflammatory Surface for Neural Electrodes*. Advanced Materials, 2007. **19**(21): p. 3529-3533.
247. Azemi, E., et al., *Surface immobilization of neural adhesion molecule L1 for improving the biocompatibility of chronic neural probes: In vitro characterization*. Acta Biomaterialia, 2008. **4**(5): p. 1208-1217.
248. Winslow, B.D., et al., *A comparison of the tissue response to chronically implanted Parylene-C-coated and uncoated planar silicon microelectrode arrays in rat cortex*. Biomaterials, 2010. **31**(35): p. 9163-9172.
249. Chen, C.-H., et al., *Three-dimensional flexible microprobe for recording the neural signal*. Journal of Micro/Nanolithography, MEMS and MOEMS, 2010. **9**(3): p. 031007.
250. Kozai, T.D.Y. and D.R. Kipke, *Insertion shuttle with carboxyl terminated self-assembled monolayer coatings for implanting flexible polymer neural probes in the brain*. Journal of Neuroscience Methods, 2009. **184**(2): p. 199-205.
251. Foley, C.P., et al., *Flexible microfluidic devices supported by biodegradable insertion scaffolds for convection-enhanced neural drug delivery*. Biomedical Microdevices, 2009. **11**(4): p. 915-924.
252. Seymour, J.P. and D.R. Kipke, *Neural probe design for reduced tissue encapsulation in CNS*. Biomaterials, 2007. **28**(25): p. 3594-3607.
253. Jaroch, D.B., et al., *Magnetic insertion system for flexible electrode implantation*. Journal of Neuroscience Methods, 2009. **183**(2): p. 213-222.
254. Kipke, D.R., et al., *Advanced Neurotechnologies for Chronic Neural Interfaces: New Horizons and Clinical Opportunities*. J. Neurosci., 2008. **28**(46): p. 11830-11838.
255. Freeman, M.R., *Specification and Morphogenesis of Astrocytes*. Science, 2010. **330**(6005): p. 774-778.
256. Chao, T.I., et al., *Carbon nanotubes promote neuron differentiation from human embryonic stem cells*. Biochemical and Biophysical Research Communications, 2009. **384**(4): p. 426-430.
257. Tay, C.Y., et al., *Cellular behavior of human mesenchymal stem cells cultured on single-walled carbon nanotube film*. Carbon. **48**(4): p. 1095-1104.
258. Spinks, G.A., et al., *A novel "dual mode" actuation in chitosan/polyaniline/carbon nanotube fibers*. Sensors and Actuators B-Chemical, 2007. **121**(2): p. 616-621.
259. Xu, X.Z., et al., *Fabrication of high strength PVA/SWCNT composite fibers by gel spinning*. Carbon, 2010. **48**(7): p. 1977-1984.
260. Rago, A.P., et al., *Miniaturization of an Anoikis assay using non-adhesive micromolded hydrogels*. Cytotechnology, 2008. **56**(2): p. 81-90.
261. Nisbet, D.R., et al., *Neural tissue engineering of the CNS using hydrogels*. Journal of Biomedical Materials Research Part B: Applied Biomaterials, 2008. **87B**(1): p. 251-263.
262. Luo, Y. and M.S. Shoichet, *A photolabile hydrogel for guided three-dimensional cell growth and migration*. Nat Mater, 2004. **3**(4): p. 249-253.
263. Yu, X.J., G.P. Dillon, and R.V. Bellamkonda, *A laminin and nerve growth factor-laden three-dimensional scaffold for enhanced neurite extension*. Tissue Engineering, 1999. **5**(4): p. 291-304.
264. Kohn, J. and M. Wilchek, *The Use of Cyanogen-Bromide and Other Novel Cyanylating Agents for the Activation of Polysaccharide Resins*. Applied Biochemistry and Biotechnology, 1984. **9**(3): p. 285-305.
265. Pernodet, N., M. Maaloum, and B. Tinland, *Pore size of agarose gels by atomic force microscopy*. Electrophoresis, 1997. **18**(1): p. 55-58.
266. Gros, T., et al., *Regeneration of long-tract axons through sites of spinal cord injury using templated agarose scaffolds*. Biomaterials, 2010. **31**(26): p. 6719-6729.

267. Sharp, A.A., et al., *In Vivo Penetration Mechanics and Mechanical Properties of Mouse Brain Tissue at Micrometer Scales*. Biomedical Engineering, IEEE Transactions on, 2009. **56**(1): p. 45-53.
268. Hrapko, M., et al., *Characterisation of the mechanical behaviour of brain tissue in compression and shear*. Biorheology, 2008. **45**(6): p. 663-76.
269. Shafer, D.E., et al., *Activation of soluble polysaccharides with 1-cyano-4-dimethylaminopyridinium tetrafluoroborate (CDAP) for use in protein-polysaccharide conjugate vaccines and immunological reagents. II. Selective crosslinking of proteins to CDAP-activated polysaccharides*. Vaccine, 2000. **18**(13): p. 1273-1281.
270. Normand, V., et al., *New insight into agarose gel mechanical properties*. Biomacromolecules, 2000. **1**(4): p. 730-738.
271. Jones, D.G., E.R. Anderson, and K.A. Galvin, *Spinal cord regeneration: Moving tentatively towards new perspectives*. Neurorehabilitation, 2003. **18**(4): p. 339-351.
272. Gheith, M.K., et al., *Single-walled carbon nanotube polyelectrolyte multilayers and freestanding films as a biocompatible platform for neuroprosthetic implants*. Advanced Materials, 2005. **17**(22): p. 2663-+.
273. Hu, H., et al., *Chemically functionalized carbon nanotubes as substrates for neuronal growth*. Nano Letters, 2004. **4**(3): p. 507-511.
274. Lovat, V., et al., *Carbon nanotube substrates boost neuronal electrical signaling*. Nano Letters, 2005. **5**(6): p. 1107-1110.
275. Galano, A., *Carbon nanotubes: promising agents against free radicals*. Nanoscale, 2010. **2**(3): p. 373-380.
276. Hajj Hassan, M., V. Chodavarapu, and S. Musallam, *NeuroMEMS: Neural Probe Microtechnologies*. Sensors, 2008. **8**(10): p. 6704-6726.
277. Shvedova, A.A., et al., *Exposure to carbon nanotube material: Assessment of nanotube cytotoxicity using human keratinocyte cells*. Journal of Toxicology and Environmental Health-Part A, 2003. **66**(20): p. 1909-1926.
278. Shvedova, A.A., et al., *Unusual inflammatory and fibrogenic pulmonary responses to single-walled carbon nanotubes in mice*. American Journal of Physiology-Lung Cellular and Molecular Physiology, 2005. **289**(5): p. L698-L708.
279. Bjornsson, C.S., et al., *Associative image analysis: A method for automated quantification of 3D multi-parameter images of brain tissue*. Journal of Neuroscience Methods, 2008. **170**(1): p. 165-178.
280. Szarowski, D.H., et al., *Brain responses to micro-machined silicon devices*. Brain Research, 2003. **983**(1-2): p. 23-35.
281. Grill, W.M., S.E. Norman, and R.V. Bellamkonda, *Implanted Neural Interfaces: Biochallenges and Engineered Solutions*. Annual Review of Biomedical Engineering, 2009. **11**: p. 1-24.
282. Webb, K., et al., *Substrate-bound human recombinant L1 selectively promotes neuronal attachment and outgrowth in the presence of astrocytes and fibroblasts*. Biomaterials, 2001. **22**(10): p. 1017-1028.
283. Ruiter, G.C.W., et al., *Designing ideal conduits for peripheral nerve repair*. Neurosurgical Focus, 2009. **26**(2): p. 9.
284. Keller, G., *Embryonic stem cell differentiation: emergence of a new era in biology and medicine*. Genes & Development, 2005. **19**(10): p. 1129-1155.
285. Murry, C.E. and G. Keller, *Differentiation of embryonic stem cells to clinically relevant populations: Lessons from embryonic development*. Cell, 2008. **132**(4): p. 661-680.
286. Thomson, J.A., et al., *Embryonic stem cell lines derived from human blastocysts*. Science, 1998. **282**(5391): p. 1145-1147.
287. Alexander, J.K., B. Fuss, and R.J. Colello, *Electric field-induced astrocyte alignment directs neurite outgrowth*. Neuron Glia Biology, 2006. **2**: p. 93-103.
288. Gordon, T., et al., *Brief Electrical Stimulation Accelerates Axon Regeneration in the Peripheral Nervous System and Promotes Sensory Axon Regeneration in the Central Nervous System*. Motor Control, 2009. **13**(4): p. 412-441.
289. Wood, M.D. and R.K. Willits, *Applied electric field enhances DRG neurite growth: influence of stimulation media, surface coating and growth supplements*. Journal of Neural Engineering, 2009. **6**(4): p. 8.

290. Ustinov, E.A., D.D. Do, and M. Jaroniec, *Equilibrium adsorption in cylindrical mesopores: A modified Broekhoff and de boer theory versus density functional theory*. Journal of Physical Chemistry B, 2005. **109**(5): p. 1947-1958.
291. Ghasemi-Mobarakeh, L., et al., *Electrical Stimulation of Nerve Cells Using Conductive Nanofibrous Scaffolds for Nerve Tissue Engineering*. Tissue Engineering Part A, 2009. **15**(11): p. 3605-3619.
292. Jeong, S.I., et al., *Development of electroactive and elastic nanofibers that contain polyaniline and poly(L-lactide-co-epsilon-caprolactone) for the control of cell adhesion*. Macromolecular Bioscience, 2008. **8**(7): p. 627-637.
293. Schmidt, C.E., et al., *Stimulation of neurite outgrowth using an electrically conducting polymer*. Proceedings of the National Academy of Sciences of the United States of America, 1997. **94**(17): p. 8948-8953.
294. Lee, J.Y., J.W. Lee, and C.E. Schmidt, *Neuroactive conducting scaffolds: nerve growth factor conjugation on active ester-functionalized polypyrrole*. Journal of the Royal Society Interface, 2009. **6**(38): p. 801-810.
295. Zhang, Z., et al., *Electrically conductive biodegradable polymer composite for nerve regeneration: Electricity-stimulated neurite outgrowth and axon regeneration*. Artificial Organs, 2007. **31**(1): p. 13-22.
296. Rowlands, A.S. and J.J. Cooper-White, *Directing phenotype of vascular smooth muscle cells using electrically stimulated conducting polymer*. Biomaterials, 2008. **29**(34): p. 4510-4520.
297. Shi, G.X., Z. Zhang, and M. Rouabhia, *The regulation of cell functions electrically using biodegradable polypyrrole-polylactide conductors*. Biomaterials, 2008. **29**(28): p. 3792-3798.
298. Kimura, K., et al., *Gene expression in the electrically stimulated differentiation of PC12 cells*. Journal of Biotechnology, 1998. **63**(1): p. 55-65.
299. Supronowicz, P.R., et al., *Novel current-conducting composite substrates for exposing osteoblasts to alternating current stimulation*. Journal of Biomedical Materials Research, 2002. **59**(3): p. 499-506.
300. Xie, J.W., et al., *Conductive Core-Sheath Nanofibers and Their Potential Application in Neural Tissue Engineering*. Advanced Functional Materials, 2009. **19**(14): p. 2312-2318.
301. Thompson, B.C., et al., *Conducting polymers, dual neurotrophins and pulsed electrical stimulation - Dramatic effects on neurite outgrowth*. Journal of Controlled Release. **141**(2): p. 161-167.
302. Huang, L.H., et al., *Synthesis of biodegradable and electroactive multiblock polylactide and aniline pentamer copolymer for tissue engineering applications*. Biomacromolecules, 2008. **9**(3): p. 850-858.
303. Huang, J.H., et al., *Electrical regulation of Schwann cells using conductive polypyrrole/chitosan polymers*. Journal of Biomedical Materials Research Part A. **93A**(1): p. 164-174.
304. Sun, S., I. Titushkin, and M. Cho, *Regulation of mesenchymal stem cell adhesion and orientation in 3D collagen scaffold by electrical stimulus*. Bioelectrochemistry, 2006. **69**(2): p. 133-141.
305. Fong, H.R., D. H. , *Electrospinning and Formation of Nanofibers: In Structure Formation in Polymer Fibres*. Eds.; Chapter 6; Hanser, Munich, 2001; pp225., 2001.
306. Formhals, U.S. Patent 1 975 504, 1934.
307. Shin, Y.M.H., M.M; Brenner, M.P.; Rutledge, G.C., Polymer, 2001. **42**: p. 9955.
308. Yarin, A.L.K., S., J. Applied Physics, 1990(9): p. 4836.
309. Agic, A. and B. Mijovic, *Mechanical properties of electrospun carbon nanotube composites*. Journal of the Textile Institute, 2006. **97**(5): p. 419-427.
310. Kannan, P., S.J. Eichhorn, and R.J. Young, *Deformation of isolated single-wall carbon nanotubes in electrospun polymer nanofibres*. Nanotechnology, 2007. **18**(23): p. 7.
311. Liu, Y., et al., *Bio-nanowebs based on poly(styrene-beta-isobutylene-beta-styrene) (SIBS) containing single-wall carbon nanotubes*. Chemistry of Materials, 2007. **19**(11): p. 2721-2723.
312. Salalha, W., et al., *Single-walled carbon nanotubes embedded in oriented polymeric nanofibers by electrospinning*. Langmuir, 2004. **20**(22): p. 9852-9855.
313. Sundaray, B., et al., *Preparation and Characterization of Electrospun Fibers of Poly(methyl methacrylate) - Single Walled Carbon Nanotube Nanocomposites*. Journal of Engineered Fibers and Fabrics, 2008. **3**(4): p. 39-45.

314. Quilliet, C. and B. Berge, *Electrowetting: a recent outbreak*. Current Opinion in Colloid & Interface Science, 2001. **6**(1): p. 34-39.
315. L. Valenti, P.A.F., C.D. Garcia, C. E. Giacomelli, J. Colloid and Interface Science, 2007. **307**: p. 349-356.
316. Matsuura K., S.T., Okazaki T., Ohshima S., Yumura M., Iijima S., Chemical Physics Letters, 2006. **429**: p. 497-502.
317. Schwartz, A.B., Annu. Rev. Neurosci., 2004. **27**: p. 487-507.
318. V. S. Polikov, P.A.T., W. M. Reichert, J. Neuroscience Methods, 2005. **148**: p. 1-18.
319. Gheith, M.K., et al., *Stimulation of neural cells by lateral layer-by-layer films of single-walled currents in conductive carbon nanotubes*. Advanced Materials, 2006. **18**(22): p. 2975-+.
320. Godwin, J.W. and J.P. Brookes, *Regeneration, tissue injury and the immune response*. Journal of Anatomy, 2006. **209**(4): p. 423-432.
321. Jagur-Grodzinski, J., *Polymers for tissue engineering, medical devices, and regenerative medicine. Concise general review of recent studies*. Polymers for Advanced Technologies, 2006. **17**(6): p. 395-418.
322. Wu, J.D., et al., *Gradient biomaterials and their influences on cell migration*. Interface Focus, 2012. **2**(3): p. 337-355.
323. Spijker, H.T., et al., *Protein adsorption on gradient surfaces on polyethylene prepared in a shielded gas plasma*. Colloids and Surfaces B-Biointerfaces, 1999. **15**(1): p. 89-97.
324. Shin, Y.N., et al., *Adhesion comparison of human bone marrow stem cells on a gradient wettable surface prepared by corona treatment*. Applied Surface Science, 2008. **255**(2): p. 293-296.
325. Li, B., et al., *A technique for preparing protein gradients on polymeric surfaces: effects on PC12 pheochromocytoma cells*. Biomaterials, 2005. **26**(13): p. 1487-1495.
326. Zhu, Y.B., et al., *Endothelium regeneration on luminal surface of polyurethane vascular scaffold modified with diamine and covalently grafted with gelatin*. Biomaterials, 2004. **25**(3): p. 423-430.
327. Tomlinson, M.R. and J. Genzer, *Formation of grafted macromolecular assemblies with a gradual variation of molecular weight on solid substrates*. Macromolecules, 2003. **36**(10): p. 3449-3451.
328. Chaudhury, M.K. and G.M. Whitesides, *HOW TO MAKE WATER RUN UPHILL*. Science, 1992. **256**(5063): p. 1539-1541.
329. Childs, W.R. and R.G. Nuzzo, *Decal transfer microlithography: A new soft-lithographic patterning method*. Journal of the American Chemical Society, 2002. **124**(45): p. 13583-13596.
330. Irimia, D., D.A. Geba, and M. Toner, *Universal microfluidic gradient generator*. Analytical Chemistry, 2006. **78**(10): p. 3472-3477.
331. Righetti, P.G. and A. Bossi, *Isoelectric focusing in immobilized pH gradients: an update*. Journal of Chromatography B, 1997. **699**(1-2): p. 77-89.
332. Richardson, J.T., *Principles of Catalyst Development*. Fundamental and Applied Catalysis, ed. M.V. Twigg and M.S. Spencer. 1992, New York City: Plenum Press.
333. Davis, M.E., *Ordered porous materials for emerging applications*. Nature, 2002. **417**(6891): p. 813-821.
334. Joo, S.H., et al., *Ordered nanoporous arrays of carbon supporting high dispersions of platinum nanoparticles*. Nature, 2001. **412**(6843): p. 169-172.
335. Ravikovitch, P.I., et al., *Evaluation of pore structure parameters of MCM-41 catalyst supports and catalysts by means of nitrogen and argon adsorption*. Journal of Physical Chemistry B, 1997. **101**(19): p. 3671-3679.
336. Sayari, A., *Catalysis by crystalline mesoporous molecular sieves*. Chemistry of Materials, 1996. **8**(8): p. 1840-1852.
337. Zhang, F.Q., et al., *Ordered bimodal mesoporous silica with tunable pore structure and morphology*. Microporous and Mesoporous Materials, 2007. **98**(1-3): p. 6-15.
338. He, J.J., et al., *Multiple-functional capsule catalysts: A tailor-made confined reaction environment for the direct synthesis of middle isoparaffins from syngas*. Chemistry-a European Journal, 2006. **12**(32): p. 8296-8304.
339. Ananthakumar, S., P. Manohar, and K.G.K. Warriar, *Effect of boehmite and organic binders on extrusion of alumina*. Ceramics International, 2004. **30**(6): p. 837-842.
340. Iveson, S.M., et al., *Nucleation, growth and breakage phenomena in agitated wet granulation processes: a review*. Powder Technology, 2001. **117**(1-2): p. 3-39.

341. Tardos, G.I., M.I. Khan, and P.R. Mort, *Critical parameters and limiting conditions in binder granulation of fine powders*. Powder Technology, 1997. **94**(3): p. 245-258.
342. Benbow, J.J., S. Blackburn, and H. Mills, *The effects of liquid-phase rheology on the extrusion behaviour of paste*. Journal of Materials Science, 1998. **33**(24): p. 5827-5833.
343. Eggerstedt, P.M., J.F. Zievers, and E.C. Zievers, *CHOOSE THE RIGHT CERAMIC FOR FILTERING HOT GASES*. Chemical Engineering Progress, 1993. **89**(1): p. 62-68.
344. Cejka, J., *Organized mesoporous alumina: synthesis, structure and potential in catalysis*. Applied Catalysis a-General, 2003. **254**(2): p. 327-338.
345. Lesaint, C., et al., *Synthesis and characterization of mesoporous alumina materials with large pore size prepared by a double hydrolysis route*. Microporous and Mesoporous Materials, 2009. **119**(1-3): p. 245-251.
346. Bagshaw, S.A. and T.J. Pinnavaia, *Mesoporous alumina molecular sieves*. Angewandte Chemie-International Edition in English, 1996. **35**(10): p. 1102-1105.
347. Cabrera, S., et al., *Surfactant-assisted synthesis of mesoporous alumina showing continuously adjustable pore sizes*. Advanced Materials, 1999. **11**(5): p. 379-381.
348. Krashennnikov, A.V. and K. Nordlund, *Ion and electron irradiation-induced effects in nanostructured materials*. Journal of Applied Physics. **107**(7): p. 70.
349. Jiao, F., et al., *Synthesis of ordered mesoporous NiO with crystalline walls and a bimodal pore size distribution*. Journal of the American Chemical Society, 2008. **130**(15): p. 5262-5266.
350. Kuemmel, M., et al., *Thermally stable nanocrystalline gamma-alumina layers with highly ordered 3D mesoporosity*. Angewandte Chemie-International Edition, 2005. **44**(29): p. 4589-4592.
351. Niesz, K., P.D. Yang, and G.A. Somorjai, *Sol-gel synthesis of ordered mesoporous alumina*. Chemical Communications, 2005(15): p. 1986-1987.
352. Tian, B.Z., et al., *Self-adjusted synthesis of ordered stable mesoporous minerals by acid-base pairs*. Nature Materials, 2003. **2**(3): p. 159-163.
353. Zhang, Y., et al., *Synthesis and catalysis of nanometer-sized bimodal mesoporous aluminosilicate materials*. Catalysis Today, 2004. **93-5**: p. 615-618.
354. Ravikovitch, P.I., G.L. Haller, and A.V. Neimark, *Density functional theory model for calculating pore size distributions: pore structure of nanoporous catalysts*. Advances in Colloid and Interface Science, 1998. **76**: p. 203-226.
355. Terashita, K., S. Watano, and K. Miyanami, *DETERMINATION OF END-POINT BY FREQUENCY-ANALYSIS OF POWER-CONSUMPTION IN AGITATION GRANULATION*. Chemical & Pharmaceutical Bulletin, 1990. **38**(11): p. 3120-3123.
356. Li, Y.D., et al., *Measurement and statistics of single pellet mechanical strength of differently shaped catalysts*. Powder Technology, 2000. **113**(1-2): p. 176-184.
357. Holm, P., T. Schaefer, and H.G. Kristensen, *GRANULATION IN HIGH-SPEED MIXERS .5. POWER-CONSUMPTION AND TEMPERATURE-CHANGES DURING GRANULATION*. Powder Technology, 1985. **43**(3): p. 213-223.
358. Geim, A.K. and K.S. Novoselov, *The rise of graphene*. Nature Materials, 2007. **6**(3): p. 183-191.
359. Lee, C., et al., *Measurement of the elastic properties and intrinsic strength of monolayer graphene*. Science, 2008. **321**(5887): p. 385-388.
360. Balandin, A.A., et al., *Superior thermal conductivity of single-layer graphene*. Nano Letters, 2008. **8**(3): p. 902-907.
361. Wehling, T.O., M.I. Katsnelson, and A.I. Lichtenstein, *Adsorbates on graphene: Impurity states and electron scattering*. Chemical Physics Letters, 2009. **476**(4-6): p. 125-134.
362. Pereira, V.M., J. dos Santos, and A.H. Castro, *Modeling disorder in graphene*. Physical Review B, 2008. **77**(11): p. 17.
363. Pereira, V.M., et al., *Disorder induced localized states in graphene*. Physical Review Letters, 2006. **96**(3): p. 4.
364. Peres, N.M.R., F. Guinea, and A.H.C. Neto, *Electronic properties of disordered two-dimensional carbon*. Physical Review B, 2006. **73**(12): p. 23.
365. Ugeda, M.M., et al., *Electronic and structural characterization of divacancies in irradiated graphene*. Physical Review B, 2012. **85**(12): p. 5.
366. Tapasztó, L., et al., *Tuning the electronic structure of graphene by ion irradiation*. Physical Review B, 2008. **78**(23): p. 4.

367. Banhart, F., *Irradiation effects in carbon nanostructures*. Reports on Progress in Physics, 1999. **62**(8): p. 1181-1221.
368. Krasheninnikov, A.V. and F. Banhart, *Engineering of nanostructured carbon materials with electron or ion beams*. Nature Materials, 2007. **6**(10): p. 723-733.
369. Liu, X., et al., *Palladium Nanoparticles/Defective Graphene Composites as Oxygen Reduction Electrocatalysts: A First-Principles Study*. Journal of Physical Chemistry C, 2012. **116**(4): p. 2710-2719.
370. Machado, B.F. and P. Serp, *Graphene-based materials for catalysis*. Catalysis Science & Technology, 2012. **2**(1): p. 54-75.
371. Zhao, Z., et al., *Synthesis of a hierarchical three-component nanocomposite structure system with enhanced electrocatalytic and photoelectrical properties*. Chemistry (Weinheim an der Bergstrasse, Germany), 2012. **18**(17): p. 5248-55.
372. Guo, S.J. and S.H. Sun, *FePt Nanoparticles Assembled on Graphene as Enhanced Catalyst for Oxygen Reduction Reaction*. Journal of the American Chemical Society. **134**(5): p. 2492-2495.
373. Moussa, S., et al., *Pd-Partially Reduced Graphene Oxide Catalysts (Pd/PRGO): Laser Synthesis of Pd Nanoparticles Supported on PRGO Nanosheets for Carbon-Carbon Cross Coupling Reactions*. Acs Catalysis, 2012. **2**(1): p. 145-154.
374. Lv, X.J., et al., *Hydrogen evolution from water using semiconductor nanoparticle/graphene composite photocatalysts without noble metals*. Journal of Materials Chemistry, 2012. **22**(4): p. 1539-1546.
375. Liu, X., C.G. Meng, and Y. Han, *Substrate-mediated enhanced activity of Ru nanoparticles in catalytic hydrogenation of benzene*. Nanoscale, 2012. **4**(7): p. 2288-2295.
376. Liu, F., et al., *Fabrication of free-standing graphene composite films as electrochemical biosensors*. Carbon, 2012. **50**(1): p. 123-133.
377. Liang, Y.Y., et al., *Covalent Hybrid of Spinel Manganese-Cobalt Oxide and Graphene as Advanced Oxygen Reduction Electrocatalysts*. Journal of the American Chemical Society, 2012. **134**(7): p. 3517-3523.
378. Guardia, L., et al., *UV light exposure of aqueous graphene oxide suspensions to promote their direct reduction, formation of graphene-metal nanoparticle hybrids and dye degradation*. Carbon, 2012. **50**(3): p. 1014-1024.
379. Bajpai, R., et al., *Graphene supported nickel nanoparticle as a viable replacement for platinum in dye sensitized solar cells*. Nanoscale, 2012. **4**(3): p. 926-930.
380. Kou, R., et al., *Stabilization of Electrocatalytic Metal Nanoparticles at Metal-Metal Oxide-Graphene Triple Junction Points*. Journal of the American Chemical Society, 2011. **133**(8): p. 2541-2547.
381. Wu, H.M., D. Wexler, and H.K. Liu, *Durability investigation of graphene-supported Pt nanocatalysts for PEM fuel cells*. Journal of Solid State Electrochemistry, 2011. **15**(5): p. 1057-1062.
382. Wang, S.Y., X. Wang, and S.P. Jiang, *Self-assembly of mixed Pt and Au nanoparticles on PDDA-functionalized graphene as effective electrocatalysts for formic acid oxidation of fuel cells*. Physical Chemistry Chemical Physics, 2011. **13**(15): p. 7187-7195.
383. Sato, J., et al., *Oxygen Reduction Reaction Activity of Pt/Graphene Composites with Various Graphene Size*. Electrochemistry, 2011. **79**(5): p. 337-339.
384. Moussa, S., V. Abdelsayed, and M.S. El-Shall, *Laser synthesis of Pt, Pd, CoO and Pd-CoO nanoparticle catalysts supported on graphene*. Chemical Physics Letters, 2011. **510**(4-6): p. 179-184.
385. Lee, S.H., et al., *Hydrothermal synthesis of PtRu nanoparticles supported on graphene sheets for methanol oxidation in direct methanol fuel cell*. Materials Letters, 2011. **65**(21-22): p. 3281-3284.
386. Lee, J.S., et al., *Ionic liquid modified graphene nanosheets anchoring manganese oxide nanoparticles as efficient electrocatalysts for Zn-air batteries*. Energy & Environmental Science, 2011. **4**(10): p. 4148-4154.
387. Chen, X.M., et al., *Synthesis of "Clean" and Well-Dispersive Pd Nanoparticles with Excellent Electrocatalytic Property on Graphene Oxide*. Journal of the American Chemical Society. **133**(11): p. 3693-3695.

388. Choi, Y., et al., *Hybrid gold nanoparticle-reduced graphene oxide nanosheets as active catalysts for highly efficient reduction of nitroarenes*. Journal of Materials Chemistry, 2011. **21**(39): p. 15431-15436.
389. Chang, F., et al., *Highly efficient solvent-free catalytic hydrogenation of solid alkenes and nitroaromatics using Pd nanoparticles entrapped in aluminum oxy-hydroxide*. Tetrahedron Letters, 2010. **51**(32): p. 4250-4252.
390. Liu, S., et al., *"Green" electrochemical synthesis of Pt/graphene sheet nanocomposite film and its electrocatalytic property*. Journal of Power Sources, 2010. **195**(15): p. 4628-4633.
391. Li, Y., et al., *Palladium nanoparticle-graphene hybrids as active catalysts for the Suzuki reaction*. Nano Research, 2010. **3**(6): p. 429-437.
392. He, H.K. and C. Gao, *A General Strategy for the Preparation of Carbon Nanotubes and Graphene Oxide Decorated with PdO Nanoparticles in Water*. Molecules, 2010. **15**(7): p. 4679-4694.
393. Seger, B. and P.V. Kamat, *Electrocatalytically Active Graphene-Platinum Nanocomposites. Role of 2-D Carbon Support in PEM Fuel Cells*. Journal of Physical Chemistry C, 2009. **113**(19): p. 7990-7995.
394. Ferrari, A.C., et al., *Raman spectrum of graphene and graphene layers*. Physical Review Letters, 2006. **97**(18): p. 4.
395. Fan, Z.J., et al., *Facile Synthesis of Graphene Nanosheets via Fe Reduction of Exfoliated Graphite Oxide*. Acs Nano, 2011. **5**(1): p. 191-198.
396. Fasolino, A., J.H. Los, and M.I. Katsnelson, *Intrinsic ripples in graphene*. Nature Materials, 2007. **6**(11): p. 858-861.
397. Guo, H.L., et al., *A Green Approach to the Synthesis of Graphene Nanosheets*. Acs Nano, 2009. **3**(9): p. 2653-2659.
398. Simon, P. and Y. Gogotsi, *Materials for electrochemical capacitors*. Nature Materials, 2008. **7**(11): p. 845-854.
399. Lee, H., et al., *Fabrication of polypyrrole (PPy)/carbon nanotube (CNT) composite electrode on ceramic fabric for supercapacitor applications*. Electrochimica Acta. **56**(22): p. 7460-7466.
400. Futaba, D.N., et al., *Shape-engineerable and highly densely packed single-walled carbon nanotubes and their application as super-capacitor electrodes*. Nature Materials, 2006. **5**(12): p. 987-994.
401. Portet, C., G. Yushin, and Y. Gogotsi, *Electrochemical performance of carbon onions, nanodiamonds, carbon black and multiwalled nanotubes in electrical double layer capacitors*. Carbon, 2007. **45**(13): p. 2511-2518.
402. Yang, C.M., et al., *Nanowindow-regulated specific capacitance of supercapacitor electrodes of single-wall carbon nanohorns*. Journal of the American Chemical Society, 2007. **129**(1): p. 20-21.
403. Cheng, Q., et al., *Graphene and carbon nanotube composite electrodes for supercapacitors with ultra-high energy density*. Physical Chemistry Chemical Physics. **13**(39): p. 17615-17624.
404. Wang, Y., et al., *Supercapacitor Devices Based on Graphene Materials*. Journal of Physical Chemistry C, 2009. **113**(30): p. 13103-13107.
405. Si, Y.C. and E.T. Samulski, *Exfoliated Graphene Separated by Platinum Nanoparticles*. Chemistry of Materials, 2008. **20**(21): p. 6792-6797.
406. Sun, Y.Q., Q.O. Wu, and G.Q. Shi, *Graphene based new energy materials*. Energy & Environmental Science. **4**(4): p. 1113-1132.
407. Wei, W.F., et al., *Manganese oxide-based materials as electrochemical supercapacitor electrodes*. Chemical Society Reviews. **40**(3): p. 1697-1721.
408. Subramanian, V., et al., *Hydrothermal synthesis and pseudocapacitance properties of MnO₂ nanostructures*. Journal of Physical Chemistry B, 2005. **109**(43): p. 20207-20214.
409. Yu, P., et al., *Solution-combustion synthesis of epsilon-MnO(2) for supercapacitors*. Materials Letters. **64**(1): p. 61-64.
410. Subramanian, V., H.W. Zhu, and B.Q. Wei, *Nanostructured MnO₂: Hydrothermal synthesis and electrochemical properties as a supercapacitor electrode material*. Journal of Power Sources, 2006. **159**(1): p. 361-364.
411. Wang, X.L., A.B. Yuan, and Y.Q. Wang, *Supercapacitive behaviors and their temperature dependence of sol-gel synthesized nanostructured manganese dioxide in lithium hydroxide electrolyte*. Journal of Power Sources, 2007. **172**(2): p. 1007-1011.

- 412. Ye, C., Z.M. Lin, and S.Z. Hui, *Electrochemical and capacitance properties of rod-shaped MnO₂ for supercapacitor*. Journal of the Electrochemical Society, 2005. **152**(6): p. A1272-A1278.
- 413. Qu, Q.T., et al., *Electrochemical Performance of MnO(2) Nanorods in Neutral Aqueous Electrolytes as a Cathode for Asymmetric Supercapacitors*. Journal of Physical Chemistry C, 2009. **113**(31): p. 14020-14027.
- 414. Hu, C.C., Y.T. Wu, and K.H. Chang, *Low-temperature hydrothermal synthesis of Mn₃O₄ and MnOOH single crystals: Determinant influence of oxidants*. Chemistry of Materials, 2008. **20**(9): p. 2890-2894.
- 415. Xu, M., et al., *Hydrothermal synthesis and pseudocapacitance properties of alpha-MnO₂ hollow spheres and hollow urchins*. Journal of Physical Chemistry C, 2007. **111**(51): p. 19141-19147.
- 416. Zolfaghari, A., et al., *Capacitive behavior of nanostructured MnO₂ prepared by sonochemistry method*. Electrochimica Acta, 2007. **52**(8): p. 2806-2814.
- 417. Ghaemi, M., et al., *Charge storage mechanism of sonochemically prepared MnO₂ as supercapacitor electrode: Effects of physisorbed water and proton conduction*. Electrochimica Acta, 2008. **53**(14): p. 4607-4614.
- 418. Ni, J.P., et al., *Low-Temperature Synthesis of Monodisperse 3D Manganese Oxide Nanoflowers and Their Pseudocapacitance Properties*. Journal of Physical Chemistry C, 2009. **113**(1): p. 54-60.
- 419. Yu, P., et al., *Preparation and pseudo-capacitance of birnessite-type MnO(2) nanostructures via microwave-assisted emulsion method*. Materials Chemistry and Physics, 2009. **118**(2-3): p. 303-307.